ACTIVE VIBRATION AND NOISE ALLEVIATION IN ROTORCRAFT USING MICROFLAPS

by

Ashwani Kumar Padthe

A dissertation submitted in partial fulfillment
of the requirements for the degree of
Doctor of Philosophy
(Aerospace Engineering)
in The University of Michigan
2011

Doctoral Committee:

Professor Peretz P. Friedmann, Chair
Professor Dennis S. Bernstein
Professor Carlos E. Cesnik
Associate Professor Bogdan Epureanu

ॐ प्र णो॑ दे॒वी सर॑स्वती॒ वाजे॑भिर्वा॒जिनी॑वती ।
धी॒नामं॑वि॒त्र्यं॑वतु ॥ ३६ ॥

To Thee, the Knowledge of Which is the Source of my Strength.

ACKNOWLEDGEMENTS

The road that ends in the completion of this thesis has been a long one - arduous and rewarding. I could not have traversed it without the support and guidance of several people. I would like to thank some of them here. First and foremost, I would like to thank my advisor Prof. Peretz Friedmann for his unwavering support through the ups and downs of this project. His systematic and thoughtful way of conducting research inspired me and are likely to have an influence on all my future endeavors. I would like to thank Dr. Li Liu, whose saintly patience and willingness to share his expertise in various aspects of this work kept me going through the tough times. I find it difficult to overstate my gratefulness to him. I would also like to thank Prof. Dennis Bernstein for his support during my Masters and encouraging me to pursue a PhD degree. I would like to acknowledge Drs. Thomas Millott, Tim Myrtle, Marino de Terlizzi, Richard Cribbs, Gilles Depailler, and Dan Patt whose work was the foundation on which this research was built. I would also like to acknowledge the support I received from the Vertical Lift Research Center of Excellence (VLRCOE) sponsored by the NRTC with Dr. M. Rutkowski as grant monitor.

I would like to thank my friends Nikhil Sharma, Jay Patel, Gaurav Agrawal, Kranthi Bandaru, Manu Misra and their families and the Swadhyay Parivar, whose love and affection have been my primary sources of strength through my stay in

Ann Arbor. I would like to thank my family back in India for their love, support and encouragement. I would like to thank my officemates Abhijit Gogulapati, Bryan Glaz, Eric Muir, and Nicolas Lamorte for tolerating me and making my work experience more pleasurable. Thanks to Denise Phelps for her caring and friendly attitude while helping me through the administrative duties. Finally, I would like to thank my friends at the University of Michigan - Amit Salvi, Aseem Agarwal, Paul Davidson, Saumil Ambani, Nalin Chaturvedi, Vishal Jariwala, Satish Chimakurthi, Rahul Ahlawat, Rajit Johri, Siddharth Misra, Chandan Damannagari, and Devesh Kumar.

TABLE OF CONTENTS

LIST OF FIGURES

Figure

LIST OF TABLES

Table

LIST OF APPENDICES

Appendix

LIST OF SYMBOLS

a_l, a_m, a_d, a_{l0}, a_{l2}, a_{m0}, a_{m2}, a_{d0}, a_{d2}	Coefficients used in the ONERA dynamic stall model
A	Blade cross sectional area
A_{cs}	Control surface cross sectional area
b	Blade semi-chord
c	Speed of sound
c_b	Blade chord
c_{cs}	Control surface chord
c_p	Sectional pressure coefficient
c_{wu}	Weighting on the control input used in auto-weighting saturation approach
$\mathbf{c}$	Vector containing RFA coefficients
C_{df}	Parasitic drag coefficient of the fuselage
C_l, C_m, C_{hm}	Sectional lift, moment and hinge moment coefficients
C_Q	Torque coefficient
C_T	Thrust coefficient
C_W	Helicopter weight coefficient
$\mathbf{C_0}, \mathbf{C_1}, \mathbf{C}_n, \mathbf{D}, \mathbf{E}, \mathbf{R}$	Coefficient matrices from the RFA aerodynamic model
$\mathbf{C}_{Oj}$, $\mathbf{C}_{Ij}$, $\mathbf{C}_{NWij}$	Influence coefficients used in the free wake calculation
$\Delta C_L, \Delta C_M, \Delta C_D$	Contributions to the sectional lift, moment, and drag from the dynamic stall model
D	Drag force
D_0, D_1	Generalized normal velocity distributions corresponding to flap deflection
D_f	Parasitic drag of the fuselage
$\mathbf{D}(\psi, \phi)$	Wake distortion
e	Blade root offset from center of rotation
$\hat{e}_{xi}, \hat{e}_{yi}, \hat{e}_{zi}$	Unit vectors associated with the i^{th} coordinate system

E_l, E_m, E_d, E_{l0}, E_{l2}, E_{m0}, E_{m2}, E_{d0}, E_{d2}	Coefficients used in the ONERA dynamic stall model
$EI_{\eta\eta}$, $EI_{\zeta\zeta}$	Principal bending stiffness of the blade cross-section
f	Function that describes the moving surface generating sound
$\mathbf{f}$	Generalized load vector
$\mathbf{f_b}(.)$	Blade motion equations
$\mathbf{f_t}(.)$	Trim equations
F_T	Vertical force
$F_{HX4}, F_{HY4}, F_{HZ4}$	4/rev components of hub shear
$\mathbf{F_H}$	Instantaneous hub shear
$\mathbf{F_{Rk}}$	Resultant blade root forces for the k^{th} blade
g	Acceleration due to gravity
$g_{S_L}, g_{S_F}, g_{S_T}$	Distributed structural damping factors in lag, flap and torsion
$\mathbf{g_a}(.)$	Aerodynamic (RFA) state equations
$\mathbf{g_{aR}}(.)$	Reduced form of the aerodynamic (RFA) state equations
GJ_b	Torsional stiffness of the blade cross-section
GJ_c	Torsional stiffness of the control surface
$\mathbf{G}$	Laplace transform of $\mathbf{f}$
h	Plunge displacement at 1/4-chord
$\mathbf{h}$	Generalized motion vector
H	Horizontal force
$H(f)$	Heaviside function
H_m	Sectional hinge moment
$\mathbf{H}$	Laplace transform of the generalized motion vector
$\imath$	$= \sqrt{-1}$
I_{MB2}, I_{MB3}	Principal mass moments of inertia of the blade cross-section
I_{MC2}, I_{MC3}	Principal mass moments of inertia of the control surface cross-section
$\mathbf{I}$	Identity matrix
$J(\mathbf{z}_k, \mathbf{u}_k)$	Quadratic-form objective function
k	Reduced frequency = $\omega b/U$
K_p	Kernel for Possio integral equation
K_{NW}	Number of azimuthal steps for near wake retained

l_i	Components of local force intensity that acts on the fluid, $l_i = P_{ij} n_j$
l_r	Local force intensity on fluid in radiation direction $l_r = l_i r_i$
$\mathbf{l}$	Left rectangular matrix used in RFA coefficient evalution
L_b	Blade length
L_{cs}	Control surface length
m_{cs}	Mass of control surface per unit length
M	Local mach number
M_b	Mass of one blade
M_c	Mass of one control surface
M_r	Mach number in the radiation direction
M^{pt}	Rotor pitching moment about the hub center
M^{rl}	Rotor rolling moment about the hub center
M^{yw}	Rotor yawing moment about the hub center
$M_{HX4}, M_{HY4}, M_{HZ4}$	4/rev components of hub moment
$\mathbf{M_H}$	Instantaneous hub moment
$\mathbf{M_{Rk}}$	Resultant blade root moments for the k^{th} blade
n_d	Number of reduced frequency data points at which aerodynamic load responses are generated
n_L	Number of aerodynamic lag terms in the RFA approach
N_b	Number of rotor blades
N_δ	Number of control surfaces on the blade
$N_{H06}, \ldots, N_{H17}$	Noise levels of the 6^{th} - 17^{th} harmonics of blade passage frequency
p	Air pressure
p'	Acoustic pressure
$\bar{p}$	Nondimensional air pressure
$\mathbf{p_A}$	Distributed aerodynamic load per unit length of the blade
$\mathbf{p_D}$	Distributed structural damping load per unit length of the blade
$\mathbf{p_{Gb}}$	Distributed gravitational load per unit length of the blade
$\mathbf{p_{Ib}}$	Distributed inertial load per unit length of the blade
P_{cs}	Power needed to actuate the flap
P_{ij}	Compressive stress tensor $P_{ij} = p' \delta_{ij}$

P_R	Average rotor shaft power
$q_{wi}, q_{vi}, q_{\phi i}$	Coefficients of the flap/lead-lag/torsional mode shapes
q_∞	Dynamic Pressure
$\mathbf{q}$	Induced velocity
$\mathbf{q_b}$	Vector of blade degrees of freedom
$\mathbf{q_t}$	Vector of trim variables
$\mathbf{q_A}$	Distributed aerodynamic moment per unit length of the blade
$\mathbf{q_D}$	Distributed structural damping moment per unit length of the blade
$\mathbf{q_{Gb}}$	Distributed gravitational moment per unit length of the blade
$\mathbf{q_{Ib}}$	Distributed inertial moment per unit length of the blade
Q_t	Tail rotor torque
$\mathbf{Q}$	Aerodynamic transfer matrix
$\tilde{\mathbf{Q}}$	RFA approximation of the aerodynamic transfer matrix
$\mathbf{Q_z}$	Weighting matrix for plant output
r_l, r_m, r_d, , r_{l0}, r_{l2}, r_{m0}, r_{m2}, r_{d0}, r_{d2}	Coefficients used in the ONERA dynamic stall model
r	Distance between observer and source $\lvert\mathbf{x}-\mathbf{y}\rvert$
r_i	Components of vector $\hat{r}$
$\hat{r}$	Unit vector in radiation direction $(\mathbf{x}-\mathbf{y})/r$
$\mathbf{r}$	Right column vector used in RFA coefficient evalution
$\mathbf{r_b}$	Position of the blade when it generates the wake element
$\mathbf{r_p}$	Position vector of a point on the deformed blade
$\mathbf{r_w}$	Position of a wake element
$\mathbf{r_{EA}}$	Position vector for a point on the elastic axis
R	Blade radius
R_{LM}, R_D	Reverse flow factors for lift(moment) and drag, respectively
$\mathbf{R}$	Weighting matrix for control input
$\mathbf{R}_0$	Position vector of deformed elastic axis
$\mathbf{R_p}$	Position vector of a point on the blade before deformation
$\mathbf{R_t}$	Vector of trim residuals

$\bar{s}$	Nondimensional Laplace variable $\bar{s} = \frac{sb}{U}$
$\mathbf{S}$	Cross-weighting term in objective function J
t	Time
$\bar{t}$	Nondimensional time, reduced time
t_k	Time of controller update
T	Axial tension
T_t	Tail rotor thrust
T_{ij}	Lighthill stress tensor $T_{ij} = \rho v_i v_j + P_{ij} - a_\infty \rho' \delta_{ij}$
$\mathbf{T}$	Sensitivity matrix relating control input to plant output
$\hat{\mathbf{T}}$	Estimate of the sensitivity matrix $\mathbf{T}$
$\hat{\mathbf{T}}_{LS}$	Least-squares estimate of the sensitivity matrix $\mathbf{T}$
u, v, w	Displacements of a point on the blade's elastic axis due to blade deformation
U	Air velocity relative to the blade section
U_P,U_T	Perpendicular and tangential components of freestream velocity experienced by the blade
$\mathbf{u}(\mathbf{x}, t)$	Disturbance in flow velocity
$\mathbf{u}_k$	Control input at time t_k
$\mathbf{u}_{k,\text{opt}}$	Optimal control input
$\Delta\mathbf{u}_k$	$= \mathbf{u}_k - \mathbf{u}_{k-1}$
$\Delta\mathbf{U}_k$	Matrix composed of $\Delta\mathbf{u}_k$
v_n	Noise generating surface normal velocity
v_i, v_j	Components of fluid velocity in directions x_i and x_j
$\mathbf{v}$	Velocity vector
$\mathbf{V_A}$	Total air velocity vector
$\mathbf{V_{A1}}$	Airflow velocity due to forward flight, blade rotation and induced inflow
$\mathbf{V_{A2}}$	Airflow velocity due to blade dynamics
$\mathbf{V_{EA}}$	Velocity of a point on the elastic axis of the blade due to blade dynamics
$\bar{w}$	Normal velocity
$\mathbf{w}$	Disturbance to plant
W	Helicopter weight
$W(x, t)$	Normal velocity distribution
W_0, W_1	Generalized normal velocity distributions on the airfoil
$\mathbf{W}$	Matrix relating plant response to disturbance
x	Streamwise coordinate

x_{cs}	Distance from the hub to the center of the control surface
x_{rev}	Reverse flow boundary
$\mathbf{x}$	Aerodynamic state vector
X_t	Horizontal offset of tail rotor center from hub
X_A	Offset between the aerodynamic center and the elastic axis
X_H	Offset between the hinge point and the elastic axis
X_{Ib}	Offset of the blade cross-sectional center of mass from the elastic axis
X_{Ic}	Offset of the control surface cross-sectional center of mass from the hinge point
X_{IIb}	Offset of the blade cross-sectional center of area from the elastic axis
X_{IIc}	Offset of the control surface cross-sectional center of area from the hinge point
X_{FA}	Longitudinal offset between rotor hub and helicopter aerodynamic center
X_{FC}	Longitudinal offset between rotor hub and helicopter center of gravity
$\mathbf{X}$	Laplace transform of the aerodynamic state vector
$\bar{y}_{ob}, \bar{z}_{ob}$	Coordinates of a point on a blade cross-section relative to the elastic axis, measured in the "5" System.
Y	Lateral force
$\mathbf{z}_0$	Initial output condition of plant output
$\mathbf{z}_k$	Plant output at time t_k
$\mathbf{z}_{\text{NR}}$	Output vector for noise reduction
$\mathbf{z}_{\text{PWR}}$	Output vector for power reduction
$\mathbf{z}_{\text{VR}}$	Output vector for vibration reduction
Z_t	Vertical offset of tail rotor center from hub
Z_{FA}	Vertical offset between rotor hub and helicopter aerodynamic center
Z_{FC}	Vertical offset of fuselage center of gravity from hub
$\Delta\mathbf{z}_k$	$= \mathbf{z}_k - \mathbf{z}_{k-1}$
$\Delta\mathbf{Z}_k$	Matrix composed of $\Delta\mathbf{z}_k$
α	Angle of attack of the airfoil
α_{cr}	Critical angle of attack of the airfoil used for the separation criterion in the ONERA model
α_{re}	Relaxation factor

α_{tpp}	Tip-path plane angle
α_A	Blade local angle of attack
α_D	Descent angle
α_R	Rotor shaft angle of attack
β	Prandtl-Glauert compressibility correction, $\sqrt{1-M^2}$
β_p	Blade precone angle
δ	Dirac delta function
δ_f	Flap deflection
δ_{ij}	Kronecker delta
δ_{limit}	Saturation limit on flap deflection
$\delta_{\max}$	Maximum flap deflection
δ_{Nc}, δ_{Ns}	N/rev cosine and sine amplitude of the flap deflection
ϵ	Small dimensionless magnitude of the order of the blade slopes
$\lambda_x, \lambda_y, \lambda_z$	Main rotor inflow ratio components
λ_t	Tail rotor uniform inflow ratio
Π_l, Π_m, Π_d	States of the ONERA dynamic stall model
ϕ	Elastic twist about the elastic axis
ϕ_w	Wake age
ϕ_R	Lateral roll angle
ν	Airfoil or microflap oscillation frequency
ρ	Air density
ρ_b	Density of blade structure
ρ_c	Density of control surface structure
ρ_I	Radial position of interior circulation peak
γ	Lock number
γ_b	Intersection angle between vortex and blade
γ_n	Poles for RFA
γ_s	Strength of shed vorticity
γ_t	Strength of trailed vorticity
$\Gamma(r)$	Circulation distribution
Γ_I, Γ_O	Inboard and outboard circulation peaks, in dual wake model
η_b, ζ_b	Principal coordinates of a point in the blade cross-section
η_c, ζ_c	Coordinates in the flap attached coordinate system
μ	Advance ratio $= V_\infty \cos\alpha / \Omega R$
θ_0, θ_{1s},θ_{1c}	Collective and cyclic pitch components

θ_{0t}	Tail rotor collective pitch
θ_{pc}	Pilot pitch input $\theta_0 + \theta_{1c}\cos\psi + \theta_{1s}\sin\psi$
θ_{tw}	Blade pretwist angle
θ_G	Geometric pitch angle, $\theta_{pc} + \theta_{tw}$
ψ	Azimuth angle
σ	Rotor solidity
σ_t	Tail rotor solidity
τ	Source time
ω	Airfoil or microflap angular frequency of oscillation
ω_{Fi}	ith flapping frequency of the rotating blade
ω_{Li}	ith lead-lag frequency of the rotating blade
ω_{Ti}	ith torsional frequency of the rotating blade
Ω	Rotor angular velocity
ξ	Nondimensional quantity $\xi = x/b$

CHAPTER I

INTRODUCTION, LITERATURE REVIEW, AND OBJECTIVES

Due to their unique capability to hover, perform low-speed maneuvers in tightly constrained environments, and take-off and land vertically; helicopters are widely used for various civilian and military missions that fixed-wing aircraft cannot perform. To perform these tasks, helicopters have to operate in a complex aerodynamic environment, depicted in Fig. 1.1. In forward flight, blades on the side of the rotor that is advancing into the relative wind experience a higher dynamic pressure than the blades on the retreating side resulting in an asymmetry in the aerodynamic environment on the rotor disk. This inherent asymmetry combined with the flapping, lead-lag, and pitching motions of the rotor blades generates highly unsteady aerodynamic loads which are transmitted to the hub and the fuselage as vibrations. Vibratory loads, predominantly the N_b/rev harmonic components, where N_b is the number of rotor blades, have been a source of concern in the design and maintenance of helicopters since their early developmental days [81]. Vibra-

tions cause crew and passenger discomfort and reduce the airframe and component fatigue lives resulting in high maintenance costs. Like vibrations, noise has also been an undesirable characteristic of rotorcraft since their inception and has become an increasingly important problem for modern helicopters due to stringent limitations imposed by the regulations. The high noise levels generated during low speed approach flight conditions can severely limit a civilian helicopter's community acceptance and render a military helicopter vulnerable to easy detection. High levels of vibration and noise at low speed descending flight conditions are attributed to the blade-vortex interaction (BVI) phenomenon which occurs when a rotating blade encounters the tip vortices shed by the preceding blades. At high speeds, dynamic stall, which is characterized by time dependent flow separation on the retreating side of the rotor disk, is a dominant source of vibratory loads. Also at high speeds, transonic effects at the blade tip generate noise known as the high-speed impulsive (HSI) noise.

Increasingly stringent requirements on acceptable noise and vibration levels of modern helicopters have motivated substantial research in the rotary-wing community towards designing efficient control technologies that can produce quieter and smoother helicopters while showing minimal impact on the airwothiness and structural integrity of the helicopter. During the last four decades, various active control approaches, such as the higher harmonic control, individual blade control, actively controlled conventional plain trailing-edge flaps, and the active twist rotor have been explored and shown to have potential as effective means for noise and

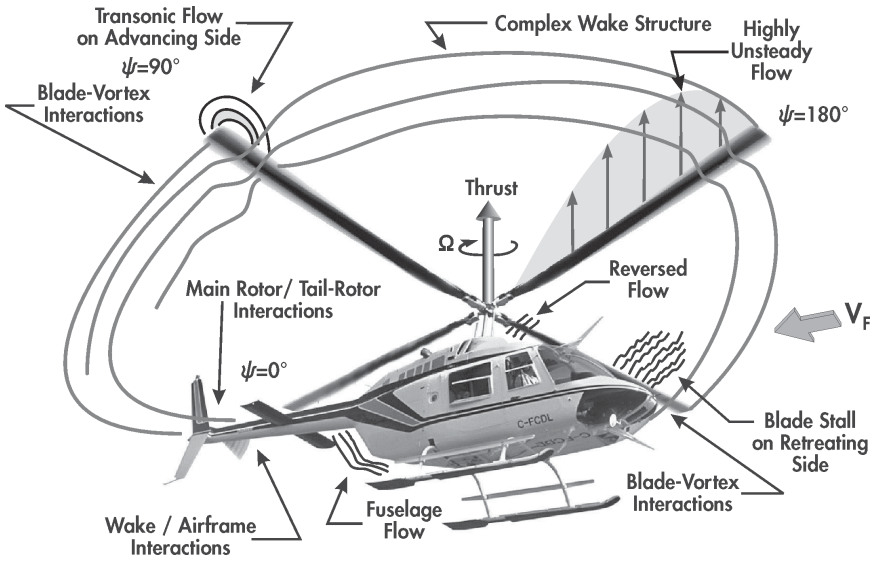

Figure 1.1: Various elements of the complex aerodynamic environment of a helicopter.

vibration reduction in rotorcraft. Several factors such as: excessive implementation costs, mechanical complexities, high control power requirements, limitations on actuation frequencies, and reliability concerns have prevented the implementation of these approaches on a production helicopter. This current state of active control is motivating the search for more cost effective approaches such as microflaps.

The microflap, which is a small tab typically 1-5% in chord, located near the trailing edge of an airfoil as shown in Fig. 1.2, has recently emerged as a promising device for active control in helicopters. The microflap is derived from the Gurney flap, shown in Fig. 1.3, which was originally conceived by Dan Gurney to increase the downward force generated by the spoiler on his race car. The Gurney flap causes the flow to turn around the trailing edge resulting in the formation of two counter-rotating vortices behind the microflap, shown in Fig. 1.3. The turning of the flow shifts the trailing edge stagnation point to the bottom edge of the mi-

croflap thus changing the Kutta condition and increasing the effective camber of the airfoil [23,76].

Unlike the Gurney flap that is permanently fixed to the airfoil, the microflap can be deployed normal to the airfoil surface. In spite of its small size, the microflap has been shown to enhance the maximum lift coefficient of an airfoil by up to 30% without significant drag penalties [6,84,127]. The microflap when deployed also increases the nose-down pitching moment of the airfoil. The microflap's ability to effect the lift and pitching moment on an airfoil indicates its potential as an active on-blade vibration and noise control device for helicopters. Furthermore, the size of the microflap when compared to plain trailing-edge flaps represents a distinct advantage permitting high bandwidth actuation with small actuation power requirements, minimal loss in structural stiffness of the wing, and lower wing warping. Another interesting aspect of the microflaps is that their small size might allow them to be retrofitted on existing helicopter blades with suitable modifications. Despite its potential benefits, the microflap has not been carefully examined for helicopter noise and vibration reduction applications, primarily due to its recent emergence on the scene combined with the lack of computational tools suitable for active control studies using the microflap. The overall goal of this thesis is to develop such computational tools and use them to investigate and evaluate the effectiveness of the microflap in reducing helicopter noise and vibrations.

A review of the various existing approaches to helicopter vibration and noise reduction is provided in section 1.1. Various computational and experimental

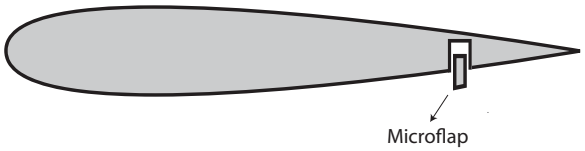

Figure 1.2: An illustration of the microflap.

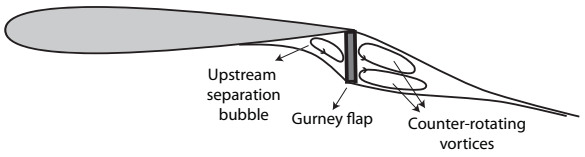

Figure 1.3: An illustration of the flow behind a Gurney flap.

studies examining the aerodynamic effects of the Gurney flap and the microflap are reviewed in section 1.2.1. Section 1.2.2 provides a literature review of the various applications of microflap that have been studied so far. A literature review of various actuation systems that have been developed for practical implementation of the microflap are discussed in section 1.2.3. Finally, the objectives and the contributions of this dissertation are presented in section 1.3.

1.1 Review of the Available Helicopter Vibration and Noise Reduction Approaches

1.1.1 Helicopter Vibration Reduction Approaches

Two fundamentally different approaches to reducing vibrations in helicopters have evolved over time. The traditional approaches which are relatively more mature and widely implemented are based on passive techniques involving absorbers, isolators, and attenuators [81, 108, 139]. However, these devices have significant weight penalties. A more recent passive approach that has been examined for helicopter vibration reduction involves the use of structural optimization to minimize vibrations through modification of the mass, stiffness, and geometrical properties of the rotor blade. A detailed survey of the developments in the structural optimization approach can be found in Refs. 20, 43, 48.

During the last forty years, a remarkable reduction in the acceptable levels of vibrations lead to the development of various active control approaches, including the actively controlled trailing edge flaps. Detailed reviews of the various active control approaches to the vibration reduction problem can be found in Refs. 46, 98. Active control approaches that have been widely studied are: 1) higher harmonic control (HHC), 2) conventional individual blade control (IBC), 3) active control of structural response (ACSR), 4) active twist rotor blades (ATR), and 5) actively controlled trailing-edge flaps (ACF). All the active control approaches, except ACSR, influence the vibration levels by modifying the aerodynamic loading on the rotor,

or the rotating system.

The HHC approach was the first approach and has received considerable attention. The HHC system minimizes the rotor vibrations by actively controlling the blade pitch angle through the non-rotating lower portion of a conventional swashplate. Effectiveness of the HHC controller in reducing vibrations has been demonstrated through computations, wind-tunnel tests, and flight tests [46]. However, despite its initial success the HHC approach has not been implemented on a production helicopter. The primary reasons are: (1) limitation on the control potential due to the fact that all blades use the same pitch input, and (2) excessive implementation costs.

An alternative to controlling vibrations through a stationary swashplate is the conventional individual blade control approach, where each blade is individually controlled by introducing pitch inputs in the rotating reference frame. This approach, pioneered by Kretz [70], overcomes some of the limitations associated with the HHC approach. The IBC approach allows independent control of each blade, with actuators located between the swashplate and the blade in the rotating frame. An IBC approach based on blade root actuation has been tested on the MBB BO-105 and UH-60 rotor systems at the NASA Ames 40 x 80 foot wind tunnel [58,130]. The IBC system has also been flight tested on an MBB BO-105 helicopter [113]. In spite of its effectiveness, implementation of the conventional IBC on a production helicopter has been prevented due to high control power requirements, mechanical complexity, and cost.

An alternative approach to individual blade control is the active twist rotor which has been shown to be an effective means for helicopter vibration reduction. Anisotropic piezo-composite actuators are implemented by embedding active fibers in a composite. The application of a voltage on the actuator modifies the twist distribution of the blade, and changes the aerodynamic environment and the vibratory loads. Wind tunnel tests performed on the NASA/Army/MIT active twist rotor [118,119,142] in hover and forward flight have shown that the ATR is an effective vibration reduction technology. Closed-loop control tests were conducted on the ATR system demonstrating excellent reduction in the 4/rev and 1/rev vibratory normal hub shear force over a range of flight conditions [120]. Another implementation of the ATR which utilizes a piezo-electrically twisted composite beam with bending-torsion coupling to twist the entire blade was developed and tested in a wind-tunnel by Bernhard and Chopra [9]. The active piezo-electric fiber is a relatively new technology and has several challenges associated with its implementation. The primary challenges are achieving uniformity of material properties and actuation characteristics, reducing fabrication costs, and requirement for very high actuation voltages [9].

The active control of structural response approach is the only approach that has been implemented on a production helicopter, the Westland EH101 [126]. In the ACSR approach, actuators placed at select locations are used to excite the fuselage and produce vibratory loads. The excitation is chosen such that the effective response of the fuselage due to the rotor hub loads and the controlled excitation is

reduced to a minimum at a selected location, such as the pilot seat. A comprehensive analytical simulation of the ACSR was developed by Cribbs, Friedmann and Chiu [29] using a finite element model for the fuselage. Acceleration amplitudes at the pilot seat and the rear cabin were reduced below 0.05g over a range of advance ratios.

In the past twenty years, the actively controlled flaps (ACF) have been proven to be an effective means for helicopter vibration reduction [44, 45]. The ACF system reduces vibrations through a time-dependent deflection of the flap resulting in a redistribution of the unsteady aerodynamic loads on the rotor blade. The ACF requires significantly lower actuation power when compared to the HHC and conventional IBC systems. Furthermore, the ACF system has no adverse effects on the helicopter airworthiness as it operates independent from the primary control system [46]. The ACF approach thus represents a more cost effective approach to individual blade control.

The first comprehensive computational study demonstrating the effectiveness of active flaps for helicopter vibration reduction was conducted by Millott and Friedmann [87]. In this study, a coupled flap-lag-torsional isotropic blade model, including geometric nonlinearities due to moderate deflections was used. Modified quasi-steady Theodorsen theory was used to determine the aerodynamic loads for the blade/trailing-edge flap combination. The actively controlled flap was modeled as a 12% span, 25% chord, servo flap centered at the 75% span location. The 4/rev hub shears and moments were reduced by 90% for a torsionally soft

blade and by 80% for a torsionally stiff blade at an advance ratio $\mu = 0.3$.

Myrtle and Friedmann [92] extended this work by replacing the quasi-steady aerodynamic model with a two-dimensional, compressible, time-domain, unsteady aerodynamic model based on the rational function approximation (RFA) approach. Subsequently, a free-wake model was introduced in to the analysis by deTerlizzi and Friedmann [31, 32] in order to accurately model the vibrations induced by blade-vortex interaction at low advance ratios. With the improved aerodynamic model, over 80% vibration reduction was recorded under BVI conditions. In order to capture the dynamic stall induced vibrations at high speeds, a dynamic stall model based on the ONERA dynamic stall model [105] was incorporated into the analysis by Depailler and Friedmann [33, 34]. The ONERA dynamic stall model can be expressed as a time-domain, state-space aerodynamic model and hence is suitable for aeroelastic analysis. Significant vibration reduction was noticed using the active flaps at high speeds where dynamic stall is predominant. Subsequently, a modified version of the noise prediction code WOPWOP [15] was incorporated into the analysis by Patt, Liu, and Friedmann [78, 98]. The code was used to investigate the effectiveness of actively-controlled flaps for simultaneous BVI noise and vibration reduction. A consolidation of the previously mentioned research efforts resulted in a comprehensive rotorcraft analysis tool referred to as the Active VIbration and NOise Reduction (AVINOR) code [52]. A modified version of this code is used for all the rotorcraft vibration and noise control studies presented in this thesis.

Recently the AVINOR code was used to develop combined active/passive rotor blade optimization approaches based on surrogate based optimization and the actively controlled flaps [51]. A surrogate is an approximation, of the objective function used for optimization, generated using a limited number of function evaluations over the design space. An efficient global optimization (EGO) algorithm combined with kriging surrogates was used to identify blade designs that are suitable for vibration reduction at high and low advance ratios. A blade design yielding 71% vibration reduction under BVI conditions and 26% vibration reduction at high-speed forward flight conditions was identified using multi-objective function optimization techniques.

The ACF approach for helicopter vibration reduction has also been experimentally validated [30,36,47,69,86]. Whirl-tower tests of a full-scale, five-bladed bearingless MD 900 helicopter rotor modified with a piezoelectric-actuated trailing edge flap on each blade, were conducted by the Boeing company as part of the SMART (Smart Material Actuated Rotor Technology) Rotor Demonstration Program funded jointly by NASA, DARPA, and the Boeing company [129]. Recently, wind-tunnel tests of the SMART active flap rotor were conducted at the NASA Ames 40x80 foot wind tunnel [128]. The tests demonstrated up to 80% reduction in vibratory hub loads. The impact of the active flap on rotor smoothing and performance was also demonstrated. These tests were conducted primarily using open-loop control inputs with $\pm 3^{\circ}$ saturation limits on the flap deflection. The ACF technology was also flight tested by Eurocopter on a BK-117 hingeless rotor

system equipped with three piezoelectrically actuated active flaps [68]. Up to 90% reduction was observed in the 4/rev vibratory loads using open loop control.

Based on the foregoing literature review it is evident that various active and passive control technologies have been explored and shown to reduce helicopter vibrations successfully.

1.1.2 Helicopter Noise Reduction Approaches

Helicopter noise is composed of contributions from the main rotor, tail rotor, engine, and gearbox. However, the major source is usually the main rotor. High-speed impulsive noise which is dominant at high speed flight conditions, propagates primarily in the plane of the rotor with peak noise observed in the region forward of the helicopter [17]. Blade-vortex interaction noise is dominant at low-speeds and propagates out of the rotor plane making it more audible to the observers on the ground [17]. Consequently, BVI noise has been the primary focus of many helicopter noise reduction studies.

Both passive and active control methods have been studied for rotorcraft noise reduction applications. Several computational and wind tunnel studies conducted using passive methods such as modification of blade tip shapes, blade planform, and twist distribution to reduce rotorcraft noise have been reported by Yu in Ref. 144. Blade tip shapes play an important role in blade airloads, which influence tip vortex formation. Noise reductions of up to 5 dB were demonstrated using modified tip geometries [144].

Active blade control concepts such as the higher-harmonic control, conventional individual blade control, and the active flaps have been successfully shown to reduce rotor noise. These active control techniques reduce BVI noise by modifying the blade airloads and blade aeroelastic deflections which in turn influence the tip vortex strength, blade-vortex miss distance, and the blade-vortex interaction angle. Comprehensive reviews of various active noise reduction studies are provided in Refs. 144, 145.

The HHC technology has been experimentally tested at the NASA Langley Transonic Dynamics Tunnel (TDT) [18, 19] and the German-Dutch Wind Tunnel (DNW) [122, 123, 125, 146] demonstrating up to 6 dB BVI noise reduction using open-loop control methods. It was also noted in these tests that the control inputs that yielded maximum noise reduction caused an increase in the vibration levels. The Higher-harmonic control Aeroacoustics Rotor Test (HART) conducted at the DNW is the most comprehensive experimental study of the effects of the HHC technique on BVI noise and vibration reduction conducted so far [122]. Wind-tunnel tests were conducted with a 40% geometrically and dynamically scaled BO-105 main rotor. A detailed set of data including blade airloads, blade deflections, acoustic signatures, blade surface pressure distribution, and tip vortex geometry and strength was acquired using extensive instrumentation. A reduction of 6 dB in BVI noise was achieved using a 3/rev open-loop control input. A follow-up to the original HART test known as the HART II [77,115,135,146] has been conducted using more extensive instrumentation aiming to further improve the physical un-

derstanding behind BVI noise generation and reduction. Computational studies were conducted by the Army Aeroflightdynamics Directorate (AFDD), the DLR, the ONERA, and NASA Langley as complementary studies to the HART experiments [133]. The blade-vortex miss distance was identified as playing a major role in reducing BVI noise. In a different study, results obtained from the University of Maryland Advanced Rotor Code (UMARC) were validated against HART test data by Tauszig [131]. In another study, Wachspress and Quackenbush [140] compared their comprehensive analysis code, CHARM, with HART test data. The correlation between the HART experimental results and the computational results obtained in the studies described above was inconsistent, showing good agreement for only a few cases. It was suggested in Ref. 133 that further improvements in wake modeling are required to get consistently accurate predictions. The University of Michigan AVINOR simulation code was also validated against the HART test data by Patt, Liu, and Friedmann [101, 102]. Blade tip deformations, aerodynamic loads, and acoustic pressure levels obtained from the simulation code and the HART experiments were compared. Excellent agreement was obtained for the baseline case while the comparisons for the minimum vibration and minimum noise cases were reasonably good.

The IBC system was first studied for noise reduction at the NASA Ames 40×80 wind tunnel [56, 57] on a full-scale BO-105 rotor. Open loop tests conducted at a heavy BVI flight condition indicated that the 2/rev input was the most effective for noise reduction. Noise levels were reduced by up to 9 dB on the advancing side by

appropriately choosing the phase of the control input. Similar to the HHC tests, the optimal control inputs for reducing BVI noise usually resulted in an increase in the vibration levels. Subsequently, the IBC system was tested at the NASA Ames 40×80 wind tunnel facility on a UH-60 rotor using open-loop control inputs yielding up to 10 dB noise reduction on the advancing side [58]. The IBC system was also flight tested on a BO-105 [7, 8] demonstrating up to 5 dB noise reduction using a 2/rev control input. Results from the flight tests were compared to computations showing marginal agreement [82, 124].

Actively controlled trailing-edge flaps have been shown to be effective for BVI noise reduction through several experimental and computational studies [22,30,54, 101, 102, 128, 141]. Experiments conducted under the SMART rotor project demonstrated reductions of up to 6dB in both BVI noise during low-speed descending flight and in-plane noise during high-speed level flight using active flaps [128]. Application of ACF for BVI noise reduction was examined through several analytical studies performed at the Mc-Donnel Douglas Helicopter company [22, 54]. These studies were conducted using a modified version of the Comprehensive Analytical Model of Rotorcraft Aerodynamics and Dynamics (CAMRAD/JA) [62] code and the WOPWOP code [15] for acoustic prediction. Noise reductions of the order of 5 dB were obtained. Subsequently, tests performed at the NASA Langley 14×22 wind tunnel [30] on a two-bladed rotor with a single flap equipped on each blade demonstrated up to 4 dB reduction in noise levels. In another interesting study, tests were conducted at the NASA Ames 7×10 foot wind tunnel on a 2-

bladed rotor using steady flap deflections and up to 7 dB BVI noise reduction was recorded [141].

Application of actively-controlled flaps for BVI noise and vibration reduction was extensively studied using the comprehensive rotorcraft analysis code AVINOR [101, 102]. Acoustic calculations were performed using the WOPWOP code, which was modified to account for a fully flexible blade model. The effect of BVI noise reduction on vibrations and vice-versa was examined at a heavy BVI descending flight condition. Simultaneous reduction of noise and vibration was successfully demonstrated using a dual active flap configuration. A reduction of about 5 dB on the advancing side noise combined with about 40% vibration reduction was achieved. The flap deflections were restricted to $\pm 4^{\circ}$ saturation limits.

As for the case of vibrations, active control approaches such as the HHC, conventional IBC, and the ACF have been extensively studied and shown to be effective for helicopter BVI noise reduction. However, none of these approaches has been implemented on a production helicopter.

1.2 Literature on Gurney Flaps and Microflaps

The microflap due to its unique combination of aerodynamic effectiveness and small size, can potentially overcome some of the limitations associated with the implementation of the active control approaches discussed in the preceding sections. The microflap is a relatively new device, consequently, limited number of

studies have been conducted examining its aerodynamic effects. However, the Gurney flap, which is a static microflap, has been extensively studied using both experiments and computations. This section provides a review of the literature on microflap aerodynamics and its applications. A brief review of different approaches to implementing a microflap actuation system is also provided.

1.2.1 Gurney Flap and Microflap Aerodynamics

The Gurney flap was first studied for aerospace applications by Liebeck, who conducted one of the earliest experimental studies investigating the aerodynamics of a Gurney flap [76]. Liebeck observed, using a tufted probe, significant turning of the flow around the trailing-edge towards the Gurney flap. He also observed a reverse flow region behind the Gurney flap which he hypothesized was due to the formation of two counter-rotating vortices behind the flap as shown in Fig. 1.3. The turning of the flow around the trailing-edge shifts the trailing-edge stagnation point to the bottom edge of the Gurney flap. This shift in the stagnation point changes the Kutta condition of the airfoil which in turn increases the effective camber of the airfoil [23]. Several experimental and computational studies have been conducted analyzing the aerodynamic effects of a Gurney flap. Depending on its size and location, the Gurney flap is capable of increasing the maximum lift coefficient of an airfoil by up to 30%, based on experiments conducted at Reynolds numbers over 1 million [6,25,84,127]. Wind-tunnel test results reported in Refs. 6, 26, 75, 84, 127 indicate that Gurney flaps placed on the lower

surface of the airfoil increase the maximum lift, accompanied by a positive shift in the lift curve. These findings have also been confirmed using computational fluid dynamics (CFD) simulations [6,23,59]. The increase in lift was found to be a result of an increase in the lower-surface pressures near the trailing-edge of the airfoil accompanied by a decrease in the upper-surface pressures near the leading edge and over the middle parts of the airfoil. These phenomena also result in an increased nose-down pitching moment. It was also noted that placing a Gurney flap on the upper surface of the airfoil can have a negative effect on the lift resulting in a downward shift of the lift curve [6].

The lift increment generated from the Gurney flap improves with increasing free-stream angles of attack [23]. The drag penalty due to the Gurney flap also increases with increasing free-stream angle of attack. This is because with increasing angle of attack, the lower surface boundary layer thickness is reduced due to the more favorable pressure gradient, and hence the ratio of flap height to boundary layer thickness is increased. The effects of Gurney flap size on the aerodynamic characteristics of an airfoil have been studied [6,50,84]. It was noted that increasing the Gurney flap height generally tends to augment its lift enhancing effects. However, the additional lift gained from a Gurney flap is not a linear function of its height [50]. The gain in lift diminishes with increasing Gurney flap height. Also, increasing the Gurney flap height to a magnitude that exceeds the boundary layer thickness results in a significant increase in drag. Thus, for a Gurney flap to yield a beneficial lift-to-drag ratio, its height needs to be smaller than the boundary-layer

thickness [50]. Several studies have discovered that a Gurney flap close to 2%c in height yields the best lift-to-drag ratio [76, 96].

The chordwise location of the Gurney flap was found to have a strong effect on its ability to increase the airfoil lift. The Gurney flap is most effective when placed at the trailing edge of the airfoil [6, 50, 75]. However, the trailing edge of a typical airfoil section does not provide sufficient structural volume to house a retractable Gurney flap and an actuation device. Therefore, the optimal tab location is likely to exist as far aft on the airfoil section as the volume requirements permit.

The effect of Gurney flap shape and its angle of attachment was experimentally studied in Refs. 75 and 134. Introducing spanwise variations in the Gurney flap geometry, such as serrations, was found to have a beneficial effect on the Gurney flap's performance [134]. A Gurney flap attached perpendicular to the airfoil surface produced the largest increase in the lift coefficient but also caused the highest drag penalty [75]. A Gurney flap attached at a 45° angle to the airfoil surface was found to produce the best lift-to-drag ratio.

An oscillating microflap is a recent innovation and therefore very few studies examining its unsteady aerodynamics can be found in the available literature. The unsteady aerodynamic effects of a deployable microflap were computationally studied in Refs. 23, 24, 66, 73. It was found that the unsteady lift amplitude due to an oscillating microflap reduces with increasing reduced frequency, a phenomenon similar to that predicted by Theodorsen's theory for an airfoil oscillating in pitch. It was also found that the peak lift generated by an oscillating microflap

is less than the lift due to a static Gurney flap and the peak drag is greater than that due to a static Gurney flap [24]. Similar results were also found in the current study using three different microflap configurations [97] as discussed in Chapter II.

1.2.2 Microflap Applications

Microflaps have been studied for various applications such as flutter suppression of high aspect ratio flexible wings, aeroelastic control of a blended-wing-body configuration, wing trailing edge vortex alleviation, aerodynamic load control for wind turbine blades, and for rotorcraft performance enhancement [11,23,65–67,71, 74,83,93,95,138,143]. Computational studies and wind-tunnel experiments were conducted in Ref. 74 to show that microflaps can increase the flutter speed of a highly flexible wing by up to 22%. For the computational analysis, aerodynamic effects of the microflap were modeled using a modified thin airfoil theory with some empirical inputs. The microflap was modeled as being either fully deployed or fully retracted. Another study proposed the use of microflap for control of aeroelastic response at the wing tip of a flexible blended-wing-body configuration [71]. Recent studies for fixed wing applications [83,95,138] suggest that microflaps can also be used for wake manipulation, by inducing time-varying perturbations that excite vortex instability in the wake.

The potential of microflaps with application to active load control in wind turbine blades has been explored computationally and experimentally on represen-

tative turbine airfoil sections by van Dam and colleagues [23, 27, 93]. Specifically, the capability of microflaps to mitigate turbine blade root loading due to wind gusts was demonstrated [27]. Substantial reduction in turbine blade root bending moment (reduction of peak bending moment ranging from 30-50%) was observed in Ref. 143 using microflaps. Aerodynamic effects of the microflap were modeled based on experimental measurements obtained using a static Gurney flap.

Few other studies using permanently fixed Gurney flaps have been conducted and are discussed here for completeness. The effectiveness of Gurney flaps in increasing the maximum lift coefficient and the lift-to-drag ratio of a micro aerial vehicle's thin-airfoil wing at low Reynolds numbers was demonstrated experimentally in Ref. 3. The effect of a Gurney flap on a compressor cascade model at low Reynolds numbers was experimentally investigated in Ref. 90. Experimental results indicated that the Gurney flap can be used to improve compressor performance by delaying stall on the compressor blades. The effect of Gurney flaps on the aerodynamic performance of microscale rotors was studied in Ref. 94. Spin tests were conducted on a small-scale microrotor (blade tip Reynolds number $< 20,000$) with a 2%c Gurney flap attached along the trailing edge of the rotor blade. An increase of 50-75% in the rotor thrust accompanied by only 20-30% increase in power penalty was observed over a range of collective pitch settings. Preliminary studies on rotorcraft performance enhancement using permanently attached Gurney flaps (of size less than 2%c) were conducted by Kentfield in Ref. 65. The effect of Gurney flaps on the airfoil lift and drag was modeled as a curve fit

of experimental data obtained for Gurney flaps of various sizes. Wind-tunnel tests conducted on a model helicopter confirmed that Gurney flaps may have beneficial effects on rotorcraft performance.

More recently, deployable microflaps have been studied as active control devices for rotorcraft performance enhancement [66,67]. A relatively simple deployment schedule where the microflaps were deployed primarily on retreating side of the disk was used. The maximum thrust of the rotor was enhanced by 10% using microflaps with a height of 1%c distributed along the entire blade span. The unsteady aerodynamics of the microflap were modeled using a modified version of the Hariharan-Leishman unsteady flapped airfoil model [53]. Indicial responses from CFD simulations were used to develop the aerodynamic model for microflaps. However, this model is suitable only for a microflap located at the trailing edge.

A Navier-Stokes flow solver coupled with a structural dynamics solver was employed in Refs. 88,89 to study the effectiveness of microflap for rotor vibration reduction. The oscillating microflap was simulated in CFD using a dynamic wall boundary condition. The magnitude and phase angles of the microflap deflection schedule were manually adjusted in order to identify the optimal values for vibration reduction. More than 80% reduction in the vertical vibratory hub loads was observed. However, no closed-loop control studies were performed.

Based on the literature review provided here, it is evident that despite its relative novelty, the microflap has been studied quite extensively and its potential for

various active control applications has been demonstrated. The potential of microflap for rotorcraft performance enhancement has also been shown. However, application of the microflap for rotorcraft noise and vibration reduction has not been considered. Specifically, closed-loop control studies have not been conducted to investigate the effectiveness of microflap for rotorcraft noise and vibration reduction.

1.2.3 Practical Implementation of Microflaps

Due to the small size of the microflaps, their practical implementation can pose a variety of challenges. An ideal actuation system for the microflaps needs to be compact and lightweight with a capability to provide high frequency actuation with low power requirements. Conventional hydraulic and pneumatic actuation systems may not be a viable option for microflap actuation because of their large size and weight. Actuation methods based on electro-mechanical, electromagnetic, and piezoelectric systems are viable options for microflaps. This section briefly describes the various actuation mechanisms that were implemented for microflaps as part of the studies mentioned in Section 1.2.2.

In the wind-tunnel experiments conducted at Stanford University for application of microflaps to flutter suppression of high aspect ratio flexible wings [74], a set of 26 microflaps were attached along the trailing edge of a fixed wing and were actuated using DC motor actuators shown in Fig. 1.4. The actuator and the microflap setup used by Matalanis and Eaton [83] for their experiments conducted at

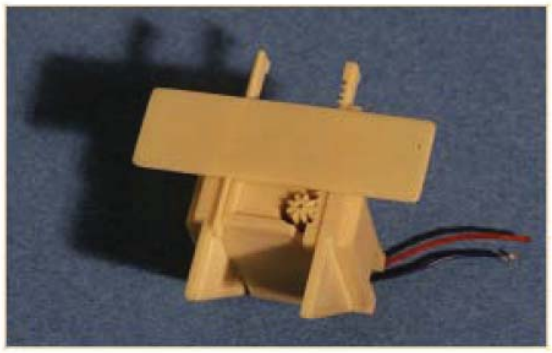

Figure 1.4: A DC motor based actuator for microflaps used in flutter suppression studies at the Stanford Flow Control Wind Tunnel [74].

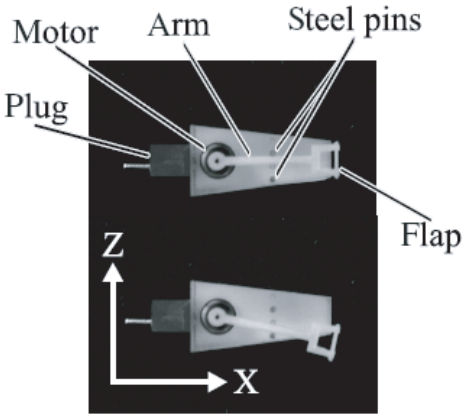

Figure 1.5: A DC motor based rotating actuation system for microflaps implemented at the Stanford Flow Control Wind Tunnel [83].

the Stanford Flow Control Wind Tunnel is shown in Fig. 1.5. The outer body of the setup is machined out of acrylic and the microflap and arm are made out of Delrin machined by laser ablation. The connecting plug in front of the body is used to transmit current to the dc motor that moves the microflap. Steel pins are used as stops to limit the motion of the flap.

For the experiments in Ref. 93 studying microflaps for active load control in wind turbine blades, the microflap was modeled as a translational slider shown

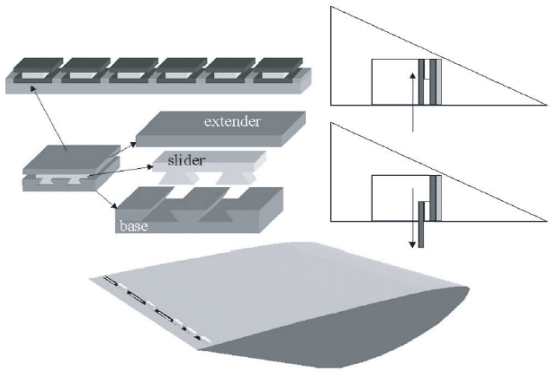

Figure 1.6: A translational sliding actuation system for microflaps implemented at the UC Davis Aeronautical Wind Tunnel Facility [93].

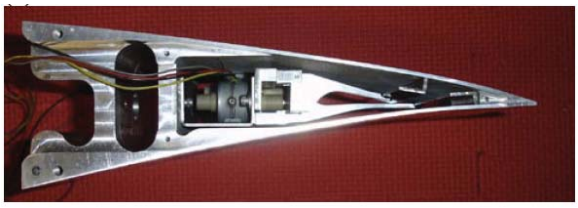

Figure 1.7: A linear actuator system for microflaps implemented at the UC Davis Aeronautical Wind Tunnel Facility [27].

in Fig. 1.6. The microflap assembly consists of three pieces, a base, a slider, and an extender. This unique design allows the microflaps to slide without incurring any hinge moments. As shown in Fig. 1.6, these small modular assemblies may be readily mounted in to slots on a wing or a blade. The actuating mechanism was based on a mechanical linkage operated using a servo-motor. In another experimental study conducted at the UC Davis Aeronautical Wind Tunnel a linear actuator based microflap actuation system was used [27]. The microflaps were deployed using lever arms controlled by linear actuators located at 0.60% chordwise location from the leading edge as shown in Fig. 1.7. The microflap is controlled in a binary fashion implying that it is either fully deployed or fully retracted.

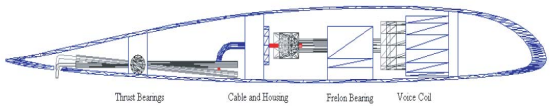

Figure 1.8: A voice coil actuator based setup for microflap actuation developed at the Penn State University [132].

A microflap actuation system based on a voice coil actuator was developed and tested in Ref. 132. The key features of this design are the frelon-lined bearings and the cable and housing assembly, shown in Figs. 1.8 and 1.9. The bearings allow for the tight tolerances that are required in order to hold the moving coil assembly of the voice coil in place. Frelon bearing was chosen over a ball bearing in order to avoid binding under the high centrifugal loads experienced in the helicopter blade. The cable and housing, shown in Fig. 1.9, are used to transfer the motion from the voice coil to the flap arms. The voice coil is placed as far forward in the airfoil as possible to locate the center of gravity of the assembly close to the aerodynamic center (for aeroelastic stability). A concept involving the use of a piezoelectric bimorph actuator was also considered as an actuation method in Ref. 132. A piezoelectric bimorph is a cantilevered beam consisting of two ceramic layers, which are glued together. When opposite electrical fields are applied to the piezoceramics, pure bending occurs.

1.3 Objectives and Key Novel Contributions of this Dissertation

The literature review provided in the previous sections demonstrates the need for a comprehensive and systematic assessment of the potential of microflaps for

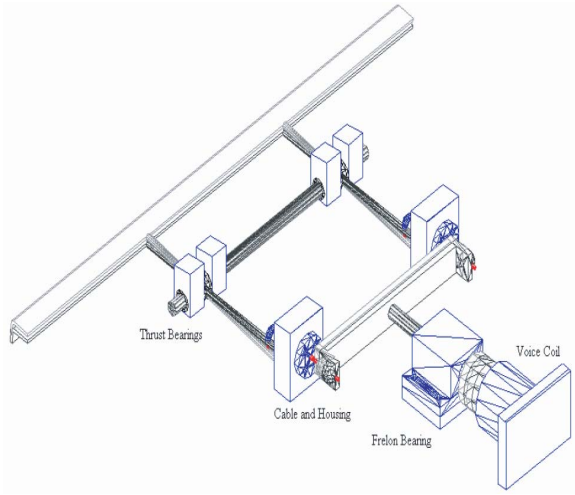

Figure 1.9: Microflap actuation setup developed at the Penn State University using cables and bearings designed to transfer the motion from a voice coil actuator to the microflap [132].

noise and vibration reduction in helicopters. Conducting such an assessment is the overall objective of this thesis. Modeling the unsteady aerodynamics of a rotor blade equipped with microflaps is the biggest challenge in conducting an aeroelastic analysis of a helicopter rotor with on blade control. The complex unsteady flow features around a microflap can not be modeled using conventional potential flow methods. Even though CFD tools can be used to determine unsteady aerodynamic characteristics of the microflap with reasonable accuracy, the computational costs are prohibitive when conducting parametric trend studies involving active control. Therefore, a reduced-order aerodynamic model (ROM) is essential for the conduct of studies aimed at determining the helicopter noise and vibration reduction capabilities of microflaps. Such a ROM needs to have the capability to a) predict unsteady aerodynamic load responses to arbitrary motion of the blade/microflap combination, b) capture compressibility effects, and c) capture unsteady effects due to variations in the free-stream velocity. Furthermore, such a ROM has to be

expressed in time domain and a mathematical form suitable for coupling with the structural dynamics equations of the helicopter rotor. One of the key contributions of this thesis is the development of such a ROM based on CFD data. This CFD based ROM has the capability to capture aerodynamic effects due to the microflap and other nonlinear flow effects. The CFD based ROM is incorporated into the comprehensive rotorcraft analysis code AVINOR, which is subsequently used to conduct closed-loop active noise and vibration reduction studies using microflap on a representative rotor configuration.

The specific objectives of this thesis are:

1. Use CFD to conduct a numerical investigation of the microflap under steady and dynamic conditions, and determine the effects of the microflap on lift, moment, and drag coefficients of a 2D airfoil.

2. Study and compare the aerodynamics of various oscillating microflap configurations using time-accurate Navier-Stokes simulations, so as to identify the configuration most suitable for rotorcraft applications.

3. Develop a CFD based nonlinear reduced-order aerodynamic model that can capture the aerodynamic effects of a microflap and is suitable for incorporation in to a comprehensive rotorcraft simulation code.

4. Validate the aerodynamic load predictions from the CFD based ROM against full order CFD simulations at various flow conditions.

5. Incorporate the CFD based ROM into the comprehensive rotorcraft simula-

tion code AVINOR and validate the aerodynamic and acoustic computations obtained from AVINOR against experimental data from the HART test.

6. Demonstrate the potential of various microflap configurations for vibration reduction at a high BVI low-speed descending flight condition as well as a high speed level flight condition with dynamic stall effects.

7. Explore the potential of various microflap configurations for active control of BVI noise at a low-speed descending flight condition, on a representative rotor configuration.

8. Study the effect of BVI noise reduction using microflaps on the vibration levels and vice versa.

9. Explore the potential of various microflap configurations for simultaneous noise and vibration reduction under BVI conditions.

10. Compare the microflap to a conventional trailing-edge plain flap in terms of its vibration and noise reduction capabilities.

11. Examine the potential of microflap for rotor performance enhancement at a high speed cruise condition.

Accomplishing these objectives represents a significant enhancement in the understanding of microflap's potential as an active control device for rotorcraft applications.

The last phase of this study examines the effect of actuator saturation on the vibration reduction performance of the higher harmonic control algorithm, which is used for all the closed-loop control studies performed in this thesis. The specific objectives of this phase are:

1. Develop an efficient approach to handling actuator saturation in the HHC algorithm, that does not compromise on the controller performance and is suitable for multiple control surfaces.

2. Compare the effectiveness of the new approach, to the different existing actuator saturation approaches in reducing vibrations on a representative rotor configuration using the single and dual configurations of a 20%c conventional plain trailing-edge flap and a 1.5%c microflap.

The key novel contributions of this dissertation are:

1. Development of a CFD based nonlinear reduced-order aerodynamic model which is expressed in a form suitable for use with a comprehensive rotorcraft simulation code. The reduced-order model provides an estimate of the unsteady drag force in addition to the unsteady lift and moment.

2. An assessment of the potential of microflap to reduce vibrations on a representative rotor configuration at advance ratios corresponding to BVI and dynamic stall conditions.

3. An assessment of the potential of different microflap configurations to reduce BVI noise.

4. Demonstration of simultaneous BVI noise and vibration reduction using different microflap configurations.

5. An assessment of the effectiveness of microflaps for rotor performance enhancement.

6. Development of a new efficient approach to handling actuator saturation in the higher harmonic control algorithm.

CHAPTER II

A NUMERICAL STUDY OF GURNEY FLAPS AND MICROFLAPS USING CFD

This chapter provides a detailed description of the CFD code and the computational grids used in the current study. A CFD framework that can be used to study and identify a microflap configuration suitable for rotorcraft applications is developed. A commercially available compressible Navier-Stokes solver CFD++ [103, 104], developed by Metacomp Technologies Inc., is used for all the CFD computations performed in this study. The effects of a Gurney flap on the 2D aerodynamic loads of an airfoil are first studied using the NACA0012 airfoil profile. Grid refinement studies are conducted to validate the CFD grids. The CFD setup is validated by comparing the 2D aerodynamic loads obtained from CFD with the experimental results presented in Ref. 75. The computations are carried out using two different turbulence models, namely the 1-equation SA (Spalart-Allmaras) model and the 2-equation k-ω SST (Shear Stress Transport) model [85] in order to determine the effect of turbulence modeling on the airloads and stall

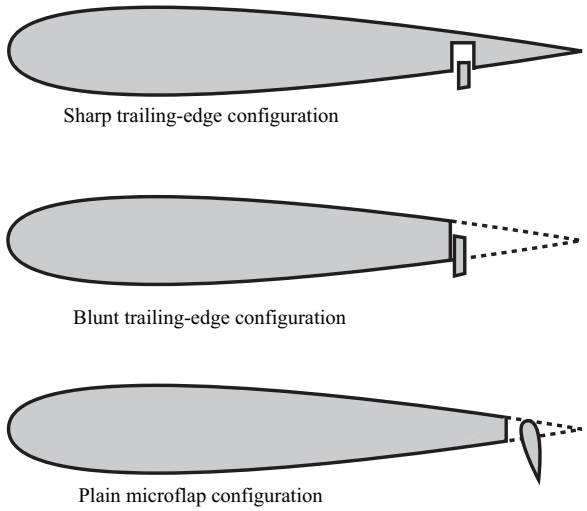

Figure 2.1: Various configurations of a dynamic microflap considered.

angle predictions.

Computations using time-accurate RANS simulations are carried out to determine unsteady aerodynamic loads on a NACA0012 airfoil with an oscillating microflap. Three different configurations of the oscillating microflap shown in Fig. 2.1 are studied and compared. The first configuration has a microflap sliding in and out of a gap near the trailing-edge of the airfoil, the second has a microflap oscillating up and down behind the blunt trailing-edge of the airfoil, and the third has a microflap resembling a plain flap at the trailing-edge. Based on the comparisons, the configuration best suitable for rotorcraft applications is selected.

2.1 The CFD Code and Grid Geometries

The CFD++ code is capable of solving compressible unsteady Reynolds-averaged Navier-Stokes (RANS) equations. It uses a unified grid methodology that can han-

dle a variety of grids including structured, unstructured, multi-block meshes and cell types, including patched and overset grid features. The overset grid approach is used extensively in this study. Spatial discretization of the Navier-Stokes equations is based on a second order multi-dimensional Total Variation Diminishing (TVD) scheme [21]. For temporal discretization an implicit algorithm with dual time-stepping and multigrid acceleration is used. Dual time-stepping schemes are constructed by appending a pseudo time-derivative term to the Navier-Stokes equations. The pseudo time-derivative term is solved using subiterations for improved accuracy. The multigrid acceleration scheme uses levels of grid coarsening to increase the speed of the simulation. Several turbulence models are available in CFD++, ranging from 1-equation to 3-equation transport models. The CFD code is Message Passing Interface (MPI) compatible, allowing the user to perform computations on multiple CPU clusters.

The NACA0012 airfoil profile is used for all the CFD computations performed in this study. The computations are carried out by solving the RANS equations over structured grids. The flow is assumed to be fully turbulent in all of the simulations. For steady flow simulations involving a Gurney flap, the CFD code is run until the aerodynamic forces converge to their asymptotic values or the residuals converge to zero. For the oscillating microflap, where the flow is unsteady, time-accurate simulations are run with time-steps sufficiently small to capture the significant frequencies in the aerodynamic loads.

The computational grids used in this study are generated using the ANSYS

ICEM CFD meshing software. The software has the facility to output the grid files in the plot3D format which is compatible with the CFD++ code. The computational domain is a C-shaped structured grid wrapped around the airfoil as shown in Fig. 2.2. The far field boundary extends to 50 chord lengths in all directions. A distance of 30-50 chord lengths is typically used between the airfoil and far field boundaries in order to diminish the effects of numerical reflection from the far field boundary. The grids are clustered at the airfoil wall boundaries such that the dimensionless distance of the first grid point from the boundary, defined as $y^+ = \frac{y\sqrt{\tau_w}}{\mu\sqrt{\rho}}$, is maintained below 1 and the equations are directly solved to the walls without assuming any wall functions. Grids for the various microflap configurations are generated using the overset approach. Overset grids are used to simulate complex fluid flow problems where the geometry cannot be well represented using a single contiguous grid or where the geometry consists of moving components with large relative motions. In this approach, different grids, typically structured grids, representing the various features of the geometry are overlapped to obtain a single grid representing the complete geometry.

The grid for the Gurney flap simulations is generated by oversetting a U-shaped microflap grid on the airfoil grid near the trailing-edge as shown in Fig. 2.3. The Gurney flap is 1.5%c in height and is fixed at a location 6%c from the trailing-edge of the airfoil. The surface representing the airfoil and the microflap is set as an adiabatic wall boundary for the simulations. Three candidate oscillating microflap configurations are examined and compared in order to identify a configuration

suitable for practical implementation in rotorcraft. The microflap height is set to 1.5%c in all the configurations. The first configuration consists of a microflap that slides in and out of a cavity located at 6%c upstream from the sharp trailing-edge of the airfoil, as shown in Fig. 2.4. The location of the microflap is chosen to be as close to the trailing-edge as the thickness requirements permit. This configuration is similar to that employed in Refs. 23 and 132. The grid for this configuration is obtained by successive combination of several overset refinement grids for the microflap and the airfoil cavity housing the microflap. The first step of oversetting creates a gap in the airfoil and in the next step the microflap grid is overset to fit into the gap created in the airfoil as shown in Fig. 2.4. The second configuration consists of a microflap that moves up and down behind the blunt trailing-edge of the airfoil, shown in Fig. 2.5. The blunt trailing edge is created by removing the aft portion of the airfoil such that there is enough space for accommodating the microflap when it is fully retracted. The third microflap configuration has a rotational hinge at the trailing-edge and thus resembles a miniature plain flap, as shown in Fig. 2.6. The total number of grid points for the three microflap configurations depicted in Figs. 2.4, 2.5, and 2.6 is 120k, 138k and 124k, respectively.

For comparison purposes, computational studies were also conducted with a 20%c conventional plain flap. The details of the grid near the airfoil and the flap are given in Fig. 2.7(a). The hinge gap is shown in Fig. 2.7(b). The flap is oscillating about a hinge located at $0.80c$. The nominal length of the flap is $0.225c$, with a $0.005c$ gap between the main airfoil and flap. The upper and lower surfaces of the main

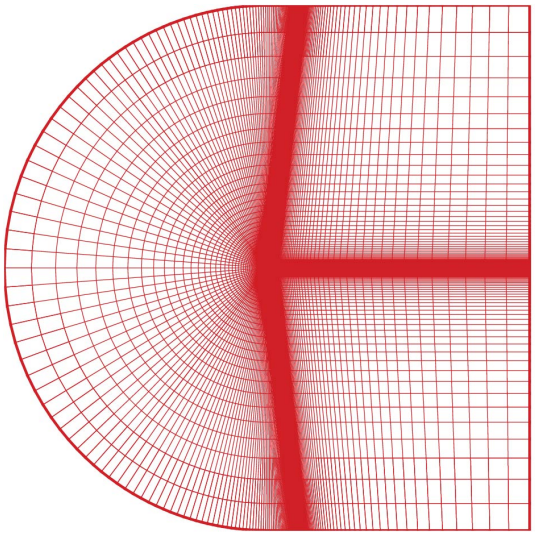

Figure 2.2: C-grid around a plain NACA0012 airfoil.

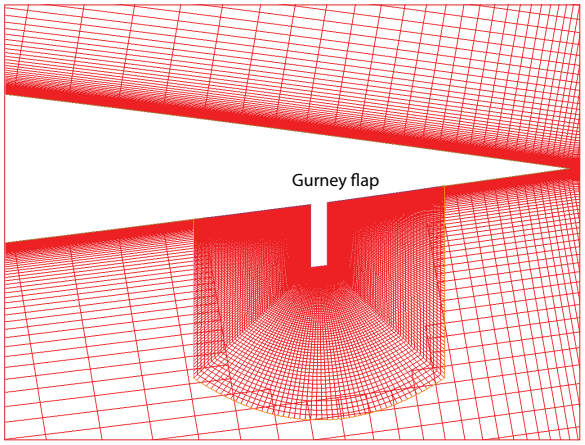

Figure 2.3: Overset grid showing the trailing-edge of a NACA0012 airfoil with a 1.5%c Gurney flap permanently attached at 6%c from the trailing-edge.

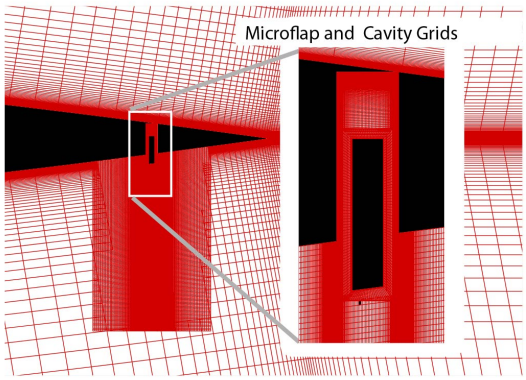

Figure 2.4: Overset grid showing the trailing-edge of a NACA0012 airfoil with a 1.5%c microflap that can slide in and out of the gap located at 6%c from the trailing-edge of the airfoil.

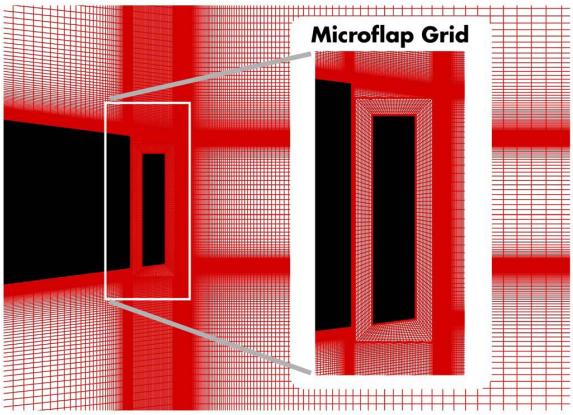

Figure 2.5: Overset grid showing a 1.5%c microflap that can slide up and down at the blunt trailing-edge of a NACA0012 airfoil.

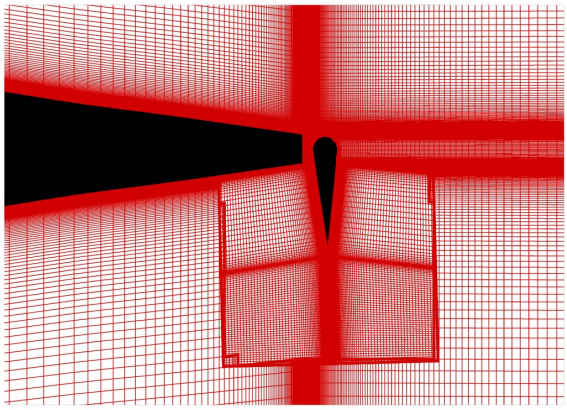

Figure 2.6: Overset grid showing a 1.5%c microflap resembling a plain flap oscillating at the trailing-edge of a NACA0012 airfoil.

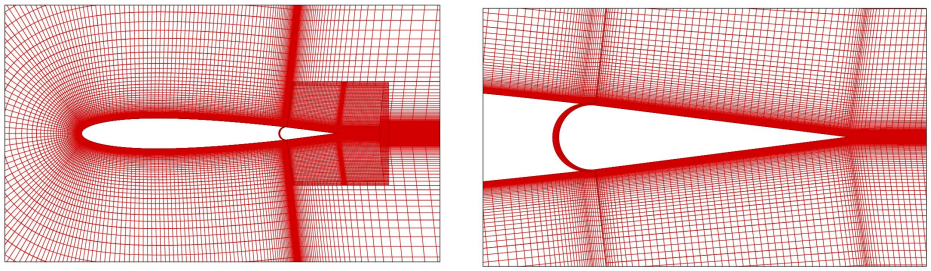

(a) Airfoil and flap (b) Flap gap

Figure 2.7: Grid for the NACA0012 airfoil with a 20%c conventional plain flap.

airfoil extend aft in order to reduce the pressure losses between the upper and lower surfaces, so that the effective length of the flap is 20% of the airfoil chord.

2.2 Gurney Flap Simulations

2.2.1 Grid refinement study

Grid refinement studies are performed first to examine the effect of grid resolution on the CFD simulation results. Three different grids with varying levels of

		Number of Nodes	C_l	C_m	C_d
$\alpha = 2°$, M = 0.1, and Re = 2.1 x 10^6	Coarse	21540	0.2076	0.0023	0.0106
	Medium	55736	0.2156	0.0017	0.0095
	Fine	122992	0.2156	0.0017	0.0095
$\alpha = 4°$, M = 0.3, and Re = 6.3 x 10^6	Coarse	21540	0.4488	0.0031	0.0110
	Medium	55736	0.4583	0.0029	0.0084
	Fine	122992	0.4586	0.0028	0.0084

Table 2.1: Grid refinement study for the plain NACA0012 airfoil at two different flow conditions.

refinement are generated for the airfoil. The aerodynamic lift, moment, and drag coefficients obtained from the various airfoil grids are listed in Table 2.1 for two different flow conditions: 1) $\alpha = 2°$, M = 0.1, Re = 2.1 x 10^6 and 2) $\alpha = 4°$, M = 0.3, Re = 6.3 x 10^6. The total number of nodes in each of the grids is also listed. The aerodynamic load coefficients converge with increasing levels of grid refinement. The medium refinement grid predicts the aerodynamic loads within 1% of those predicted from the fine grid. Therefore, the medium airfoil grid is used for all the subsequent simulations in this thesis. A similar study is performed for a 1.5%c Gurney flap located at 6%c from the trailing-edge of the airfoil. The aerodynamic lift, moment, and drag coefficients obtained from the Gurney flap grids with varying refinement are listed in Table 2.2. The medium refinement Gurney flap grid predicts the aerodynamic loads within 1% of those predicted by the fine grid and hence, it has been for all the simulations in this study.

		Number of Nodes	C_l	C_m	C_d
$\alpha = 2°$, M = 0.1, and Re = 2.1 x 10^6	Coarse	37890	0.5355	-0.0629	0.0167
	Medium	78056	0.5460	-0.0639	0.0151
	Fine	101936	0.5454	-0.0637	0.0150
$\alpha = 4°$, M = 0.3, and Re = 6.3 x 10^6	Coarse	37890	0.7888	-0.0639	0.0199
	Medium	78056	0.8258	-0.0700	0.0149
	Fine	101936	0.8279	-0.0704	0.0148

Table 2.2: Grid refinement study for a 1.5%c Gurney flap located at 6%c from the trailing-edge of a NACA0012 airfoil.

2.2.2 Validation of the CFD setup

The CFD setup is validated against experimental results presented in Ref. 75. The experiments were performed on a NACA0012 airfoil section with a 1.5%c Gurney flap located at 6%c from the trailing-edge. The free stream Mach number is 0.1 and the Reynolds number is 2.1 x 10^6. The experiments were conducted in the NF-3 Low-speed Wind Tunnel at the Northwestern Polytechnical University of China. The test-section of the wind tunnel is 8 m long with a constant height of 1.6 m and a width of 3 m. The airfoil used in the experiments had a chord length of 1 m, spanning the 1.6 m height of the wind tunnel. The test-section turbulence intensity level is estimated to be less than 0.45%. Turbulence intensity is defined as $\frac{u'}{U}$ where u' is the root-mean-square of the turbulent velocity fluctuations and U is the mean velocity. The turbulence intensity serves as a measure of the amount of turbulence in the flow and is a user-prescribed parameter in the turbulence models used in CFD++. The moment coefficient C_m is measured about the quarter chord point which coincides with the aerodynamic center for the NACA0012 airfoil. The stall angle is defined as the angle of attack where the lift coefficient attains its max-

imum value. At high angles of attack the flow is unsteady due to flow separation and vortex shedding resulting in time dependent aerodynamic loads. The mean value of the aerodynamic coefficients is shown for all the results at high angles of attack.

Lift coefficient C_l obtained from the experiments and the CFD code for a plain airfoil and an airfoil with a Gurney flap is shown in Fig. 2.8. In the legend, 'Exp' refers to experimental results and 'CFD' refers to the computational results. The computational results are shown for two different turbulence models namely, the 1-equation SA model (referred to as 'SA' in the legend) and the 2-equation k-ω SST model (referred to as 'SST' in the legend). Also shown in Fig. 2.8 is the experimental C_l curve for a plain NACA0012 airfoil obtained from the book *Theory of Wing Sections* by Abbott and Doenhoff [1]. Attaching a Gurney flap to the airfoil increases the C_l value by 25% at $\alpha = 0^\circ$. The maximum C_l value is approximately 20% higher with the Gurney flap. The moment coefficient C_m obtained from experiments and the CFD code for a plain airfoil and an airfoil with a Gurney flap is shown in Fig. 2.9. The Gurney flap induces a negative pitching moment on the airfoil. Flow behind the Gurney flap has low velocity and therefore a high static pressure. The high static pressure combined with large moment arm near the trailing-edge of the airfoil results in a negative pitching moment. It is evident from Figs. 2.8 and 2.9 that the lift and moment predictions of the Gurney flap are in reasonable agreement with the experiments for angles of attack less than 15°. In particular, the differences in the lift and moment due to the Gurney flap when

compared to the clean airfoil are well captured by CFD. Note that the stall onset angles predicted by CFD significantly exceed those obtained in the experiments, for both the clean airfoil and the airfoil with the Gurney flap. The disagreement in the stall onset predictions can be attributed to the limitations of the turbulence model, as well as the fact that boundary layer transition is not considered in the CFD calculations, where the boundary layer is assumed to be fully turbulent. It is also important to note that the onset of stall is sensitive to factors such as freestream turbulence level, airfoil skin roughness, etc., which are hard to measure. The lift curve for a clean NACA0012 airfoil under similar flow conditions obtained from another experiment [1] shows a stall onset angle closer to the CFD prediction. The large variance in stall angle predictions from various experiments found in literature is an indication of the difficulties involved in modeling flow separation. Other studies comparing experimental and computational aerodynamic coefficients of airfoils with Gurney flaps have also shown discrepancies in the stall angle prediction [59, 121, 127]. Note that the aerodynamic loads are relatively insensitive to the choice of turbulence model at low angles of attack.

The drag coefficient C_d obtained from experiments and the CFD code for a plain airfoil and an airfoil with a Gurney flap is shown in Fig. 2.10. Drag for the clean airfoil is over-predicted by CFD for angles of attack less than 12°, which is mainly due to the fact that the boundary layer is assumed to be fully turbulent and no boundary layer transition is considered in the CFD calculations. Drag over-prediction by CFD when compared to experimental data was also noted in Ref. 66. The drag due

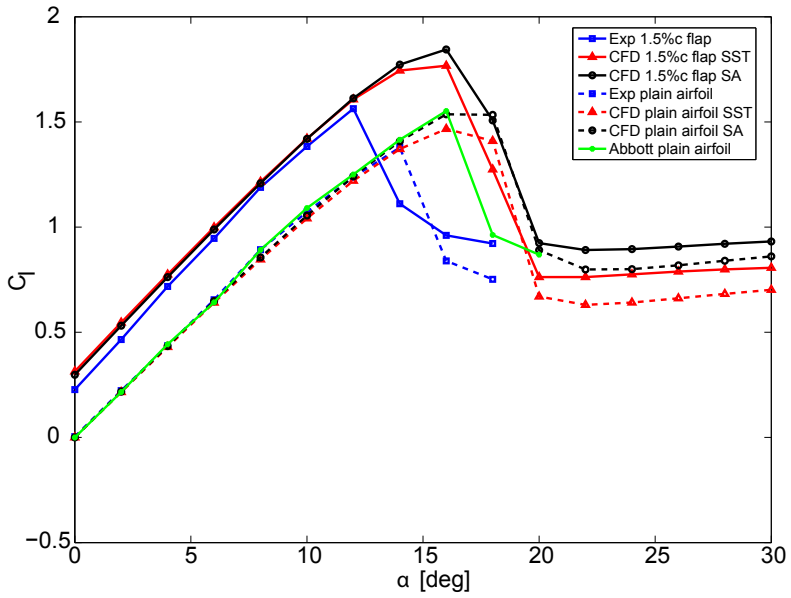

Figure 2.8: Validation of the lift curve prediction for a NACA0012 airfoil with a 1.5%c Gurney flap located at 6%c from the trailing-edge. Lift curve is also shown for a plain airfoil.

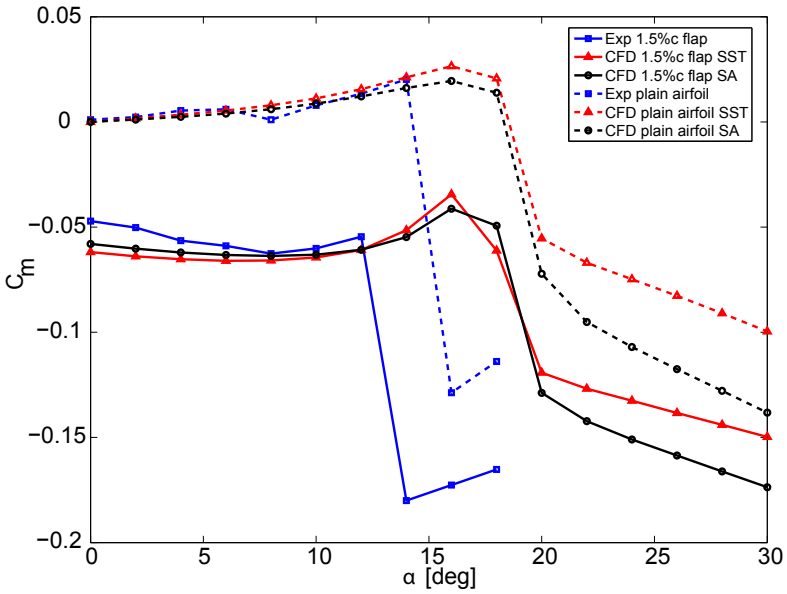

Figure 2.9: Validation of the moment coefficient prediction for a NACA0012 airfoil with a 1.5%c Gurney flap located at 6%c from the trailing-edge. Moment coefficient is also shown for a plain airfoil.

to the 1.5%c Gurney flap predicted from the experiments does not show a smooth variation with angle of attack. However, the computed drag due to the Gurney flap is in reasonable agreement with the experimental predictions. Variation of the lift-to-drag ratio with C_l is shown in Fig. 2.11. The Gurney flap has a beneficial effect on the lift-to-drag ratio at high values of C_l, that is, around the stall region. The maximum lift-to-drag ratio obtained with the 1.5%c Gurney flap is smaller when compared to a plain NACA0012 airfoil. Experiments conducted in Ref. 134 observed an increase in the airfoil maximum lift-to-drag ratio due to a Gurney flap. A Gurney flap smaller than 1%c was found to increase the maximum lift-to-drag ratio [127]. Variation of the lift-to-drag ratio with angle of attack α is shown in Fig. 2.12.

2.3 Oscillating Microflap Simulations

Various oscillating microflap configurations, described in Section 2.1, are studied using unsteady RANS simulations. In the computations, the flow is first allowed to reach steady state before starting time-accurate simulations. The 2-equation k-ω SST model is used for turbulence modeling. The time step used for the unsteady simulations is 0.0001 sec and 5 sub-iterations were used in each global time step in order to ensure convergence. The free stream Mach number is 0.5142 and the Reynolds number is 3.36 x 10^6. These flow conditions correspond to 80% span location on a MBB BO-105 helicopter rotor blade (dimensions listed in Table 2.3) in hover.

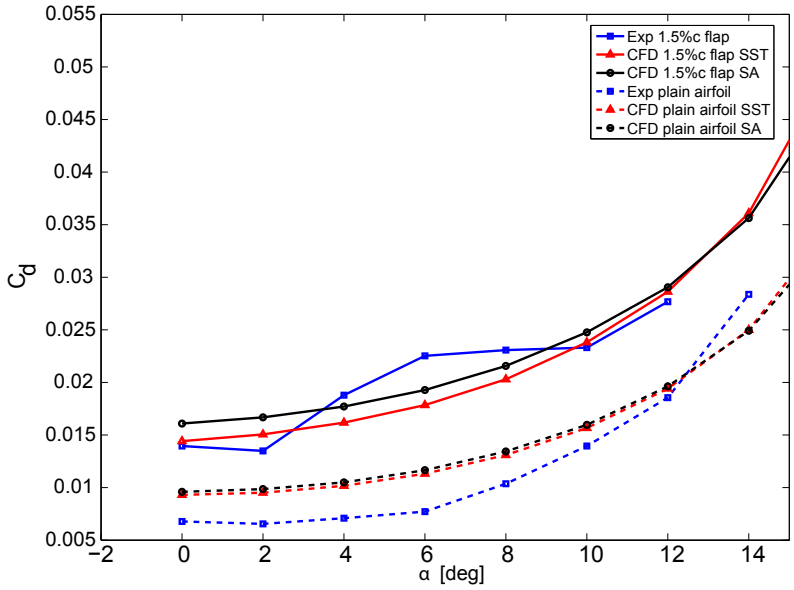

Figure 2.10: Validation of drag coefficient predictions for a NACA0012 airfoil with a 1.5%c Gurney flap located at 6%c from the trailing-edge. Drag coefficient is also shown for a plain airfoil.

Rotor Blade Data
R = 4.91 m c = 0.27 m Ω = 425 RPM
80% Span Location
M = 0.5142 Re = 3.36x10^6 2/rev $\sim$ 14 Hz

Table 2.3: Dimensions for a MBB BO-105 rotor blade.

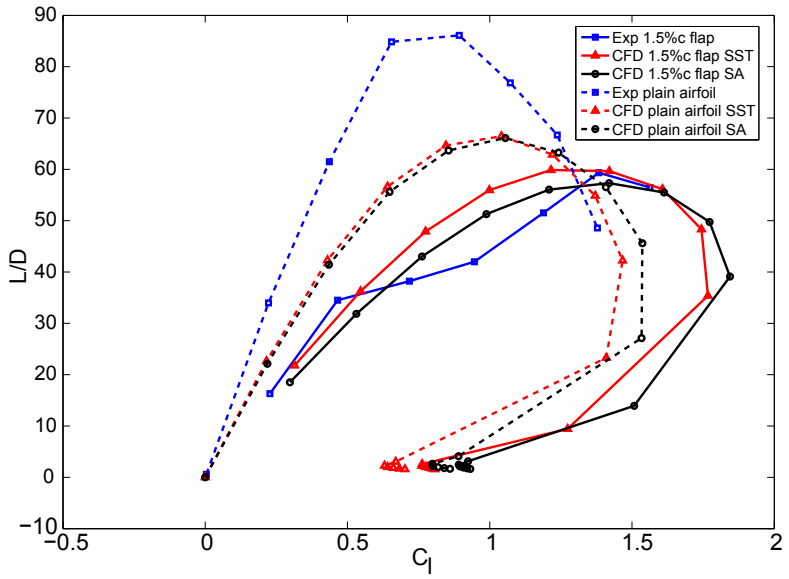

Figure 2.11: Lift-to-drag ratio vs C_l for a NACA0012 airfoil with a 1.5%c Gurney flap located at 6%c from the trailing-edge.

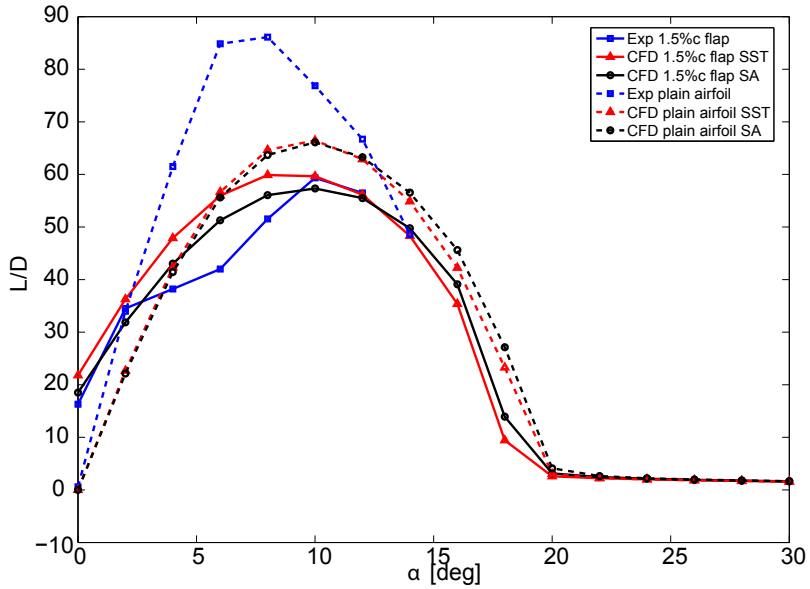

Figure 2.12: Lift-to-drag ratio vs α for a NACA0012 airfoil with a 1.5%c Gurney flap located at 6%c from the trailing-edge.

Computations are performed for frequencies $\nu = 14$ and 28 Hz which approximately correspond to the 2/rev and 4/rev rotor frequencies. The equivalent reduced frequencies are $k = 0.0688$ and 0.1376 based on the chord length of the airfoil section. Note that the reduced frequency is defined as

$$k = \frac{\omega b}{U}, \tag{2.1}$$

where ω is the radian frequency, $b = \frac{c}{2}$ is the semi-chord, and U is the free-stream velocity. The airfoil is set at 0° angle of attack.

2.3.1 Sharp trailing-edge configuration

The first configuration has a microflap oscillating in and out of the airfoil as shown in Fig. 2.13. The microflap is 1.5%c in height and is located in a gap at 6%c from trailing edge of the airfoil. The width of the gap is 0.6%c. The microflap is 0.3%c wide and is centered in the gap. Microflap deflection δ_f at any given instance in time is defined as the distance from the bottom surface of the flap to the bottom surface of the airfoil as shown in Fig. 2.13. The deflection profile used for the microflap is given by

$$\delta_f = A\sin(2\pi\nu t - \frac{\pi}{2}) + A, \tag{2.2}$$

$$\iff \quad \delta_f = A[1 - \cos(2\pi\nu t)], \tag{2.3}$$

where A = 0.75%c is the amplitude and ν is the frequency of oscillation. Equation 2.2 indicates that the microflap deflection profile is a sine waveform with a phase shift of $\frac{\pi}{2}$ radians and an amplitude offset equal to A. The microflap starts from the totally retracted position, $\delta_f = 0$ and slides completely out of the gap to attain a peak deflection of δ_f = 1.5%c. Time history of the microflap deflection δ_f given by Eq. (2.2) is shown in Fig. 2.14 for ν = 14 Hz.

The lift coefficient is plotted against the non-dimensional reduced time $\bar{t} = \frac{1}{b}\int_0^t U(\tau)d\tau$ and the microflap deflection δ_f in Figs. 2.15 and 2.16, respectively. For comparison, all the figures in this section presenting unsteady aerodynamic coefficients also show the static value of the coefficient with a fully deployed microflap indicated as '$\delta_f = 1.5\%c$' and with a fully retracted microflap indicated as '$\delta_f = 0\%c$'. The peak value of C_l for $\nu = 14$ Hz is approximately 27% less than the C_l value obtained with a static microflap, indicating lift deficiency due to unsteady effects. Amplitude of the lift coefficient decreases by 7% when ν increases from 14 Hz to 28 Hz. The moment coefficient plotted against reduced time and the microflap deflection is shown in Figs. 2.17 and 2.18, respectively. The peak value of the unsteady moment coefficient is same as obtained with a static microflap implying that the effect of the unsteady flow dynamics on the moment coefficient is negligible. The drag coefficient plotted against reduced time and the microflap deflection is shown in Figs. 2.19 and 2.20, respectively. The peak value of C_d for $\nu = 14$ Hz is 25% larger than the C_d value obtained using a static microflap, which again is due to the unsteady flow effects. Amplitude of the drag coefficient in-

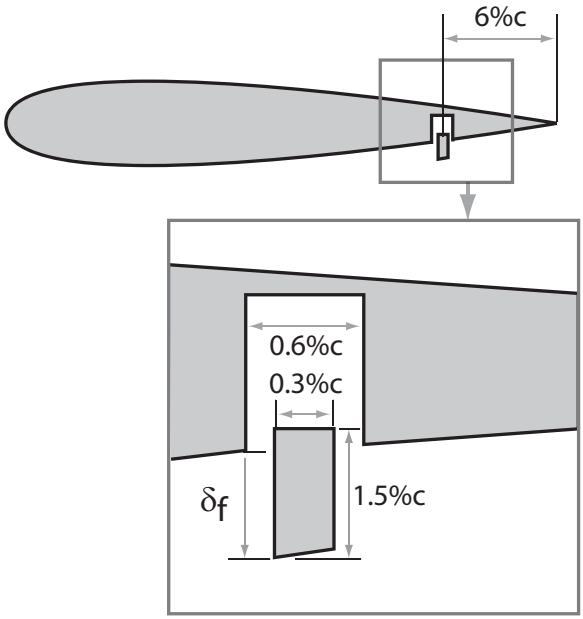

Figure 2.13: An illustration of the sharp trailing-edge microflap configuration.

creases by 5% when ν increases from 14 Hz to 28 Hz. As evident from Figs. 2.16, 2.18, and 2.20, the aerodynamic load responses to the microflap's motion are not simple harmonic. This is because the flow takes time to turn around the trailing-edge and form a vortex behind the microflap as it is sliding out. Consequently, the variation in the aerodynamic loads when the microflap is sliding out is sluggish compared to when the microflap is sliding in.

2.3.2 Blunt trailing-edge configuration

The second configuration has a microflap oscillating behind the trailing-edge of a NACA0012 airfoil as shown in Fig. 2.21. The blunt trailing-edge is created by removing a part of the aft portion of the airfoil. The microflap can be deflected both up and down from the neutral starting position. For comparison with the sharp

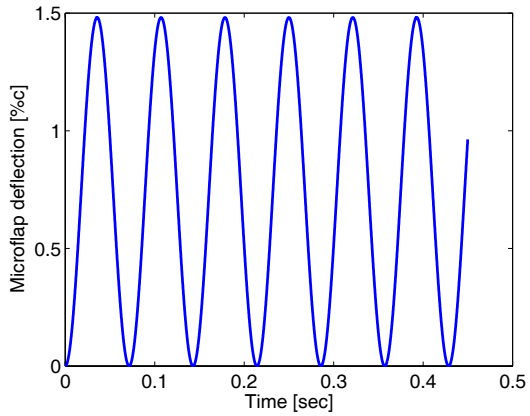

Figure 2.14: Time history of the microflap deflection given by (2.2) for ν = 14 Hz.

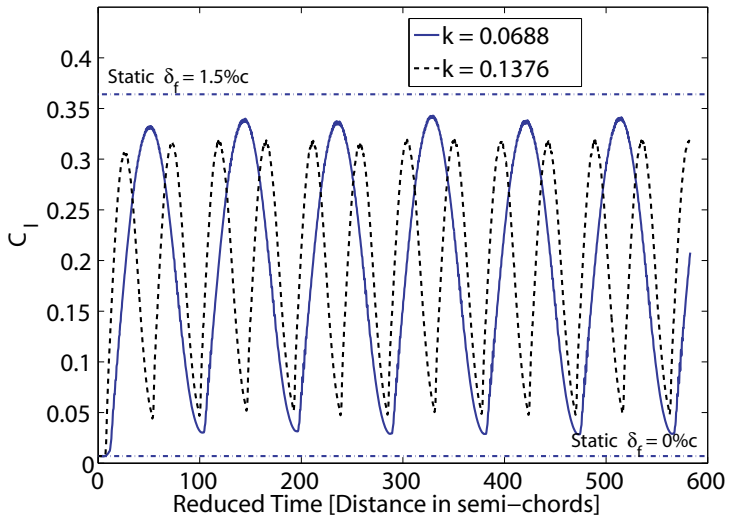

Figure 2.15: Unsteady lift coefficient versus reduced time for a NACA0012 airfoil with a 1.5%c microflap oscillating at 6%c from the trailing-edge. The free stream Mach number and Reynolds number are 0.5142 and 3.36 x 10^6, respectively.

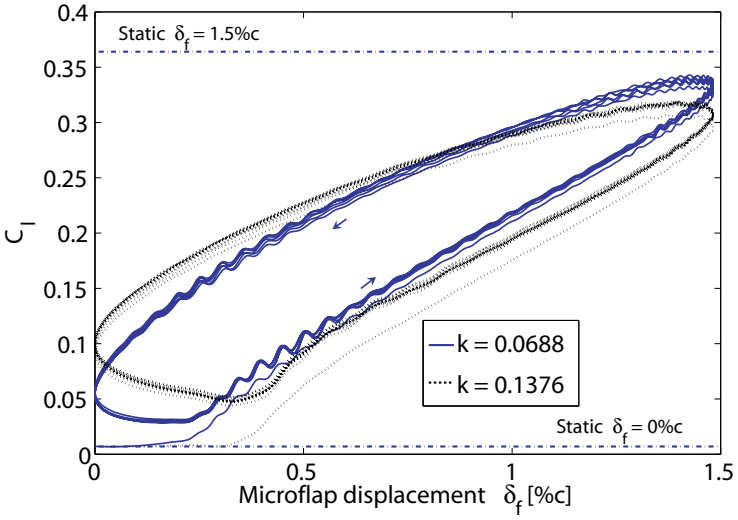

Figure 2.16: Unsteady lift coefficient versus microflap deflection for a NACA0012 airfoil with a 1.5%c microflap oscillating at 6%c from the trailing-edge. The free stream Mach number and Reynolds number are 0.5142 and 3.36 x 10^6, respectively.

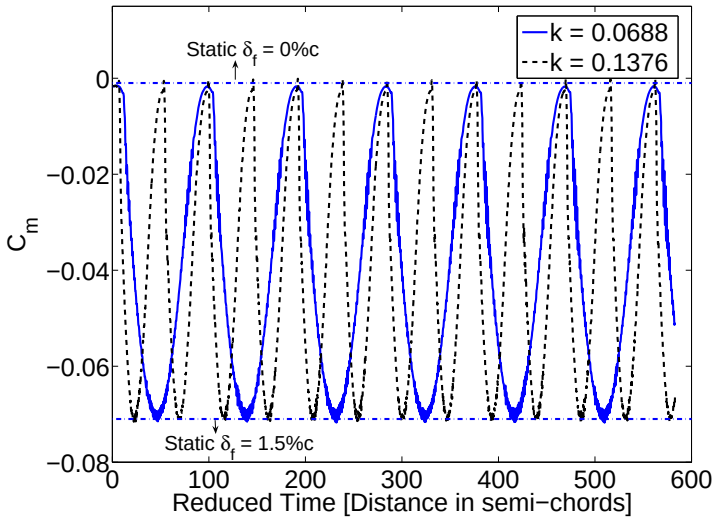

Figure 2.17: Unsteady moment coefficient versus reduced time for a NACA0012 airfoil with a 1.5%c microflap oscillating at 6%c from the trailing-edge. The free stream Mach number and Reynolds number are 0.5142 and 3.36 x 10^6, respectively.

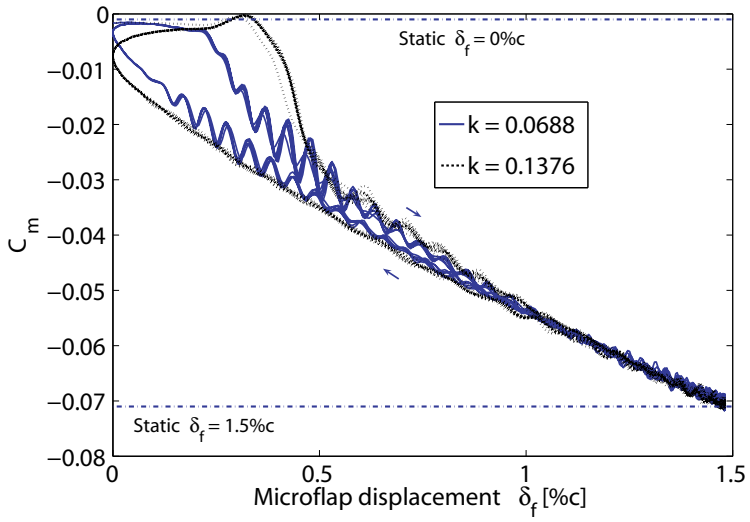

Figure 2.18: Unsteady moment coefficient versus microflap deflection for a NACA0012 airfoil with a 1.5%c microflap oscillating at 6%c from the trailing-edge. The free stream Mach number and Reynolds number are 0.5142 and 3.36 x 10^6, respectively.

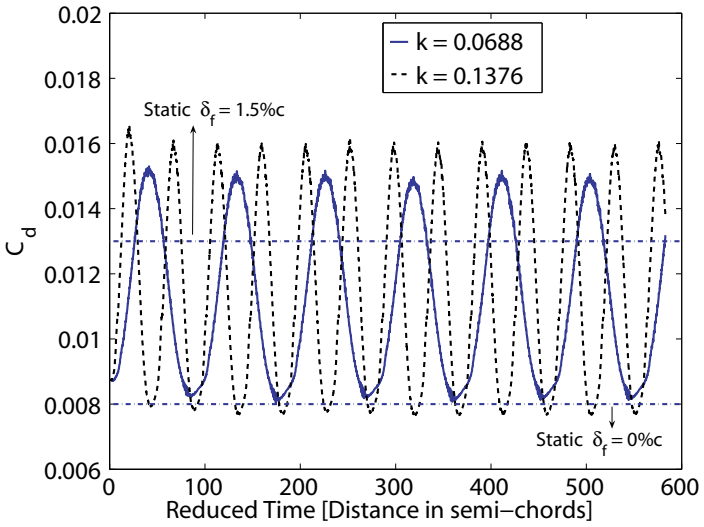

Figure 2.19: Unsteady drag coefficient versus reduced time for a NACA0012 airfoil with a 1.5%c microflap oscillating at 6%c from the trailing-edge. The free stream Mach number and Reynolds number are 0.5142 and 3.36 x 10^6, respectively.

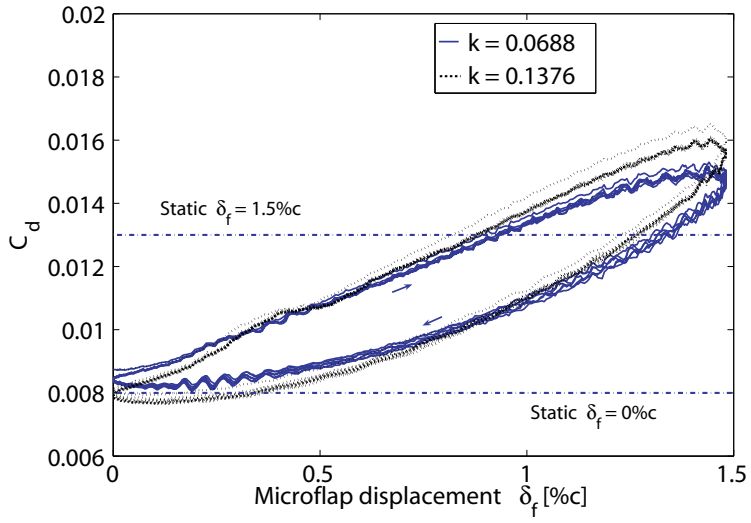

Figure 2.20: Unsteady drag coefficient versus microflap deflection for a NACA0012 airfoil with a 1.5%c microflap oscillating at 6%c from the trailing-edge. The free stream Mach number and Reynolds number are 0.5142 and 3.36 x 10^6, respectively.

trailing-edge configuration, the simulations were performed only with downward deflection of the microflap. The flow conditions, the time step settings, and the microflap deflection time histories are identical to those used for the sharp trailing-edge configuration.

The lift coefficient is plotted against the non-dimensional reduced time $\bar{t}$ and the microflap deflection δ_f in Figures 2.22 and 2.23, respectively. The peak value of C_l for $\nu = 14$ Hz is approximately 10% less than the C_l value obtained with a static microflap fully deployed at the blunt trailing-edge. Amplitude of the lift coefficient decreases by 7% when ν increases from 14 Hz to 28 Hz. The moment coefficient plotted against reduced time is shown in Fig. 2.24. The frequency of the microflap oscillation has a negligible effect on the peak value of the moment

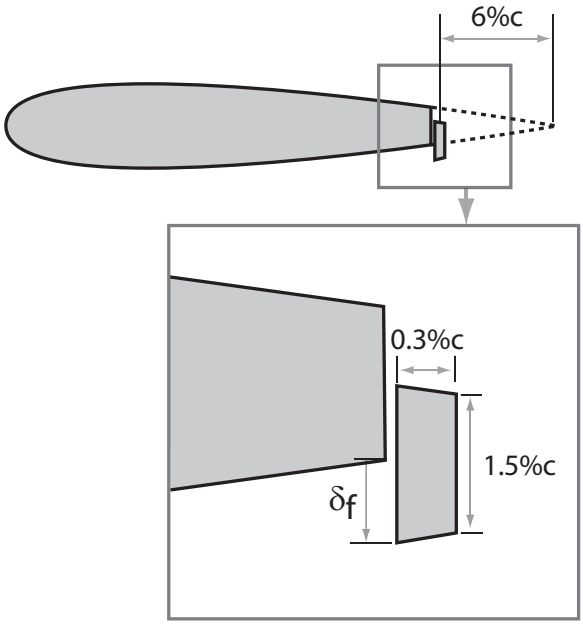

Figure 2.21: An illustration of an oscillating microflap at a blunt trailing-edge of a NACA0012 airfoil.

coefficient. The drag coefficient is plotted against reduced time and the microflap deflection δ_f in Figures 2.25 and 2.26, respectively. The peak value of C_d for $\nu = 14$ Hz is 10% larger than the C_d value obtained using a static microflap, which again is due to the unsteady flow effects. Amplitude of the drag coefficient increases by 3% when ν increases from 14 Hz to 28 Hz. Overall, the observations are similar to those made for the sharp trailing-edge configuration.

2.3.3 Plain microflap configuration

The third microflap configuration, shown in Fig. 2.27, resembles a conventional plain flap. For the purpose of comparison, simulations are conducted with the microflap deflecting downward only, that is, between $\delta_f = 0^\circ$ and $\delta_f = 90^\circ$. The

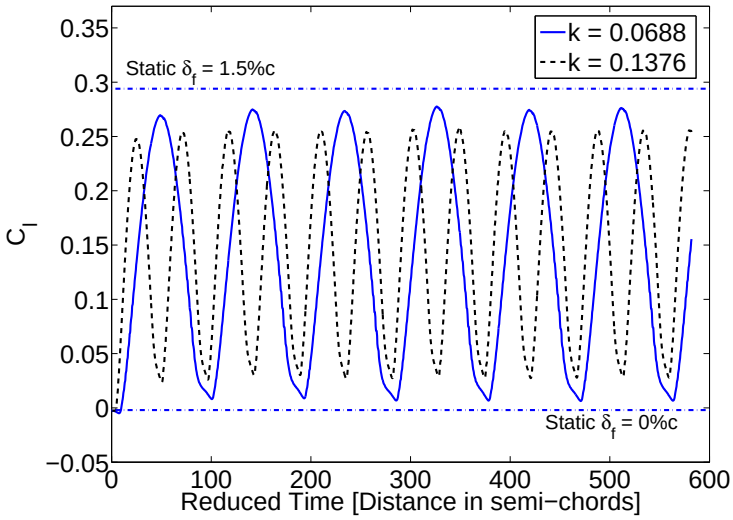

Figure 2.22: Unsteady lift coefficient versus reduced time for a NACA0012 airfoil with a blunt trailing-edge and a 1.5%c microflap oscillating at the trailing-edge.

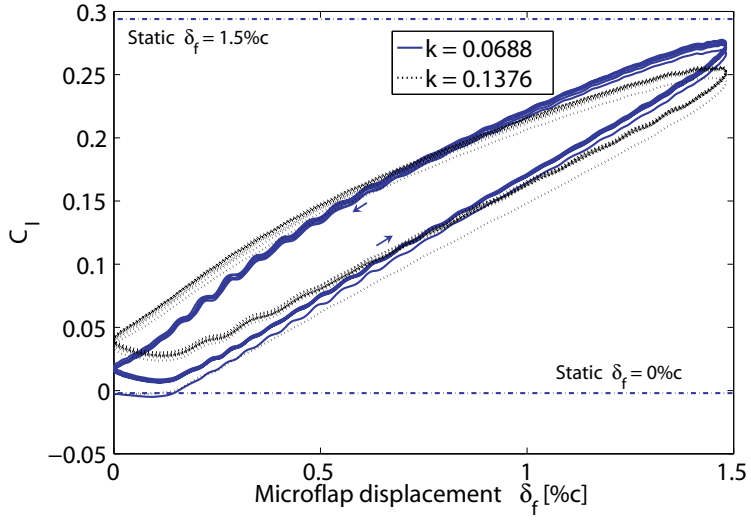

Figure 2.23: Unsteady lift coefficient versus microflap deflection for a NACA0012 airfoil with a blunt trailing-edge and a 1.5%c microflap oscillating at the trailing-edge.

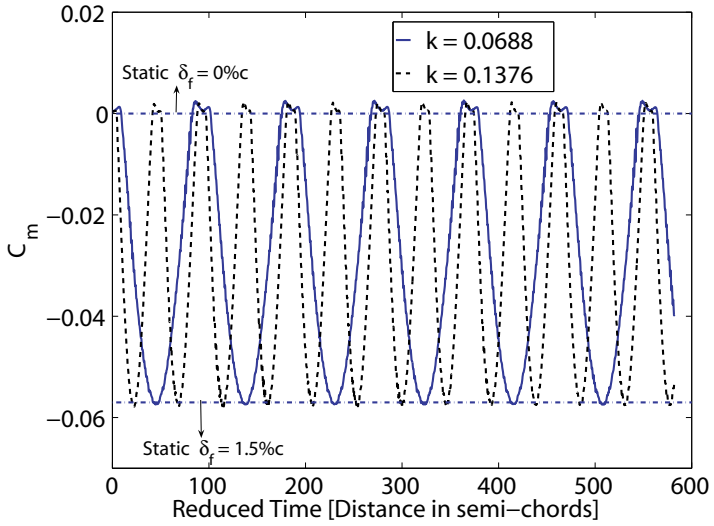

Figure 2.24: Unsteady moment coefficient versus reduced time for a NACA0012 airfoil with a blunt trailing-edge and a 1.5%c microflap oscillating at the trailing-edge.

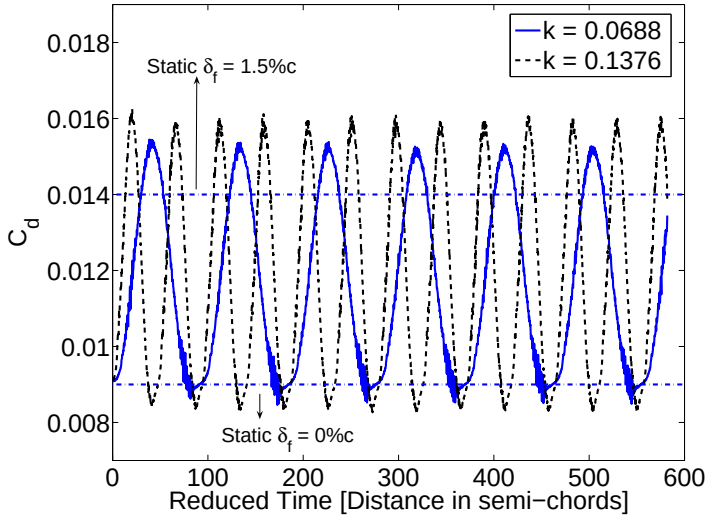

Figure 2.25: Unsteady drag coefficient versus reduced time for a NACA0012 airfoil with a blunt trailing-edge and a 1.5%c microflap oscillating at the trailing-edge.

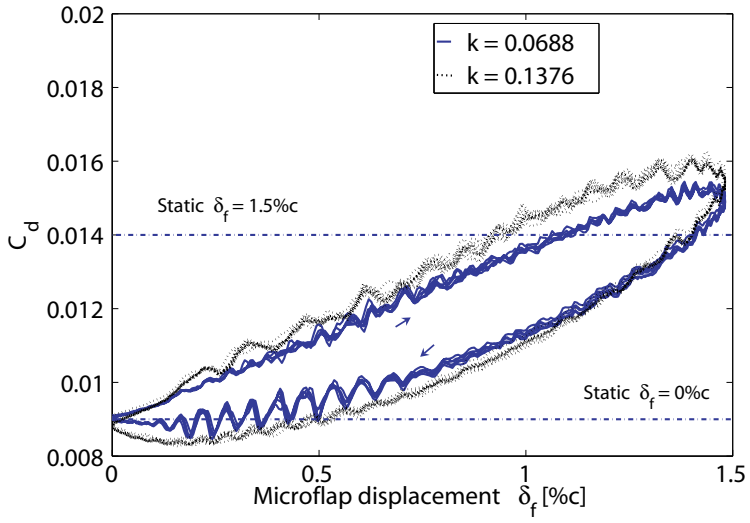

Figure 2.26: Unsteady drag coefficient versus microflap deflection for a NACA0012 airfoil with a blunt trailing-edge and a 1.5%c microflap oscillating at the trailing-edge.

flow conditions and time-step settings are identical to those used for the previous two configurations.

The lift coefficient is plotted against the non-dimensional reduced time $\bar{t}$ in Fig. 2.28. The peak value of C_l for $\nu = 14$ Hz is approximately 5% less than the C_l value obtained with a static microflap fully deployed. Amplitude of the lift coefficient decreases by about 5% when ν increases from 14 Hz to 28 Hz. The moment coefficient plotted against reduced time is shown in Fig. 2.29. The frequency of the microflap oscillation does not show a significant effect on the peak value of the moment coefficient. The drag coefficient is plotted against reduced time in Fig. 2.30. The peak value of C_d for $\nu = 14$ Hz is 20% higher than the C_d value obtained using a static microflap.

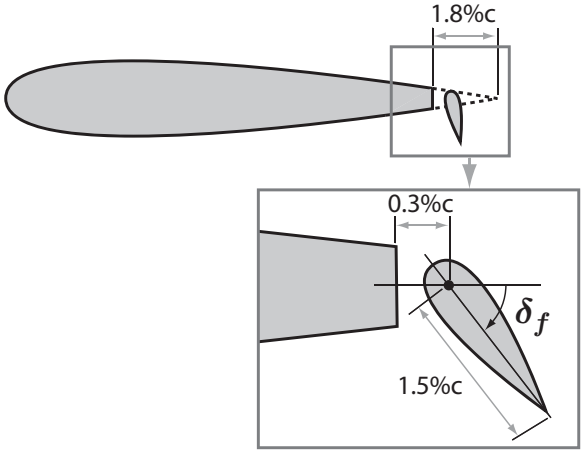

Figure 2.27: An illustration of an oscillating microflap resembling a plain flap on a NACA0012 airfoil.

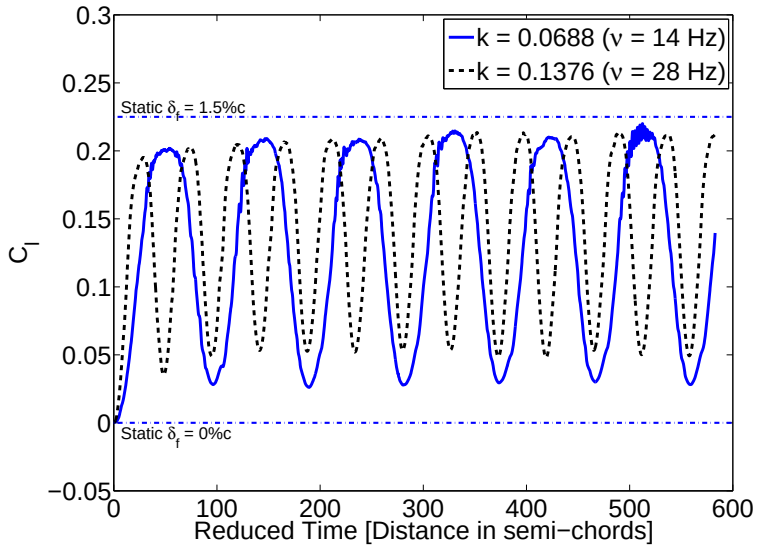

Figure 2.28: Unsteady lift coefficient versus reduced time for a NACA0012 airfoil with an oscillating 1.5%c plain microflap. The free stream Mach number and Reynolds number are 0.5142 and 3.36 x 10^6, respectively.

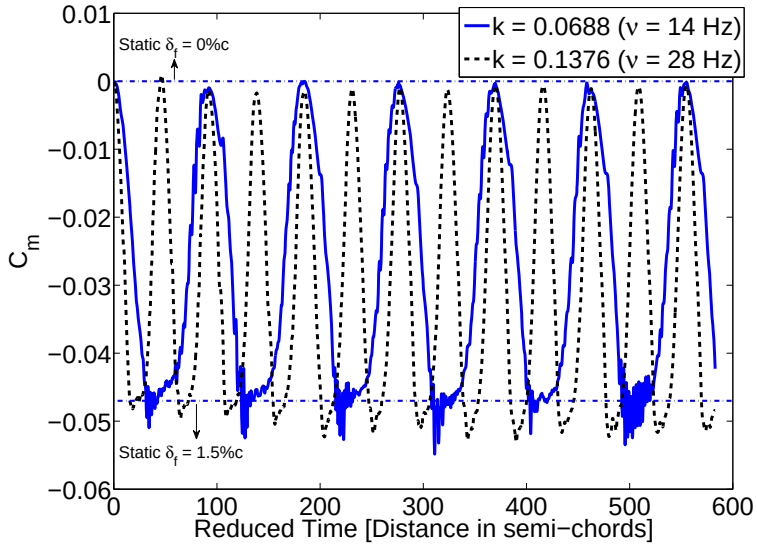

Figure 2.29: Unsteady moment coefficient versus reduced time for a NACA0012 airfoil with an oscillating 1.5%c plain microflap. The free stream Mach number and Reynolds number are 0.5142 and 3.36 x 10^6, respectively.

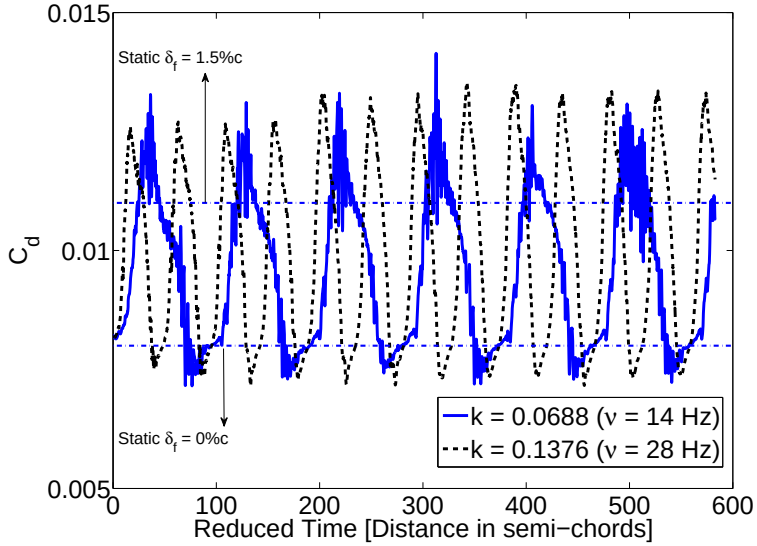

Figure 2.30: Unsteady drag coefficient versus reduced time for a NACA0012 airfoil with an oscillating 1.5%c plain microflap. The free stream Mach number and Reynolds number are 0.5142 and 3.36 x 10^6, respectively.

2.3.4 Comparison between the three microflap configurations

The three different microflap configurations discussed in the previous sections are compared in terms of their aerodynamic effectiveness. The unsteady lift coefficients corresponding to the three oscillating microflap configurations are compared in Fig. 2.31 for $\nu = 14$ Hz. The peak lift on the airfoil with a blunt trailing-edge is 20% less than the airfoil with a sharp trailing-edge. The lift coefficient for the airfoil with a plain microflap is same as that for the airfoil with a blunt trailing-edge at all times except at the maximum deflection position where the plain microflap generates a 25% smaller lift coefficient. The reason for the decrease in the peak lift coefficient is that the plain microflap when deflected by 90° is not completely exposed to the oncoming flow thus decreasing its effective size. The similarity between the sliding microflap at the blunt trailing-edge and the plain microflap configurations is not surprising since the comparison is done using a symmetric airfoil at $\alpha = 0^\circ$. The plain microflap when deflected by 90° has the same effects on the flow as a sliding microflap placed at a blunt trailing-edge, the only difference being the thickness of the blunt trailing-edge which has an effect on the drag acting on the airfoil. The time-histories of the lift-to-drag ratios corresponding to the three oscillating microflap configurations are compared in Fig. 2.32. The configuration with a sharp trailing edge yields the best lift-to-drag ratio, followed by the plain microflap and the blunt trailing-edge configurations, in that order. The unsteady moment coefficients corresponding to the three oscillating microflap configurations are compared in Fig. 2.33. The sharp trailing-edge con-

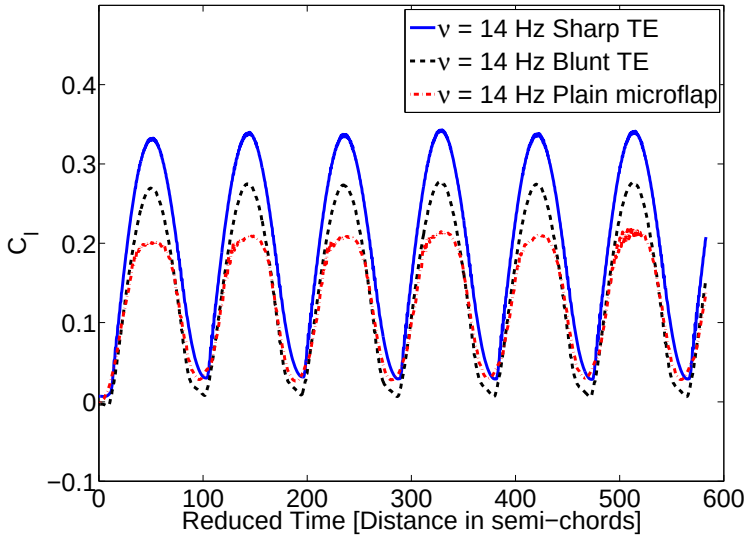

Figure 2.31: Comparison of the unsteady lift coefficient obtained for three different microflap configurations on a NACA0012 airfoil. All the three configurations are equipped with a 1.5%c microflap. $M = 0.5142$, $\nu = 14$ Hz, and $\mathrm{Re} = 3.36$ x 10^6.

figuration generates about 16% higher pitch-down moment when fully deployed compared to the other two configurations.

Similar comparisons are performed at a non-zero angle of attack $\alpha = 6^\circ$ and $\nu = 14$ Hz, where the flow conditions are similar to the earlier simulations. The unsteady lift coefficients corresponding to the three oscillating microflap configurations are compared in Fig. 2.34. The sharp trailing-edge configuration generates approximately 10% higher lift compared to the plain microflap and approximately 13% higher lift compared to the blunt trailing-edge configuration. The time-histories of the lift-to-drag ratios corresponding to the three oscillating microflap configurations at $\alpha = 6^\circ$ are compared in Fig. 2.35. The plain microflap yields a lift-to-drag ratio similar to the sharp trailing-edge configuration. The

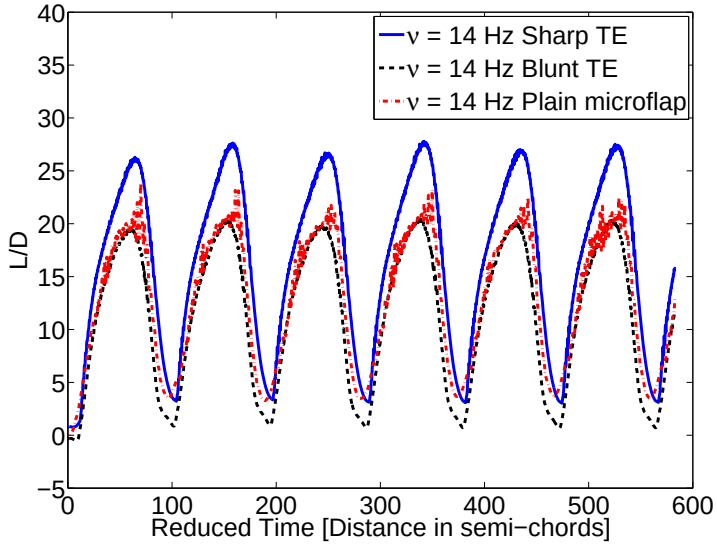

Figure 2.32: Comparison of lift-to-drag ratio obtained for three different microflap configurations on a NACA0012 airfoil. All the three configurations are equipped with a 1.5%c microflap. $M = 0.5142$, $\nu = 14$ Hz, and $\mathrm{Re} = 3.36$ x 10^6.

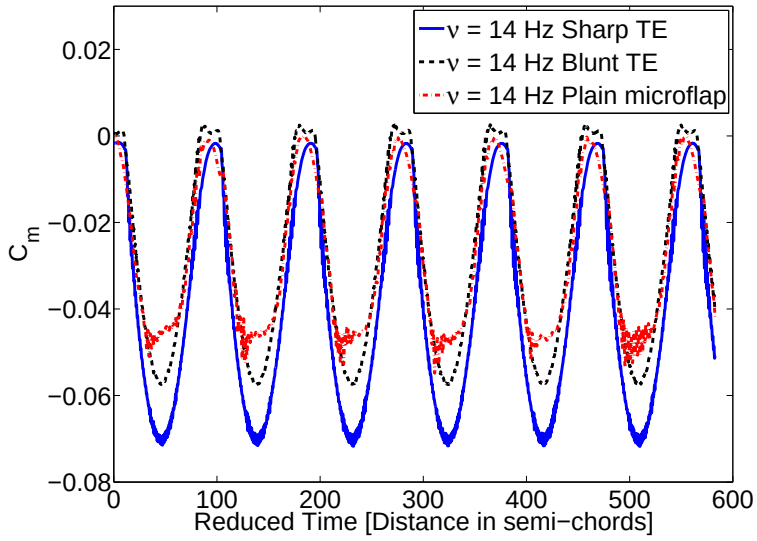

Figure 2.33: Comparison of the unsteady moment coefficient obtained for three different microflap configurations on a NACA0012 airfoil. All the three configurations are equipped with a 1.5%c microflap. $M = 0.5142$, $\nu = 14$ Hz, and $\mathrm{Re} = 3.36$ x 10^6.

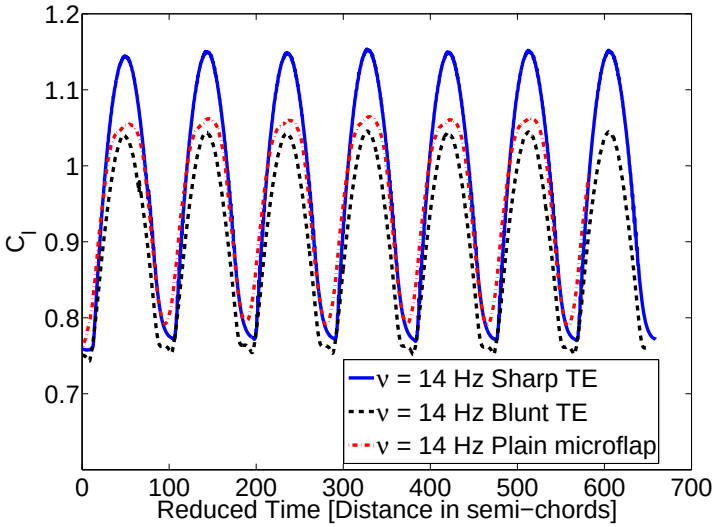

Figure 2.34: Comparison of lift coefficients corresponding to three different microflap configurations on a NACA0012 airfoil at $\alpha = 6°$. All the three configurations are equipped with a 1.5%c microflap. $M = 0.5142$, $\nu = 14$ Hz, and $\mathrm{Re} = 3.36$ x 10^6.

peak lift-to-drag ratio generated by the blunt trailing-edge configuration is approximately 30% less compared to the other two configurations. From an implementation point of view, the blunt trailing edge configuration may be the most feasible, followed by the sharp trailing-edge and the plain microflap configurations. Practical implementation of the plain microflap configuration on a rotor blade can be very difficult due to the stringent size limitations on the actuator and hinge setup. Overall, the sharp trailing-edge configuration is a good compromise between the aerodynamic benefits and the ease of implementation.

In order to provide an insight into the flow features behind an oscillating microflap, the pressure contour plot near the trailing edge of the airfoil is shown in Fig. 2.36 along with the evolution of streamlines during one cycle of microflap os-

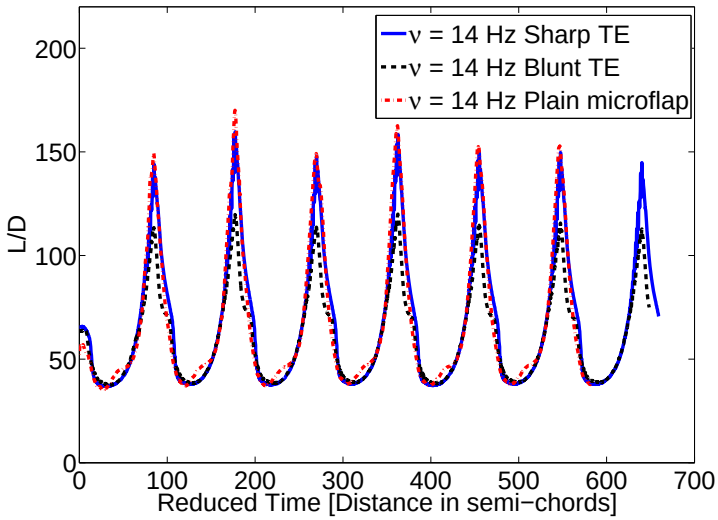

Figure 2.35: Comparison of lift-to-drag ratio obtained for three different microflap configurations on a NACA0012 airfoil at $\alpha = 6°$. All the three configurations are equipped with a 1.5%c microflap. $M = 0.5142$, $\nu = 14$ Hz, and $\mathrm{Re} = 3.36$ x 10^6.

cillation. The plain microflap configuration is used. Figure 2.36 clearly illustrates the development of the vortical structure behind the microflap which consists of two counter-rotating vortices when the microflap is fully deployed, and the pattern displayed in Fig. 2.36(b) is similar to that found on static Gurney flaps [59, 60].

2.3.5 Hinge Moment Comparison

One of the primary advantages of using the microflap for active control applications is the relatively low actuation power required for its deployment. In order to illustrate this, torque required to actuate a 1.5%c sliding sharp trailing-edge microflap using a lever arm (hinged at 75% chordwise location as shown in Fig. 2.37) is compared to the torque required to actuate a 20%c conventional plain flap. The

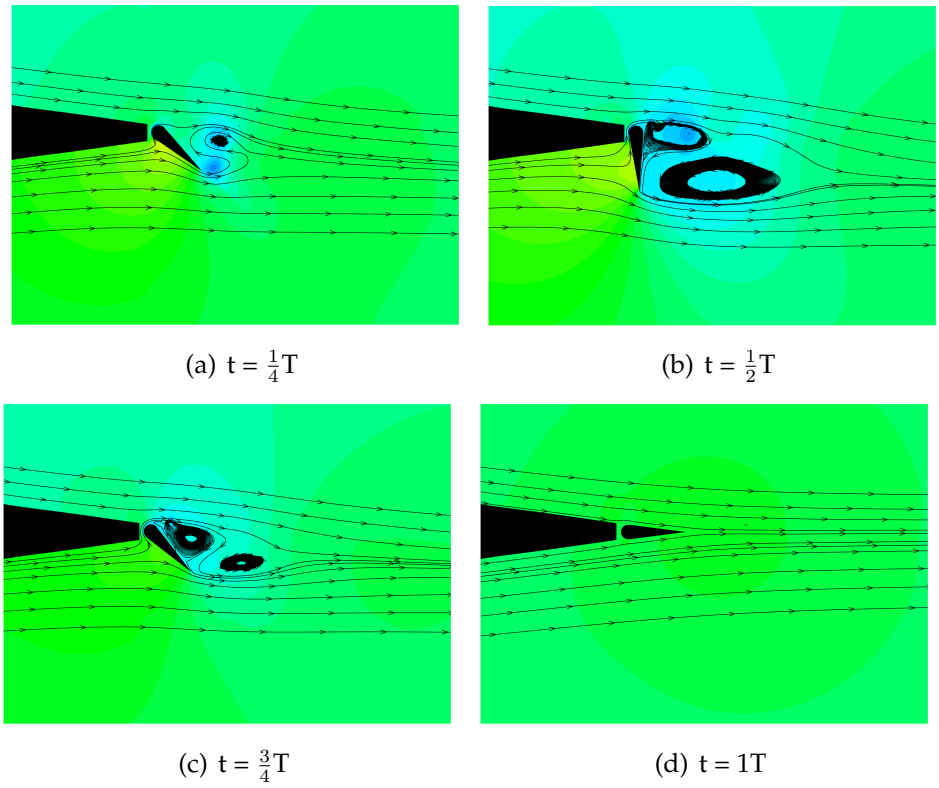

(a) t = $\frac{1}{4}$T (b) t = $\frac{1}{2}$T

(c) t = $\frac{3}{4}$T (d) t = 1T

Figure 2.36: Pressure contours and streamlines showing evolution of vortical structure during one cycle of oscillation behind the plain microflap at M = 0.51 and $\alpha = 0°$.

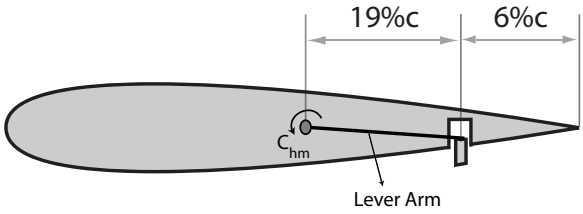

Figure 2.37: An illustration of microflap actuation using a lever arm.

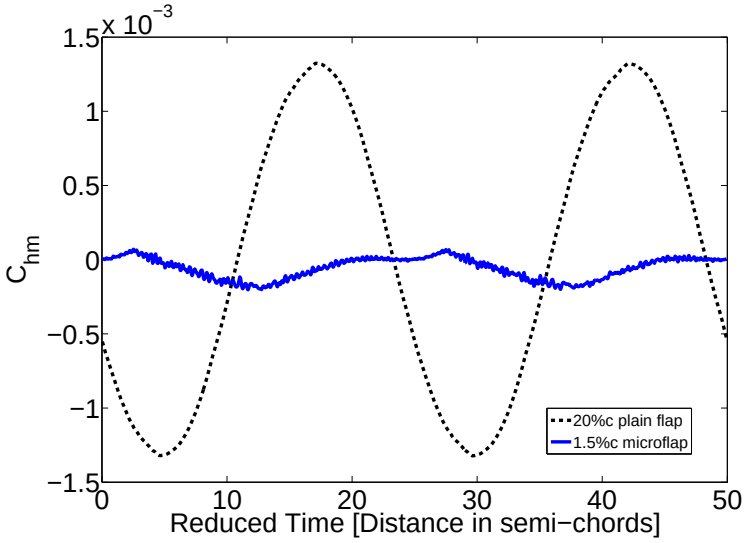

Figure 2.38: Unsteady hinge moments corresponding to a 1.5%c sharp trailing-edge microflap and a 20%c plain flap. The free stream Mach number and Reynolds number are 0.5142 and 3.36 x 10^6, respectively.

plain flap is deflected between $\pm 4^\circ$ about a hinge located at 80% chordwise location. The unsteady hinge moments corresponding to oscillating microflap and plain flap are compared in Fig. 2.38 for M = 0.5142, Re = 3.36 x 10^6, and $\nu = 14$ Hz. The hinge moment required to actuate the microflap is approximately 7 times lower compared to the plain flap.

CHAPTER III

A NONLINEAR UNSTEADY REDUCED-ORDER AERODYNAMIC MODEL

The importance of arbitrary motion unsteady aerodynamic models for accurate rotary-wing aeroelastic analysis is well discussed [42]. Two-dimensional unsteady aerodynamic theories such as Greenberg's theory, provide analytic expressions for the unsteady loads on a moving airfoil, but are usually based on the assumption of simple harmonic motion of the airfoil. These aerodynamic models are not expressed in a form directly compatible with the structural equations of motion which are usually expressed in the state variable form or as Laplace transforms. To overcome this issue, the rational function approximation (RFA) has been used to generate Laplace transform or state space representations of unsteady aerodynamic models based on oscillatory response data [35, 64, 110, 136, 137]. An RFA based state-space, time domain unsteady aerodynamic model that accounts for unsteady free-stream and compressibility effects was first developed and used for rotary-wing applications by Myrtle and Friedmann [92]. A two-dimensional

doublet-lattice (DL) method was used to obtain unsteady aerodynamic loading on an airfoil/trailing-edge flap combination over a range of reduced frequencies. Subsequently, the RFA approach was used to convert the frequency domain aerodynamic loads into the time domain. The resulting aerodynamic model, denoted here as the RFA model, is an unsteady, compressible state-space aerodynamic model, which has several important features: 1) it allows a convenient combination of the aerodynamics with the structural dynamic model; 2) it facilitates direct numerical integration for solving the combined system, which is governed by equations with periodic coefficients; and 3) it provides a degree of computational efficiency required for the study of active control devices such as conventional trailing-edge flaps. The RFA model was also incorporated into the comprehensive rotorcraft simulation code AVINOR. The code has been extensively used to examine the effect of active flaps on helicopter vibration and noise reduction as well as performance enhancement [44,79,102].

The DL method is based on linear potential flow theory and thus cannot predict the drag coefficient or account for the airfoil thickness effects. Furthermore, the flow characteristics behind a deployed microflap, which are dominated by viscous effects, cannot be determined by the DL method. These limitations are overcome in the present study by using a compressible unsteady RANS CFD solver to generate the frequency domain unsteady aerodynamic loads. These CFD based loads replace the DL based frequency domain unsteady loads used in earlier studies.

3.1 Description of the RFA Model

The RFA model developed in Ref. 92 is based on a Laplace domain representation of generalized aerodynamic load responses to generalized motions given by

$$\mathbf{G}(\bar{s}) = \mathbf{Q}(\bar{s})\mathbf{H}(\bar{s}), \tag{3.1}$$

where $\mathbf{G}(\bar{s})$ and $\mathbf{H}(\bar{s})$ represent Laplace transforms of the generalized aerodynamic load and motion vectors, respectively. A schematic description of the original doublet-lattice based RFA model is shown in Fig. 3.1. The aerodynamic transfer function matrix $\mathbf{Q}(\bar{s})$ is approximated as

$$\tilde{\mathbf{Q}}(\bar{s}) = \mathbf{C}_0 + \mathbf{C}_1\bar{s} + \sum_{n=1}^{n_L} \frac{\bar{s}}{\bar{s}+\gamma_n}\mathbf{C}_{n+1}. \tag{3.2}$$

where $\tilde{\mathbf{Q}}(\bar{s})$ is a rational function approximation of $\mathbf{Q}(\bar{s})$. Equation (3.2) is usually referred to as the Roger's approximation [110] and the n_L terms in the summation are referred to as the aerodynamic lag terms. The poles $\gamma_1, \gamma_2, ..., \gamma_{n_L}$ are chosen to be real and positive valued to ensure stability of the model. General guidelines for pole placement based on Bode plot methods will be discussed in the next section. The coefficient matrices $\mathbf{C}_0, \mathbf{C}_1, \ldots, \mathbf{C}_{n+1}$ in Eq. (3.2) are evaluated using least squares methods to provide the best fit for a given frequency domain aerodynamic

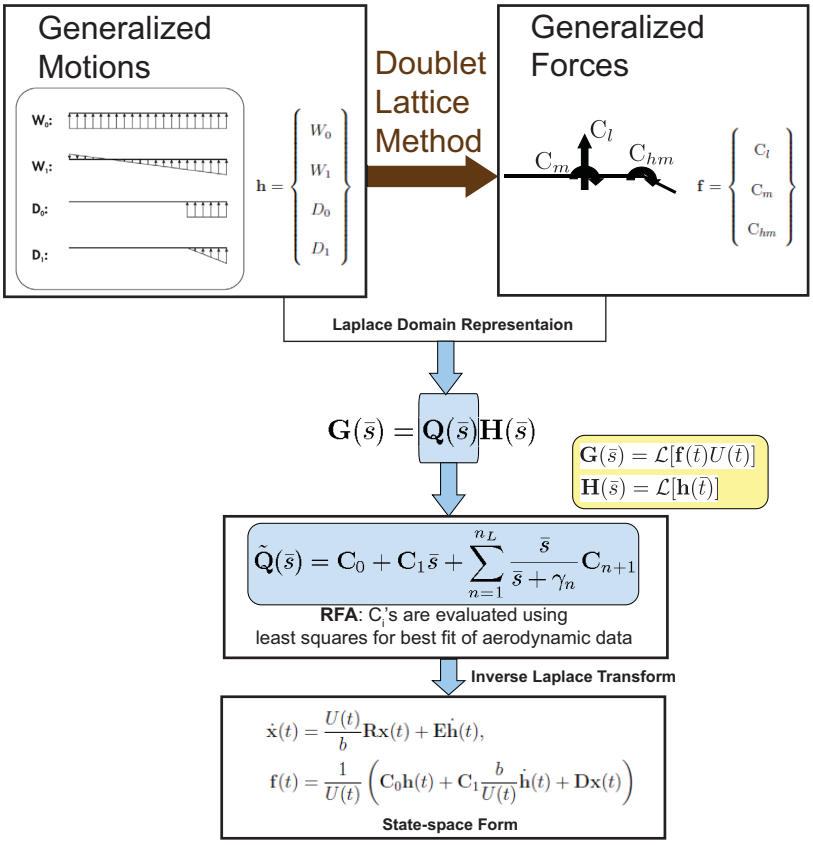

Figure 3.1: A schematic description of the original doublet lattice based RFA model.

response data, represented as

$$\mathbf{Q}(\imath k_m), \quad m = 1, \ldots, n_d, \tag{3.3}$$

where k_m represents the reduced frequency value at which aerodynamic response data is provided and n_d is the number of such reduced frequency values. The RFA model can be constrained at particular frequencies where an improved accuracy is desired. In the current model, a constraint is imposed at $k = 0$ to recover the steady state response by setting

$$\tilde{\mathbf{Q}}(0) = \mathbf{C}_0 = \mathbf{Q}(0). \tag{3.4}$$

Thus $\mathbf{C}_0$ represents the generalized load response to a static variation in the generalized motion. The fitting method used to determine the coefficients in the RFA approximation is similar to that described in Ref. 91. The first step is to replace the non-dimensional Laplace variable $\bar{s}$ in the Roger's approximation by $\imath k$,

$$\tilde{\mathbf{Q}}(\imath k) = \mathbf{C}_0 + \mathbf{C}_1 \imath k + \sum_{n=1}^{n_L} \frac{\imath k}{\imath k + \gamma_n} \mathbf{C}_{n+1}. \tag{3.5}$$

Using the relation

$$\frac{\imath k}{(\imath k + \gamma_n)} = \frac{k^2 + \imath k \gamma_n}{(\gamma_n^2 + k^2)}, \tag{3.6}$$

and the aerodynamic load responses given in Eq. (3.3), a set of algebraic equations corresponding to the i^{th} generalized load and the j^{th} generalized motion are obtained

$$\begin{bmatrix} 0 & \frac{k_m^2}{k_m^2+\gamma_1^2} & \cdots & \frac{k_m^2}{k_m^2+\gamma_{n_L}^2} \\ k_m & \frac{k_m\gamma_1}{k_m^2+\gamma_1^2} & \cdots & \frac{k_m\gamma_{n_L}}{k_m^2+\gamma_{n_L}^2} \end{bmatrix} \begin{Bmatrix} (\mathbf{C}_1)_{ij} \\ \vdots \\ (\mathbf{C}_{n_L+1})_{ij} \end{Bmatrix} = \begin{Bmatrix} Re[\mathbf{Q}_{ij}(\imath k_m)] - \mathbf{Q}_{ij}(0) \\ Im[\mathbf{Q}_{ij}(\imath k_m)] \end{Bmatrix}, \quad (3.7)$$

which can be expressed as

$$\mathbf{l}(k_m)\mathbf{c} = \mathbf{r}(k_m), \quad (3.8)$$

where,

$$\mathbf{l}(k_m) = \begin{bmatrix} 0 & \frac{k_m^2}{k_m^2+\gamma_1^2} & \cdots & \frac{k_m^2}{k_m^2+\gamma_{n_L}^2} \\ k_m & \frac{k_m\gamma_1}{k_m^2+\gamma_1^2} & \cdots & \frac{k_m\gamma_{n_L}}{k_m^2+\gamma_{n_L}^2} \end{bmatrix}, \mathbf{c} = \begin{Bmatrix} (\mathbf{C}_1)_{ij} \\ \vdots \\ (\mathbf{C}_{n_L+1})_{ij} \end{Bmatrix}, \text{and} \quad (3.9)$$

$$\mathbf{r}(k_m) = \begin{Bmatrix} Re[\mathbf{Q}_{ij}(\imath k_m)] - \mathbf{Q}_{ij}(0) \\ Im[\mathbf{Q}_{ij}(\imath k_m)] \end{Bmatrix}. \quad (3.10)$$

The curly braces are used to represent a vector whereas the square braces are used to represent a matrix. Equation (3.7) is generated for all the n_d frequency values at

which aerodynamic load response data is available, thus,

$$\begin{bmatrix} \mathbf{l}(k_1) \\ \mathbf{l}(k_2) \\ \vdots \\ \mathbf{l}(k_{n_d}) \end{bmatrix} \{\mathbf{c}\} = \begin{Bmatrix} \mathbf{r}(k_1) \\ \mathbf{r}(k_2) \\ \vdots \\ \mathbf{r}(k_{n_d}) \end{Bmatrix}. \tag{3.11}$$

The coefficients in $\mathbf{c}$ are solved for using least squares methods. This process is repeated for every generalized load corresponding to each generalized motion.

A two-dimensional unsteady aerodynamic model for rotary-wing applications needs to have the capability to accurately model the response to arbitrary pitch and plunge motions in an unsteady freestream. For the RFA model used in this study, an orthogonal set of normal velocity distributions on the airfoil chord are selected such that a linear combination of these normal velocity *modes* can completely describe the boundary conditions at the airfoil surface due to arbitrary pitching and plunging motion of the airfoil and unsteady freestream. Following the approach used in Ref. 92, arbitrary motion of an airfoil and trailing-edge flap combination can be represented by four generalized motions shown in Fig. 3.2. These normal velocity distributions correspond to two generalized airfoil motions (denoted by W_0 and W_1) and two generalized flap motions (denoted by D_0 and D_1). The generalized airfoil motions are assigned magnitudes equal to the normal velocity at the 3/4 chord and can be expressed in terms of the classical pitch and plunge modes

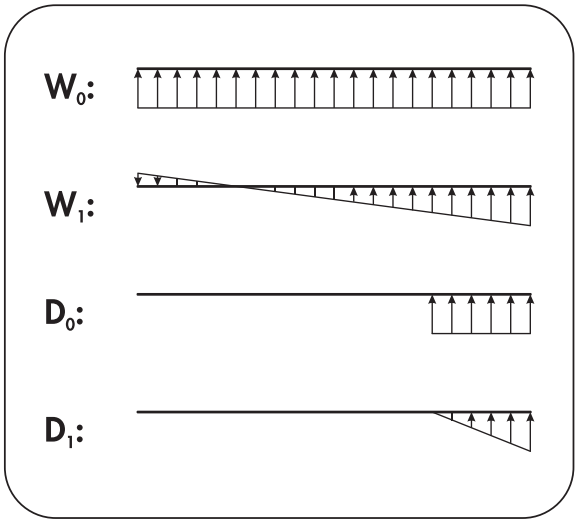

Figure 3.2: Normal velocity distribution corresponding to generalized airfoil and flap motions.

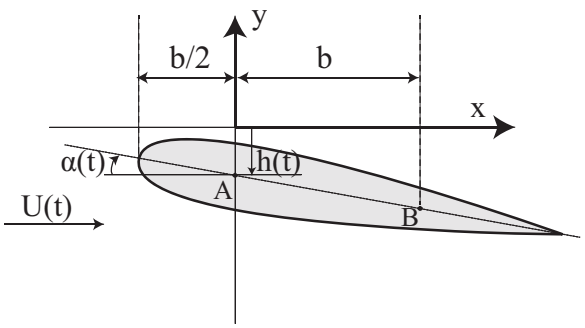

Figure 3.3: Airfoil undergoing pitching and plunging motion.

α and h, depicted in Fig. 3.3, as

$$W_0 = U\alpha + \dot{h}, \tag{3.12}$$

$$W_1 = b\dot{\alpha}. \tag{3.13}$$

In order to find the Least Squares approximations for the coefficient matrices $\mathbf{C}_0, \mathbf{C}_1, \ldots, \mathbf{C}_{n+1}$ in Eq. (3.2), aerodynamic frequency response data $\mathbf{Q}(k_m)$ corresponding to each of the four generalized motions must be obtained. In the orig-

inal RFA implementation, the oscillatory airloads in the frequency domain were obtained from a two-dimensional doublet lattice (DL) solution [109] of Possio's integral equation [12] which relates the normal velocity distribution $\bar{w}(x)$ on the surface of an oscillating airfoil to the surface pressure distribution $\bar{p}(x)$ as

$$\bar{w}(x) = \frac{1}{8\pi} \int_{-1}^{1} \bar{p}(\zeta) K_p(M, x-\zeta) d\zeta, \tag{3.14}$$

where kernel K_p is given by:

$$\begin{aligned} K_p(M,x) &= \frac{\pi k}{\beta} e^{-ikx} \left\{ e^{kx/\beta^2} \left(M \frac{|x|}{x} H_1^{(2)}(Mk|x|/\beta^2) - H_0^{(2)}(Mk|x|/\beta^2) \right) \right. \\ &\quad \left. + \frac{i2\beta}{\pi} \log(\frac{1+\beta}{M}) + i\beta^2 \int_0^{kx/\beta^2} \frac{kx}{2\beta^2} e^{iu} H_0^{(2)}(M|u|) du \right\}. \end{aligned} \tag{3.15}$$

Approximate solutions for $\bar{p}$ were obtained from Eq. (3.14) for a given normal velocity distribution $\bar{w}$ using the doublet lattice method. This approach was found to be very efficient for generating a set of aerodynamic response data for the generalized motions of airfoil/flap combination. The frequency domain information was generated for an appropriate set of reduced frequencies and Mach numbers, corresponding to the unsteady flow conditions encountered on a given rotor.

To derive a state space representation of the RFA aerodynamic model, a gener-

alized motion vector $\mathbf{h}$ and a generalized load vector $\mathbf{f}$ are defined as:

$$\mathbf{h} = \begin{Bmatrix} W_0 \\ W_1 \\ D_0 \\ D_1 \end{Bmatrix} \quad \text{and} \quad \mathbf{f} = \begin{Bmatrix} \mathrm{C}_l \\ \mathrm{C}_m \\ \mathrm{C}_{hm} \end{Bmatrix}. \tag{3.16}$$

These vectors are related to the generalized motions and the generalized forces in the Laplace transform representation, given in Eq. (3.1), as follows:

$$\mathbf{G}(\bar{s}) = \mathcal{L}[\mathbf{f}(\bar{t})U(\bar{t})] \quad \text{and} \quad \mathbf{H}(\bar{s}) = \mathcal{L}[\mathbf{h}(\bar{t})], \tag{3.17}$$

where reduced time $\bar{t} = \frac{1}{b}\int_0^t U(\tau)d\tau$, interpreted as the distance traveled by the airfoil measured in semi-chords, is used in order to properly account for the unsteady freestream effects [92]. Finally, the rational function $\tilde{\mathbf{Q}}$ in Eq. (3.2) can be transformed to the time domain using inverse Laplace transform, which yields the final form of the state space model,

$$\dot{\mathbf{x}}(t) = \frac{U(t)}{b}\mathbf{R}\mathbf{x}(t) + \mathbf{E}\dot{\mathbf{h}}(t), \tag{3.18}$$

$$\mathbf{f}(t) = \frac{1}{U(t)}\left(\mathbf{C}_0\mathbf{h}(t) + \mathbf{C}_1\frac{b}{U(t)}\dot{\mathbf{h}}(t) + \mathbf{D}\mathbf{x}(t)\right). \tag{3.19}$$

where

$$\mathbf{D} = \begin{bmatrix} \mathbf{I} & \mathbf{I} & \dots & \mathbf{I} \end{bmatrix}, \mathbf{R} = -\begin{bmatrix} \gamma_1\mathbf{I} & & & \\ & \gamma_2\mathbf{I} & & \\ & & \ddots & \\ & & & \gamma_{n_L}\mathbf{I} \end{bmatrix},$$

$$\mathbf{E} = \begin{bmatrix} \mathbf{C}_2 \\ \mathbf{C}_3 \\ \vdots \\ \mathbf{C}_{n_L+1} \end{bmatrix},$$

and $\mathbf{I}$ is an identity matrix with size equal to the number of generalized forces. Note that the relation $\frac{d}{d\bar{t}} = \frac{b}{U(t)}\frac{d}{dt}$ can be used to switch between the independent variables t and $\bar{t}$. The vector $\mathbf{x}(t)$ has $3n_L$ elements which are referred to as the aerodynamic states of the model.

3.2 A CFD-based RFA Model

The DL method is based on linear potential flow theory; as a result, the RFA model constructed based on oscillatory responses generated using the DL method is no longer valid when significant flow nonlinearities associated with viscous effects or shock wave formation are present. As mentioned earlier, flow characteristics of a fully deployed microflap are governed by viscous effects and therefore cannot be predicted from the DL method. Furthermore, unsteady drag due to the

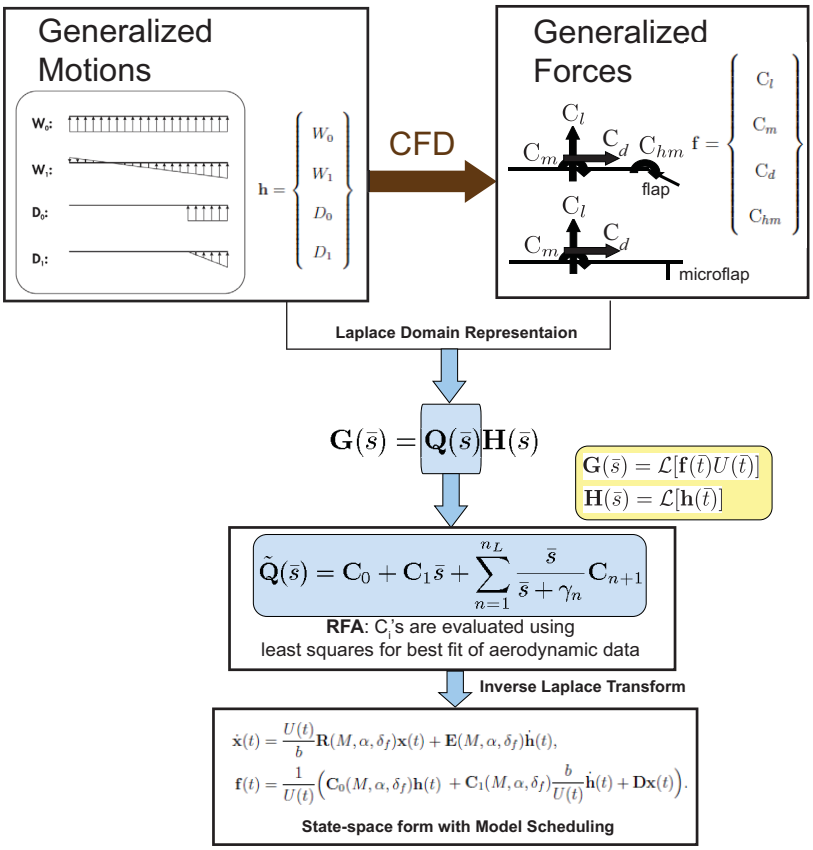

Figure 3.4: A schematic description of the new CFD based RFA model.

microflap motion, which is important for estimating the performance penalty due to such devices, cannot be obtained from potential flow theory. Therefore, in order to construct a ROM for the microflap, the frequency domain solutions required for the construction of the RFA model are obtained from a compressible unsteady RANS solver, CFD++. A schematic description of the new CFD based RFA model is shown in Fig. 3.4. When using this approach the generalized load vector $\mathbf{f}$ is

written as

$$\mathbf{f} = \begin{Bmatrix} \mathrm{C}_l \\ \mathrm{C}_m \\ \mathrm{C}_d \\ \mathrm{C}_{hm} \end{Bmatrix} \tag{3.20}$$

The hinge moment as defined for a regular flap is not applicable for the microflap. The actuation power required to deploy the microflap is a function of the vertical force exerted by the flow on the bottom surface of the microflap. The CFD simulations have indicated that this force is negligible and therefore it is not considered in the aerodynamic model.

The description of the airfoil motion is based on the two generalized airfoil motions represented by W_0 and W_1 and is identical to that used in the original RFA model. The two generalized flap motions, D_0 and D_1, that were used in the original RFA model are valid when constructing the CFD based RFA model for a conventional plain flap. However, for the microflap, these normal velocity distributions are no longer meaningful; therefore, the microflap is simply characterized by one generalized motion, namely, the deflection δ_f, where the deflection represents the deployment amplitude. The generalized motion D_1, used in the original RFA model to describe the motion of conventional flaps, is not used when constructing the CFD based RFA model for a microflap. This is justified because the generalized motion D_1 primarily represents the apparent mass effect, which is found to be

insignificant for the microflap in the CFD simulations. Therefore, the generalized motion vector $\mathbf{h}$ for the microflap is expressed as

$$\mathbf{h} = \left\{ \begin{array}{c} W_0 \\ W_1 \\ D_0 \end{array} \right\} \tag{3.21}$$

where

$$D_0 \;\; = \;\; \delta_f \tag{3.22}$$

3.2.1 Model scheduling and interpolation

In order to account for flow nonlinearities encountered at high Mach numbers, large angles of attack, and large amplitudes of microflap deflection, the RFA model is modified using a technique referred to as *model scheduling* [4]. This procedure resembles the gain scheduling approach commonly used in nonlinear control system design [4, 72]. In this approach the different sets of RFA coefficients are generated at appropriate combinations of the Mach number, angle of attack, and microflap deflection. Specifically, the RFA model is modified by allowing the coefficient matrices in the time domain RFA model, $\mathbf{R}, \mathbf{E}, \mathbf{C}_0, \mathbf{C}_1, \ldots, \mathbf{C}_{\mathbf{n_L+1}}$ to vary with M, α,

and δ_f. The resulting state space model in the time domain can be written as

$$\begin{aligned}\dot{\mathbf{x}}(t) &= \frac{U(t)}{b}\mathbf{R}(M,\alpha,\delta_f)\mathbf{x}(t) + \mathbf{E}(M,\alpha,\delta_f)\dot{\mathbf{h}}(t),\\ \mathbf{f}(t) &= \frac{1}{U(t)}\Big(\mathbf{C}_0(M,\alpha,\delta_f)\mathbf{h}(t)\\ &\quad + \mathbf{C}_1(M,\alpha,\delta_f)\frac{b}{U(t)}\dot{\mathbf{h}}(t) + \mathbf{D}\mathbf{x}(t)\Big).\end{aligned} \tag{3.23}$$

Coefficients of the RFA model are evaluated at various flow conditions (combinations of M, α, and δ_f values) and then a two-dimensional shape-preserving piecewise cubic Hermite polynomial interpolation scheme [13, 63, 106] is used to evaluate the coefficients at intermediate flow conditions. To illustrate this interpolation scheme, consider a set of data points $(x_1, y_1), (x_2, y_2), \ldots, (x_n, y_n)$ that satisfy a nonlinear function $y = f(x)$. Let h_k denote the k^{th} interval

$$h_k = x_{k+1} - x_k. \tag{3.24}$$

The corresponding divided difference is defined as

$$\delta_k = \frac{y_{k+1} - y_k}{h_k}. \tag{3.25}$$

Consider the following cubic function over the interval $x_k \leq x \leq x_{k+1}$, expressed in terms of local variables $s = x - x_k$ and $h = h_k$

$$P(x) = \frac{3hs^2 - 2s^3}{h^3}y_{k+1} + \frac{h^3 - 3hs^2 + 2s^3}{h^3}y_k + \frac{s^2(s-h)}{h^2}d_{k+1} + \frac{s(s-h)^2}{h^2}d_k. \tag{3.26}$$

The polynomial $P(x)$ satisfies four interpolation conditions, two corresponding to the function values and two corresponding to the derivative values:

$$P(x_k) = y_k, \;\; P(x_{k+1}) = y_{k+1}, \tag{3.27}$$

$$P'(x_k) = d_k, \;\; P'(x_{k+1}) = d_{k+1}. \tag{3.28}$$

Interpolating functions that satisfy conditions on the function values as well as the derivatives are known as Hermite interpolants. If the derivative values are not provided, the slopes d_k can be defined. For the shape-preserving piecewise cubic Hermite polynomial interpolation scheme, the slopes d_k are defined so that the interpolation error is minimized at the given data points. As illustrated in Fig. 3.5(a), if the divided differences δ_k and δ_{k-1} have opposite signs or if either of them is zero, implying that x_k is a local minimum or maximum, then,

$$d_k = 0. \tag{3.29}$$

The solid curved line in Fig. 3.5(a) is the shape-preserving interpolating polynomial, formed from two different cubic polynomials. The two cubic polynomials have a derivative equal to 0 at $x = x_k$. If δ_k and δ_{k-1} have the same sign, as illustrated in Fig. 3.5(b), then the slope d_k is defined as the harmonic mean of the divided differences:

$$\frac{1}{d_k} = \frac{1}{2}\left(\frac{1}{\delta_{k-1}} + \frac{1}{\delta_k}\right). \tag{3.30}$$

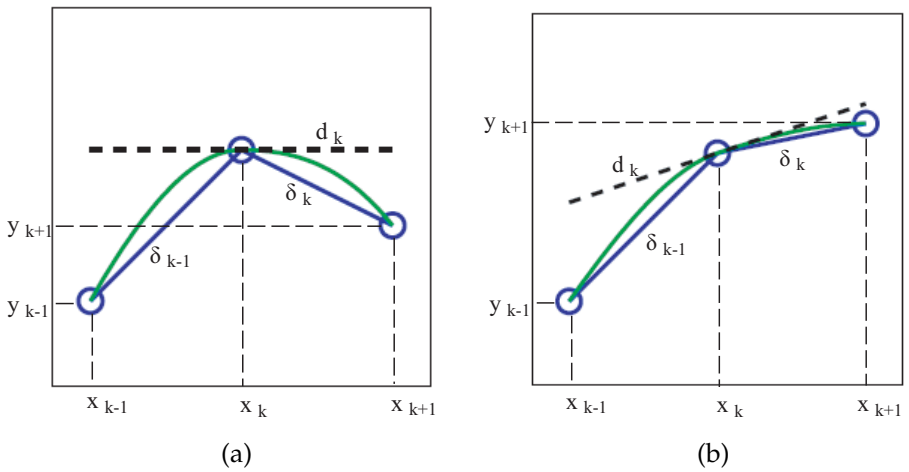

Figure 3.5: An illustration of the shape-preserving piecewise cubic Hermite polynomial interpolation scheme.

The solid curved line in Fig. 3.5(b) is the shape-preserving interpolating polynomial, formed from two different cubic polynomials. The two cubic polynomials have a derivative equal to d_k at $x = x_k$.

3.2.2 Pole placement

In the original RFA model, locations of the poles (represented by $\gamma_1, \gamma_2, ..., \gamma_{n_L}$ in Eq. 3.2) were not considered to be critical for an accurate approximation [91]. The poles were assigned certain initial values and a standard numerical optimization routine was used to adjust the pole locations such that the fitting error is minimized. The initial values of the poles have a significant influence on the final values of the poles obtained from the optimization routine. How these initial values were determined was not clear.

The pole locations can have a significant effect on the accuracy of the RFA approximation and choosing the pole locations appropriately can help improve ac-

curacy without having to increase the order of the reduced order model. Insights from the standard Bode plot design techniques [41] used in control systems design and analysis can be helpful in determining appropriate pole locations for the RFA aerodynamic model. Bode plot techniques were used in Ref. 136 to construct finite state approximations to Loewy's lift deficiency function, which is the rotary-wing counterpart of Theodorsen's lift deficiency function. The standard representation of a Bode plot consists of logarithmic magnitude of a transfer function $G(\jmath\omega)$ in decibels, where $|G(\jmath\omega)|_{dB} = 20\log_{10}|G(\jmath\omega)|$, and the phase of the transfer function plotted against frequency ω.

For the purpose of illustration, consider a transfer function $G(\jmath\omega) = \frac{\jmath\omega+1}{\jmath\omega+0.1}$. The Bode magnitude and phase plots for $G(\jmath\omega)$ are shown in Fig. 3.6 (note that a a logarithmic scale is used to represent frequency ω on the horizontal axis). Around the frequency value 0.1 rad/sec, the slope of the Bode magnitude plot changes from 0 db/decade to -20 db/decade, indicating the presence of a real pole at 0.1 in the transfer function. At frequency 1 rad/sec, the slope of the Bode magnitude plot changes from -20 db/decade to 0 db/decade, indicating the presence of a real zero at 1 in the transfer function. The frequencies at which the Bode magnitude plot undergoes a change in slope are referred to as *corner frequencies*. These frequencies correspond to the pole and zero locations in the transfer function. The corner frequencies also mark changes in slope of the Bode phase plot. Thus, the locations of the poles and zeros have a significant influence on the overall shape and orientation of the Bode plots.

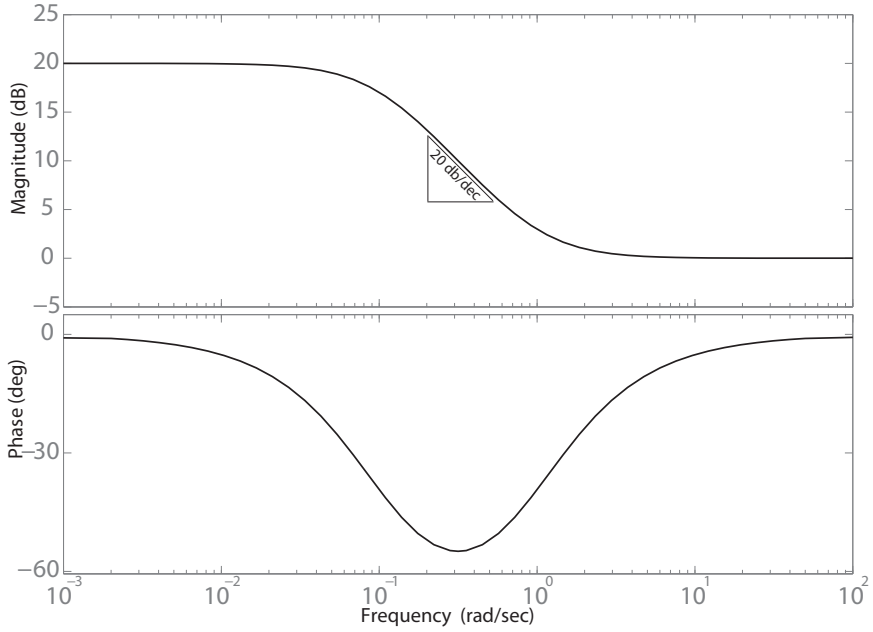

Figure 3.6: Bode magnitude and Phase plots for the transfer function $G(\jmath\omega) = \frac{\jmath\omega+1}{\jmath\omega+0.1}$.

To illustrate the effect of pole locations in the RFA model, the CFD based RFA approximation is constructed using two different sets of poles, listed in Table 3.1, for a sinusoidal pitching motion of the airfoil with amplitude 1° at $M = 0.3$ and $\alpha = 2^\circ$. The C_l amplitude and phase response corresponding to various reduced frequencies obtained from CFD simulations and the two CFD based RFA approximations are compared are shown in Fig. 3.7. The CFD data is generated over the reduced frequency range 0.02-0.2. The RFA approximation in Fig. 3.7(a) is based on the 7 poles in Set 1 whereas the approximation in Fig. 3.7(b) is based on the 7 poles in Set 2. The poles in Set 2 were calculated by the optimization routine in the code. The first set which has all the poles located close to the frequency range of interest (0.02 rad/sec - 0.2 rad/sec) clearly yields an accurate approximation compared to

Set 1	Set 2
0.0100000	0.0532568
0.0150000	1.3066788
0.0560000	2.9389403
0.0920000	5.2245369
0.1280000	8.1632758
0.1640000	11.7551047
0.3500000	16.0000008

Table 3.1: Two sets of poles used to demonstrated the effect of pole locations on the accuracy of the RFA model.

the second set which has only one pole in the frequency range 0.02 rad/sec - 0.2 rad/sec.

Based on this illustration, one can conclude that placing poles close to the frequency range being modeled is beneficial for obtaining an accurate RFA approximation. In the current study, poles are evenly distributed over the relevant reduced frequency range 0.02 rad/sec - 0.2 rad/sec. In order to accurately capture the frequency response at the edges of the relevant frequency range, poles are placed at 0.015 and 0.35. As mentioned earlier, the RFA model is constrained at $k = 0$ in order to recover the steady state value. For high angles of attack, difference in the magnitude of steady state aerodynamic loads corresponding to $k = 0$ and the unsteady aerodynamic load amplitudes at reduced frequency $k = 0.02$ is significant. To capture this transition, an additional pole is placed at 0.01. Moving the pole

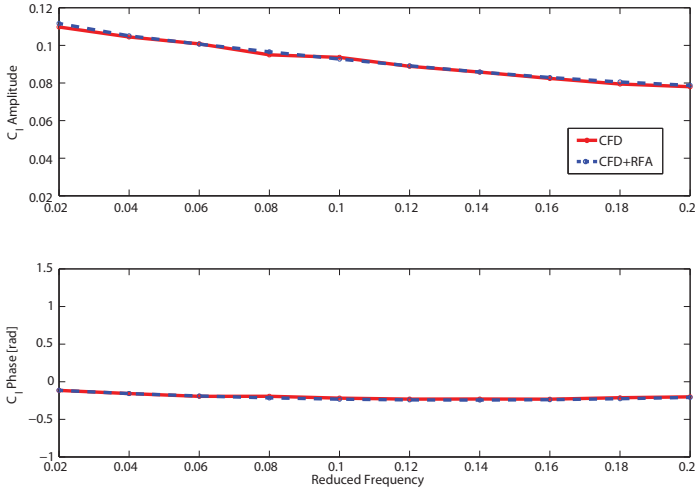

(a) Set 1

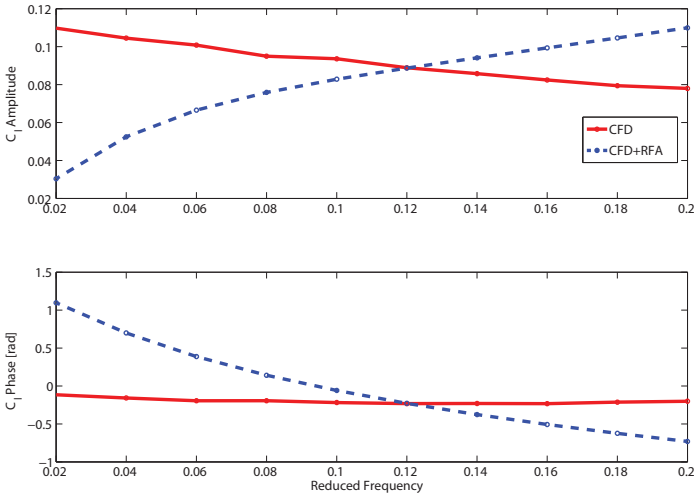

(b) Set 2

Figure 3.7: Comparison of C_l frequency response to a sinusoidal pitching motion of the airfoil obtained from CFD and the CFD based RFA approximation using two different sets of poles listed in Table 3.1. Mach number $M = 0.3$ and $\alpha = 2°$.

too close to 0 should be avoided since it reduces the damping in the model and increases the settling time.

3.3 Constructing the CFD-based RFA Model

Procedure used for constructing the CFD-based RFA model is described in this section. Based on the studies described in Chapter II, the sharp trailing-edge microflap configuration with a 1.5%c microflap, shown in Fig. 2.13, was selected as the basic configuration. In order to generate a reduced order model that can represent the entire range of flow conditions encountered by the rotor blades at various advance ratios, CFD based aerodynamic load responses to various generalized motions are obtained for Mach number range 0.05 to 0.8 with an increment of 0.05 and an angle of attack range -2° to 15° with an increment of 1°. At each flow condition defined by the free stream Mach number and the airfoil mean angle of attack, simulations are performed to generate frequency domain load responses for reduced frequency values ranging from 0.02 to 0.2 with an increment of 0.02. Note that the 5/rev frequency, which is the highest actuation frequency used for vibration reduction in this study, corresponds to a reduced frequency value of approximately 0.18 based on the average local freestream velocity for a blade section at 0.75R span location. A 1° oscillation amplitude is used for the generalized motions W_0 and W_1. In the case of a conventional plain flap, a 1° flap deflection amplitude is used for the D_0 and D_1 generalized motions and for the microflap, 1.5%c flap deflection amplitude is used for the D_0 generalized motion. Each simulation is run for 4 complete

oscillation cycles with 400 time steps in each cycle. Some transients are observed during the first cycle but a periodic steady state response is achieved by the third cycle. Sensitivity of the aerodynamic load predictions to the number of time steps used in each cycle was examined at Mach number $M = 0.6$ and static airfoil angle of attack $\alpha = 5^{\circ}$. The C_l amplitude predictions corresponding to various number of time steps are shown in Fig. 3.8 for the W_0 generalized motion. The predictions converge with increasing number of time steps. A good compromise between the accuracy of the aerodynamic load predictions and the computational time requirements can be obtained when using 400 time steps per cycle. Each simulation takes approximately 45 minutes to finish when run using 4 Intel 2.6 GHz Xeon parallel processors. The aerodynamic load response data obtained from CFD is processed using the FFT (Fast Fourier Transform) tool in MATLAB. The frequency domain data thus obtained is tabulated and used to generate the coefficients $\mathbf{C}_0$, $\mathbf{C}_1$, ... , $\mathbf{C}_{n_L+1}$ in the RFA model (see Eq. 3.23). The dependence of the RFA coefficients on the microflap deployment δ_f is not considered in this study. The Reynolds number is 2.1 x 10^6 for all the simulations.

3.4 Verifications and Discussion

3.4.1 Verifications for the Microflap

In order to verify the reduced order aerodynamic model, predictions from the CFD based RFA model are compared to direct CFD simulations at various reduced

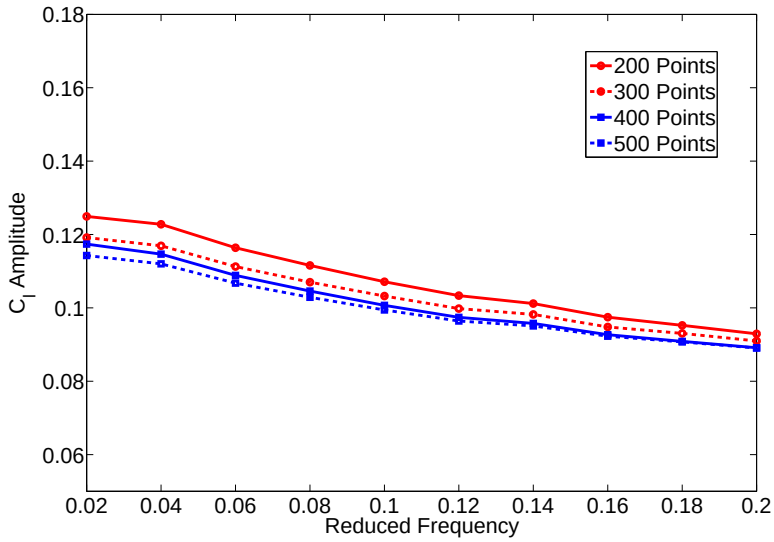

Figure 3.8: C_l amplitude corresponding to the W_0 generalized motion predicted using various number of time steps per cycle. Mach number $M = 0.6$ and static airfoil angle of attack $\alpha = 5°$.

frequencies and flow conditions. The microflap motion is given by Eq. (2.2) with A = 0.75%c. In the figures, predictions from the CFD based RFA model are referred to as the CFD+RFA model. The first set of results are generated at Mach number M=0.6 and the airfoil angle of attack $\alpha = 0°$. Figures 3.9(a), 3.9(d), and 3.9(g) show the unsteady lift variation corresponding to the microflap motion at reduced frequencies 0.06, 0.1, and 0.2, respectively. The direct CFD results, indicated by the circles, are compared to the CFD based RFA model predictions represented by the full line. The agreement for all reduced frequencies shown is excellent and the CFD based RFA model captures the unsteady lift deficiency effect as the reduced frequency is increased from 0.06 to 0.2. Similarly, the unsteady moment is also captured accurately by the CFD based RFA model, as shown in Figs. 3.9(b), 3.9(e),

and 3.9(h). The unsteady drag predictions are compared in Figs. 3.9(c), 3.9(f), and 3.9(i). The unsteady drag predictions exhibit some error in the mean values (less than 10%) when compared to the CFD calculations. This error in the mean value predictions may be reduced by using more CFD fitting points when generating the reduced order model. Nevertheless, it is evident from Fig. 3.9 that the oscillating amplitudes of lift, moment and drag coefficients due to the microflap motion are captured well.

Another set of results comparing the CFD based RFA model predictions to direct CFD simulations at Mach numbers between 0.3-0.7 is shown in Fig. 3.10. The airfoil angle of attack $\alpha = 5^\circ$ and the microflap oscillating frequency is $k = 0.1$. Again, excellent agreement is found between the model predictions and direct CFD simulations. These comparisons indicate that the CFD based RFA model is accurate for the range of Mach numbers examined.

The comparisons for the CFD based RFA model and direct CFD simulations at airfoil angles of attack up to $\alpha = 10^\circ$ are shown in Fig. 3.11, at $M = 0.6$ and $k = 0.1$. It is evident from Fig. 3.11 that the reduced order model does not capture some of the strong nonlinear effects in the unsteady responses due to substantial flow separation, particularly at higher angles of attack $\alpha = 8^\circ$ and 10°. Nevertheless, good agreement in the overall trend and reasonable estimates in the mean values as well as oscillating magnitudes due to the microflap deflections are obtained.

Finally, comparisons of the ROM with direct CFD simulations conducted at an unsteady flow condition, that is representative of rotorcraft aerodynamic en-

vironment are shown in Fig. 3.12. The combined airfoil and microflap motion corresponds to a typical section on a rotor blade, with the airfoil rotating about the quarter chord and the microflap deflecting simultaneously. The unsteady motion time histories are plotted against the azimuth angle during one rotor revolution, shown in Figs. 3.12(a)-3.12(c). The overall airfoil pitching motion includes the effect of geometric pitch setting (collective and blade pretwist), as well as 1/rev cyclic pitch angles for rotor control, shown in Fig. 3.12(a). The microflap deflection consists of 2-5/rev harmonics (Fig. 3.12(b)), where each harmonic component is randomly phased with the same peak-to-peak amplitude of 0.375%c. Furthermore, the simultaneous airfoil/microflap motion is subject to freestream velocity variations, shown in Fig. 3.12(c), representing the influence of helicopter forward speed. The lift, moment and drag variations due to the combined motion are shown in Figs. 3.12(d)-3.12(f). The baseline in Figs. 3.12(d)-3.12(f) denotes the case in which the airfoil has a pitching motion given by Fig. 3.12(a) and is subject to the freestream variation shown in Fig. 3.12(c), but without the microflap deflection, which is intended to be used to identify the effects of the microflap deflection. As can be seen from Fig. 3.12(d), the unsteady lift predictions from the ROM, with or without microflap deflection, are in excellent agreement with the direct CFD calculations. It is also evident from Fig. 3.12(e) that the moment predictions agree quite well with the direct CFD results. The agreement in unsteady drag predictions (Fig. 3.12(f)) is not as good compared to lift and moment; however, the effect of the microflap on unsteady drag is captured, when comparing the unsteady drag due to the microflap to the baseline.

Overall, for a wide range of flow conditions representative of the operating conditions encountered in rotorcraft applications, the CFD based RFA model for the microflap provides excellent accuracy when compared to direct CFD calculations. Furthermore, the ability of the CFD based model to account for unsteady drag is a large improvement when compared to the original RFA model.

3.4.2 Verifications for a Conventional Plain Flap

In order to demonstrate the advantage of the new CFD based RFA model compared to the original DL based RFA model, sectional airloads obtained using the two models are compared to direct CFD computations. Since the DL based ROM can not predict the aerodynamic loads due to a microflap, a 20%c conventional plain flap configuration shown in Fig. 3.13 is used. In the figures illustrating the aerodynamic comparisons, the new reduced order model developed in this study using CFD data obtained from CFD++ is referred to as the CFD+RFA model. The previous potential flow solver based RFA model is referred to as the DL+RFA model. Oscillatory sectional aerodynamic loads on a NACA0012 airfoil at various angles of attack and Mach numbers were calculated using these two ROMs and compared to direct CFD simulations. The test cases were selected to be representative of the rotorcraft aerodynamic environment encountered by active flaps on a full-scale vehicle. For an MBB BO-105 hingeless rotor configuration, which has been widely used in the active flap studies conducted at the University of Michigan (Ref. 102), the hover tip speed corresponds to M=0.64. Since the flap is most

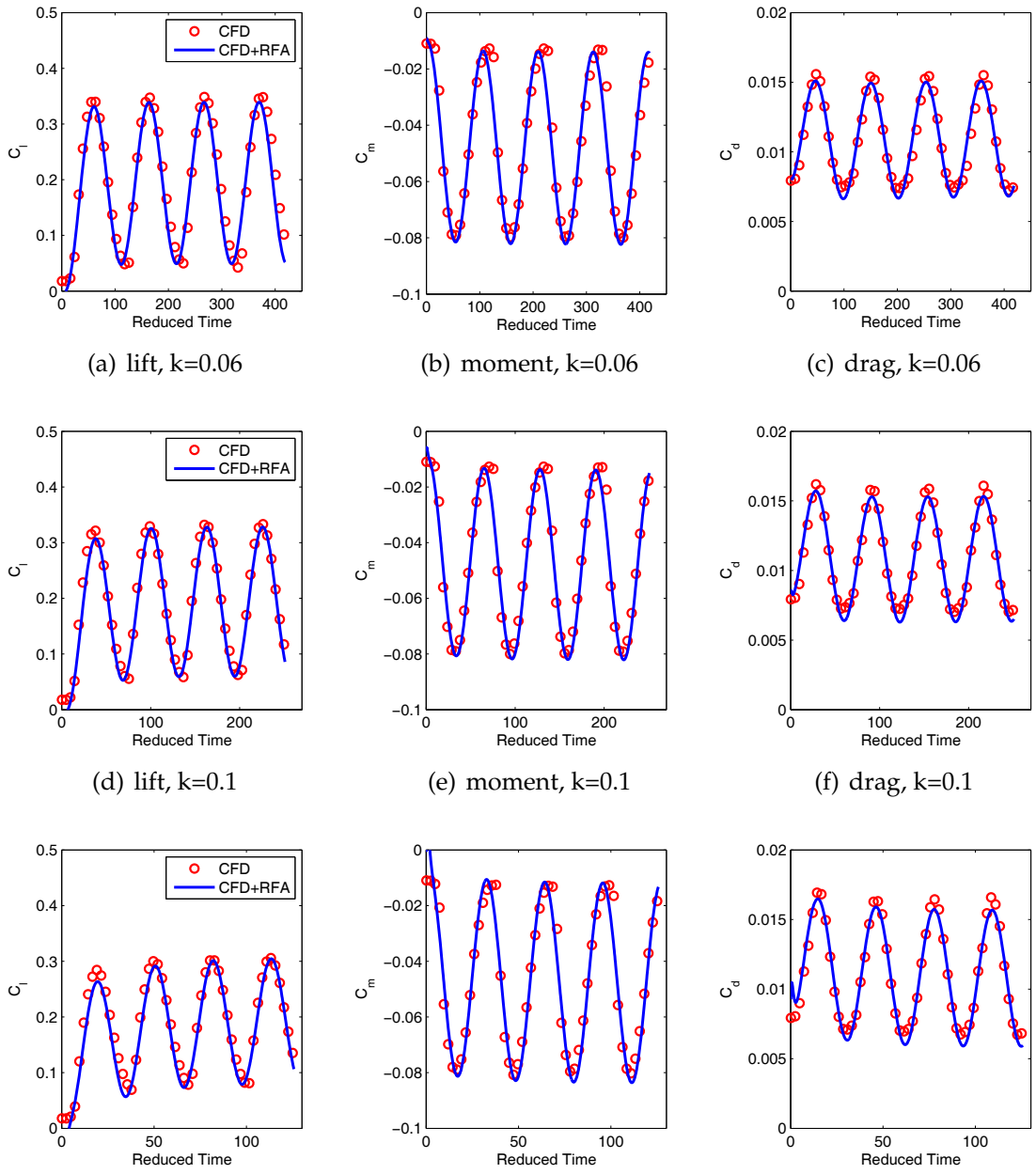

(a) lift, k=0.06 (b) moment, k=0.06 (c) drag, k=0.06

(d) lift, k=0.1 (e) moment, k=0.1 (f) drag, k=0.1

(g) lift, k=0.2 (h) moment, k=0.2 (i) drag, k=0.2

Figure 3.9: Unsteady load coefficients for an oscillating 1.5%c sharp TE microflap with varying frequencies; $\alpha = 0^\circ$ and $M = 0.6$.

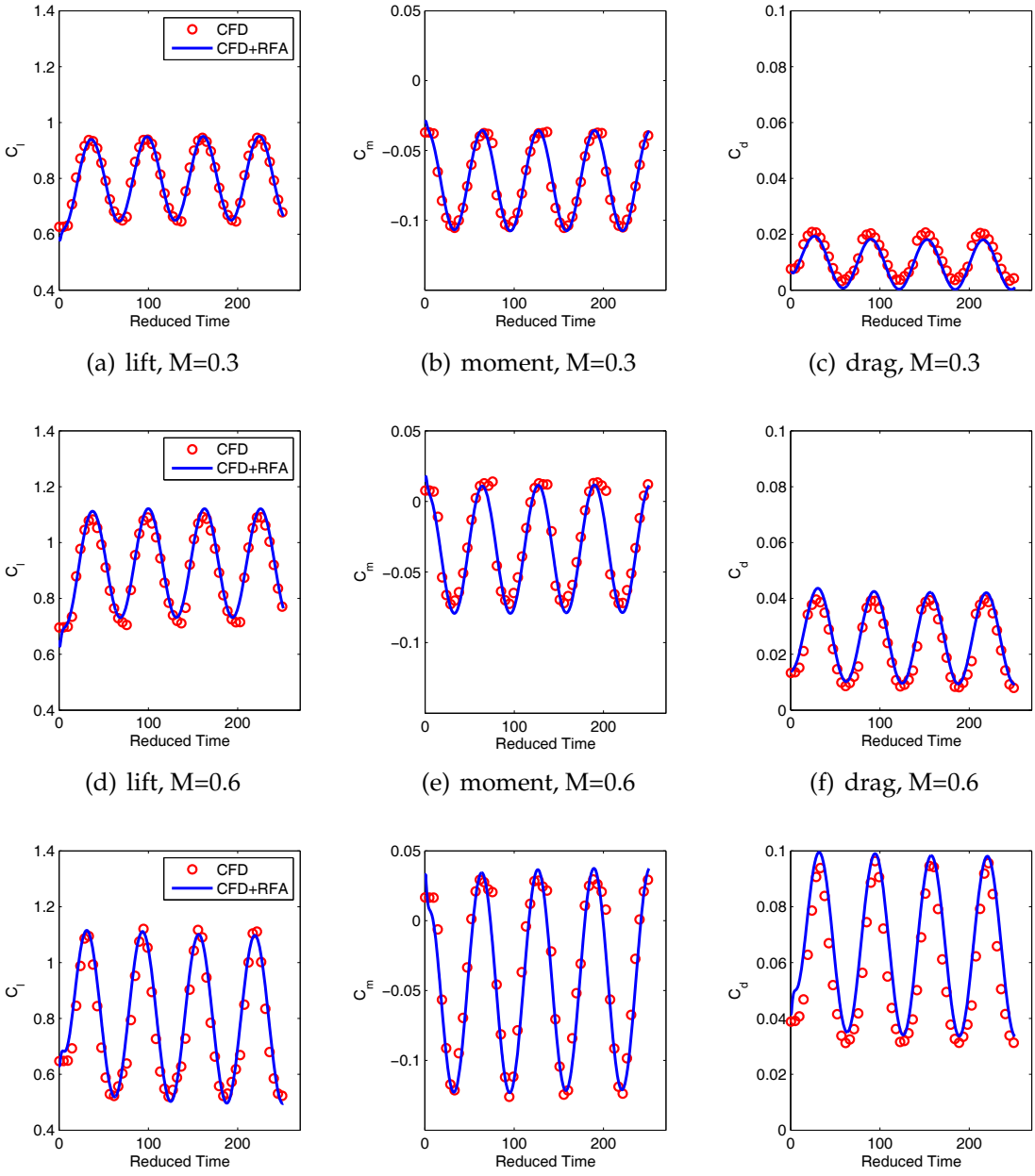

(a) lift, M=0.3 (b) moment, M=0.3 (c) drag, M=0.3

(d) lift, M=0.6 (e) moment, M=0.6 (f) drag, M=0.6

(g) lift, M=0.7 (h) moment, M=0.7 (i) drag, M=0.7

Figure 3.10: Unsteady load coefficients for an oscillating 1.5%c sharp TE microflap with varying Mach numbers; $\alpha = 5°$ and $k = 0.1$.

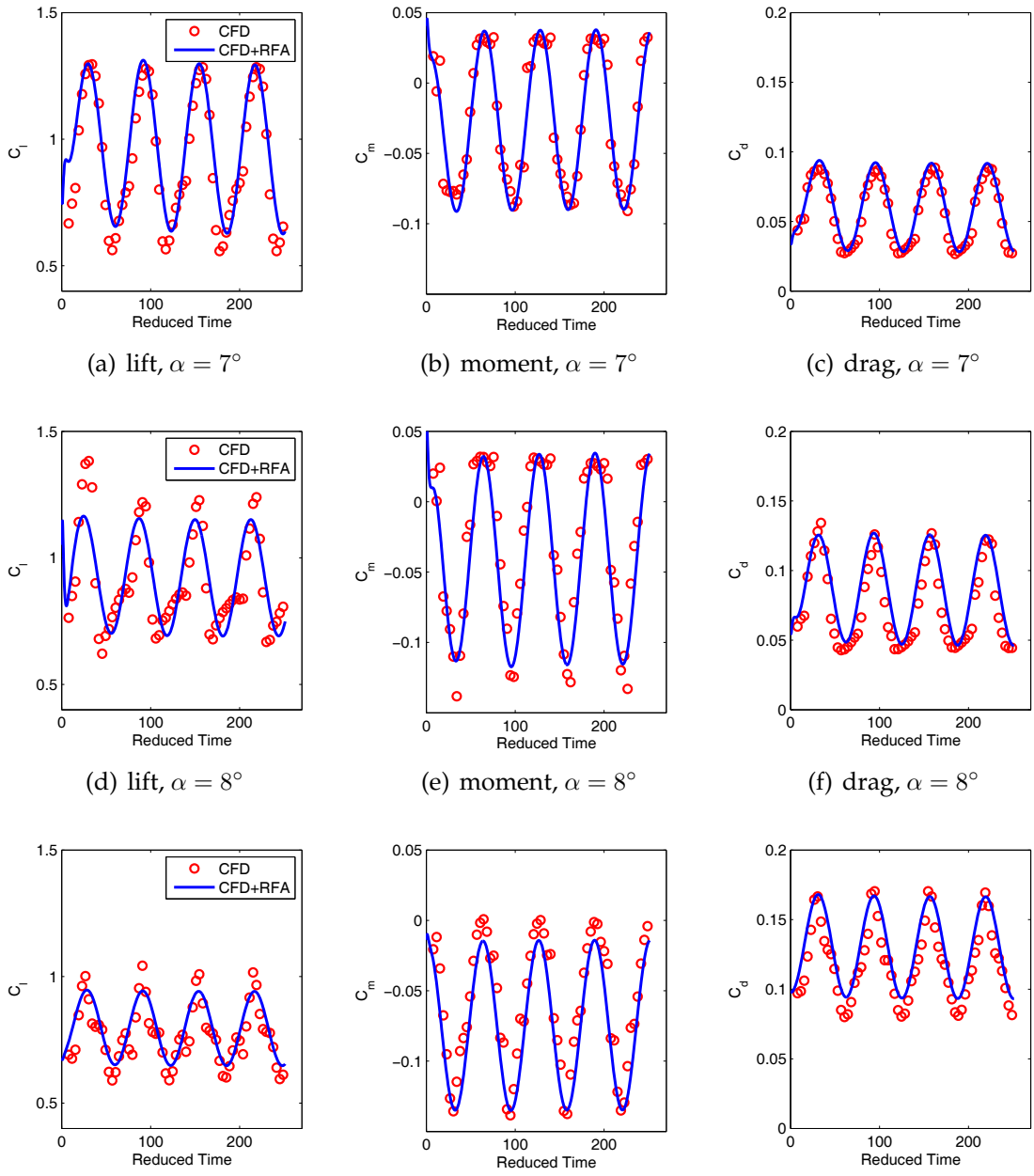

(a) lift, $\alpha = 7°$ (b) moment, $\alpha = 7°$ (c) drag, $\alpha = 7°$

(d) lift, $\alpha = 8°$ (e) moment, $\alpha = 8°$ (f) drag, $\alpha = 8°$

(g) lift, $\alpha = 10°$ (h) moment, $\alpha = 10°$ (i) drag, $\alpha = 10°$

Figure 3.11: Unsteady load coefficients for an oscillating 1.5%c sharp TE microflap with varying α; $M = 0.6$ and $k = 0.1$.

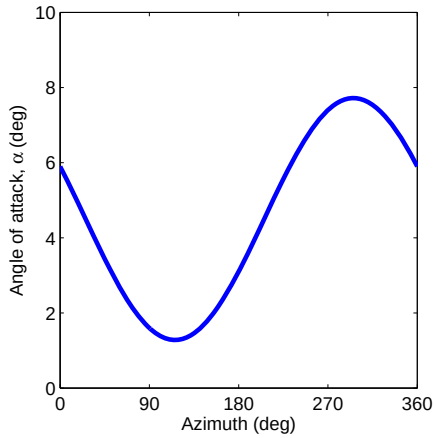

(a) angle of attack

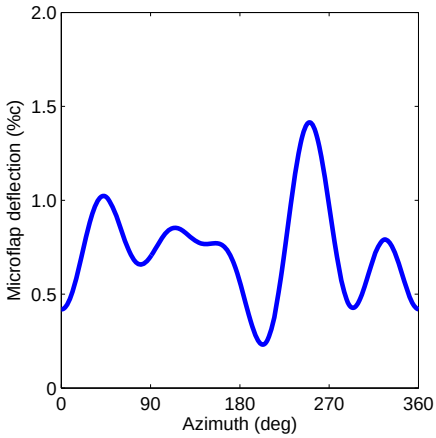

(b) microflap deflection

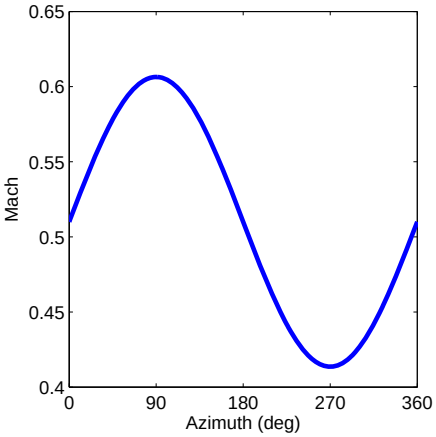

(c) Mach number

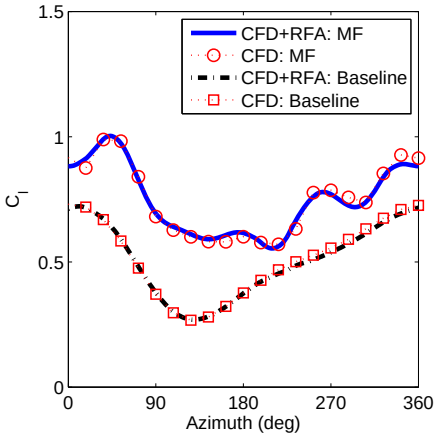

(d) lift

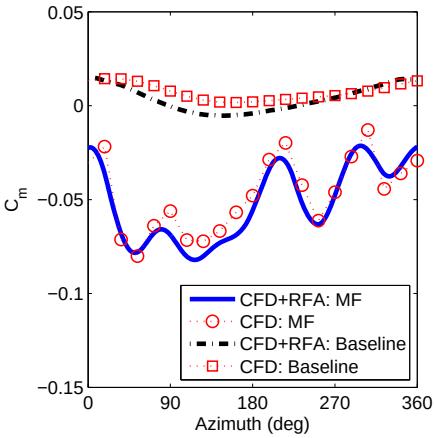

(e) moment

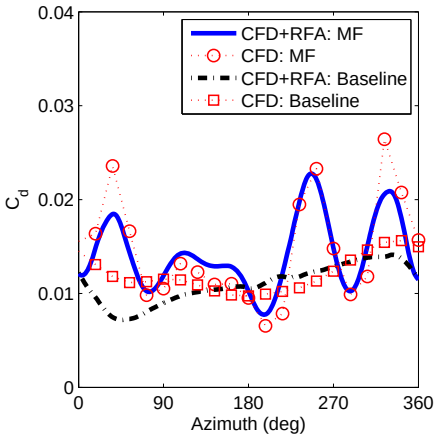

(f) drag

Figure 3.12: Comparison of ROM predictions to direct CFD results for a 1.5%c sharp TE microflap deflecting with randomly generated multi-harmonic motion, at varying angles of attack subject to freestream velocity variations.

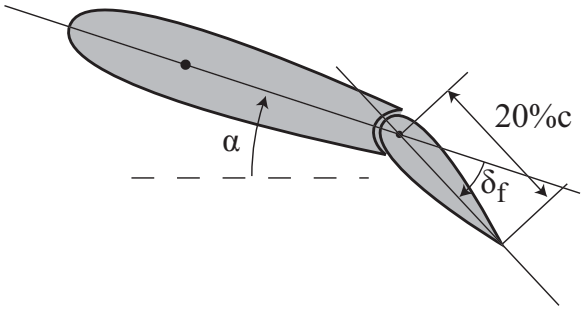

Figure 3.13: A 20%c conventional plain flap configuration.

effective on the outboard portion of the blade (0.75-0.95R), the free stream Mach number for the bulk of the study was chosen as 0.6. The unsteady effects of the flaps are examined for airfoil angles of attack of $\alpha = 0^\circ - 10^\circ$. The flap deflection amplitude δ_f is $1^\circ - 2^\circ$. Two reduced frequencies of flap oscillation, corresponding to typical 2/rev and 6/rev harmonics, were selected since they represent the lower and upper bounds of the actuation frequencies employed in active flap control studies for a four or five-bladed rotor.

The unsteady aerodynamic loads due to sinusoidal pitch oscillation of an airfoil (without flap) about the quarter-chord point are compared first. The unsteady airfoil motion is given by

$$\alpha = \alpha_0 + \bar{\alpha}\sin(k\bar{t}) \tag{3.31}$$

Results are shown for $\bar{\alpha} = 1^\circ$ and the reduced frequency $k = 0.062$. The mean angle of attack of the airfoil is $\alpha_0 = 5^\circ$, and the free stream Mach number M = 0.6. Figure 3.14(a) shows the oscillatory lift coefficient obtained from the three approaches. The DL+RFA model overpredicts the unsteady amplitude of lift C_l, with 8.5% error

between the DL+RFA model and the direct CFD simulations. By comparison, the C_l predictions obtained from the CFD+RFA model are significantly improved with only 1% error in the amplitude. The moment coefficients obtained from the three approaches are shown in Fig. 3.14(b), where predictions from the linear potential flow theory based DL+RFA model have a large error in the mean value of unsteady moment, due to viscous effects. The new CFD based ROM provides a much better moment prediction, with 12% error in the mean value. As noted earlier, the ability to provide drag predictions distinguishes the CFD based ROM from the DL+RFA model. The drag comparisons from the CFD based RFA model and the direct CFD results are shown in Fig. 3.14(c). As is evident from Fig. 3.14(c), the agreement between the CFD+RFA model and CFD results is excellent with an error of only 1.25% in the amplitude. This clearly demonstrates the accuracy of the CFD based RFA model, for the case of an oscillating airfoil.

Next, the oscillatory aerodynamic loads generated by the three aerodynamic models are shown for a sinusoidal flap deflection given by

$$\delta_f = \bar{\delta}_f \sin(k\bar{t}) \tag{3.32}$$

The results shown are obtained for the flap amplitude $\bar{\delta}_f = 1^\circ$ and two reduced frequency values of $k = 0.062$ and 0.187. The reduced frequency of $k = 0.062$ corresponds to 2/rev on a full-scale helicopter rotor, while $k = 0.187$ corresponds to 6/rev. These flap frequency harmonics represent the lower and upper frequency bounds typically employed in active control of vibrations and noise. The static

angle of attack of the airfoil is $\alpha = 5^{\circ}$, and the free stream Mach number is 0.6.

For the flap frequency of $k = 0.062$, the oscillatory lift predictions using the two ROMs are shown in Fig. 3.15(a), along with direct CFD computations denoted by circles. While there are significant errors between the amplitude predictions of the C_l values obtained from DL+RFA compared to direct CFD simulations, the predictions obtained from the CFD+RFA model are very good when compared to the CFD simulations, with less than 2% error in oscillating amplitude. From Fig. 3.15(b), it is evident that the moment coefficients obtained from the CFD+RFA model and the CFD simulations agree closely, with less than 1% error in the amplitude. By comparison, predictions of the moment from the DL+RFA model show a large discrepancy in the mean values when compared to those from direct CFD computations, due to viscous effects. Furthermore, there is also substantial error in the oscillatory moment amplitude. The hinge moment coefficient is shown in Fig. 3.15(c), where a nearly 400% error in the mean value and 200% error in the unsteady amplitude are observed comparing the DL+RFA model predictions to the CFD simulations. By comparison, the hinge moment from the CFD+RFA model is in excellent agreement with the CFD simulations, with less than 1% error in the amplitude. Clearly, the difficulties encountered for providing accurate moment predictions when using the DL+RFA model (Ref. 80) have been overcome with the new CFD based RFA approach. Furthermore, an important feature of the CFD+RFA model is demonstrated, as evidenced by its capability to provide unsteady drag predictions which are not available from potential flow based mod-

els. From Fig. 3.15(d), it is clear that the CFD+RFA model provides a reasonable unsteady drag estimation, with less than 10% error in the amplitude compared to direct CFD simulations.

Similar plots of unsteady aerodynamic responses due to flap motion are shown in Fig. 3.16(a)–3.16(b), for the higher flap reduced frequency of $k = 0.187$. The agreement between the different approaches is similar to those indicated earlier at lower reduced frequencies, which confirms the validity of the CFD based ROM across the practical range of unsteady flap motion.

In order to examine the accuracy of the ROMs in presence of strong nonlinear flow effects, both potential flow and CFD based ROMs are compared to direct CFD simulations at a higher angle of attack $\alpha = 10^\circ$ when $M = 0.6$. At this condition the airfoil encounters substantial flow separation. The oscillatory aerodynamic loads generated by the three methods are again compared for a sinusoidal flap motion, with the reduced frequency $k = 0.064$ and $\bar{\delta}_f = 1^\circ$. Oscillatory lift coefficients are shown in Fig. 3.17(a). Clearly the DL+RFA model cannot account for the stalled flow, producing a much higher C_l value compared to the CFD simulations. By comparison, the CFD+RFA model provides a reasonable prediction as is evident from Fig. 3.17(a). A similar conclusion can be drawn from the inspection of the unsteady moment and hinge moment predictions, shown in Figs. 3.17(b) and 3.17(c), respectively. The drag coefficient obtained from the CFD+RFA model and the CFD simulations is shown in Fig. 3.17(d). It is evident that the ROM still provides a reasonable approximation despite the fact that it fails to capture the high frequency

fluctuations in CFD. These results clearly demonstrate the advantages of the new CFD based reduced order model.

The aerodynamic models were also compared at transonic free stream Mach number $M = 0.85$ and static angle of attack $\alpha = 3°$. For this condition the flow is nonlinear due to the formation of strong shocks on the upper surface of the airfoil. The oscillatory aerodynamic loads for a sinusoidal flap deflection of $\bar{\delta}_f = 1°$ and $k = 0.1$ are presented. As shown in Fig. 3.18(a), the differences between unsteady lift coefficients C_l obtained from DL+RFA and CFD are in excess of 400%, indicating the shortcomings of the DL+RFA model at this flow condition. By comparison, there is less than 2% error in the amplitude of C_l obtained from the CFD+RFA model, even though high frequency oscillations, which may be attributed to shock wave motion, are not captured. The substantial improvement in accuracy in predicting unsteady airloads suggests that the new ROM may be applied to evaluate the performance of active flap systems at transonic flow regimes. The unsteady moments are shown in Fig. 3.18(b), where predictions from the CFD+RFA model have approximately 5% error in the mean value as well as noticeable error in phase. However, the ROM is still sufficient for flap performance studies since this new ROM provides vastly improved predictions when compared to the DL+RFA model. The hinge moment coefficient is also shown in Fig. 3.18(c). Similar to moment predictions, the CFD+RFA model demonstrates substantial improvement when compared to CFD simulations, with less than 3% error in the amplitude. Finally, comparisons of drag coefficients obtained from the CFD+RFA model and

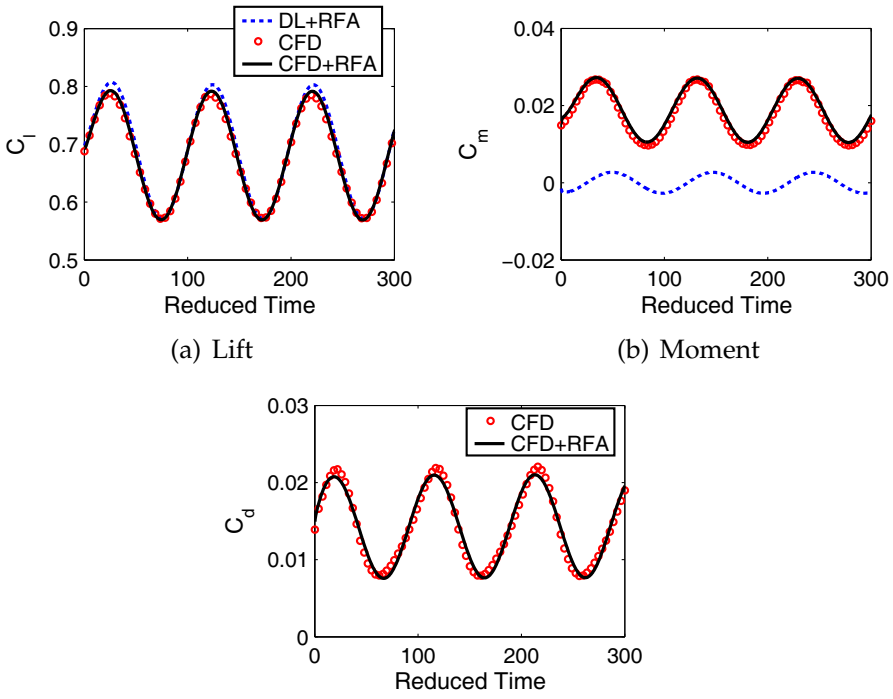

(a) Lift

(b) Moment

(c) Drag

Figure 3.14: Unsteady sectional loads for sinusoidal pitch oscillation of the airfoil; $k = 0.062$, $\alpha_0 = 5°$, $\bar{\alpha} = 1°$, $M = 0.6$.

the CFD simulations are shown in Fig. 3.18(d). There is approximately 3% error in the mean value of the unsteady drag, while the oscillating amplitudes are similar. From the comparisons shown in Fig. 3.18, it is clear that the CFD based ROM provides a good estimate even for the transonic Mach number range.

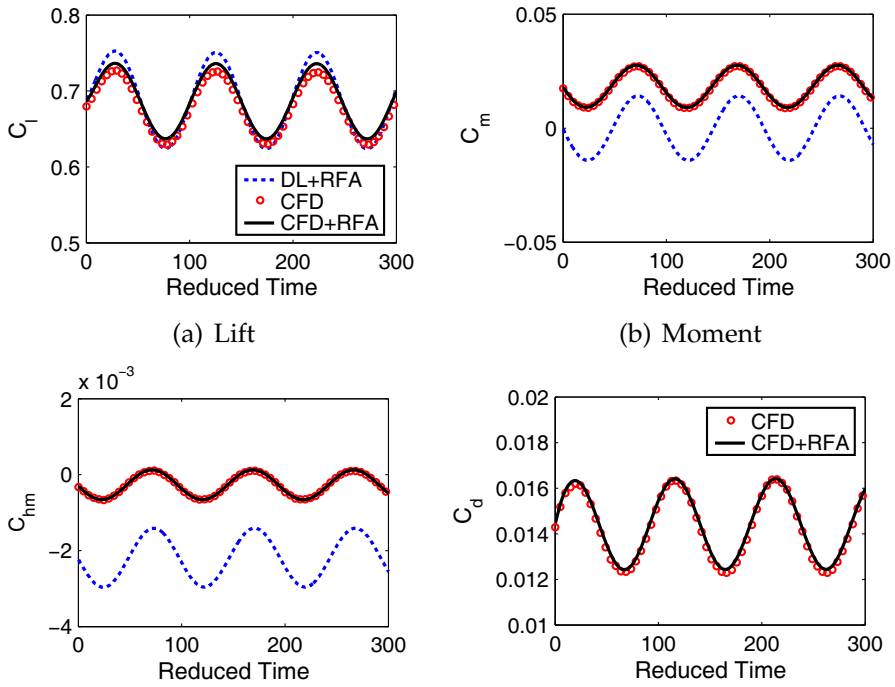

(a) Lift (b) Moment

(c) Hinge moment (d) Drag

Figure 3.15: Unsteady sectional loads for sinusoidal flap oscillation; $k = 0.062$, $\alpha = 5^\circ$ and $M = 0.6$.

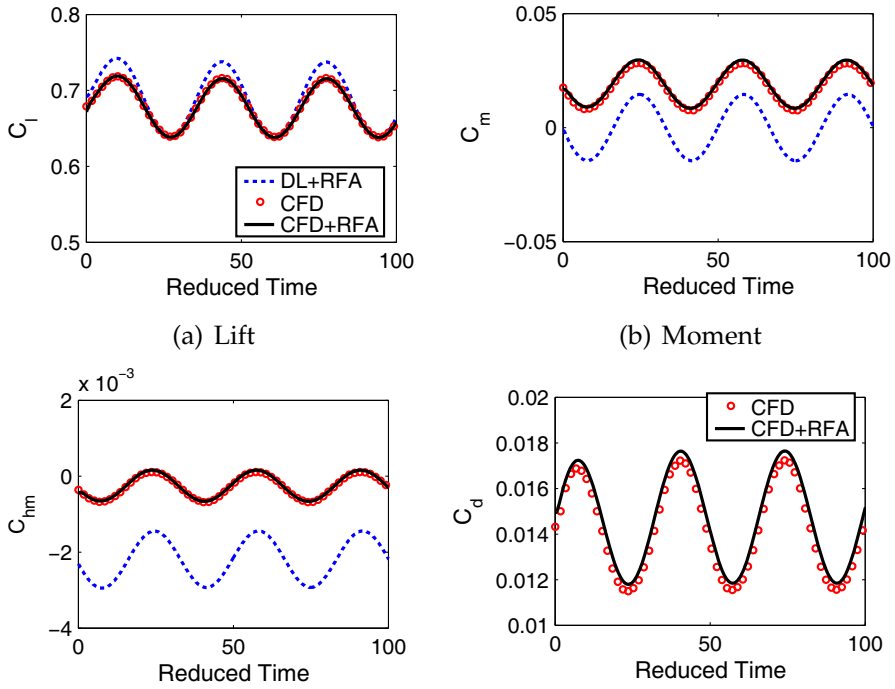

(a) Lift (b) Moment

(c) Hinge moment (d) Drag

Figure 3.16: Unsteady sectional loads for sinusoidal flap oscillation; $k = 0.187$, $\alpha = 5^\circ$ and $M = 0.6$.

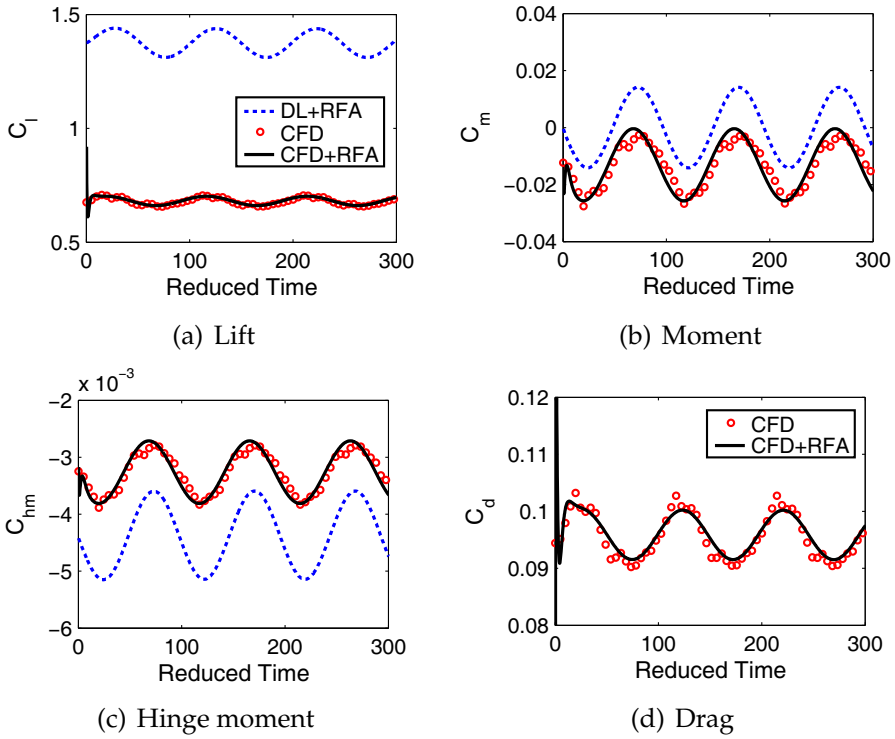

(a) Lift (b) Moment

(c) Hinge moment (d) Drag

Figure 3.17: Unsteady sectional loads for sinusoidal flap oscillation; $k = 0.062$, $\alpha = 10^\circ$ and $M = 0.6$.

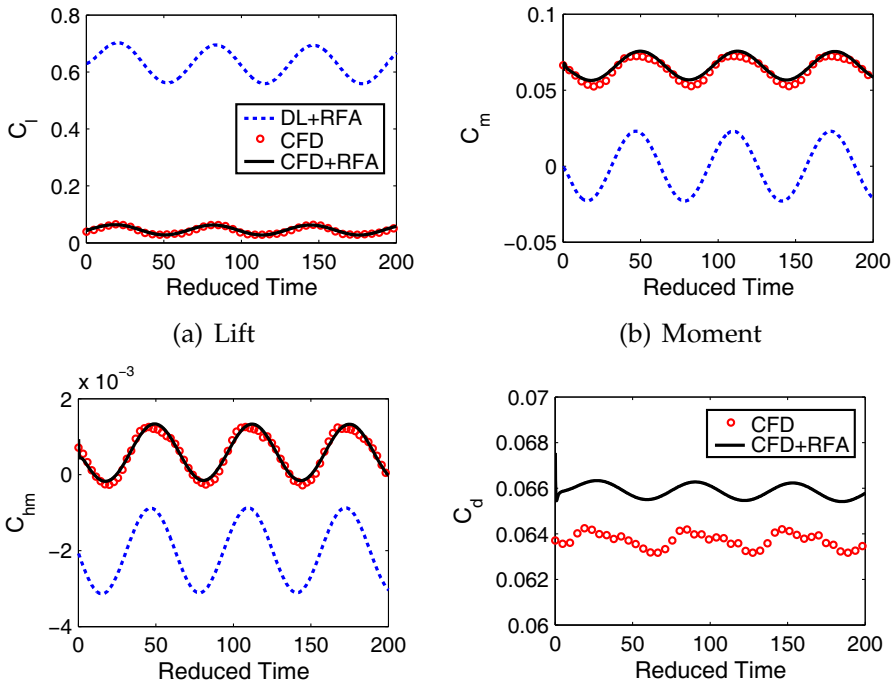

(a) Lift (b) Moment

(c) Hinge moment (d) Drag

Figure 3.18: Unsteady sectional loads for sinusoidal flap oscillation; $k = 0.1$, $\alpha = 3^\circ$ and $M = 0.85$.

CHAPTER IV

DESCRIPTION OF THE ROTORCRAFT AEROELASTIC ANALYSIS CODE

The comprehensive rotorcraft simulation code AVINOR (Active VIbration and NOise Reduction), which has been extensively validated in earlier studies [32, 52, 102], is used for all the active vibration and noise reduction studies presented in this thesis. A brief description of the principal components of the code is provided in this chapter.

4.1 Structural dynamics model

The structural dynamic model used for the present study consists of a four-bladed hingeless rotor undergoing moderate deflections with fully coupled flap-lag-torsional dynamics. The structural equations of motion are discretized using the global Galerkin method, based upon the free vibration modes of the rotating blade. The dynamics of the blade are represented by three flap, two lead-lag, and

two torsional modes. The structural dynamics model used in this study is similar to that developed in Refs. 87, 112 and is described in Appendix A along with the modeling assumptions, coordinate systems, and coordinate transformation relations used in the aeroelastic analysis model. The effect of microflaps on the rotor blade structural dynamics is assumed to be negligible, therefore no modifications have been made to the existing structural dynamics model. Control surfaces such as the trailing-edge plain flap or the microflap influence the behavior of the blade only through their effect on the aerodynamic and inertial loads.

4.2 Aerodynamic model

Aerodynamic loads for the attached flow regions on the rotor blade are calculated using the CFD based RFA model described in Chapter III. The CFD based RFA model provides the aerodynamic loads at various span-wise locations along the blade. The resulting spanwise lift distribution is used in the circulation distribution calculation for the free-wake analysis, while the free-wake influences aerodynamic loads by changing the local velocities.

The CFD based RFA aerodynamic model is based on the generalized loads

$$\mathbf{f} = \left\{ \begin{array}{c} \mathrm{C}_l \\ \mathrm{C}_m \\ \mathrm{C}_d \\ \mathrm{C}_{hm} \end{array} \right\}, \tag{4.1}$$

and the generalized motions

$$\mathbf{h} = \left\{ \begin{array}{c} W_0 \\ W_1 \\ D_0 \\ D_1 \end{array} \right\}. \tag{4.2}$$

As mentioned in Chap. III, the hinge moment C_{hm} and the response to generalized motion D_1 are not considered in the case of a microflap. Due to the presence of the partial span control surface, two forms of this aerodynamic model are necessary. The first form is described by the generalized load vector and generalized motion vector given in Eqs. 4.1 and 4.2, and is designed for blade stations with a control surface. For span-wise stations where no control surface is present, a simplified "airfoil-only" aerodynamic model is used, where the generalized load vector $\mathbf{f}$ and the generalized motion vector $\mathbf{h}$ are given by

$$\mathbf{f} = \left\{ \begin{array}{c} \mathrm{C}_l \\ \mathrm{C}_m \\ \mathrm{C}_d \end{array} \right\}, \quad \mathbf{h} = \left\{ \begin{array}{c} W_0 \\ W_1 \end{array} \right\}, \tag{4.3}$$

reducing the dimensions of the aerodynamic transfer matrix $\mathbf{Q}$ from 4×4 to 3×2.

The sectional lift, moment, and drag are given by:

$$L = \rho U^2 b(\mathrm{C}_l), \tag{4.4}$$

$$M = 2\rho U^2 b^2(\mathrm{C}_m), \tag{4.5}$$

$$D = \rho U^2 b(\mathrm{C}_d). \tag{4.6}$$

4.2.1 Derivation of U_T and U_P

To incorporate the aerodynamic model in the present analysis, expressions for W_0, W_1, U and α in terms of the blade degrees of freedom and modal parameters are needed:

$$\alpha = \theta_G + \phi \tag{4.7}$$

$$U = U_T \tag{4.8}$$

$$\dot{h} = -U_P \tag{4.9}$$

$$W_0 = U\alpha + \dot{h} \tag{4.10}$$

$$W_1 = b\dot{\alpha} \tag{4.11}$$

where U_T and U_P correspond to the components of the total air velocity $\mathbf{V_A}$ taken in the $-\hat{e}_{y5}$ and $-\hat{e}_{z5}$ directions, respectively, as illustrated in Figure 4.1. The total air velocity $\mathbf{V_A}$ is calculated as the sum of airflow velocity due to forward flight, blade rotation and induced inflow $\mathbf{V_{A1}}$ and airflow velocity due to blade dynamics $\mathbf{V_{A2}}$:

$$\mathbf{V_A} = \mathbf{V_{A1}} - \mathbf{V_{A2}}, \tag{4.12}$$

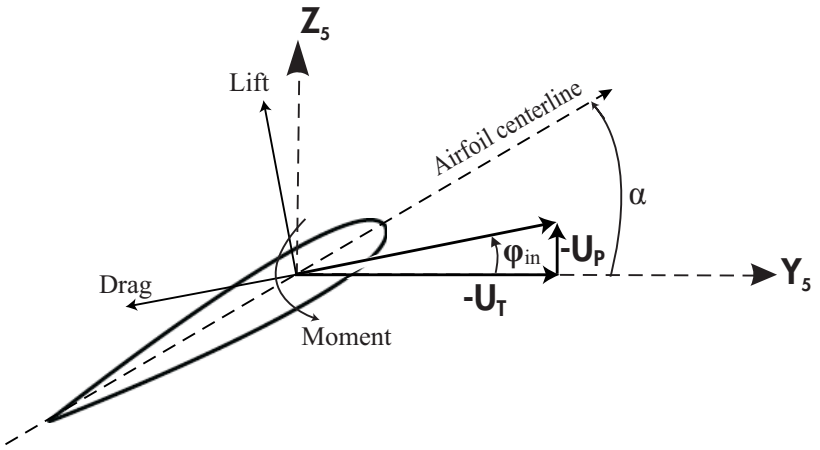

Figure 4.1: Orientation of tangential and perpendicular air velocities and aerodynamic loads.

where,

$$\mathbf{V_{A1}} = \Omega R[(\mu + \lambda_x)\hat{e}_{x1} + \lambda_y \hat{e}_{y1} + \lambda_z \hat{e}_{z1}] \tag{4.13}$$

and

$$\mathbf{V_{A2}} = \dot{\mathbf{r}}_{\mathbf{EA}} + \Omega \hat{e}_{z2} \times \mathbf{r_{EA}}. \tag{4.14}$$

The advance ratio μ and inflow ratio λ are given by

$$\mu = \frac{V_F \cos \alpha_R}{\Omega R}, \tag{4.15}$$

$$\lambda = \frac{V_F \sin \alpha_R + \nu}{\Omega R}, \tag{4.16}$$

where V_F is the freestream velocity, α_R is the rotor shaft angle, and ν is the induced flow velocity. The position vector for a point on the elastic axis $\mathbf{r_{EA}}$ is given by:

$$\mathbf{r_{EA}} = e\hat{e}_{x2} + (x + u)\hat{e}_{x3} + v\hat{e}_{y3} + w\hat{e}_{z3}. \tag{4.17}$$

The resultant velocity $\mathbf{V_A}$ is expressed in the $(\hat{e}_{x5}, \hat{e}_{y5}, \hat{e}_{z5})$ coordinate system using appropriate coordinate transformations, described in the previous section. As mentioned earlier, U_T and U_P correspond to the components of the total air velocity $\mathbf{V_A}$ in the $-\hat{e}_{y5}$ and $-\hat{e}_{z5}$ directions, respectively, which are given by the expressions [Ref. 91, Eqs. (5.176)-(5.177)]:

$$\begin{aligned} U_T &= \Omega(x+e+u) + \Omega v v_{,x} - \Omega w \beta_p + \dot{v} \\ &\quad + (\mu+\lambda_x)\Omega R v_{,x} \cos\phi + \lambda_y \Omega R v_{,x} \sin\phi \\ &\quad + (\mu+\lambda_x)\Omega R \sin\phi - \lambda_y \Omega R \cos\phi, \end{aligned} \tag{4.18}$$

$$\begin{aligned} U_P &= \dot{w} + \Omega v(w_{,x} + \beta_p) - \lambda_z \Omega R + (\mu+\lambda_x)\Omega R(w_{,x} + \beta_p)\cos\phi \\ &\quad - \lambda_y \Omega R(w_{,x} + \beta_p)\cos\phi. \end{aligned} \tag{4.19}$$

These expressions for U_T and U_P are then substituted into Eqs. (4.7-4.11) to produce explicit expressions for U, $\dot{h}$, and the generalized airfoil and flap motions.

4.2.2 Distributed Aerodynamic Loads

Expressions for sectional lift and drag have been obtained in Eqs. (4.4) and (4.6), respectively. Lift is assumed to act normal to the total air velocity, and drag is assumed to act parallel to it. Furthermore, all aerodynamic forces act at the quarter chord, which is assumed to coincide with the elastic axis, thus $X_A = 0$. Following these assumptions, the spanwise distributed aerodynamic force in the "5" system

is given by:

$$\mathbf{p_A} = p_{Ay5}\hat{e}_{y5} + p_{Az5}\hat{e}_{z5}, \tag{4.20}$$

where:

$$p_{Ay5} = -D\cos\phi_{in} - L\sin\phi_{in}, \tag{4.21}$$

$$p_{Az5} = -D\sin\phi_{in} + L\cos\phi_{in}, \tag{4.22}$$

The inflow angle ϕ_{in} is the angle between U_T and the resultant air velocity, given by:

$$\cos\phi_{in} = \frac{U_T}{\sqrt{U_T^2 + U_P^2}}. \tag{4.23}$$

The distributed aerodynamic moment in Eq. (4.5) is assumed to act about the elastic axis of the blade. It can be expressed in the "5" system as:

$$\mathbf{q_A} = q_{Ax5}\hat{e}_{x5}, \tag{4.24}$$

where:

$$q_{Ax5} = M. \tag{4.25}$$

Using appropriate transformations, the distributed aerodynamic force in the "3" system is given by:

$$\mathbf{p_A} = p_{Ax3}\hat{e}_{x3} + p_{Ay3}\hat{e}_{y3} + p_{Az3}\hat{e}_{z3}, \tag{4.26}$$

where:

$$p_{Ax3} = -v_{,x}\, p_{Ay5} - w_{,x}\, p_{Az5}, \tag{4.27}$$

$$p_{Ay3} = p_{Ay5}, \tag{4.28}$$

$$p_{Az3} = -v_{,x}\, w_{,x}\, p_{Ay5} + p_{Az5}. \tag{4.29}$$

Similarly, the distributed aerodynamic moment is expressed in the "3" system as:

$$\mathbf{q_A} = q_{Ax3}\hat{e}_{x3} + q_{Ay3}\hat{e}_{y3} + q_{Az3}\hat{e}_{z3}, \tag{4.30}$$

where:

$$q_{Ax3} = q_{Ax5}, \tag{4.31}$$

$$q_{Ay3} = v_{,x}\, q_{Ax5}, \tag{4.32}$$

$$q_{Az3} = w_{,x}\, q_{Ax5}. \tag{4.33}$$

The CFD based RFA model is linked to a free wake model, which produces a spanwise and azimuthally varying inflow distribution. An accurate free-wake analysis is crucial for capturing BVI noise and vibrations at low speed flight conditions. The free-wake model used in this study is based on the CAMRAD/JA wake analysis and was incorporated into the AVINOR code by de Terlizzi and Friedmann [31,32]. This model was later modified by Patt, Liu, and Friedmann [78,98] to provide the desired resolution for acoustic calculations.

At high speeds, dynamic stall is a dominant source of vibratory loads. In this study, dynamic stall effects are modeled using a modified version of the ONERA dynamic stall model [105]. This model was incorporated into the AVINOR code by Depailler and Friedmann [33, 34]. The aerodynamic states associated with the dynamic stall model and the CFD based RFA model are combined to produce a time-domain, state-space aerodynamic model. The free wake model and the dynamic stall model are described in Appendix B.

4.2.3 Reversed-flow model

In forward flight, there is a region on the retreating side of the rotor disk, represented in Fig. 4.2, where the airflow encountered by the blade is reversed, flowing from the trailing edge to the leading edge. The boundary of this reverse flow region is described by the locus of points on the rotor disk where the velocity of the airflow parallel to the blade is zero. The approximate boundary of this region on the blade span as a function of azimuth ψ and advance ratio μ is given by

$$x_{rev}(\psi) = -(e + \mu R \sin\psi). \tag{4.34}$$

In the present analysis, it is assumed that the aerodynamic lift and moment are zero within the reverse flow region. This is accomplished by multiplying the aerodynamic lift and moment expressions by the reverse flow parameter R_{LM}, defined

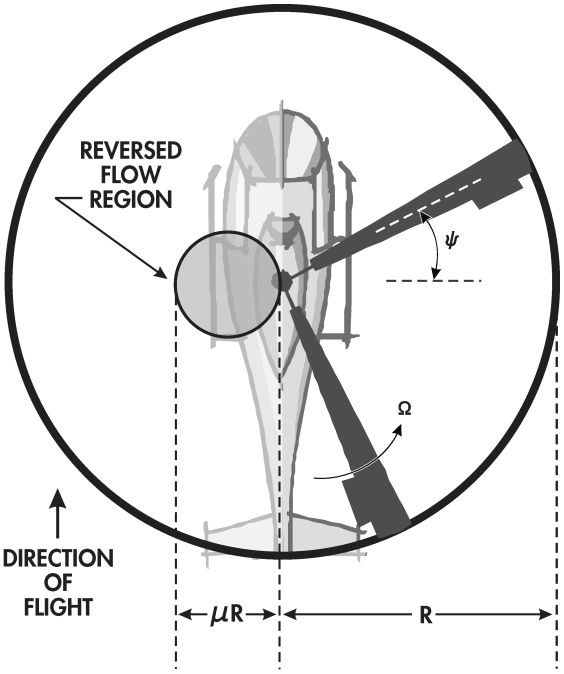

Figure 4.2: Position of the reversed flow region in forward flight

as follows:

$$R_{LM} = \begin{cases} 0 \quad \text{for} \quad 0 \leq x \leq x_{rev}(\psi) \\ 1 \quad \text{for} \quad x > x_{rev}(\psi) \end{cases}$$

4.3 Coupled aeroelastic response/trim solution

The combined structural and aerodynamic equations form a system of coupled differential equations that are written in a state-variable form. These equations are further coupled with the rotor trim equations. The trim procedure used is based on a propulsive trim with three force equations (longitudinal, lateral, and vertical) and three moment equations (roll, pitch, and yaw) corresponding to a helicopter in free flight. A simplified tail rotor model, based on uniform inflow and blade element theory, is used. A detailed description of the procedure used to solve

the combined system of equations is provided in Appendix C. Spatial discretization of the aeroelastic equations of motion is performed using Galerkin's method of weighted residuals. This procedure is similar to the one developed in Ref. 91. The coupled trim/aeroelastic equations are solved in time using the ordinary differential equation solver DDEABM, which is a predictor-corrector based Adams-Bashforth differential system solver. The acoustic calculations do not influence the aeroelastic solution, and hence are performed separately after the aerodynamic and structural time histories of the blade have been determined.

CHAPTER V

ACOUSTIC MODEL

The noise prediction code used in this study is based on a modified version of the WOPWOP code and was incorporated into the AVINOR code by Patt, Liu, and Friedmann [101, 102]. Acoustic formulation in the WOPWOP code is based on the Ffowcs Williams-Hawkings (FW-H) equation:

$$4\pi p'(\mathbf{x},t) = \frac{\partial^2}{\partial x_i \partial x_j}\iiint \left[\frac{T_{ij}}{r|1-M_r|}\right] dV$$

$$-\frac{\partial}{\partial x_i}\iint \left[\frac{P_{ij}n_j}{r|1-M_r|}\right] dS + \frac{\partial}{\partial t}\iint \left[\frac{\rho_o v_n}{r|1-M_r|}\right] dS \tag{5.1}$$

which was derived from first principles following the acoustic assumption of small disturbances in Ref. 39. Under these assumptions, it is the exact solution for the noise generated by a rotor blade or any other object in arbitrary motion. The sources of rotational noise are best described using the three terms of Eq. (5.1):

1. Quadrupole noise:

$$\frac{\partial^2}{\partial x_i \partial x_j}\iiint \left[\frac{T_{ij}}{r|1-M_r|}\right] dV,$$

this noise is due to fluid stress and becomes important only at high Mach numbers

2. Dipole (loading) noise:

$$\frac{\partial}{\partial x_i} \iint \left[\frac{P_{ij} n_j}{r|1 - M_r|} \right] dS,$$

this noise is due to the surface pressures on the blade pushing back against the fluid.

3. Monopole (thickness) noise:

$$\frac{\partial}{\partial t} \iint \left[\frac{\rho_o v_n}{r|1 - M_r|} \right] dS,$$

this source of noise is caused by the displacement of the fluid by the volume of the rotating blade.

The rotational noise (thickness and loading noise) and BVI noise can be predicted with sufficient accuracy using the FW-H equation, neglecting the quadrupole source term [101].

5.1 Solution to the FW-H Equation

There exist a number of solutions to the FW-H equation, as documented in Ref. 37. One of Farassat's solutions known as Formulation 1A [38] has been imple-

mented in several helicopter noise prediction codes due to its numerical efficiency.

Using Green's function of the wave equation in the unbounded domain $\delta(g)/4\pi r$, where

$$g = \tau - t + r/c \tag{5.2}$$

a retarded time solution to FW-H equation is obtained

$$4\pi p'(\mathbf{x},t) = \frac{1}{c}\frac{\partial}{\partial t}\int_{f=0}\left[\frac{\rho_0 c v_n + l_r}{r(1-M_r)}\right]_{\text{ret}} dS + \int_{f=0}\left[\frac{l_r}{r^2(1-M_r)}\right]_{\text{ret}} dS \tag{5.3}$$

To improve the speed and accuracy of the solution, mathematical manipulations are carried out to move the time derivative inside the first integral of Eq. (5.3) by using the following relation

$$\left.\frac{\partial}{\partial t}\right|_{\mathbf{x}} = \left[\frac{1}{1-M_r}\left.\frac{\partial}{\partial \tau}\right|_{\mathbf{x}}\right]_{\text{ret}} \tag{5.4}$$

this yields Formulation 1A

$$\begin{aligned} 4\pi p'_L(\mathbf{x},t) &= \frac{1}{c}\int_{f=0}\left[\frac{\dot{l}_i \hat{r}_i}{r(1-M_r)^2}\right]_{\text{ret}} dS + \int_{f=0}\left[\frac{l_r - l_i M_i}{r^2(1-M_r)^2}\right]_{\text{ret}} dS \\ &\quad + \frac{1}{c}\int_{f=0}\left[\frac{l_r(r\dot{M}_i\hat{r}_i + cM_r - cM^2)}{r^2(1-M_r)^3}\right]_{\text{ret}} dS \end{aligned} \tag{5.5a}$$

$$4\pi p'_L(\mathbf{x},t) = \int_{f=0}\left[\frac{\rho_0 v_n(r\dot{M}_i\hat{r}_i + cM_r - cM^2)}{r^2(1-M_r)^3}\right]_{\text{ret}} dS \tag{5.5b}$$

$$p'(\mathbf{x},t) = p'_L(\mathbf{x},t) + p'_T(\mathbf{x},t) \tag{5.5c}$$

where p'_L, p'_T, p' denotes the loading noise, thickness noise and overall noise, re-

spectively.

5.2 BVI Noise Prediction

As described in Chapter I, BVI noise dominates the low speed descent flight regime, and is characterized by its impulsiveness and high intensity. The frequency contents of BVI noise mostly fall in the mid-frequency range, which is most sensitive to human hearing. A widely accepted definition of BVI noise frequency range is the sum of $6^{\text{th}} - 40^{\text{th}}$ harmonics of blade passage frequency [122].

5.2.1 Calculation of Chord-wise Pressure Distribution

The BVI noise is generated by unsteady pressure fluctuations on the blade induced by interaction with trailed vortices. More specifically, it originates primarily from the dipole or loading source term p'_L in Eq. (5.5). In previous studies conducted in Refs. 101 and 102, the chordwise pressure distribution on the surface of the blade, required as input to the acoustic computations, was calculated using an extended RFA approach that produces the unsteady compressible chordwise and spanwise pressure distribution over the entire rotor disk. This extended RFA approach to obtain pressure distribution was based on pressure fitting data in the frequency domain generated from a DL based potential flow solver, described in detail in Ref. 101. This approach is not feasible for the present study, because generation of RFA models using CFD based pressure distribution data is computationally too expensive. Therefore, the blade pressure distributions are estimated using

the velocity superposition method [1,2], where the pressures are obtained from the sectional lift coefficients. Specifically, based on potential flow theory the pressure distribution on the surface of the airfoil is related to the local velocity distribution, which can be considered to be composed of three independent components

$$c_p = \left(\frac{v}{V} \pm \frac{\Delta v}{V} \pm \frac{\Delta v_a}{V} \right)^2 \tag{5.6}$$

where the velocity ratios $\frac{v}{V}$, $\frac{\Delta v}{V}$, and $\frac{\Delta v_a}{V}$ represent the contributions due to airfoil thickness, camber, and angle of attack, respectively. The signs in Eq. 5.6 are positive for the upper surface and negative for the lower surface. For the symmetric NACA0012 airfoil used in the present study, $\frac{\Delta v}{V} = 0$, and the values of the other two components can be found using the approach outlined in Ref. 2. Clearly this approach can introduce errors because it is based on potential flow theory. However, reasonable approximations are obtained since the integrated lift coefficients, used to generate the pressure, are obtained with the CFD based model that accounts for compressibility and unsteady effects.

5.3 Modified WOPWOP Code

The present study is based on a modified version of the helicopter aeroacoustic code WOPWOP [15] developed at NASA Langley. The WOPWOP code implements Farassat's Formulation 1A(Eq. (5.5)), and has been extensively validated [16,17] for helicopter noise predictions.

The original version of the WOPWOP code requires blade harmonics and surface loading information as input. A simple blade model based on the assumption of an offset hinged rigid blade was used in the original WOPWOP code. However, this simplified assumption is incompatible with realistic elastic blade model used in this study. In order to take into account the effects of blade flexibility, the blade dynamics in WOPWOP were replaced by the fully flexible blade model with partial span trailing-edge flaps and microflaps [78, 98, 102]. This was accomplished by discretizing the blade into a number of individual panels as shown in Fig. 5.1. The acoustic code then calculates the contribution from each panel, each having its own velocity, normal vector and pressure distribution. The time domain response of each of these panels was obtained from the aeroelastic response analysis. This information, together with the unsteady pressure distribution on the panel, serves as the basis of the acoustic computations. Unlike some computational studies performed with WOPWOP [14], a surface pressure distribution is used in the acoustic calculation, such that no reduction to a chordwise compact loading is made. Tail rotor and engine noise were not considered in this study. Further, aerodynamic effects of the fuselage have been excluded, and thus the acoustic results represent the noise generated by the main rotor only.

After the acoustic-pressure time history at an observer location (such as the noise feedback locations on the helicopter or points on the carpet plane) is obtained, discrete frequency components of the sound pressure level are calculated using conventional Fourier analysis. Fourier coefficients are calculated through

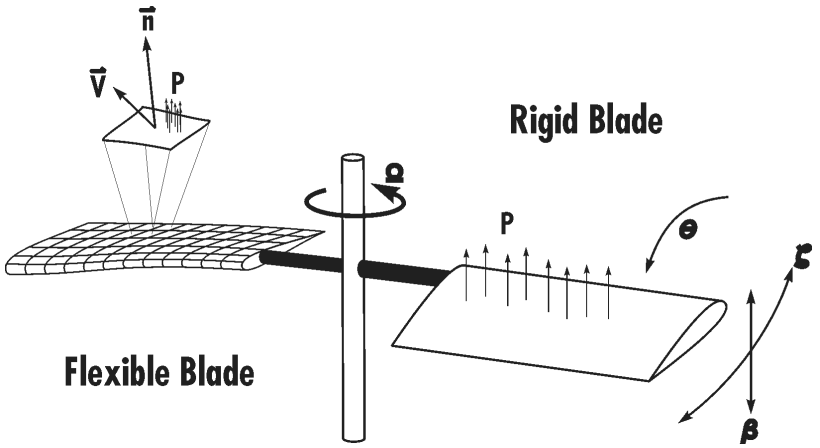

Figure 5.1: Rigid and flexible blade representations

an integration of the acoustic-pressure time history. The numerical integration is done using Simpson's rule [15]. The BVI noise level is then obtained by summing the $6^{th} - 40^{th}$ harmonic components of the blade passage frequency. The acoustic computations are time-consuming, hence, the full sound pressure levels on a carpet plane beneath the rotor are not evaluated until the trim solution or controller reaches a fully-converged solution.

CHAPTER VI

CONTROL APPROACHES

This chapter provides a description of the higher harmonic control (HHC) algorithm, used for all the closed-loop control studies performed in this thesis. A comprehensive review of the HHC algorithm and its variants was written by Johnson in Ref. 61. Since then, numerous studies have employed the HHC algorithm. The implementation of the HHC algorithm in the AVINOR code has been described in Ref. 99, which contains a detailed description of three versions of the HHC algorithm: 1) the classical, invariant version, 2) an adaptive version, wherein a recursive least-squares method is used for online identification, and 3) a relaxed variant. Robustness of all three versions including their convergence and stability characteristics was analyzed from a control theory perspective. The primary reasons for the success of this disturbance rejection algorithm are its simplicity and the a priori knowledge of the frequencies of the disturbance. For general boradband disturbance rejection, fundamental tradeoffs exist such that disturbance reduction over a frequency range entails amplification at other frequencies [55]. However, in the case where disturbances have specific frequencies (tonal disturbances) known

a priori, very high gain can be applied at these frequencies of disturbance, and excellent reduction can be achieved without significant compromise. Thus, the HHC disturbance rejection algorithm is particularly suitable for rotorcraft since the disturbance is largely tonal, and the frequency of the disturbance is known a priori [99]. Application of the HHC algorithm for active noise control and simultaneous vibration and noise control using actively controlled flaps was demonstrated in Ref. 102. Flap effectiveness was examined with practical flap saturation limits imposed using an approach described in Ref. 28. A comparatively efficient approach to handling actuator saturation in the HHC algorithm developed as part of this study based on nonlinear constrained optimization techniques is discussed extensively in Chapter VIII.

6.1 The Classical HHC Algorithm

The HHC algorithm is based on the assumption that the helicopter can be represented by a linear model relating output $\mathbf{z}$ to control inputs $\mathbf{u}$. In previous studies dealing with the vibration reduction of a four-bladed rotor [34, 46, 102], the output $\mathbf{z}$ consisted of 4/rev hub shears and moments, while the input vector $\mathbf{u}$ contained harmonic control inputs including 2/rev, 3/rev, 4/rev, and 5/rev components.

The HHC algorithm is a frequency-domain approach applied to disturbances (vibrations or noise) having known frequency content that is predominantly N_b/rev, where N_b is the number of rotor blades. In the HHC algorithm, the measurement of the plant output and update of the control input are not performed continuously,

but rather at specific times $t_k = k\tau$, where τ is the time interval between updates during which the plant output reaches a steady state. In actual implementation of the algorithm, this time interval may be one or more revolutions. The system is allowed to reach a steady-state (converged) condition, and measures of the vibratory response amplitude and phase are used to determine the amplitude and phase of the required control input signal for vibration reduction. This approach is designed for a steady trimmed flight. Maneuvering flight introduces transients that would prevent the steady-state condition from being satisfied and thus the performance of the algorithm will be degraded. A schematic of the HHC architecture as implemented on a helicopter is shown in Fig. 6.1. Introduction of a disturbance

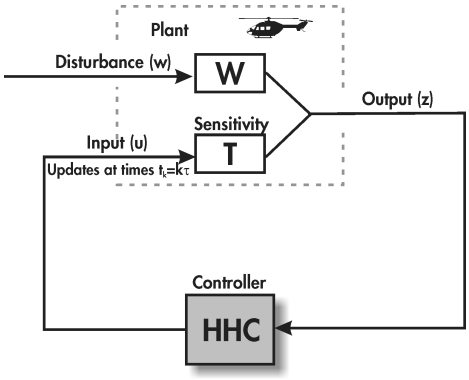

Figure 6.1: Higher harmonic control architecture

w, representative of the helicopter operating condition, and recognizing that system updates are performed at times $t_k = k\tau$, allows one to represent the system dynamics by

$$\mathbf{z}_k = \mathbf{T}\mathbf{u}_k + \mathbf{W}\mathbf{w}. \tag{6.1}$$

At the initial condition, $k = 0$,

$$\mathbf{z}_0 = \mathbf{T}\mathbf{u}_0 + \mathbf{W}\mathbf{w}. \tag{6.2}$$

Subtracting Eq. (6.2) from Eq. (6.1) to eliminate the unknown $\mathbf{w}$ yields

$$\mathbf{z}_k = \mathbf{z}_0 + \mathbf{T}(\mathbf{u}_k - \mathbf{u}_0). \tag{6.3}$$

where the sensitivity $\mathbf{T}$ is given by:

$$\mathbf{T} = \frac{\partial \mathbf{z}}{\partial \mathbf{u}}. \tag{6.4}$$

Equation (6.3) is referred to as the global model of helicopter response [61]. Note that this model depends on the assumption of linearity, and that the sensitivity $\mathbf{T}$ (and the starting condition $\mathbf{z}_0$) are invariant and known without error either through an identification procedure or direct measurement (offline identification).

The controller is based on the minimization of a general quadratic cost function

$$J(\mathbf{z}_k, \mathbf{u}_k) = \mathbf{z}_k^{\mathrm{T}}\mathbf{Q}_{\mathbf{z}}\mathbf{z}_k + 2\mathbf{z}_k^{\mathrm{T}}\mathbf{S}\mathbf{u}_k + \mathbf{u}_k^{\mathrm{T}}\mathbf{R}\mathbf{u}_k. \tag{6.5}$$

However, in most applications, the cross-weighting term in Eq. (6.5) is neglected and the cost function simplifies to

$$J(\mathbf{z}_k, \mathbf{u}_k) = \mathbf{z}_k^{\mathrm{T}}\mathbf{Q}_{\mathbf{z}}\mathbf{z}_k + \mathbf{u}_k^{\mathrm{T}}\mathbf{R}\mathbf{u}_k. \tag{6.6}$$

The optimal control input is determined from the requirement

$$\frac{\partial J(\mathbf{z}_k, \mathbf{u}_k)}{\partial \mathbf{u}_k} = 0, \tag{6.7}$$

which yields the optimal control law $\mathbf{u}_{k,\mathrm{opt}}$, given by

$$\mathbf{u}_{k,\mathrm{opt}} = -(\mathbf{T}^{\mathrm{T}}\mathbf{Q}_{\mathbf{z}}\mathbf{T} + \mathbf{R})^{-1}(\mathbf{T}^{\mathrm{T}}\mathbf{Q}_{\mathbf{z}})(\mathbf{z}_0 - \mathbf{T}\mathbf{u}_0). \tag{6.8}$$

Combining Eqs. (6.6) and (6.8), the minimum cost is found to be

$$J(\mathbf{z}_k, \mathbf{u}_{k,\mathrm{opt}}) = (\mathbf{z}_0 - \mathbf{T}\mathbf{u}_0)^{\mathrm{T}} \left[\mathbf{Q}_{\mathbf{z}} - (\mathbf{Q}_{\mathbf{z}}\mathbf{T})\mathbf{D}^{-1}(\mathbf{T}^{\mathrm{T}}\mathbf{Q}_{\mathbf{z}})\right](\mathbf{z}_0 - \mathbf{T}\mathbf{u}_0). \tag{6.9}$$

where

$$\mathbf{D} = \mathbf{T}^{\mathrm{T}}\mathbf{Q}_{\mathbf{z}}\mathbf{T} + \mathbf{R} \tag{6.10}$$

This is the most basic version of the HHC algorithm and it yields an explicit relation for optimal control input.

It is also useful to consider another, recursive, form of Eq. (6.3), where subsequent control updates are written as

$$\mathbf{z}_{k+1} = \mathbf{z}_k + \mathbf{T}(\mathbf{u}_{k+1} - \mathbf{u}_k). \tag{6.11}$$

the optimal control law is given by

$$\mathbf{u}_{k+1,\mathrm{opt}} = -\mathbf{D}^{-1}(\mathbf{T}^{\mathrm{T}}\mathbf{Q}_{\mathbf{z}})(\mathbf{z}_{k,\mathrm{opt}} - \mathbf{T}\mathbf{u}_{k,\mathrm{opt}}). \tag{6.12}$$

In this equation, the index k refers to the controller update number, an integer corresponding to each time the control algorithm updates the values of the input vector $\mathbf{u}_k$ which results in a new output vector $\mathbf{z}_k$. Note that Eq. (6.3) is a special case of Eq. (6.11), where $k = 0$. It can be shown that $\mathbf{u}_{k,\mathrm{opt}}$ is independent of k, and remains constant for all future control updates $k \geq 1$ [99]. Thus the algorithm converges to the optimum value in a single step, for a well-identified linear system. Equation (6.11) is referred to as the local controller, and it represents a linearization of the response about the current control value [61].

6.2 Relaxed HHC for Enhanced Robustness

An alternative to conventional HHC is designated "relaxed HHC", where a relaxation coefficient is introduced into the algorithm. This technique was pioneered by Depailler [33]. This variation on the HHC algorithm has proved itself useful under highly nonlinear condition induced by dynamic stall, where any estimate of $\mathbf{T}$ is uncertain. This variant of the algorithm compromises the one-step convergence property of the algorithm shown earlier, but improves robustness. Recall that when $\mathbf{T}$ is known, the optimal control law $\mathbf{u}_{k+1}$ from Eq. (6.12) can be

expressed as:

$$\mathbf{u}_{k+1} = \mathbf{u}_k + \Delta\mathbf{u}_k, \tag{6.13}$$

where one can define

$$\Delta\mathbf{u}_k = -\mathbf{D}^{-1}\mathbf{T}^{\mathrm{T}}\mathbf{Q}_{\mathbf{z}}\mathbf{z}_k + (\mathbf{D}^{-1}\mathbf{T}^{\mathrm{T}}\mathbf{Q}_{\mathbf{z}}\mathbf{T} - \mathbf{I})\mathbf{u}_k. \tag{6.14}$$

Replacing $\Delta\mathbf{u}_k$ in Eq. (6.13) by $\alpha_{re}\Delta\mathbf{u}_{k,\alpha}$, yields the relaxed control update law,

$$\mathbf{u}_{k+1,\alpha} = \mathbf{u}_{k,\alpha} + \alpha_{re}\Delta\mathbf{u}_{k,\alpha}, \tag{6.15}$$

where $\mathbf{u}_{0,\alpha} = \mathbf{u}_0$.

A detailed analysis of the convergence, stability, and robustness characteristics of the relaxed HHC algorithm can be found in Ref. 99. Relaxed HHC is only useful in the cases where T is uncertain (it increases convergence time in all other cases).

6.3 Adaptive HHC Algorithm

A third version of the HHC algorithm, discussed in Ref. 61, is known as adaptive or recursive HHC. In this version, the sensitivity $\mathbf{T}$ is identified online, and is used to implement an adaptive extension of the classical HHC. To pursue this,

relative parameters are defined, $\Delta \mathbf{z}_k$, with length $2p$ and $\Delta \mathbf{u}_k$ with length $2m$ as

$$\Delta \mathbf{z}_k = \mathbf{z}_k - \mathbf{z}_{k-1}, \;\; \Delta \mathbf{u}_k = \mathbf{u}_k - \mathbf{u}_{k-1}, \tag{6.16}$$

and, $\Delta \mathbf{Z}_k$ of size $2p \times k$ and $\Delta \mathbf{U}_k$ of size $2m \times k$ as

$$\Delta \mathbf{Z}_k \;\; = \left[\begin{array}{ccc} \Delta \mathbf{z}_1 & \cdots & \Delta \mathbf{z}_k \end{array} \right], \; \Delta \mathbf{U}_k = \left[\begin{array}{ccc} \Delta \mathbf{u}_1 & \cdots & \Delta \mathbf{u}_k \end{array} \right]. \tag{6.17}$$

The relation between the successive updates of vibration levels $\mathbf{z}_k$ is

$$\mathbf{z}_{k+1} = \mathbf{z}_k + \mathbf{T}(\mathbf{u}_{k+1} - \mathbf{u}_k). \tag{6.18}$$

This can be represented in another form,

$$\Delta \mathbf{z}_k = \mathbf{T} \Delta \mathbf{u}_k. \tag{6.19}$$

Hence, it follows from Eqs. (6.19) and (6.17) that

$$\Delta \mathbf{Z}_k = \mathbf{T} \Delta \mathbf{U}_k. \tag{6.20}$$

Assuming $\Delta \mathbf{U}_k \Delta \mathbf{U}_k^{\mathrm{T}}$ is nonsingular, one can define

$$\mathbf{P}_k = (\Delta \mathbf{U}_k \Delta \mathbf{U}_k^{\mathrm{T}})^{-1}, \tag{6.21}$$

and from Eq. (6.20) the least squares estimate $\hat{\mathbf{T}}_{\mathrm{LS}_k}$ of $\mathbf{T}$ is given by

$$\hat{\mathbf{T}}_{\mathrm{LS}_k} = \Delta\mathbf{Z}_k \Delta\mathbf{U}_k^{\mathrm{T}} \mathbf{P}_k. \tag{6.22}$$

The recursive least squares method is used to iteratively update $\hat{\mathbf{T}}_{\mathrm{LS}_k}$ based on the past and current values of $\Delta\mathbf{z}_k$ and $\Delta\mathbf{u}_k$. The updated estimate $\hat{\mathbf{T}}_{\mathrm{LS}_k}$ is used at each control update step to calculate the control law $\mathbf{u}_{k+1}$.

6.4 Implementation of the HHC Algorithm

The higher-harmonic control algorithm is used in this study for three different problems. Hub load vibration reduction, BVI noise reduction, and simultaneous BVI noise and vibration reduction. For a 4-bladed rotor, the control input $\mathbf{u}$ is a combination of 2/rev, 3/rev, 4/rev, and 5/rev harmonics components of the control surface deflection. The term 'control surface' refers to both the microflap and the conventional plain trailing-edge flap. The total control surface deflection is given by

$$\delta(\psi) = \sum_{N=2}^{5} \left[\delta_{Nc} \cos(N\psi) + \delta_{Ns} \sin(N\psi)\right]. \tag{6.23}$$

where the quantities δ_{Nc} and δ_{Ns} correspond to the cosine and sine components of the N/rev control input harmonic. Thus, the control vector $\mathbf{u}$ is given by

$$\mathbf{u} = \left\{\delta_{2c}, \delta_{2s}, ..., \delta_{5c}, \delta_{5s}\right\}^T. \tag{6.24}$$

The AVINOR code was modified as part of the current study to accommodate more than two control surfaces. When multiple control surfaces are used, the control inputs are given by

$$\delta_i(\psi) = \sum_{N=2}^{5} (\delta_{Nci} \cos(N\psi) + \delta_{Nsi} \sin(N\psi)), \tag{6.25}$$

$$\tag{6.26}$$

where $i = 1, \ldots, N_\delta$ and N_δ is the total number of control surfaces. The control vector $\mathbf{u}$ then becomes

$$\mathbf{u} = \{\delta_{2c1}, \delta_{2s1}, ..., \delta_{5c1}, \delta_{5s1}, \ldots, \delta_{2cN_\delta}, \delta_{2sN_\delta}, ..., \delta_{5cN_\delta}, \delta_{5sN_\delta}\}^T. \tag{6.27}$$

Unlike a conventional plain flap, the microflap deflects only downward. In order to be able to use the HHC algorithm for the microflap, a two step approach has been used. In the first step, the microflap is given a constant deflection $\frac{\delta_{\mathrm{mf}}}{2}$, where δ_{mf} is the size of the microflap. In the next step, the HHC algorithm is engaged to determine the 2/rev-5/rev harmonic control inputs given in Eq. 6.27 with a saturation limit of $\frac{\delta_{\mathrm{mf}}}{2}$. Thus the microflap deflection determined by the HHC algorithm is restricted to $\pm\frac{\delta_{\mathrm{mf}}}{2}$. Combined with the constant deflection $\frac{\delta_{\mathrm{mf}}}{2}$, provided during the first step, the overall microflap deflection is restricted to lie between 0 and δ_{mf}.

For vibration reduction (VR) studies, the output vector $\mathbf{z}_k$ consists of 4/rev vi-

bration levels as given in Eqs. (C.46-C.49),

$$\mathbf{z}_{\text{VR}} = \begin{bmatrix} F_{HX4} \\ F_{HY4} \\ F_{HZ4} \\ M_{HX4} \\ M_{HY4} \\ M_{HZ4} \end{bmatrix} \tag{6.28}$$

Recall that the weighting matrix $\mathbf{Q_z}$ in the cost function is a diagonal matrix, and, for vibration control, is described by six weights corresponding to the three vibratory hub shears and the three vibratory hub moments. Based on previous studies [78, 98], the weights for the hub shears were assumed to be identical, and a similar assumption was used for the weights of the hub moments. The weighting matrix used in this study for vibration reduction, $\mathbf{Q}_{\text{VR}}$, is:

$$\mathbf{Q}_{\text{VR}} = \begin{bmatrix} 1 & 0 & 0 & 0 & 0 & 0 \\ 0 & 1 & 0 & 0 & 0 & 0 \\ 0 & 0 & 1 & 0 & 0 & 0 \\ 0 & 0 & 0 & 10 & 0 & 0 \\ 0 & 0 & 0 & 0 & 10 & 0 \\ 0 & 0 & 0 & 0 & 0 & 10 \end{bmatrix}. \tag{6.29}$$

For BVI noise reduction (NR) studies, the output vector consists of the 6^{th}-17^{th}

harmonic components of BVI noise, as measured at a microphone installed at a suitable location. This location is usually on the skid or landing gear of the helicopter, and

$$\mathbf{z}_{\text{NR}} = \begin{bmatrix} N_{H06} \\ N_{H07} \\ N_{H08} \\ \vdots \\ N_{H17} \end{bmatrix} \tag{6.30}$$

The noise control law is identical to the control law used for vibration reduction except that the objective function J consists of the 6^{th}-17^{th} blade passage frequency harmonic components of acoustic pressure (the most significant part of BVI noise) in quadratic form. The weighting matrix used in this study for noise reduction is:

$$\mathbf{Q}_{\text{NR}} = \begin{bmatrix} 1 & 0 & 0 & 0 & \dots & \dots & 0 \\ 0 & 1 & 0 & 0 & \dots & \dots & 0 \\ 0 & 0 & 1 & 0 & \dots & \dots & 0 \\ & & & \ddots & & & \\ 0 & \dots & \dots & 0 & 1 & 0 & 0 \\ 0 & \dots & \dots & 0 & 0 & 1 & 0 \\ 0 & \dots & \dots & 0 & 0 & 0 & 1 \end{bmatrix}. \tag{6.31}$$

Note that all the components of the BVI noise are weighted equally.

For rotor performance enhancement studies, the output vector is defined as

$$\mathbf{z}_{\text{PWR}} = [P_R] \tag{6.32}$$

where P_R denotes the average rotor shaft power. The average rotor shaft power is defined as the power required to drive the rotor at a constant angular velocity Ω averaged over one revolution,

$$P_R = \frac{\Omega}{2\pi} \int_0^{2\pi} -M_{Hz1}(\psi) d\psi, \tag{6.33}$$

where M_{Hz1} is the total yawing moment about the hub and includes the effect of unsteadiness, compressibility, dynamic stall, and the additional drag due to control surface deflection.

6.5 Actuator Saturation

For microflaps, the thickness of the airfoil imposes a limitation on the size of the microflap thus constraining the maximum deflection of the microflap. For the active control simulations conducted in this study using a microflap, the issue of restricting microflap's maximum deflection to be less than its size is implemented as an actuator saturation problem. Similarly, for a conventional trailing-edge flap, the maximum acceptable deflection is set to 4° so as to avoid interactions with the flight control system. The effect of actuator saturation on active vibration reduction using conventional plain flaps was studied by Cribbs and Friedmann [28].

Three different approaches, namely truncation, scaling, and auto-weighting, to constraining the flap deflections were considered. It was observed that the auto-weighting approach produced the best vibration reduction performance. Hence, it has been used in the active control simulations conducted in this study. However, the auto-weighting approach has several shortcomings. It is computationally expensive and in the case of multiple control surfaces, it does not utilize all of them to the maximum possible extent. These shortcomings can be remedied using a new approach developed in this study, based on constrained nonlinear optimization. A detailed description of this approach and a comparison of its performance to the various existing actuator saturation approaches is provided in Chapter VIII.

6.6 Control With Multiple Objectives

6.6.1 Approach for Minimizing Noise and Vibration

For simultaneous vibration and noise reduction (SR) problems, a combined output vector can be defined

$$\mathbf{z}_{\mathrm{SR}} = \left[\begin{array}{c} \mathbf{z}_{\mathrm{VR}} \\ \hline \mathbf{z}_{\mathrm{NR}} \end{array}\right], \tag{6.34}$$

where the vector $\mathbf{z}_{\mathrm{SR}}$ is simply a partitioned combination of the vibration and noise levels. The weighting matrix $\mathbf{Q}_{\mathbf{z}}$ can be used to adjust the control effort so as to achieve a desirable balance between the vibration reduction and noise reduction.

For the combined noise and vibration problem, when the output vector is de-

fined by Eq. (6.34), the weighting matrix $\mathbf{Q}_{\text{SR}}$ becomes

$$\mathbf{Q}_{\text{SR}} = \begin{bmatrix} [\mathbf{Q}_{\text{VR}}] & 0 \\ 0 & [\mathbf{Q}_{\text{NR}}] \end{bmatrix}. \tag{6.35}$$

A scalar factor W_α can be introduced to adjust the relative weighting between noise and vibration as objectives for the controller. The weighting matrix then appears as:

$$\mathbf{Q}_{\text{SR}} = \begin{bmatrix} (W_\alpha) \cdot [\mathbf{Q}_{\text{VR}}] & 0 \\ 0 & (1 - W_\alpha) \cdot [\mathbf{Q}_{\text{NR}}] \end{bmatrix}. \tag{6.36}$$

When the factor $W_\alpha = 1$, full control effort is focused on vibration reduction, while when $W_\alpha = 0$, only noise is reduced by the controller. During landing approach, BVI noise might be the reduction priority, while vibration might be the concern at higher-speed cruise flight. The system could adjust between these objectives. The weighting matrices $\mathbf{Q}_{\text{VR}}$ and $\mathbf{Q}_{\text{VR}}$ used for simultaneous noise and vibration reduction performed in this study are:

$$\mathbf{Q}_{\text{VR}} = \begin{bmatrix} 1 & 0 & 0 & 0 & 0 & 0 \\ 0 & 1 & 0 & 0 & 0 & 0 \\ 0 & 0 & 10 & 0 & 0 & 0 \\ 0 & 0 & 0 & 10 & 0 & 0 \\ 0 & 0 & 0 & 0 & 10 & 0 \\ 0 & 0 & 0 & 0 & 0 & 10 \end{bmatrix}, \tag{6.37}$$

and

$$\mathbf{Q}_{\mathrm{NR}} = \begin{bmatrix} 100 & 0 & 0 & 0 & \dots & \dots & 0 \\ 0 & 100 & 0 & 0 & \dots & \dots & 0 \\ 0 & 0 & 100 & 0 & \dots & \dots & 0 \\ & & & \ddots & & & \\ 0 & \dots & \dots & 0 & 100 & 0 & 0 \\ 0 & \dots & \dots & 0 & 0 & 100 & 0 \\ 0 & \dots & \dots & 0 & 0 & 0 & 100 \end{bmatrix}. \tag{6.38}$$

Note that these weighting matrices are different from those used for individual vibration or noise control, shown in Eqs. 6.29 and 6.31. Specifically, the weighting on the vertical hub shear is increased 10 times and the weighting on the noise components is increased 100 times. Its not the actual weights but the relative weighting between the vibration and noise components that is important for simultaneous noise and vibration reduction.

6.6.2 Approach for Minimizing Vibration and Rotor Power

For simultaneous vibration and power reduction, a combined output vector can be defined as

$$\mathbf{z}_{\mathrm{PV}} = \begin{bmatrix} \mathbf{z}_{\mathrm{VR}} \\ \hline \mathbf{z}_{\mathrm{PWR}} \end{bmatrix}. \tag{6.39}$$

The combined weighting matrix with a relative weighting parameter W_α is given as

$$\mathbf{Q}_{\text{PV}} = \begin{bmatrix} (W_\alpha) \cdot [\mathbf{Q}_{\text{VR}}] & 0 \\ 0 & (1 - W_\alpha) \cdot [\mathbf{Q}_{\text{PWR}}] \end{bmatrix}. \tag{6.40}$$

The weighting matrices $\mathbf{Q}_{\text{VR}}$ and $\mathbf{Q}_{\text{PWR}}$ used for simultaneous vibration and power reduction performed in this study are:

$$\mathbf{Q}_{\text{VR}} = \begin{bmatrix} 1 & 0 & 0 & 0 & 0 & 0 \\ 0 & 1 & 0 & 0 & 0 & 0 \\ 0 & 0 & 1 & 0 & 0 & 0 \\ 0 & 0 & 0 & 1 & 0 & 0 \\ 0 & 0 & 0 & 0 & 1 & 0 \\ 0 & 0 & 0 & 0 & 0 & 1 \end{bmatrix}, \tag{6.41}$$

and

$$\mathbf{Q}_{\text{PWR}} = [1]. \tag{6.42}$$

Note that the vibration components and the rotor power consumption are weighted equally.

CHAPTER VII

RESULTS AND DISCUSSION

This chapter presents results demonstrating the effectiveness of a microflap in reducing rotor vibrations and noise. The relaxed and adaptive versions of the HHC algorithm are used. Various spanwise configurations of the microflap are considered. The effects of BVI noise reduction on the vibration levels and vice versa are studied. Subsequently, simultaneous BVI noise and vibration reduction using various microflap configurations is examined. Vibration reduction using microflap is also studied at a high speed level cruise flight condition. Combined vibration and power reduction is examined at the high speed flight condition. The capabilities of the microflap in reducing rotor noise and vibration are evaluated through comparisons to a conventional trailing-edge plain flap.

7.1 Simulation Setup

7.1.1 Rotor and Control Surface Configurations

The results presented in this chapter are obtained for a helicopter configuration resembling a full-scale four-bladed MBB BO-105 hingeless rotor. The rotor parameters are listed in Table 7.1. The data in the table (except $C_W, \gamma,$ and σ) have been nondimensionalized using M_b, L_b, and $1/\Omega$ for mass, length and time, respectively. The mass and stiffness distributions are assumed to be constant along the span of the blade. Additional information on nondimensionalization can be found in Section 9.2.

The vibratory hub shears and moments are obtained from the integration of the distributed inertial and aerodynamic loads over the entire blade span in the rotating frame. Subsequently, the loads are transformed to the hub-fixed non-rotating system, and the contributions from the individual blades are combined. In this process, the blades are assumed to be identical. Reduction is performed on the N_b/rev components, which are the dominant components, of the hub shears and moments. The rotor is trimmed using a propulsive trim procedure where six equilibrium equations (three forces and three moments) for the helicopter in a steady forward flight condition are enforced.

The acoustic environment in the vicinity of the helicopter is characterized by the noise decibel levels computed on a carpet plane located 1.15R beneath the rotor, as depicted in Fig. 7.1. Various potential locations for placing a feedback mi-

Table 7.1: Rotor parameters used for the computations.

Dimensional Rotor Data	
$R = 4.91$ m	
$M_b = 27.35$ kg	
$\Omega = 425$ RPM	
Nondimensional Main Rotor Data	
$N_b = 4$	$c_b = 0.05498R$
$L_b = 1.0$	$e = 0$
$X_A = 0$	$\beta_p = 2.5^\circ$
$X_{Ib} = 0$	$X_{IIb} = 0$
$X_{Ic} = 0$	$X_{IIc} = 0$
$I_{MB2} = 0$	$I_{MB3} = 0.0004$
$EI_{\eta\eta} = 0.0302$	$EI_{\zeta\zeta} = 0.0105$
$GJ_b = 0.0015$	$\omega_{F1} = 1.124$
$\omega_{F2} = 3.404$	$\omega_{F3} = 7.606$
$\omega_{L1} = 0.732$	$\omega_{L2} = 4.458$
$\omega_{T1} = 3.170$	$\omega_{T2} = 9.079$
$\gamma = 5.5$	$\sigma = 0.07$
$\theta_{tw} = -8^\circ$	
Nondimensional Tail Rotor Data	
$X_t = 1.20$	$Z_t = 0$
Helicopter Data	
C_W = 0.005	fC_{df} = 0.031
$X_{FA} = 0.0$	$Z_{FA} = 0.3$
$X_{FC} = 0.0$	$Z_{FC} = 0.3$

crophone on a helicopter, shown in Fig. 7.1, were examined in Ref. 78 for effective advancing side BVI noise reduction. A feedback microphone located at the rear of the right skid was found to be most effective for reducing advancing side noise on the carpet plane. This location is used as the feedback microphone location supplying noise output signal to the controller in this study.

The sharp trailing edge configuration, shown in Fig. 7.2, was chosen as the microflap configuration. The microflap, 1.5%c in height, slides in and out of a cavity, located at 6%c from the sharp trailing edge of the airfoil. Three different span-

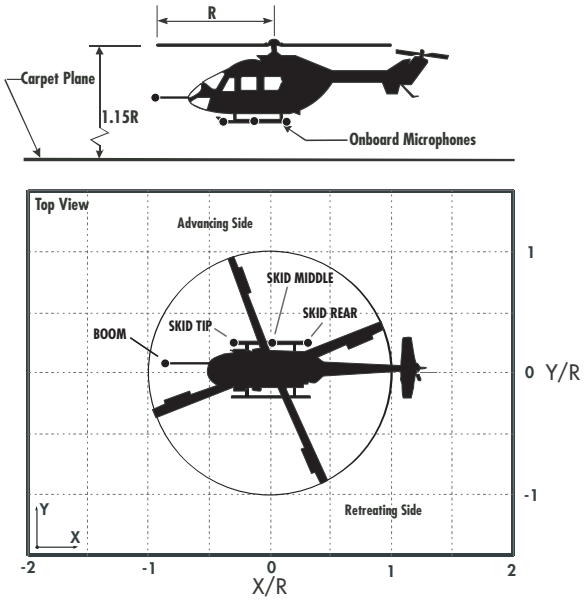

Figure 7.1: Microphone locations on and around the helicopter for noise measurements.

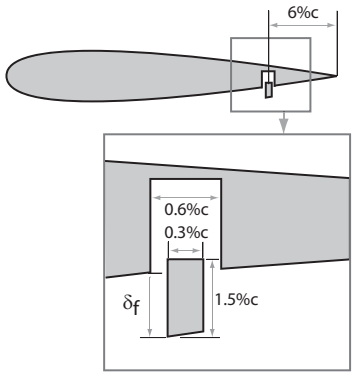

Figure 7.2: Oscillating microflap referred to as the sharp trailing-edge configuration used for active control studies.

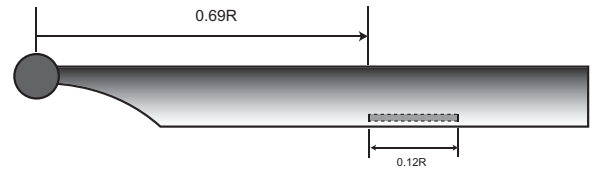

(a) Single Microflap

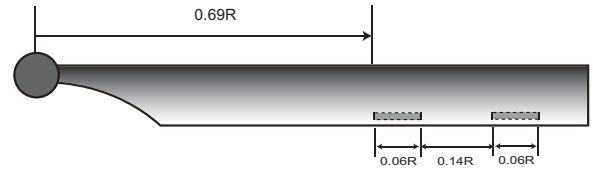

(b) Dual Microflap

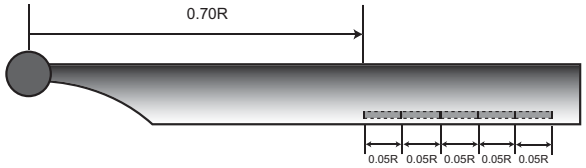

(c) Five Microflaps

Figure 7.3: Various spanwise configurations of the microflap on the rotor blade

wise configurations of microflaps on the rotor blade are considered in this study. The first configuration, shown in Figure 7.3(a), consists of a single microflap with 0.12R spanwise length centered at 0.75R. The second configuration, shown in Figure 7.3(b), consists of two microflaps each with 0.06R spanwise length centered at 0.72R and 0.92R, respectively. The first two configurations are similar to those used in Ref. 91 for active control studies with conventional flaps. A new configuration used in this study for the microflaps consists of five microflaps each 0.05R in spanwise length placed next to each other, as shown in Figure 7.3(c). Such a configuration consisting of multiple adjacent microflaps has been used in several microflap application studies mentioned in Chapter I.

For comparison, active control studies were also conducted using a 20%c conventional plain flap, shown in Fig. 7.4. Single and dual spanwise configurations,

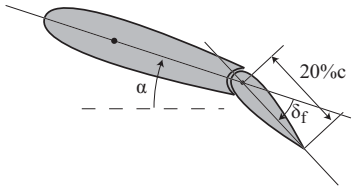

Figure 7.4: A 20%c conventional plain flap configuration.

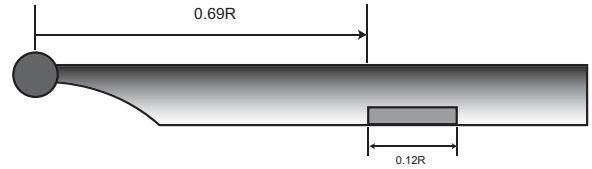

(a) Single plain flap

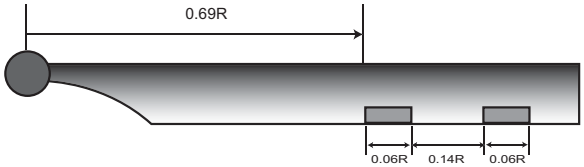

(b) Dual plain flap

Figure 7.5: Single and dual spanwise configurations of the 20%c plain flap on the rotor blade

shown in Fig. 7.5, are considered for the plain flap. The spanwise configurations are similar to those used for the microflap.

7.1.2 Aerodynamic Model Setup

The CFD based RFA model, described in Chapter III, is a 2-dimensional model and is implemented at various spanwise locations on the rotor blade. The number of spanwise locations have to be chosen such that the aerodynamic loading distribution over the entire rotor disk is properly captured. However, each implementation of the aerodynamic model at a specific spanwise location contributes a certain number of aerodynamic states which is proportional to the number of generalized aerodynamic loads being modeled and the number of lag terms used in the RFA

approximation. To develop a computationally efficient aeroelastic simulation, the number of aerodynamic states used has to be minimized.

Optimization studies were conducted in Ref. 91 to determine the appropriate number of spanwise locations and lag terms required for the RFA model. Based on studies described in Ref. 91, the blade is partitioned into segments as shown in Fig. 7.6. The aerodynamic loading on the inner 20% of the blade, represented by segment A, is assumed to be negligible and hence aerodynamic loads in this region are neglected. For consistency with the structural dynamic model, within each of the remaining segments, aerodynamics are modeled at a selected number of stations located at the Gaussian integration points of the segment. The number of stations and the corresponding number of aerodynamic states used are listed in Tables 7.2 and 7.3 for the single and dual microflap configurations, respectively. The aerodynamic lift, moment, and drag forces are modeled using 6 RFA poles each. In order to determine the optimum number of poles to be used, a sensitivity analysis was performed by varying the number of RFA poles. The 4/rev vibratory hub loads obtained at $\mu = 0.3$ using 9, 8, 7, 6, and 5 RFA poles are compared in Fig. 7.7. The vibratory loads corresponding to 9 poles are chosen as the reference. The vibratory objective function, which is a weighted sum of the squares of the vibratory loads, corresponding to 8, 7, 6, and 5 poles is compared to the objective function corresponding to 9 poles. The percentage error is shown in the Fig. 7.7. The minimum number of poles to yield less than 10% error is 6, which is chosen for the aerodynamic model setup. The number of generalized motions is 2 (W_0

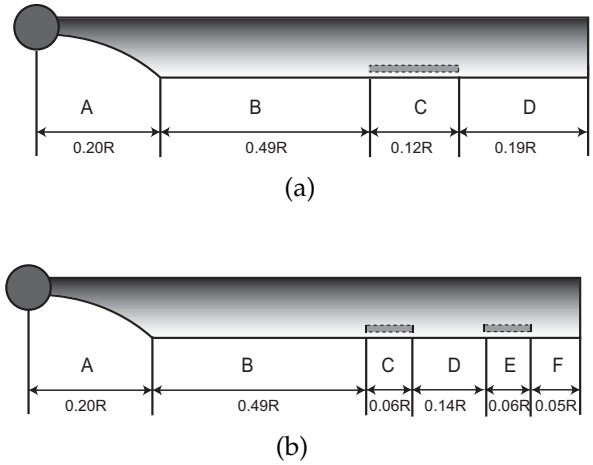

Figure 7.6: Segments on the rotor blade used for aerodynamic modeling.

and W_1) for the stations without a microflap and 3 (W_0, W_1, and D_0) for those with a microflap. For the simulations conducted with a conventional plain flap, all 4 generalized motions (W_0, W_1, D_0, and D_1) are considered. For acoustic calculations, based on the studies described in Ref. 98, additional blade stations are used in order to improve the accuracy of noise predictions. The number of stations and the corresponding aerodynamic states used for acoustic calculations are listed in Tables 7.4 and 7.5.

Segment	Blade stations	Poles	Generalized forces	Generalized motions	Aerodynamic states
B	4	6	3	2	144
C	5	6	3	3	270
D	4	6	3	2	144
Total					558

Table 7.2: Aerodynamic states of the CFD+RFA aerodynamic model setup used for the single microflap configuration.

Segment	Blade stations	Poles	Generalized forces	Generalized motions	Aerodynamic states
B	4	6	3	2	144
C	2	6	3	3	108
D	2	6	3	2	72
E	2	6	3	3	108
F	2	6	3	2	72
Total					504

Table 7.3: Aerodynamic states of the CFD+RFA aerodynamic model setup used for the dual microflap configuration.

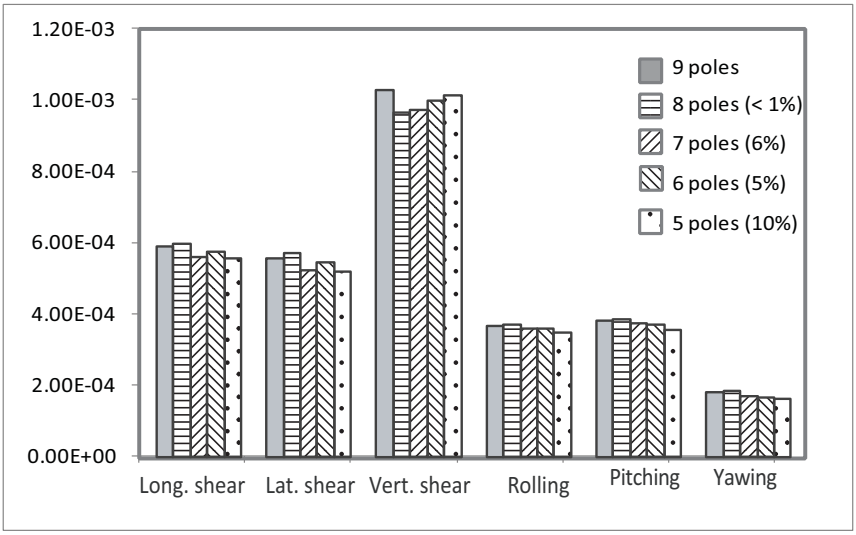

Figure 7.7: Effect of change in number of RFA poles on the 4/rev vibratory hub shears and moments obtained at $\mu = 0.3$.

7.2 Validation Studies

In this section, the combined aeroelastic-aeroacoustic simulation code using the CFD based ROM is validated against the experimental data obtained in the Higher-harmonic-control Aeroacoustic Rotor Tests (HART) program conducted in the German-Dutch wind tunnel [122]. The HART rotor is a 40% dynamically and Mach-scaled model of a 4-bladed hingeless MBB BO-105 main rotor, with -8° linear

Segment	Blade stations	Poles	Generalized forces	Generalized motions	Aerodynamic states
B	10	6	3	2	360
C	4	6	3	3	216
D	8	6	3	2	288
Total					864

Table 7.4: Aerodynamic states of the CFD+RFA aerodynamic model setup used for noise calculation with the single microflap configuration.

Segment	Blade stations	Poles	Generalized forces	Generalized motions	Aerodynamic states
B	10	6	3	2	360
C	2	6	3	3	108
D	4	6	3	2	144
E	2	6	3	3	108
F	2	6	3	2	72
Total					792

Table 7.5: Aerodynamic states of the CFD+RFA aerodynamic model setup used for noise calculations with the dual microflap configuration.

twist and standard rectangular planform. The test setup is depicted in Fig. 7.8. One of the blades was equipped with pressure transducers so that the blade airloads could be measured at various radial locations. Microphone arrays were placed on a traverse stand at a distance of 1.15 rotor radius underneath the rotor hub, and moved across the horizontal plane to measure the rotor noise at various locations. The rotor was trimmed for a given advance ratio μ, thrust coefficient C_T, and rotor shaft angle α_R, using collective and 1/rev cyclic pitch inputs. The comparisons presented in this section correspond the baseline condition (i.e. no active control) in the HART experiments. The baseline flight condition corresponds to a typical BVI flight condition, with $\mu = 0.15$, $C_T = 0.044$ and $\alpha_R = 5.3°$.

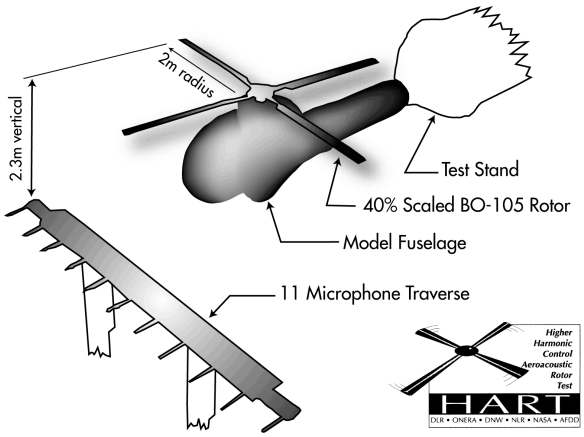

Figure 7.8: HART test setup.

The aerodynamic loads measured at a location $r/R = 0.87$ along the span of the blade obtained from the simulation and those measured in the HART study are compared in Fig. 7.9. Aerodynamic loads obtained using the original Doublet-Lattice based and the new CFD based aerodynamic models are shown in Fig. 7.9. The vertical axis in Fig. 7.9 represents a non-dimensional quantity equal to the product of the normal force coefficient and the square of the local Mach number. Both simulations capture the BVI events represented by the high frequency fluctuations in the aerodynamic loads, also found in the experimental data. Note that the prediction from the CFD+RFA model captures the overall shape of the aerodynamic load time histories better than the DL based aerodynamic model.

As indicated earlier, the acoustic environment was measured by traversing a microphone array positioned 1.15 R below the rotor, as shown in Fig. 7.8. From these data, time-averaged noise levels in decibel (dB) could be computed on a "carpet plane" parallel to and below the rotor. Comparison of the noise levels obtained from the simulations and the HART experiments is shown in Fig. 7.10, where the

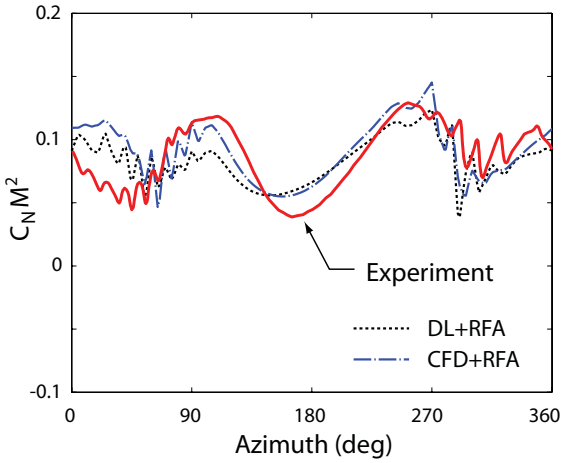

Figure 7.9: Validation of the aerodynamic load computations with the HART experimental data at $r/R = 0.87$.

noise predicted by the DL+RFA model was obtained from Ref. 101. The magnitudes of the BVI noise levels are predicted reasonably well by both the DL+RFA and CFD+RFA aerodynamic models. However, the DL+RFA model produced better agreement with the experimental data than the CFD+RFA model in the location of the high BVI noise region on the advancing side. As noted in Chapter V, the unsteady chordwise pressure distribution, required as input to the acoustic computations, is calculated differently for the two models. In Ref. 101, the chordwise pressure distribution was calculated using an extended RFA approach which was based on pressure data in the frequency domain generated from a DL based potential flow solver. For the present study, generating RFA models using CFD based pressure distribution data is computationally expensive. Therefore, the chordwise pressure distributions are estimated using the potential flow theory based velocity superposition method, described in Section 5.2.1, where the pressures are obtained from the sectional lift coefficients. The discrepancies observed in Fig. 7.10 can be

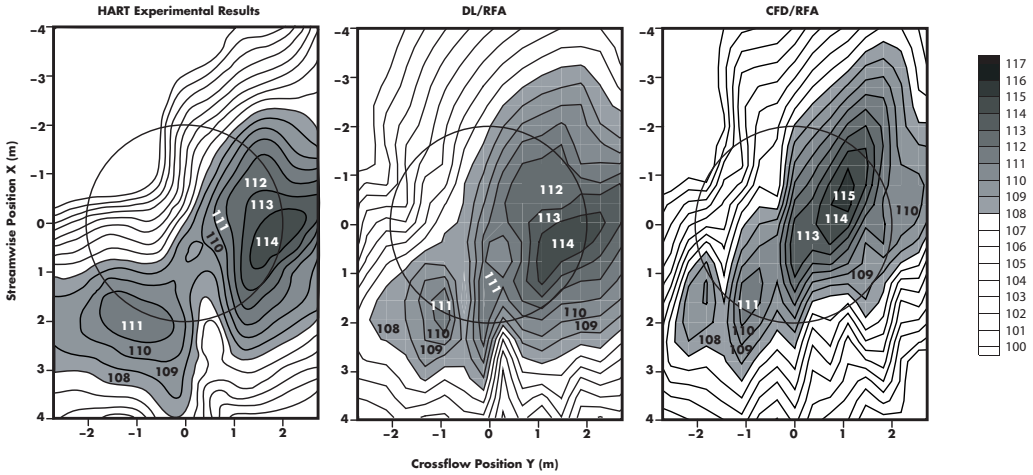

Figure 7.10: Validation of the acoustic computations with the HART experimental data.

attributed to the differences in pressure calculations.

7.3 Open Loop Phase Sweep

First, results simulating vibration reduction with the microflap operating in the open loop mode are presented. An open loop phase sweep is conducted by varying the phase angle ϕ_c for four discrete oscillating frequencies corresponding to 2/rev-5/rev, where the microflap motion is defined by

$$\delta_f = A[1 - \cos(\omega t + \phi_c)] \tag{7.1}$$

where $A = 0.75\%c$ for the 1.5%c microflap. The effect of the open loop sweep on the 4/rev vertical hub shear vibratory component is examined at a level forward flight condition with $\mu = 0.15$. Figure 7.11 shows the effects of each microflap harmonic on the 4/rev vertical shear. The results indicate that the microflap control inputs

have a significant effect on the 4/rev vertical shear. This suggests that the microflap has sufficient control authority for vibration reduction. It was found that the 3/rev and 4/rev harmonics are most effective and capable of producing maximum vibration reduction of approximately 80%, at phase angle settings of $\phi_c = 180^\circ$ and 330°, respectively. The 2/rev and 5/rev control inputs produce somewhat smaller vertical shear reduction levels, with maximum reductions of 17% and 38%, respectively. When compared to a conventional flap configuration with a servo flap having chord of 25%c [100], which produced 90% maximum vibration reduction with 3/rev harmonics, the microflap generates comparable amount of vibration reduction.

7.4 Vibration Reduction

Vibration reduction is examined in the closed-loop mode using the relaxed HHC algorithm described in Chapter VI. The three spanwise microflap configurations shown in Fig. 7.3 are considered at a heavy BVI descending flight condition with advance ratio $\mu = 0.15$ and descent angle $\alpha_D = 6.5^\circ$. The control objective function is a weighted sum of the squares of the 4/rev vibratory hub shears and moments. The control input is a combination of the 2/rev, 3/rev, 4/rev, and 5/rev harmonic components of the microflap deflection. The baseline vibratory hub shears and moments as well as the reduced vibrations obtained using the three microflap configurations are shown in Fig. 7.12. All three configurations yield a significant reduction in the vibration levels demonstrating excellent con-

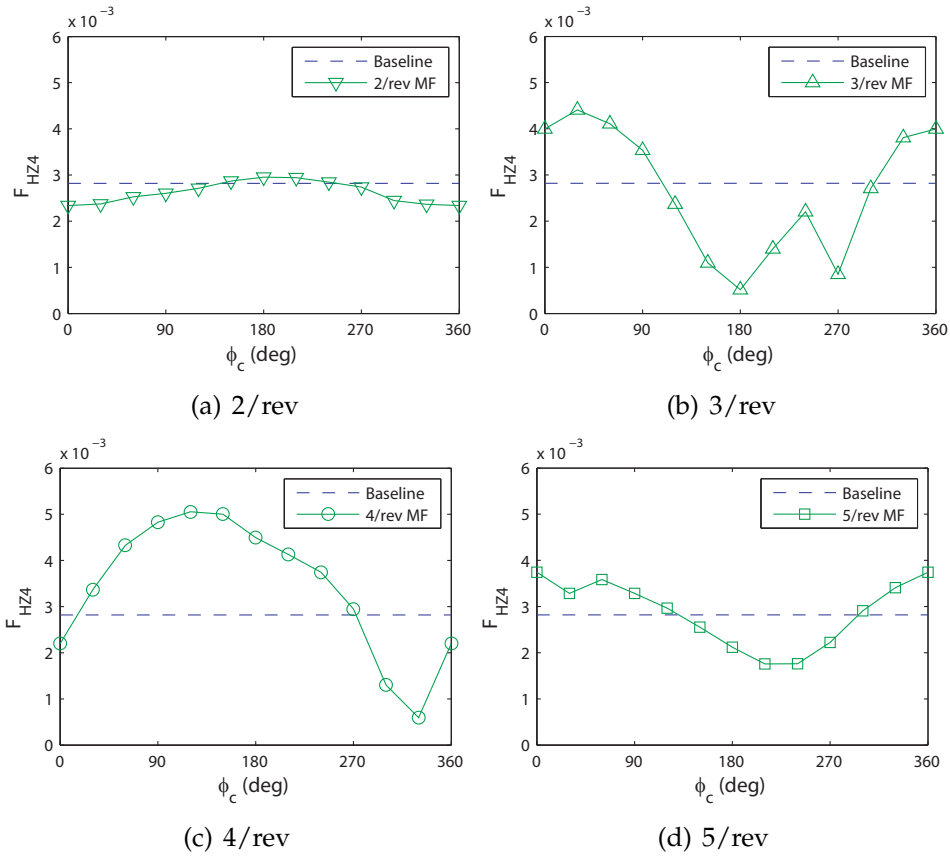

(a) 2/rev (b) 3/rev

(c) 4/rev (d) 5/rev

Figure 7.11: Effect of phase sweep on 4/rev vertical hub shear F_{HZ4} with the microflap at $\mu = 0.15$.

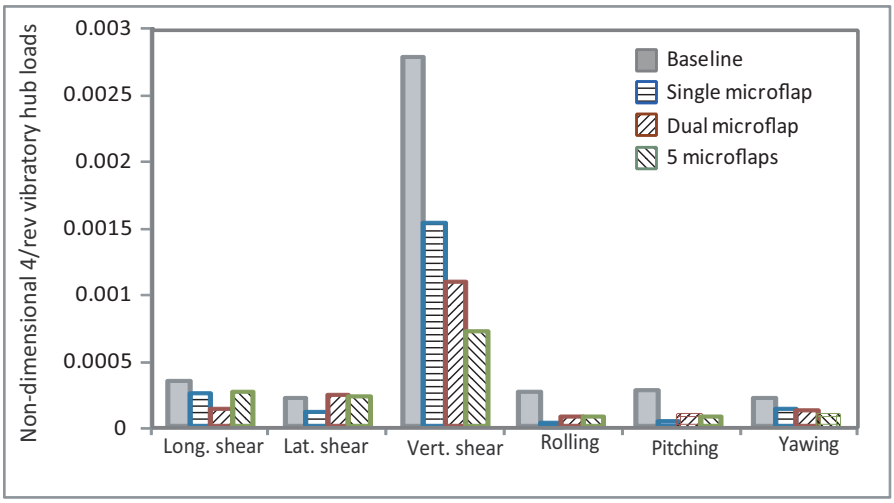

Figure 7.12: Reduction in 4/rev vibratory hub shears and moments obtained using the single, dual, and 5 microflap configurations for a heavy BVI descending flight condition.

trol authority. The single microflap yields a 73% reduction in the vibration control objective, while the dual microflap and the five-microflap configurations produce 84% and 92% reduction, respectively. The microflap deflection histories for the single and dual microflap configurations over one complete revolution are shown in Figs. 7.13(a) and 7.13(b).

In order to assess the effect of vibration reduction on the noise levels, the noise levels on the carpet plane were computed during active vibration reduction using microflaps. The noise contours on the carpet plane are shown in Fig. 7.18(a) for the baseline case. The noise contours computed during active vibration reduction using the single, dual, and five-microflap configurations are shown in Figs. 7.14 (b), 7.14 (c), and 7.14 (d), respectively. During vibration reduction, the single microflap generated a significant increase of about 2-3 dB in the noise levels on the advancing side. By comparison, the dual microflap configuration produced a smaller noise

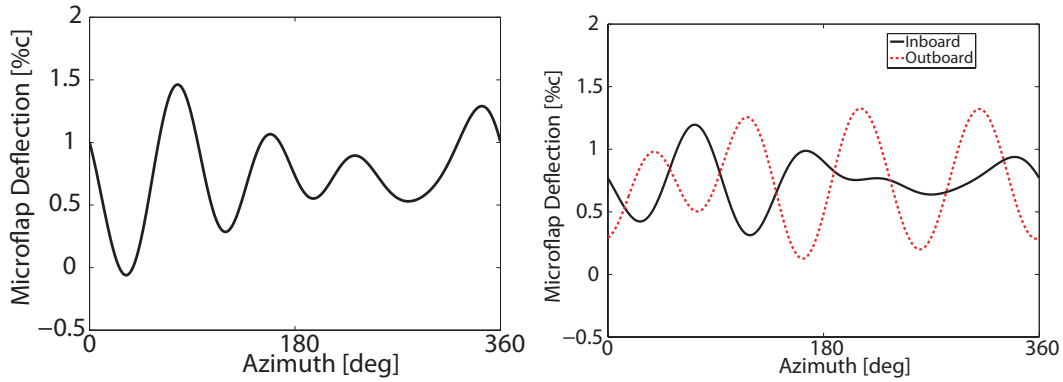

(a) Single microflap (b) Dual microflap

Figure 7.13: Microflap deflection histories over one complete revolution for the single and dual microflap configurations during active vibration reduction at a heavy BVI flight condition.

penalty on the advancing side noise of about 1 dB. It is very interesting to note that the five-microflap configuration does not produce a significant noise penalty. The noise levels on the retreating side are not affected significantly by any of the three configurations.

7.4.1 Comparison to a Plain Flap

Next, the vibration reduction capabilities of the microflap are compared to those of a 20%c trailing-edge plain flap. The plain flap deflection is constrained between $\pm 4^{\circ}$. The 4/rev vibratory hub loads computed during active vibration control using the single microflap and the single plain flap configurations are compared to the baseline vibration levels in Fig. 7.15. The microflap and the plain flap show similar effectiveness producing 73% and 76% reductions in the virbation objective, respectively. The noise contours computed on the carpet plane during active vibration control using the single microflap and the single plain flap are shown

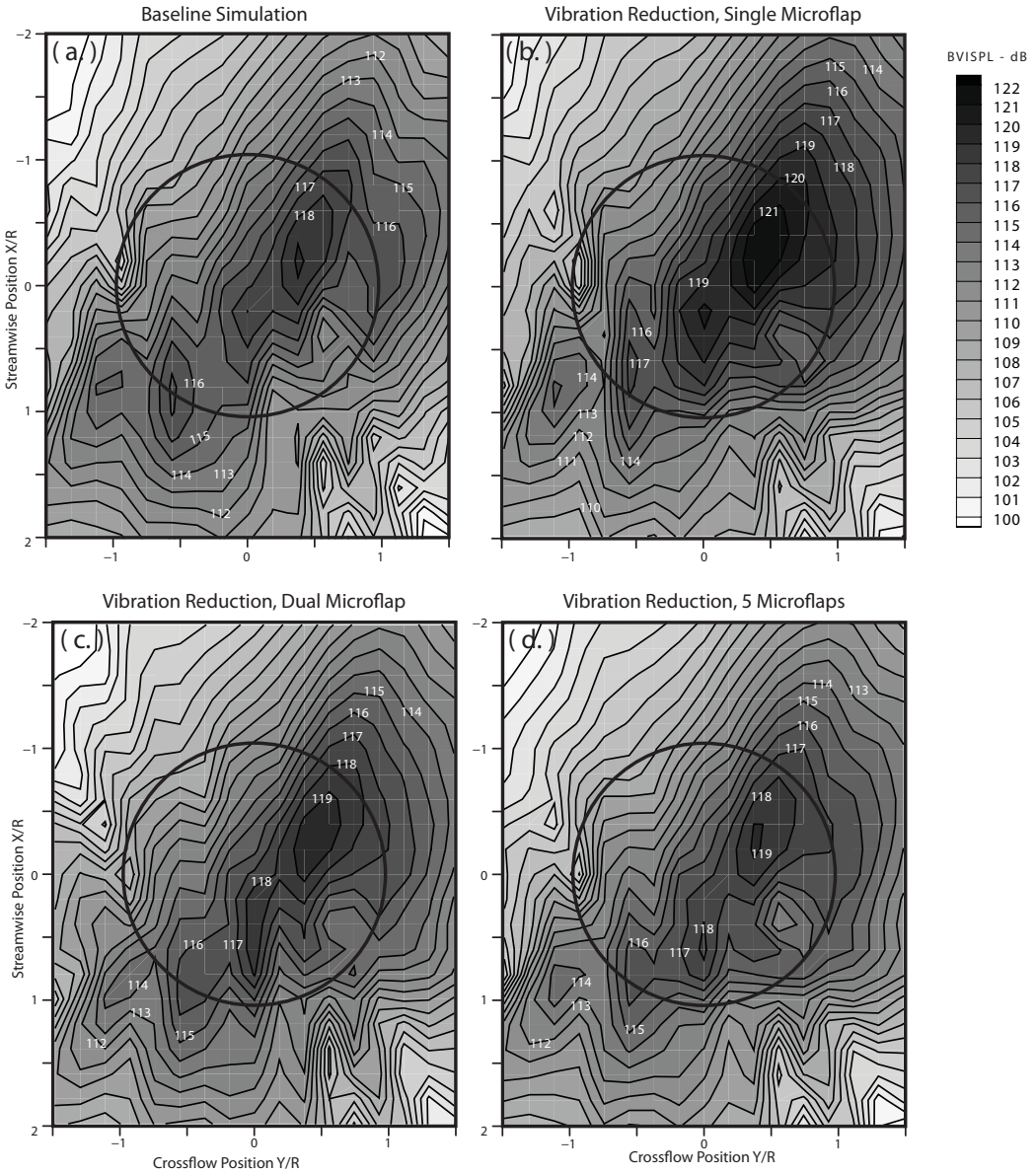

Figure 7.14: Noise levels computed on the carpet plane during active vibration reduction using microflaps at a heavy BVI flight condition.

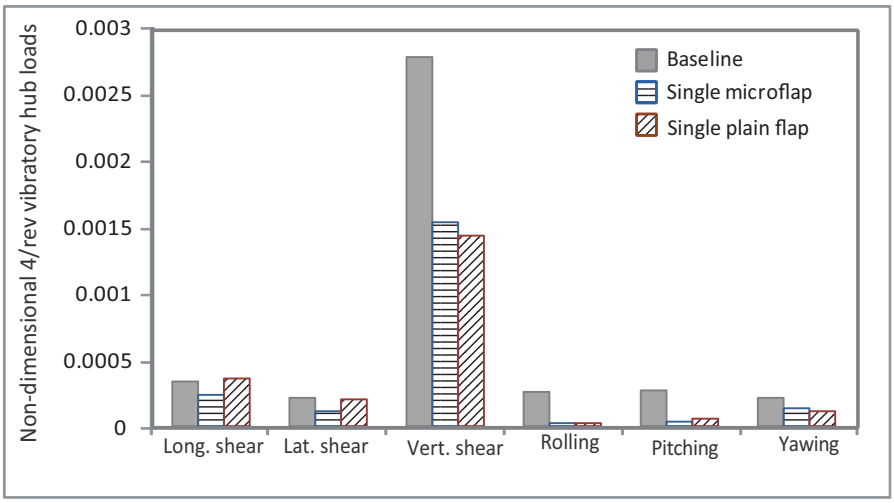

Figure 7.15: Comparison of the vibration levels computed during active vibration control using a single microflap and a single plain flap for a heavy BVI descending flight condition.

in Fig. 7.16. The plain flap causes a 2 dB increase in the noise levels on the advancing side while the microflap causes up to 3 dB increase in the advancing side noise levels. Neither of the two flaps shows any significant effect on the retreating side noise levels.

The flap deflection histories for the single microflap and the single plain flap configurations over one complete revolution are shown in Figures 7.17(a) and 7.17(b), respectively. The deflection histories for the microflap and the plain flap show similarity in the overall shape.

7.5 BVI Noise Reduction

Noise reduction studies are conducted using the three spanwise microflap configurations for a heavy BVI descending flight condition with advance ratio $\mu = 0.15$ and descent angle $\alpha_D = 6.5°$. The adaptive HHC control algorithm is used to re-

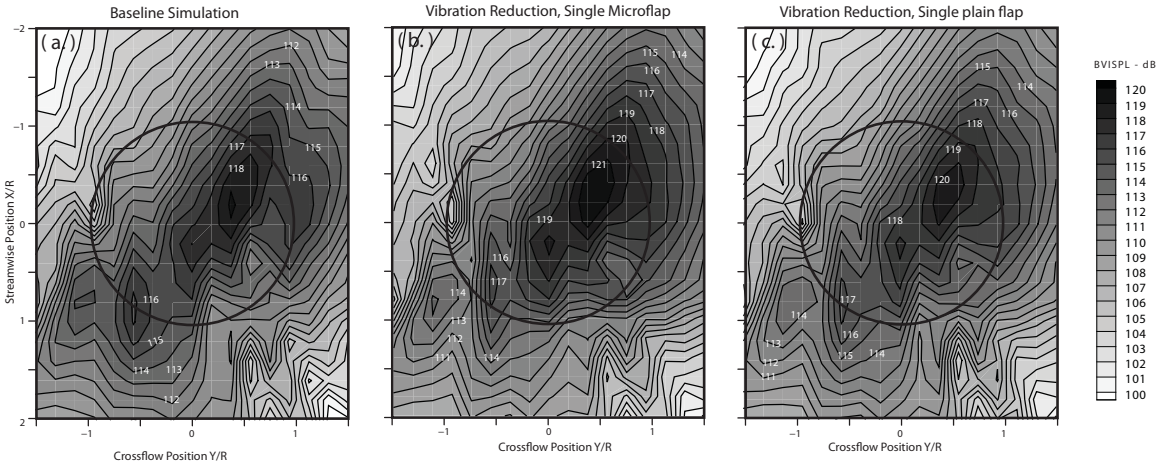

Figure 7.16: Comparison of the noise levels computed on the carpet plane during active vibration control using a single microflap and a single plain flap for a heavy BVI descending flight condition.

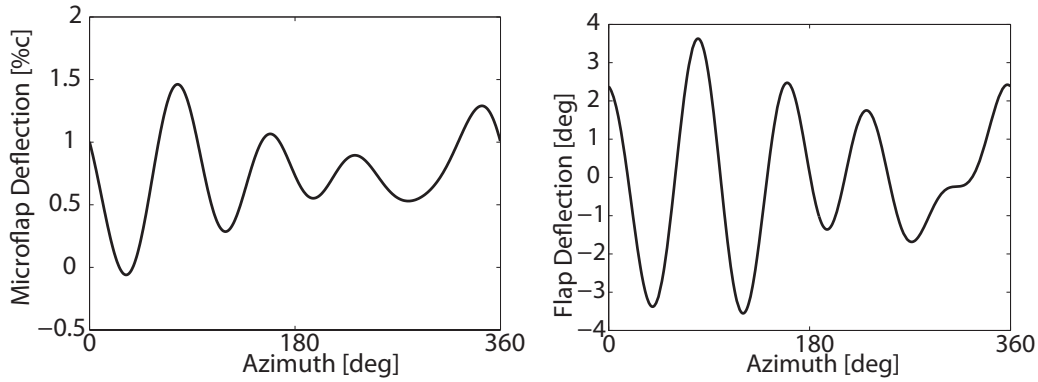

(a) Single microflap (b) Single plain flap

Figure 7.17: Deflection histories over one complete revolution for the single microflap and the single plain flap configurations during active vibration reduction at a heavy BVI flight condition.

duce noise levels at the feedback microphone located on the right rear skid. The BVI noise contours on the carpet plane are shown in Fig. 7.18(a) for the baseline case. The noise levels computed after active noise control using the single, dual, and the five-microflap configurations are shown in Figs. 7.18(b), 7.18(c), and 7.18(d), respectively. The single microflap configuration yields up to 3 dB noise reduction on the advancing side and 2 dB reduction on the retreating side of the rotor disk. The dual microflap configuration yields up to 5 dB noise reduction on the advancing side and close to 3 dB reduction on the retreating side. Clearly, it is beneficial for noise reduction to have a control device placed closer to the blade tip as in the case of the dual microflap configuration. The five-microflaps configuration reduces the advancing side noise by almost 6 dB and the retreating side noise by 3 dB. It is interesting to note that the BVI noise is reduced by the microflap configurations for the whole carpet plane; this is in contrast to the earlier active control studies performed using the single and dual conventional ACFs, where a noise increase of 1 dB on the retreating side was observed [102]. Overall, significant control authority is demonstrated by the microflaps for rotorcraft noise reduction.

The vibration levels were also monitored during the active noise reduction process. The vibration levels obtained after active noise reduction using the single, dual, and five-microflaps configurations are compared to the baseline vibration levels in Fig. 7.19. The vertical hub shear is increased by 45% in the case of the single and dual microflap configurations and by 100% in the case of the five-microflaps configuration. An increase in vibration levels during active noise re-

duction was also noticed in the earlier active control studies using conventional flaps [102, 128], as well as in noise control studies using other active control approaches [122]. The microflap deflection histories for the single and dual microflap configurations over one complete revolution are shown in Figures 7.20(a) and 7.20(b).

7.5.1 Comparison to a Plain Flap

Next, the noise reduction capabilities of the microflap are compared to those of a 20%c trailing-edge plain flap. The plain flap deflection is constrained between $\pm 4^{\circ}$. The noise levels computed on the carpet plane during active noise control using the single microflap and the single plain flap configurations are shown in Figs. 7.21(b), 7.21(c). It is interesting to note that although the plain flap and the microflap configurations seem to yield similar overall reductions on the advancing side, the single plain flap yields 1 dB less reduction on the retreating side when compared to the single microflap configuration. The vibration levels computed during active noise control using the single plain flap and the single microflap configurations are compared to the baseline levels in Fig. 7.22. The vertical hub shear is increased by 23% in the case of the plain flap and by 45% in the case of the microflap.

The flap deflection histories for the single microflap and the single plain flap configurations over one complete revolution are shown in Figures 7.29(a) and 7.29(b), respectively. The flap deflection histories are fairly similar in overall shape.

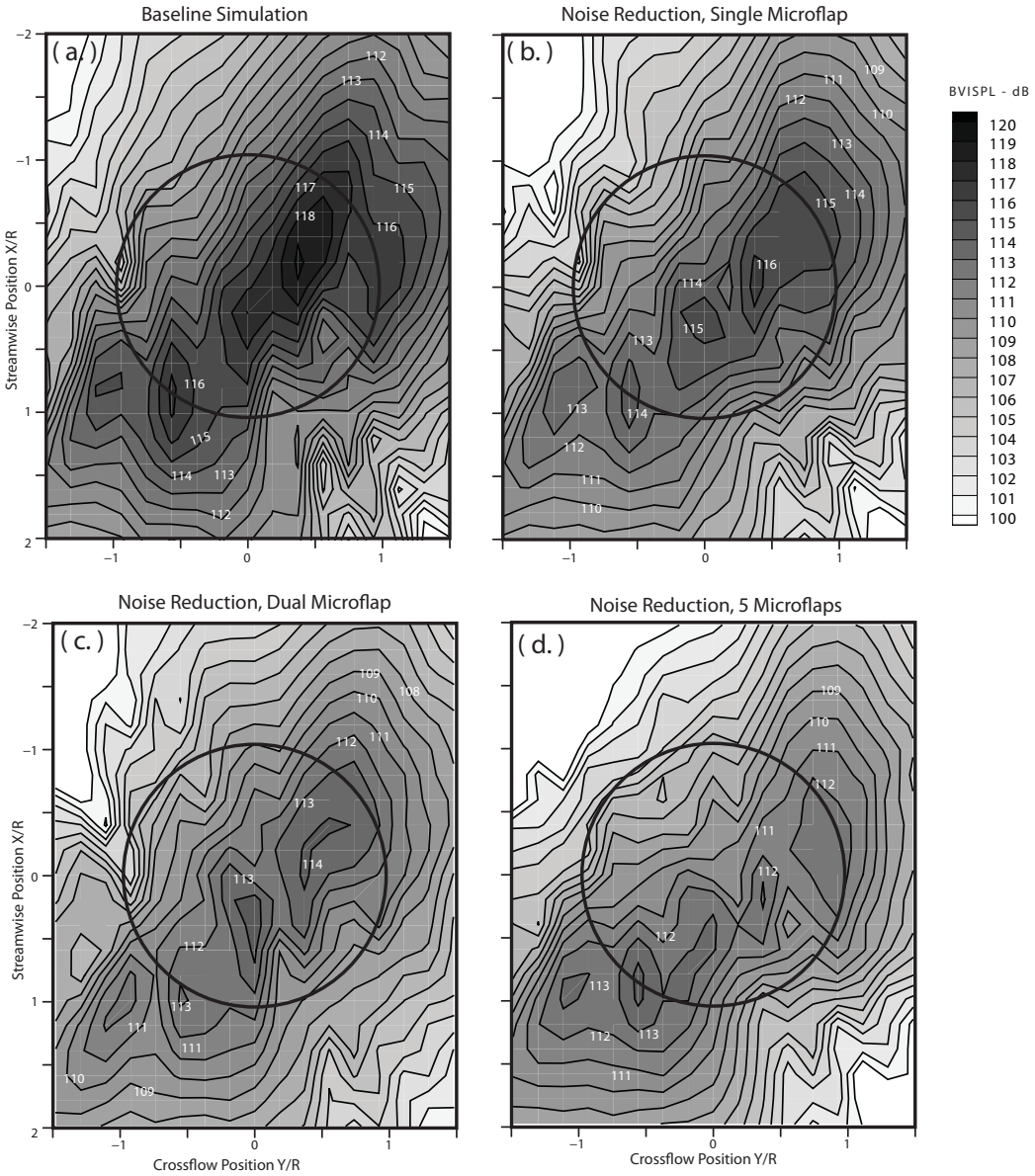

Figure 7.18: Noise levels computed on the carpet plane during active noise reduction using microflaps.

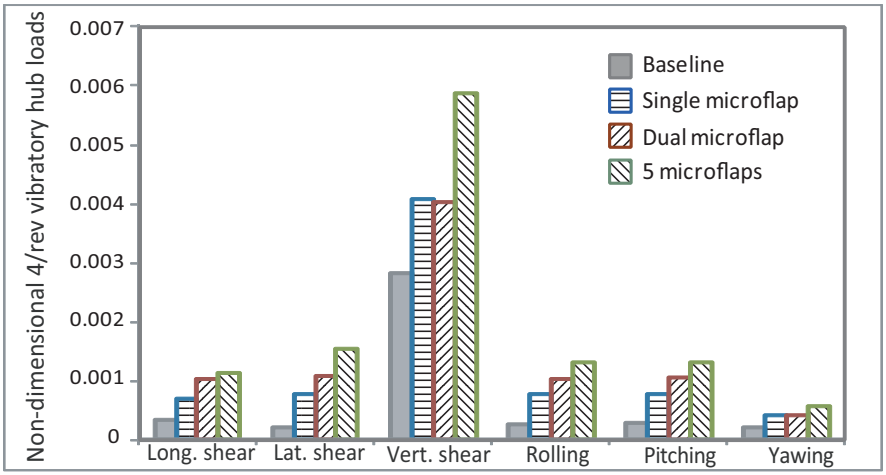

Figure 7.19: Vibration levels during active noise reduction using microflaps.

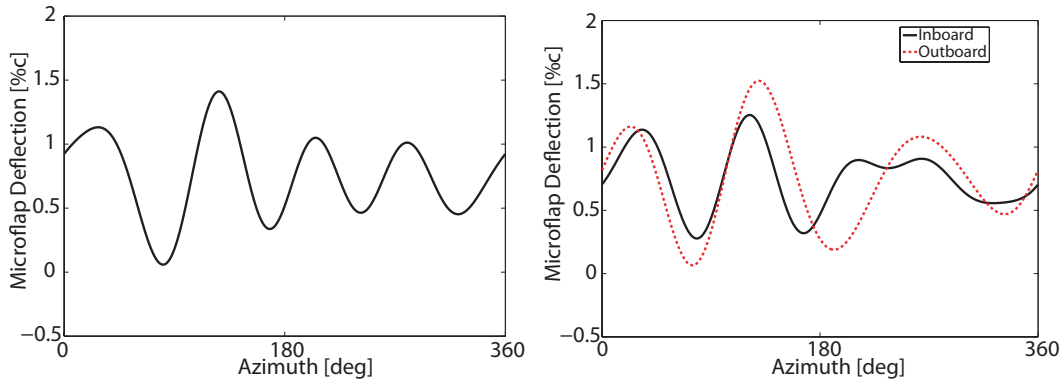

(a) Single microflap (b) Dual microflap

Figure 7.20: Microflap deflection histories over one complete revolution for the single and dual microflap configurations during active noise reduction.

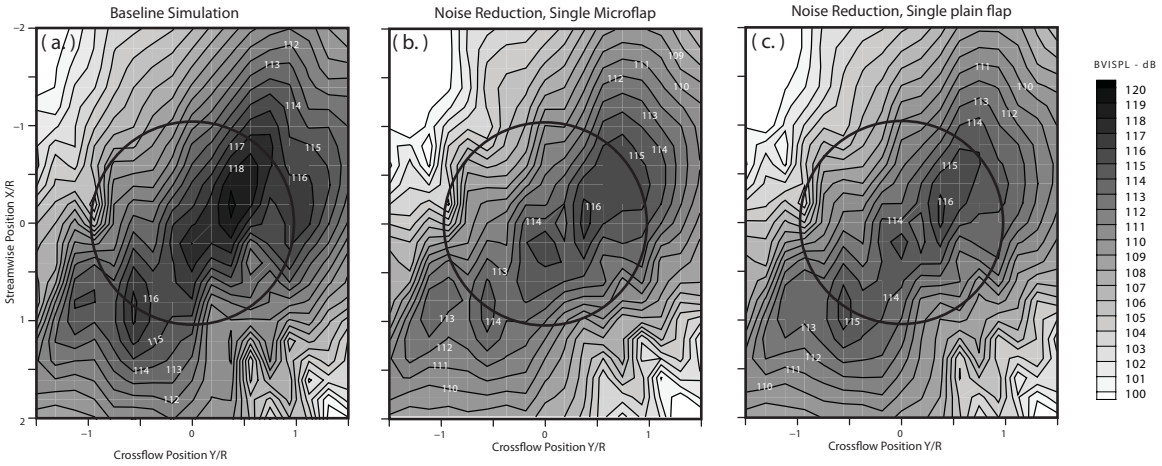

Figure 7.21: Comparison of the noise levels computed on the carpet plane during active noise control using a single microflap and a single plain flap.

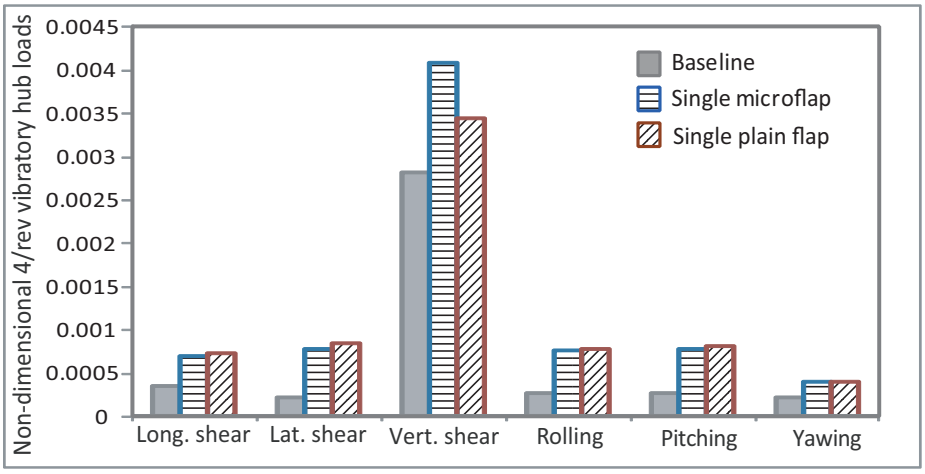

Figure 7.22: Comparison of the vibration levels computed during active noise control using a single microflap and a single plain flap.

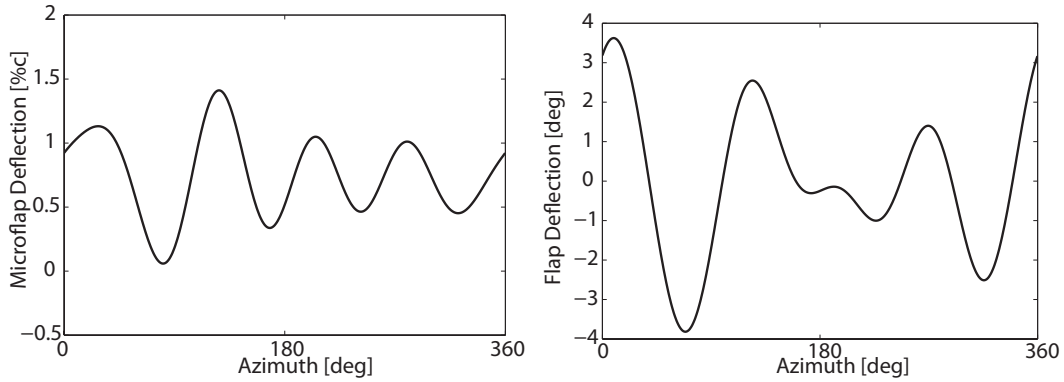

(a) Single microflap (b) Single plain flap

Figure 7.23: Deflection histories over one complete revolution for the single microflap and the single plain flap configurations during active noise reduction.

7.6 Simultaneous BVI Noise and Vibration Reduction

As indicated by the results presented in the preceding sections, BVI noise reduction using microflaps is often accompanied by increased vibration levels and vice versa, a phenomenon similar to that encountered with other active control implementations. The feasibility of reducing both BVI noise and vibrations simultaneously using microflaps is explored in this section. The adaptive HHC algorithm is implemented for simultaneous noise and vibration reduction using the output weighting matrix, $\mathbf{Q}_{\text{SR}}$ described in Section 6.6

$$\mathbf{Q}_{\text{SR}} = \begin{bmatrix} (W_\alpha) \cdot [\mathbf{Q}_{\text{VR}}] & 0 \\ 0 & (1 - W_\alpha) \cdot [\mathbf{Q}_{\text{NR}}] \end{bmatrix}, \tag{7.2}$$

where W_α can be used to adjust the relative weighting between noise and vibrations. For $W_\alpha = 1$, full control effort is focused on vibration reduction, where as $W_\alpha = 0$ corresponds to exclusive noise reduction. Simulations were performed us-

Table 7.6: Simultaneous vibration and noise reduction using the dual microflap configuration.

W_α	% change in 4/rev vertical hub shear	dB change in right rear skid noise
0.1	16	-3.0
0.2	14	-2.5
0.3	-2	-2.4
0.4	-2	-2.3
0.5	-20	-1.8
0.6	-34	-1.6
0.7	-31	-1.3
0.8	-38	-0.3
0.9	-44	0.8

ing the dual and five-microflap configurations over a range of W_α values. Changes in the 4/rev vertical hub shear and the noise levels at the right rear skid location corresponding to various W_α values are given in Table 7.6 for the dual microflap configuration. The $W_\alpha = 0.6$ value yields the best combination of reductions in the vertical hub shear and the noise levels representing a Pareto optimal location. Similar information is provided for the five-microflap configuration in Table 7.7, where the best combination of reductions in the vertical hub shear and the noise levels is found at $W_\alpha = 0.7$. Simultaneous reduction is performed using the dual and five microflap configurations for the selected W_α values.

Noise levels computed during simultaneous vibration and noise reduction using dual and five microflap configurations are compared to the baseline noise levels in Fig. 7.24. The dual microflap configuration yields up to 2 dB noise reduction on both the advancing and retreating sides. The five microflap configuration yields up to 3 dB noise reduction on the advancing side and up to 2 dB on the retreating

Table 7.7: Simultaneous vibration and noise reduction using the five microflap configuration.

W_α	% change in 4/rev vertical hub shear	dB change in right rear skid noise
0.1	55	-6.4
0.2	55	-6.2
0.3	42	-6.2
0.4	-2	-5.7
0.5	-16	-4.8
0.6	-25	-3.6
0.7	-55	-2.5
0.8	-56	-2.1
0.9	-64	-1.7

side. The corresponding vibration levels are compared to the baseline levels in Fig. 7.25. The dual and five microflap configurations yield 34% and 55% reduction in the 4/rev vertical hub shear, respectively. This clearly demonstrates that simultaneous reduction of vibrations and noise is feasible using microflaps. Microflap deflection histories over one complete revolution during simultaneous reduction using the dual and five microflap configurations are shown in Fig. 7.26. Microflap numbering for the five microflap configuration begins from the inboard microflap, i.e. 'Flap1' in the legend refers to the inboard microflap and 'Flap5' refers to the outboard microflap. It is interesting to note that the deflection histories for the outboard microflaps in both the configurations are predominantly 4/rev.

7.6.1 Comparison to a Plain Flap

Simultaneous vibration and noise reduction capabilities of the dual microflap configuration are compared to those of the dual plain flap configuration. The noise

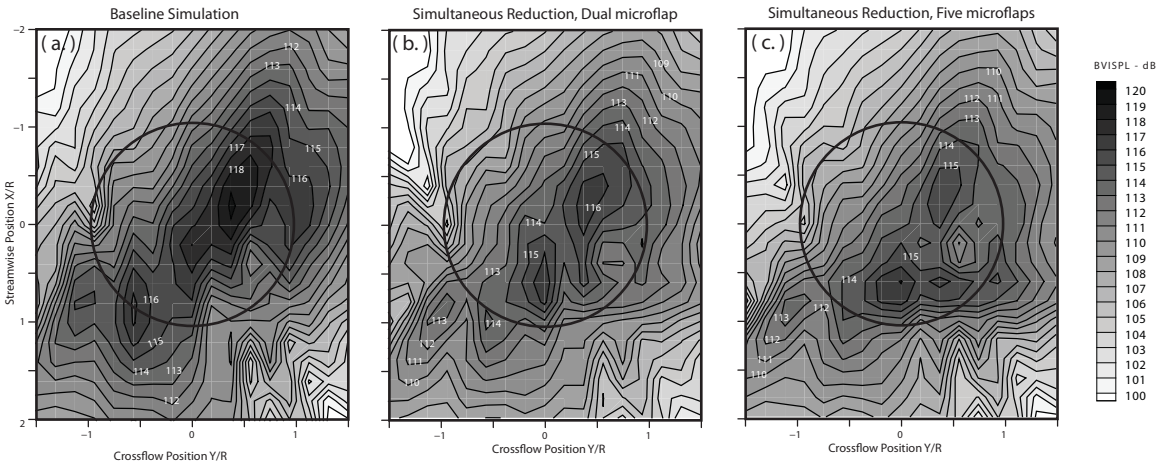

Figure 7.24: Noise levels computed on the carpet plane during simultaneous vibration and noise reduction using microflaps.

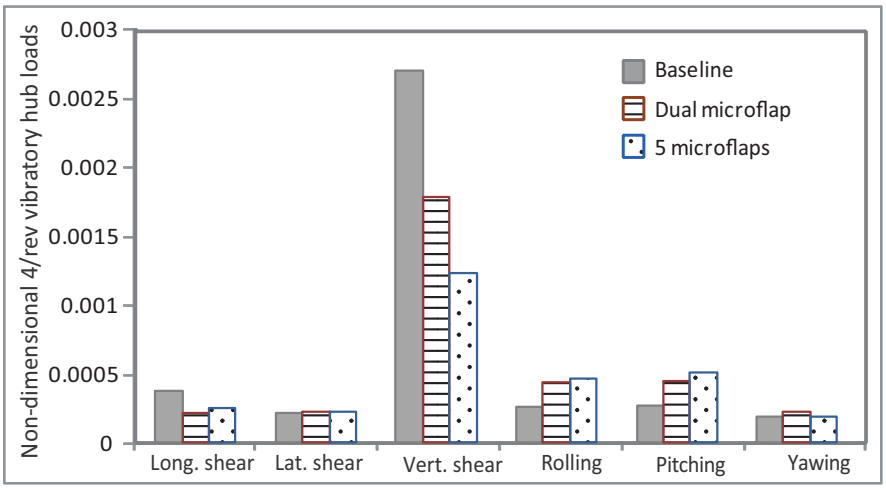

Figure 7.25: Vibration levels computed during simultaneous vibration and noise reduction using microflaps.

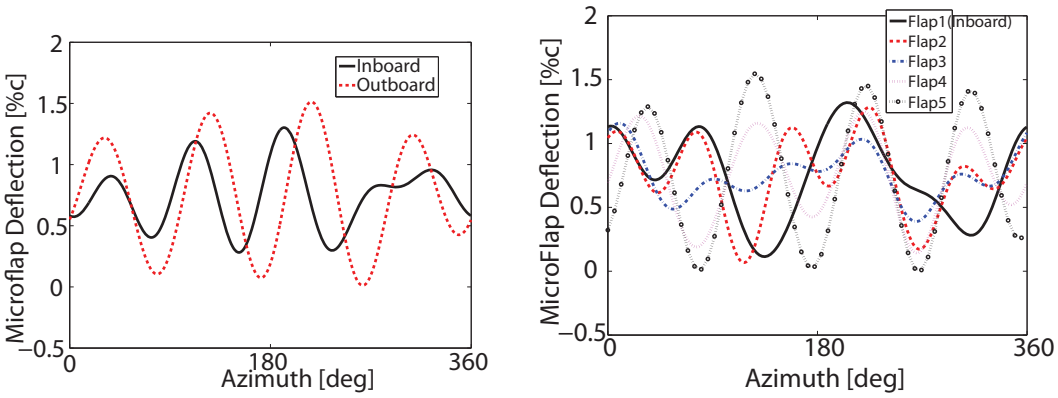

(a) Dual microflap (b) Five microflaps

Figure 7.26: Microflap deflection histories over one complete revolution for the dual and five microflap configurations during simultaneous vibration and noise reduction.

levels computed during simultaneous reduction using dual microflap and the dual plain flap are compared to the baseline levels in Fig. 7.27. On the advancing side, the dual plain flap yields up to 3 dB noise reduction whereas the dual microflap yields up to 2 dB. However, on the retreating side, the dual microflap configuration yields up to 2 dB noise reduction while the dual plain flap shows no effect. The vibration levels computed during simultaneous reduction using dual microflap and dual plain flap configurations are compared in Fig. 7.28. The dual plain flap yields up to 51 % reduction in the 4/rev vertical hub shear compared to 34% by the dual microflap. It is interesting to note that compared to the plain flap, the microflap demonstrates better effectiveness in reducing the noise levels over the entire carpet plane, i.e. both the advancing and the retreating sides, but yields less reduction in vibrations. This observation further illustrates the difficulty in simultaneously reducing vibrations and noise in helicopters. Similar trends were encountered in earlier simultaneous reduction studies conducted using conven-

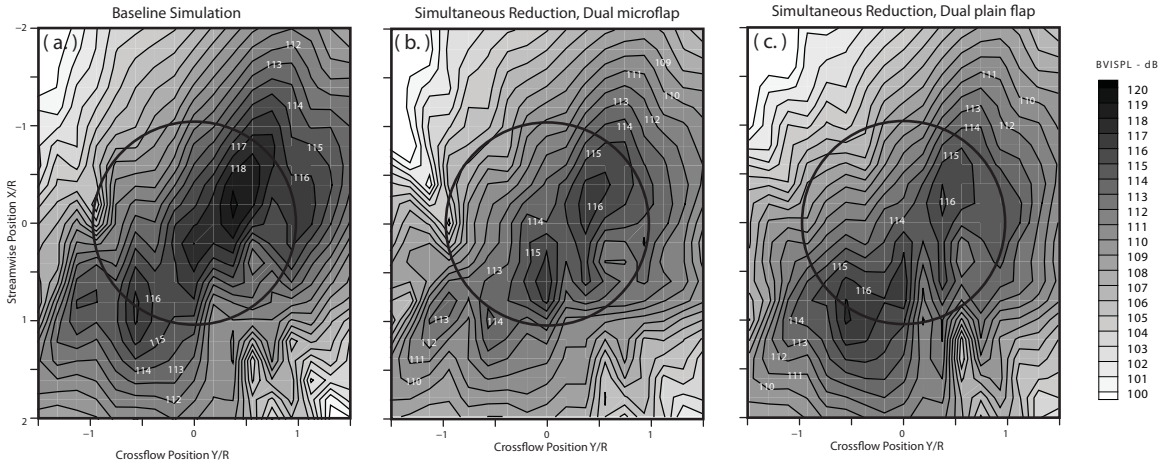

Figure 7.27: Comparison of the noise levels computed on the carpet plane during simultaneous vibration and noise reduction using a dual microflap and a dual plain flap.

tional active flaps [102, 128]. The dual microflap and dual plain flap deflection histories over one completer rotor revolution during simultaneous reduction are shown in Fig. 7.29. The deflection histories for the microflap and the plain flap show resemblance in the overall shape.

7.7 Vibration Reduction at a High Advance Ratio

In this section, results for vibration reduction using the various spanwise microflap configurations are presented for a high speed level cruise flight with $\mu = 0.3$. Vibratory hub loads obtained using the single, dual, and five-microflap configurations are shown in Fig. 7.30. All three configurations considered here produce a substantial amount of vibration reduction, again demonstrating the control authority of the microflap at the cruise flight condition. The single and dual microflap configurations yield similar reduction levels of 92% in the vibration objec-

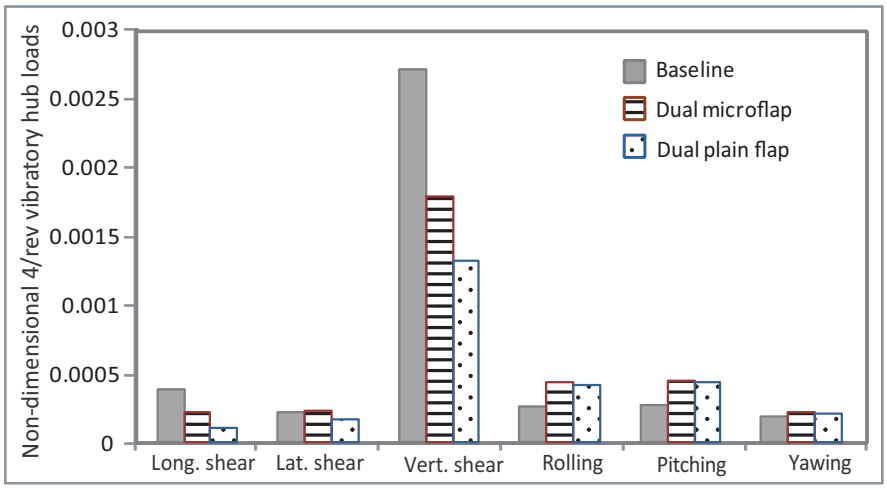

Figure 7.28: Comparison of the vibration levels computed during simultaneous vibration and noise reduction using a dual microflap and a dual plain flap.

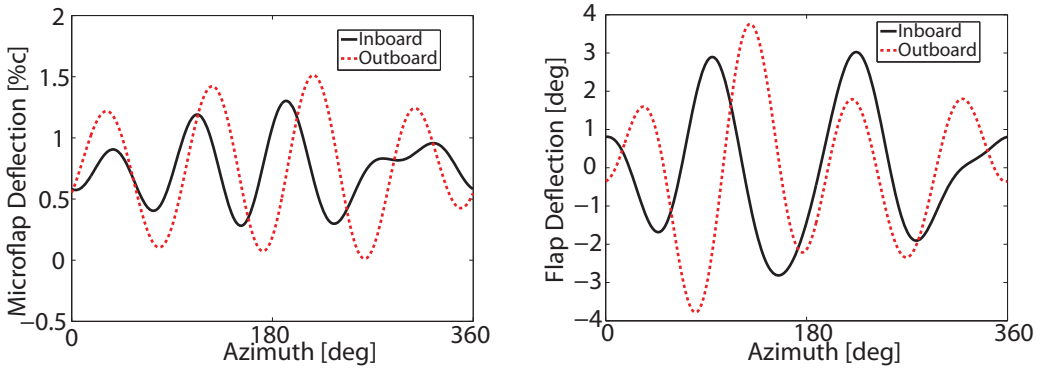

(a) Dual microflap

(b) Dual plain flap

Figure 7.29: Deflection histories over one complete revolution for the dual microflap and the dual plain flap configurations during simultaneous vibration and noise reduction.

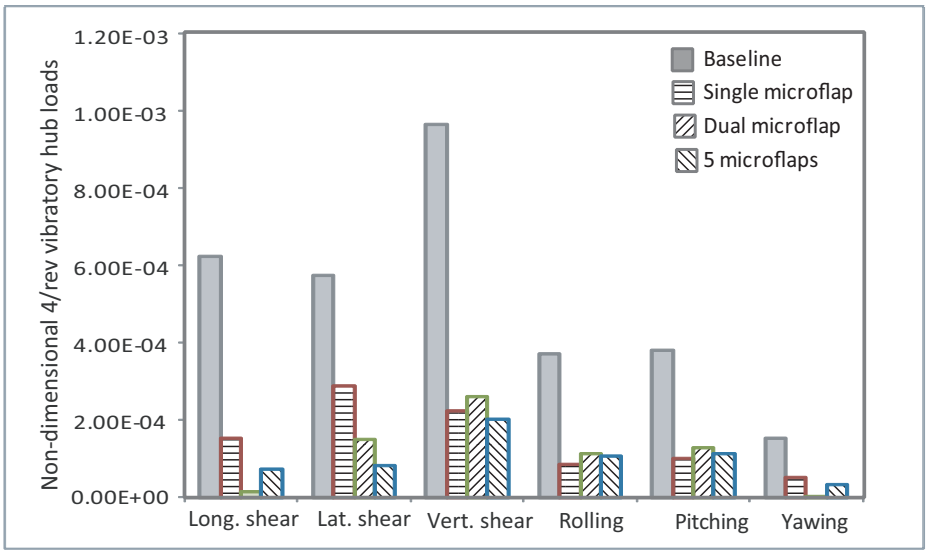

Figure 7.30: Reduction in 4/rev vibratory hub shears and moments obtained using the single, dual, and 5 microflap configurations at a high speed forward flight condition.

tive. The five-microflap configuration also provides a very similar 93% reduction in the overall vibration levels, as can be seen from Fig. 7.30.

The microflap deflection histories for the single and dual microflap configurations over one complete revolution are shown in Figs. 7.31(a) and 7.31(b), respectively. The microflap deflection is restricted between 0%c and 1.5%c.

7.7.1 Comparison to a Plain Flap

Next, the vibration reduction capabilities of the microflap are compared to those of a 20%c trailing-edge plain flap at the high speed forward flight condition. Vibration levels obtained using the single and dual flap configurations of the conventional plain flap and the microflap are shown in Figure 7.32. The single plain flap and the single microflap configurations yield 94% and 92% reduction in the

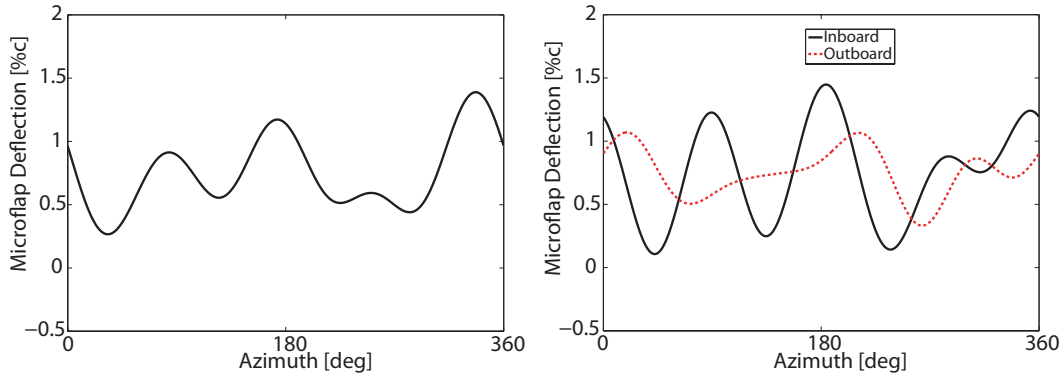

(a) Single microflap (b) Dual microflap

Figure 7.31: Microflap deflection histories over one complete revolution for the single and dual microflap configurations during active vibration reduction at a high speed forward flight condition.

vibration objective, respectively. The dual plain flap and the dual microflap configurations yield 96% and 92% reduction in the vibration objective, respectively. Therefore, the overall vibration reduction levels obtained using the microflaps and conventional plain flaps are similar. It is also important to note that the single and dual microflap configurations incur 3.4% and 5.3% performance penalties as evidenced by the increased rotor power requirement, during active vibration reduction at the cruise condition. By comparison, the corresponding plain flap configurations incur less than 1% performance penalty during vibration reduction. This significant penalty in rotor performance during vibration reduction is a result of higher sectional drag incurred by the microflaps during its deployment.

The plain flap deflection histories for the single and dual plain flap configurations over one complete revolution are shown in Figures 7.33(a) and 7.33(b), respectively. The angular deflection of the plain flap is restricted to $\pm 4^{\circ}$ as practical saturation limits. The plain flap deflection histories display a notable resemblance

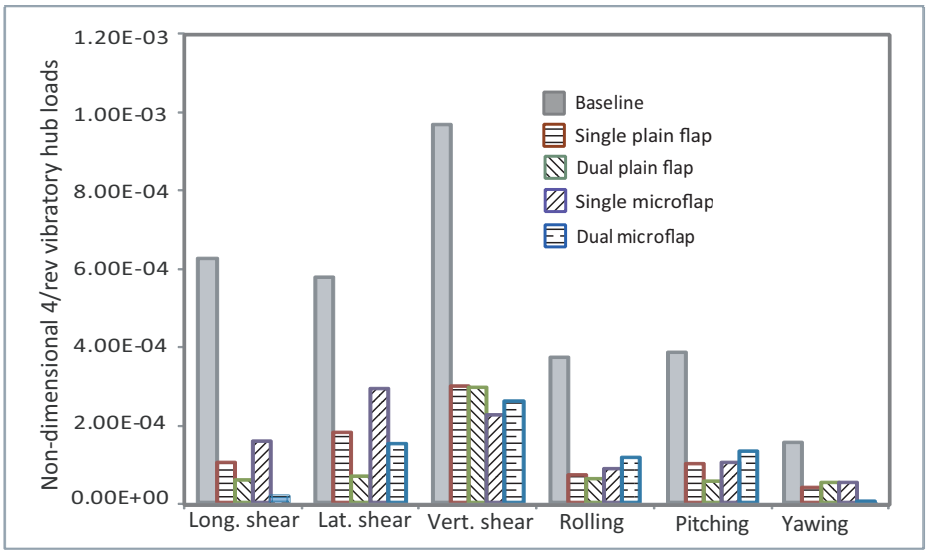

Figure 7.32: Reduction in 4/rev vibratory hub shears and moments obtained using the single and dual flap configurations of the 20%c trailing-edge plain flap and the 1.5%c microflap at a high speed forward flight condition.

to the microflap deflection histories (see Fig. 7.31), where the peaks and troughs of the deflections occur at approximately same azimuthal locations.

7.8 Performance Enhancement

In this section, the effect of microflaps on rotorcraft performance at a high speed flight condition with $\mu = 0.30$ is examined. As was mentioned earlier, vibration reduction using microflaps at a high speed forward flight condition results in a significant performance penalty. To further examine the effect of microflaps on rotor performance, closed loop control studies were conducted with a combined objective function consisting of both vibratory loads and rotor power. As was described

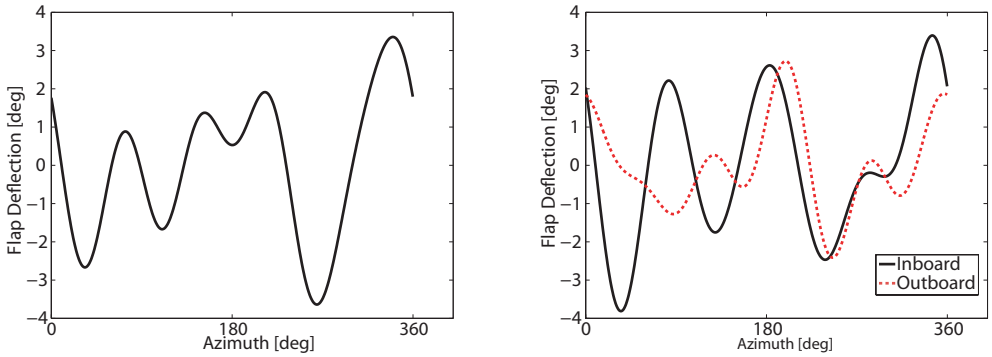

(a) Single plain flap (b) Dual plain flap

Figure 7.33: Flap deflection histories over one complete revolution for the single and dual plain flap configurations during active vibration reduction at a high speed forward flight condition..

in Chapter VI, the combined weighting matrix is given as

$$\mathbf{Q}_{\text{PV}} = \begin{bmatrix} (W_\alpha) \cdot [\mathbf{Q}_{\text{VR}}] & 0 \\ 0 & (1 - W_\alpha) \cdot [\mathbf{Q}_{\text{PWR}}] \end{bmatrix}. \tag{7.3}$$

where the parameter W_α is used to vary the relative weighting between the vibratory loads and the rotor power. As can be noted from Eq. 6.41, all the vibratory hub shears and moments are penalized equally. The single microflap configuration is used and it is employed for control of the combined vibration and power objective. Changes in vibration levels and the corresponding changes in the rotor power obtained for various values of W_α are listed in Table 7.8. The rotor power consumption is reduced by 0.57% and 1.2% for W_α values of 0.3 and 0.25, respectively. The reduced power requirement indicates that the microflap has potential for performance enhancement. However, the reductions in rotor power consumption are also accompanied by increases in the 4/rev vibratory hub loads by 78% and 171%,

Table 7.8: Effect of a single microflap on the vibratory hub loads and the rotor performance using a combined objective function.

W_α	0.45	0.4	0.35	0.3	0.25
Baseline power	0.00519928	0.00519928	0.00519928	0.00519928	0.00519928
Power after active control	0.0052977	0.00527816	0.00521893	0.00516958	0.00513685
% change in Power	1.89	1.51	0.37	-0.57	-1.2
% change in Vibrations	-33	-8	8	78	171

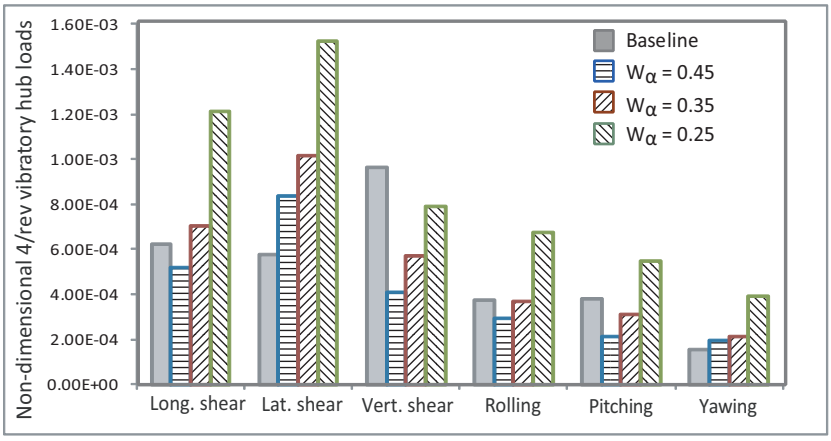

Figure 7.34: Effect of a single microflap on the vibratory hub loads during active control of vibrations and rotor power consumption using a combined objective function.

respectively, as shown in the table. The vibratory hub loads corresponding to several values of W_α are shown in Fig. 7.34. The longitudinal and lateral shear forces are significantly increased during performance enhancement, particularly for the relative weight $W_\alpha = 0.25$. Also note that for the single microflap configuration and the relative weighting range considered here, simultaneous vibration reduction and performance enhancement was not found.

CHAPTER VIII

ACTUATOR SATURATION IN INDIVIDUAL BLADE CONTROL

The actuation devices used to operate the ACFs have limited torque capacities and hence are subject to amplitude saturation. Similarly for microflaps, the thickness of the airfoil imposes a limitation on the size of the microflap thus constraining the maximum deflection of the microflap. Saturation introduces nonlinearities into a linear system thus forcing it to operate in a mode for which it was not designed [10]. Therefore, it is important to consider the effects of actuator saturation in the various active control approaches since ignoring them results in a significant degradation in the performance of the control-system. The effect of actuator saturation on the performance of the HHC algorithm has not been extensively studied. A preliminary investigation of the effect of actuator saturation on the vibration reduction capabilities of the HHC algorithm using a conventional plain flap was performed in Ref. 28. Three different approaches to constraining the flap deflections were considered. Two approaches which involve an *a posteriori* modification

of the optimal control input obtained from the HHC algorithm are: 1) *truncation* (TR): simply clipping the optimal flap deflection whenever it exceeds the saturation limits, 2) *scaling* (SC): uniformly scaling down the optimal flap deflection such that it never exceeds the saturation limits. A third approach referred to as the *auto-weighting* (AW) approach which involves iteratively adjusting the control weighting matrix in the HHC algorithm such that flap deflection is properly constrained was presented in Ref. 28. The AW approach also involves an a posteriori design modification to the controller, by modifying the control weighting matrix after obtaining the optimal control input from the HHC algorithm. It was shown that the AW approach produced excellent performance by reducing the vibration levels by up to 90%. By comparison, the TR and SC approaches were inconsistent and produced only limited vibration reduction. However, the AW approach has several shortcomings. It is based on a simplistic iterative approach which requires the user to guess a value for the upper bound on the control weighting. Depending on this value, the AW approach can take several iterations to converge, and thus can be computationally expensive. Furthermore, in the case of multiple flaps (or microflaps), the control weighting corresponding to the various control surfaces used in the AW approach is identical. This produces an optimal control input only for one of the control surfaces leaving the others under-utilized.

The shortcomings of the AW approach can be remedied by a new approach based on constrained nonlinear optimization. In this approach, actuator saturation constraints formulated as inequality constraints on the control surface deflection

are combined with the minimization of the quadratic cost function in the HHC algorithm resulting in a constrained nonlinear optimization problem. Unlike the approaches described in Ref. 28, this approach (referred to in this chapter as the *optimization* (OPT) approach) accounts for the presence of saturation nonlinearities in an *a priori* manner involving direct modifications to the HHC algorithm. The OPT approach is elegant and computationally inexpensive compared to the AW approach. It also optimizes the deflections corresponding to the various control surfaces independently thus utilizing all of them to the maximum possible extent. A similar approach to handling actuator saturation using optimization techniques was proposed in Ref. 111 for vibration reduction using a single trailing-edge flap. However, the performance of the approach was never examined in detail. Furthermore, the principal advantages of using the OPT approach over the other approaches is its effectiveness when dealing with multiple control surfaces such as the trailing-edge flaps or the microflaps. Due to the potential of the OPT approach, particularly when implemented for multiple control surfaces, it was decided to compare it in detail to the TR, SC, and AW approaches. The effectiveness of the various actuator saturation approaches for reducing vibrations is compared using the single and dual configurations of a 20%c conventional plain trailing-edge flap and a 1.5%c microflap at two different flight conditions: (a) low-speed descending flight where vibrations are high due to blade-vortex interaction and (b) high-speed cruise conditions. The effectiveness of the various saturation approaches is also compared for BVI noise reduction using a dual microflap configuration.

8.1 Approaches to Handling Actuator Saturation

For the active control simulations conducted in this study, a 1.5%c microflap is used. Similarly, for a conventional trailing-edge flap, the maximum acceptable deflection is set to 4° so as to avoid interactions with the flight control system. Actuator saturation in the HHC algorithm is examined using four different approaches: truncation, scaling, auto-weighting, and optimization.

In the truncation approach, the unconstrained optimal control input is clipped whenever it exceeds the limiting amplitude. The control surface deflection is thus defined as

$$\delta(\psi, \mathbf{u}_k) = \begin{cases} \delta(\psi, \mathbf{u}_k), & |\delta(\psi, \mathbf{u}_k)| < \delta_{\text{limit}} \\ \text{sgn}(\delta(\psi, \mathbf{u}_k)) \cdot \delta_{\text{limit}}, & |\delta(\psi, \mathbf{u}_k)| \geq \delta_{\text{limit}} \end{cases} \tag{8.1}$$

where δ_{limit} is the saturation limit on the control surface deflection.

The scaling approach uniformly scales down the optimal control input as

$$\delta(\psi, \mathbf{u}_k) = \frac{\delta_{\text{limit}}}{\max(|\delta_{\text{opt}}(\psi, \mathbf{u}_k)|)} \cdot \delta_{\text{opt}}(\psi, \mathbf{u}_k), \tag{8.2}$$

where $\delta_{\text{opt}}(\psi, \mathbf{u}_k)$ is the optimal control input obtained using the HHC algorithm. Each harmonic component of the optimal control surface deflection is scaled by a common factor such that the maximum deflection satisfies the saturation limit.

The auto-weighting approach updates the control weighting matrix, $\mathbf{R}$ in Eq. (6.6), in order to restrict the control surface deflection. The control weighting matrix $\mathbf{R}$

penalizes the control amplitude and thus can be used to constrain the optimal control surface deflection. However, the exact value of $\mathbf{R}$ required to constrain the control input amplitude within the saturation limits is not known a priori. Hence, an iterative approach which adjusts the value of $\mathbf{R}$ is used. The weighting matrix $\mathbf{R}$ is represented in a form which allows its modification:

$$\mathbf{R} = c_{wu}\mathbf{I}. \tag{8.3}$$

Note that all harmonic components are equally weighted. If the control surface deflection is overconstrained, the controller reduces the value of c_{wu} and a new optimal control is calculated. If the control surface deflection is underconstrained, the controller increases the value of c_{wu} and a new optimal control is calculated. The modifications to c_{wu} are made in the following manner:

1. Set $c_{wu}^{-} = 0$ and $c_{wu}^{+} = c_{\max}$.

2. Set $c_{wu} = \frac{1}{2}(c_{wu}^{-} + c_{wu}^{+})$

3. Calculate a new optimal control.

   If the flap deflection is properly constrained ($|\delta_{\max}| = \delta_{\text{limit}} \pm 5\%$), end the algorithm.

   If the flap deflection is underconstrained ($|\delta_{\max}| > \delta_{\text{limit}}$), set $c_{wu}^{-} = \frac{1}{2}(c_{wu}^{-} + c_{wu}^{+})$. Return to step 2.

   If the flap deflection is overconstrained ($|\delta_{\max}| < \delta_{\text{limit}}$), set $c_{wu}^{+} = \frac{1}{2}(c_{wu}^{-} + c_{wu}^{+})$. Return to step 2.

The iterative procedure increases or decreases c_{wu} until the optimal control converges to the desired deflection limits within a prescribed tolerance. This approach requires the user to guess the maximum value $c_{\max}$. The $c_{\max}$ value needs to be greater than or equal to the optimum value of c_{wu} that properly constrains the control input. Choosing a very large value for $c_{\max}$ is not recommended since depending on the proximity of $c_{\max}$ to the optimum value of c_{wu}, the AW approach can take several iterations increasing its computational costs. Furthermore, in the case of multiple control surfaces, the number of iterations required for all of them to be properly constrained can be quite high rendering the AW approach impractical.

8.1.1 Actuator saturation using optimization techniques

The deficiencies of the approaches described above can be remedied by using constrained nonlinear optimization to handle actuator saturation in the HHC algorithm. Recall from Eq. (6.6) that the HHC algorithm is based on the minimization of a quadratic cost function

$$J(\mathbf{z}_k, \mathbf{u}_k) = \mathbf{z}_k^{\mathrm{T}} \mathbf{Q}_{\mathbf{z}} \mathbf{z}_k + \mathbf{u}_k^{\mathrm{T}} \mathbf{R} \mathbf{u}_k. \tag{8.4}$$

The saturation limits on the control input can be combined with the minimization of the cost function resulting in a constrained optimization problem:

$$\underset{\mathbf{u}_k}{\text{minimize}} \quad J(\mathbf{z}_k, \mathbf{u}_k) = \mathbf{z}_k^{\mathrm{T}} \mathbf{Q}_{\mathbf{z}} \mathbf{z}_k + \mathbf{u}_k^{\mathrm{T}} \mathbf{R} \mathbf{u}_k, \tag{8.5}$$

$$\text{subject to} \quad |\delta_i(\psi, \mathbf{u}_k)| \leq \delta_{\text{limit}}, \quad i = 1, \ldots, N_\delta \tag{8.6}$$

where N_δ is the total number of control surfaces. The optimization problem represented by Eqs. (8.5) and (8.6) is a typical nonlinear constrained optimization problem with a quadratic objective function and nonlinear inequality constraints, known as the Nonlinear Programming (NP) problem. Unlike the approaches described earlier, this approach involves direct modifications to the HHC algorithm accounting for the presence of saturation nonlinearities in an a priori manner. The resulting optimal control input always satisfies the saturation limits irrespective of the values of $\mathbf{R}$ and $\mathbf{Q}$.

A NP method, Sequential Quadratic Programming (SQP) [40, 114], available as part of the FMINCON tool in MATLAB, is used to solve the optimization problem represented by Eqs. (8.5) and (8.6). The SQP method solves a quadratic programming subproblem at each iteration based on a quadratic approximation of the Lagrangian function. A stand-alone application (a .exe file) capable of performing the optimization is generated using Matlab. Subsequently, this application is invoked from the AVINOR code in order to evaluate the optimum $\mathbf{u}_k$. The stand-alone application requires approximately 1 sec to run on a 2.53 GHz Intel Xeon processor in the case of a single control surface. Note that the nonlinear constraints described

in Eq. (8.6) have to be satisfied for all values of the azimuthal angle $\psi \in [0^\circ \ \ 360^\circ]$. For the numerical implementation, the nonlinear constraints are evaluated and enforced at various values of ψ over the range $[0^\circ \ \ 360^\circ]$.

8.2 Vibration and Noise Reduction Using the Saturation Approaches Discussed

8.2.1 Low-speed results

Vibration reduction studies are conducted using the various saturation approaches described earlier for a heavy BVI descending flight condition with advance ratio $\mu = 0.15$ and descent angle $\alpha_D = 6.5^\circ$. The non-dimensional 4/rev vibratory hub shears and moments obtained using the four different saturation approaches for the single plain flap configuration are compared to the baseline vibration levels in Fig. 8.1. The TR approach yields only a 5% reduction in the vibration objective while causing some of the vibratory hub loads to increase from the baseline levels. The SC approach yields a 38% reduction in the vibration objective. The AW and OPT approaches yield similar performance yielding 76% and 78% reduction in the vibration objective, respectively. However, the OPT approach takes only 10 control updates (80 rotor revolutions) to converge compared to over 100 control updates (800 rotor revolutions) taken by the AW approach. The flap deflection histories over one complete rotor revolution corresponding to the various saturation approaches are shown in Fig. 8.2. The flap deflection histories corresponding to

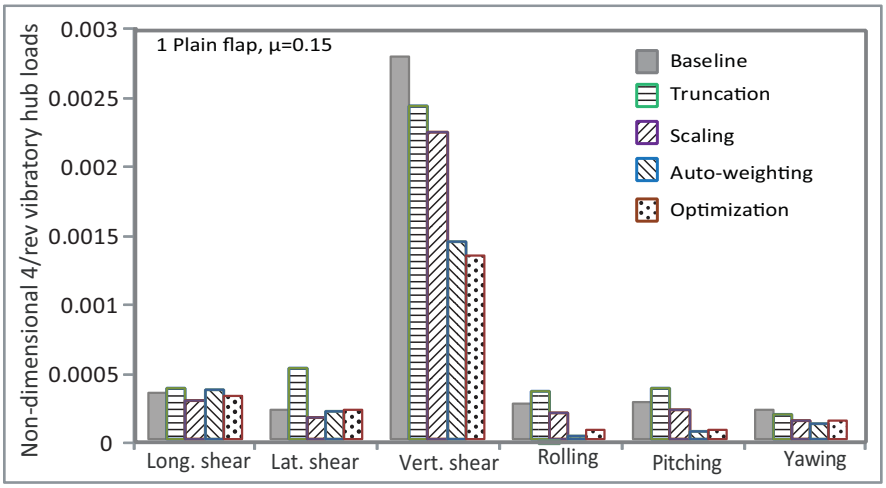

Figure 8.1: Reduction in 4/rev vibratory hub shears and moments obtained using the various saturation approaches for the single plain flap configuration at a heavy BVI descending flight condition with $\mu = 0.15$.

the AW and OPT approaches show similarities in the azimuthal locations of the peaks and troughs. However, the maximum flap deflection obtained using the OPT approach is closer to the saturation limit thus utilizing the flap to the maximum possible degree. This results from the fact that a small tolerance, typically of the order of 10^{-6}, is used on the constraint violation in the OPT approach.

The 4/rev vibratory hub loads obtained using the dual plain flap configuration are compared to the baseline levels in Fig. 8.3. The TR and SC approaches yield 81% and 57% reduction in the vibration objective, respectively. The AW approach yields 95% reduction whereas the OPT approach yields the best performance with a 98% reduction in the vibration objective. Significantly better performance obtained using the OPT approach is evident in the vertical shear component. The inboard and outboard flap deflection histories corresponding to the various saturation approaches are shown in Fig. 8.4. In the AW approach, the maximum

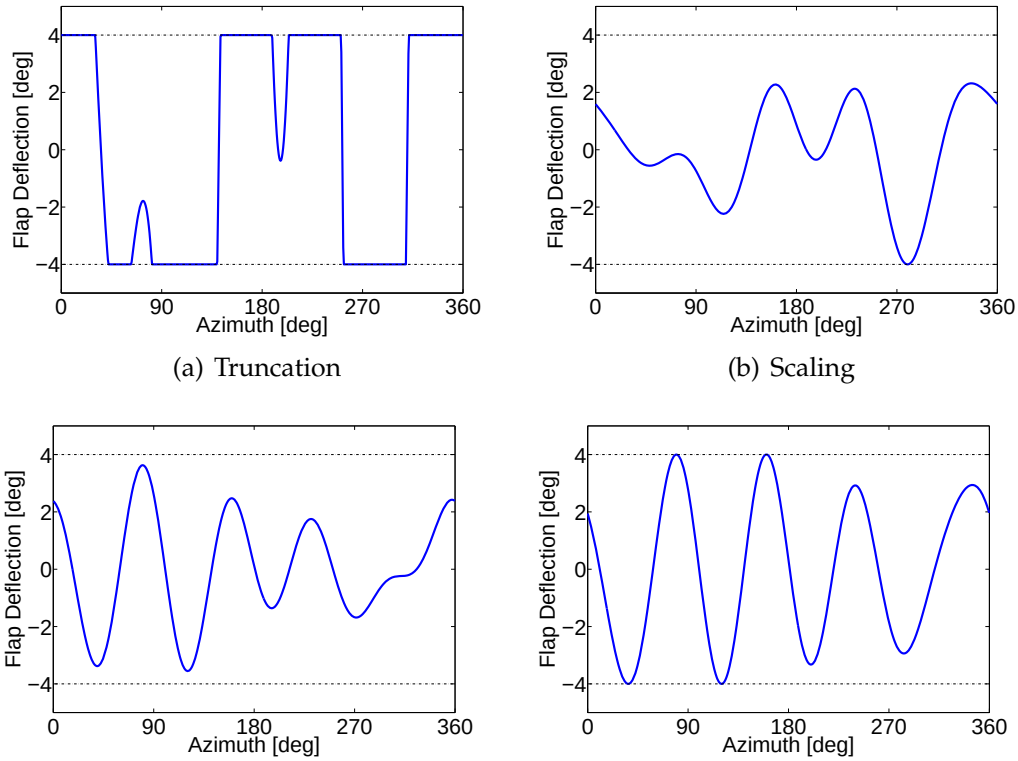

(a) Truncation

(b) Scaling

(c) Auto-weighting

(d) Optimization

Figure 8.2: Single plain flap deflection histories corresponding to the various saturation approaches at a heavy BVI descending flight condition with $\mu = 0.15$.

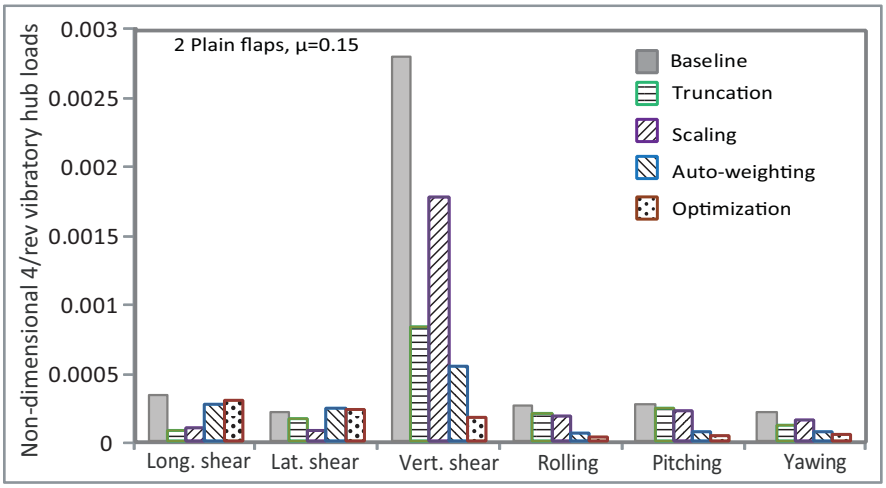

Figure 8.3: Reduction in 4/rev vibratory hub shears and moments obtained using the various saturation approaches for the dual plain flap configuration at a heavy BVI descending flight condition with $\mu = 0.15$.

deflection of the inboard flap is significantly less than the saturation limit. This is primarily because the same control weighting (c_{wu} in Eq. (8.3)) is used for both the flaps which results in the under-utilization of one of the flaps. As is evident from the constraint inequalities in Eq. (8.6), the two flaps are optimized individually in the OPT approach, thus the maximum deflection corresponding to each of the flaps is almost equal to the saturation limit. *This feature of the OPT approach facilitates the use of both the flaps to the maximum possible extent resulting in a better vibration reduction performance*.

Similar comparisons were performed for the single and dual microflap configurations. The 4/rev vibratory hub loads obtained using the various saturation approaches for a single microflap configuration are compared to the baseline levels in Fig. 8.5. The TR approach yields a 64% reduction in the vibration objective whereas the SC approach yields no significant reduction. The AW and OPT ap-

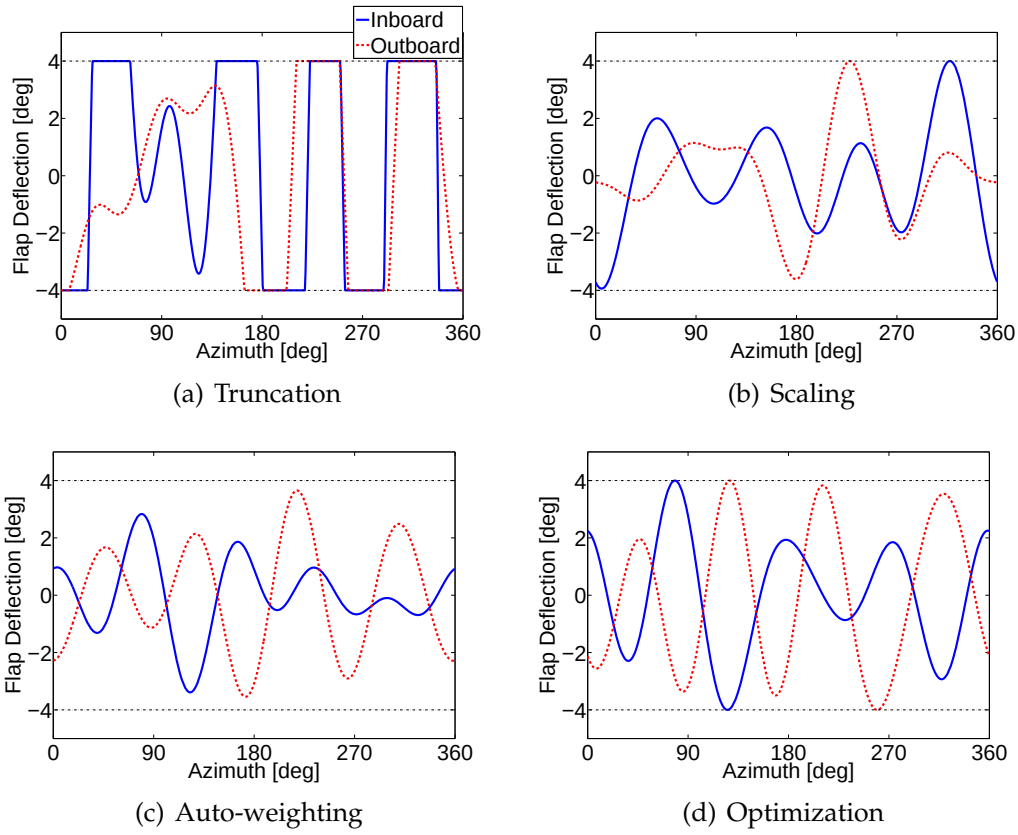

(a) Truncation

(b) Scaling

(c) Auto-weighting

(d) Optimization

Figure 8.4: Dual plain flap deflection histories corresponding to the various saturation approaches at a heavy BVI descending flight condition with $\mu = 0.15$.

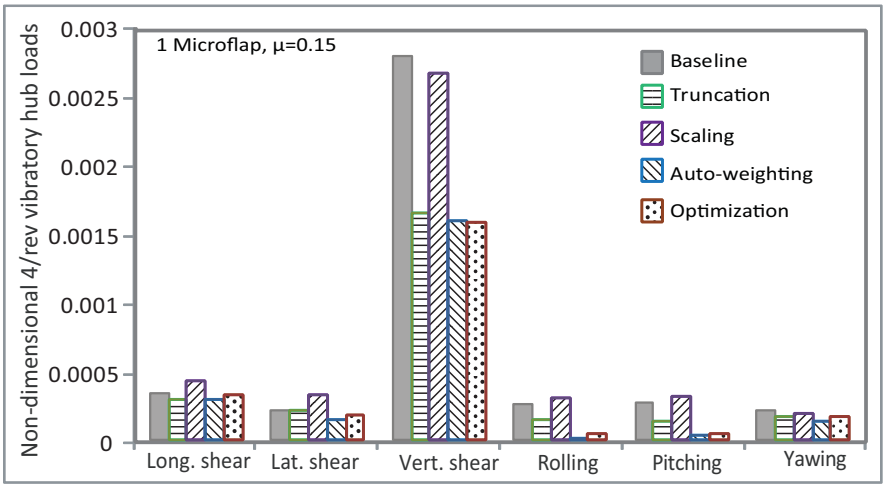

Figure 8.5: Reduction in 4/rev vibratory hub shears and moments obtained using the various saturation approaches for the single microflap configuration at a heavy BVI descending flight condition with $\mu = 0.15$.

proaches yield similar performance with 71% and 70% reductions in the vibration objective, respectively. The flap deflection histories corresponding to the various approaches are shown in Fig. 8.6 for one complete rotor revolution. The flap deflection histories obtained from the SC, AW, and OPT approaches show similarities in the azimuthal locations of the peaks and troughs.

The 4/rev vibratory hub loads obtained using the various saturation approaches for the dual microflap configuration are compared in Fig. 8.7. The TR and SC approaches yield marginal performance with 13% and 11% reductions in the vibration objective, respectively. The AW approach reduces the vibration objective by 88% whereas the OPT approach yields the best performance with 97% reduction in the vibration objective. The inboard and outboard flap deflection histories corresponding to the various saturation approaches are shown in Fig. 8.8. As in the case of the plain flaps, the AW approach under-utilizes the inboard control surface

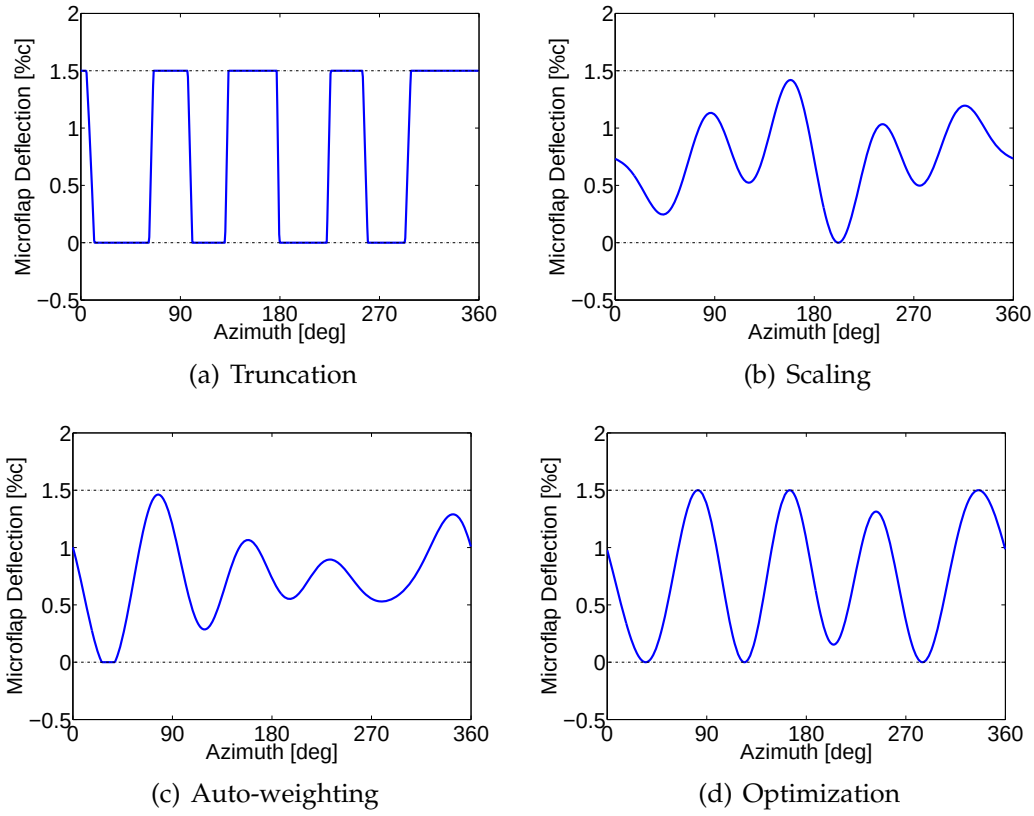

(a) Truncation

(b) Scaling

(c) Auto-weighting

(d) Optimization

Figure 8.6: Single microflap deflection histories corresponding to the various saturation approaches at a heavy BVI descending flight condition with $\mu = 0.15$.

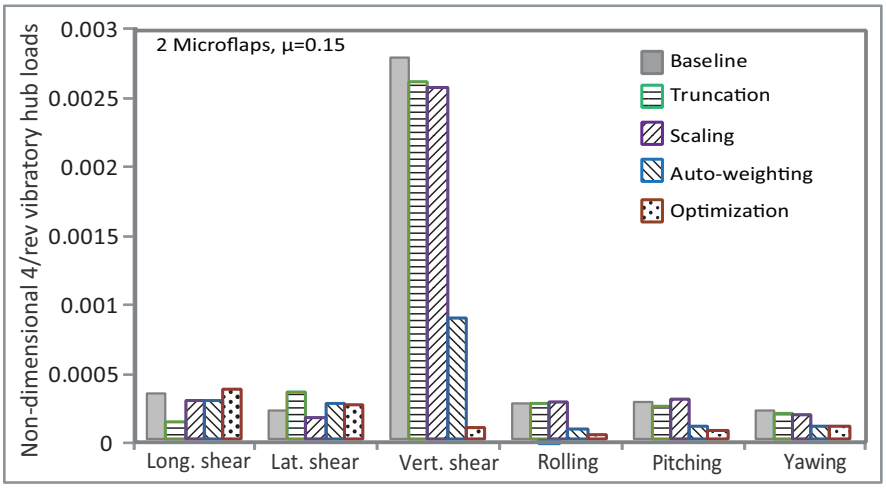

Figure 8.7: Reduction in 4/rev vibratory hub shears and moments obtained using the various saturation approaches for the dual microflap configuration at a heavy BVI descending flight condition with $\mu = 0.15$.

whereas the OPT approach utilizes both the control surfaces to the fullest possible extent resulting in a significantly better vibration reduction performance.

The different saturation approaches were also compared in terms of their BVI noise reduction capabilities using the dual microflap configuration. Noise levels computed on the carpet plane (depicted in Fig. 7.1) during active noise reduction using the different saturation approaches are compared to the baseline noise levels in Fig. 8.9. The TR and SC approaches yield similar performance with approximately 1 dB noise reduction on the advancing side and up to 2 dB reduction on the retreating side of the rotor disk. By contrast, the AW and OPT approaches yield significantly better performance with 4 dB noise reduction on both the advancing and the retreating sides of the rotor disk. The inboard and outboard microflap deflection histories corresponding to the various saturation approaches are shown in Fig. 8.10.

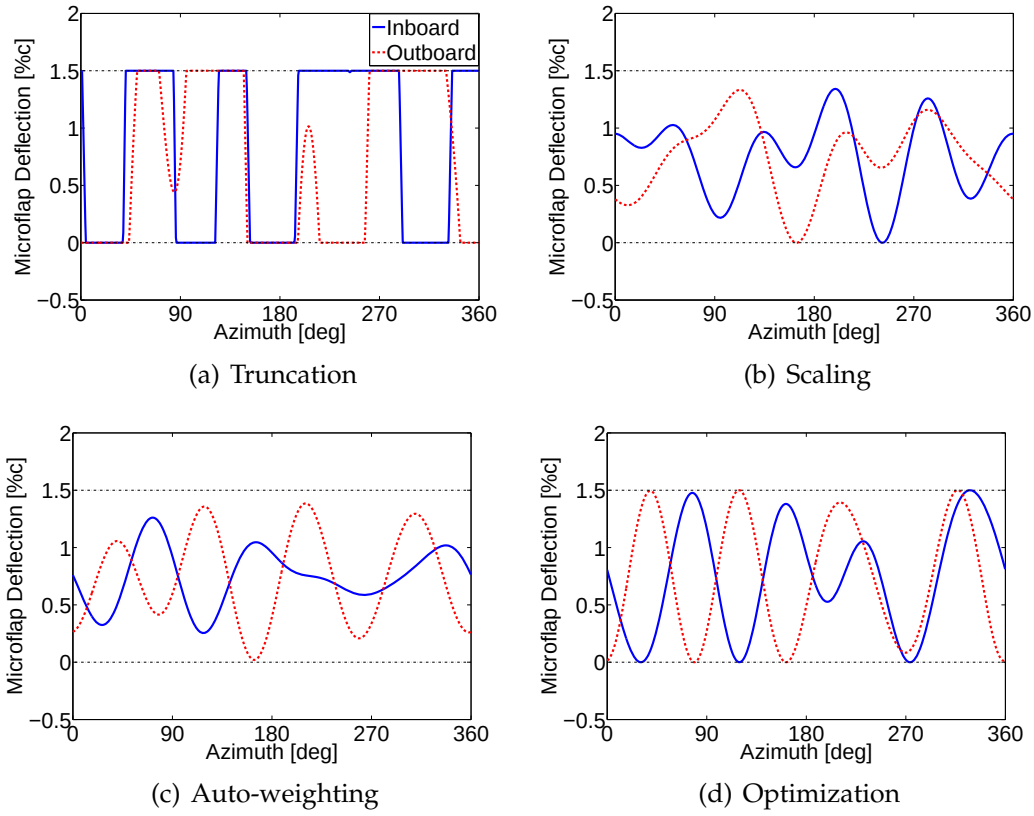

(a) Truncation

(b) Scaling

(c) Auto-weighting

(d) Optimization

Figure 8.8: Dual microflap deflection histories corresponding to the various saturation approaches at a heavy BVI descending flight condition with $\mu = 0.15$.

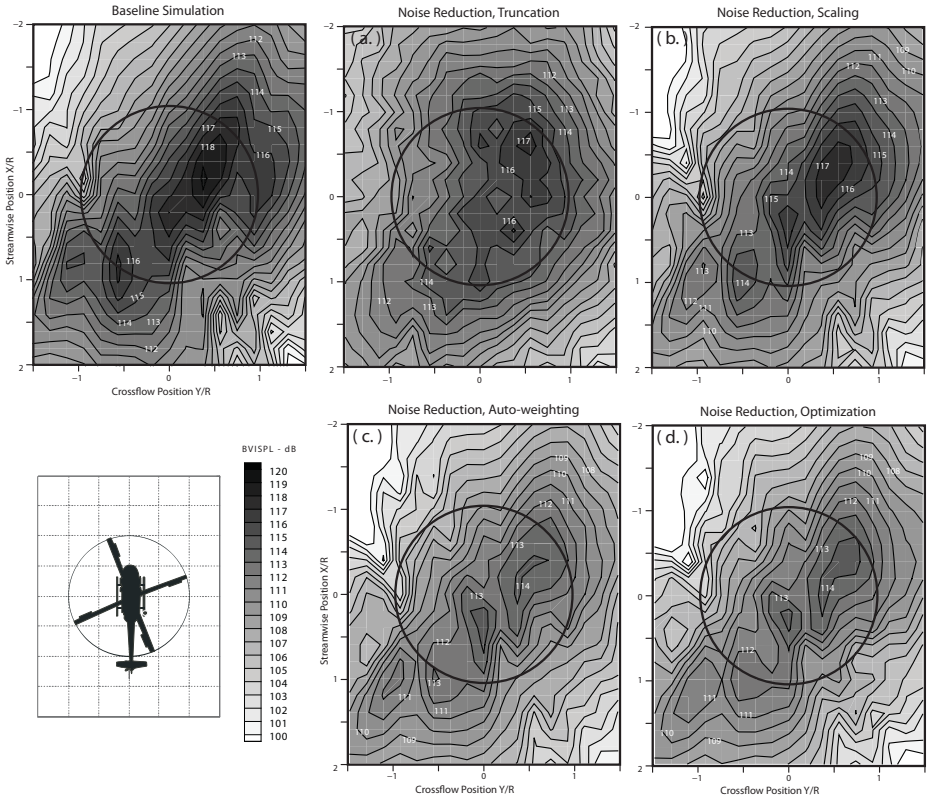

Figure 8.9: Reduction in noise levels obtained using the various saturation approaches for the dual microflap configuration at a heavy BVI descending flight condition with $\mu = 0.15$.

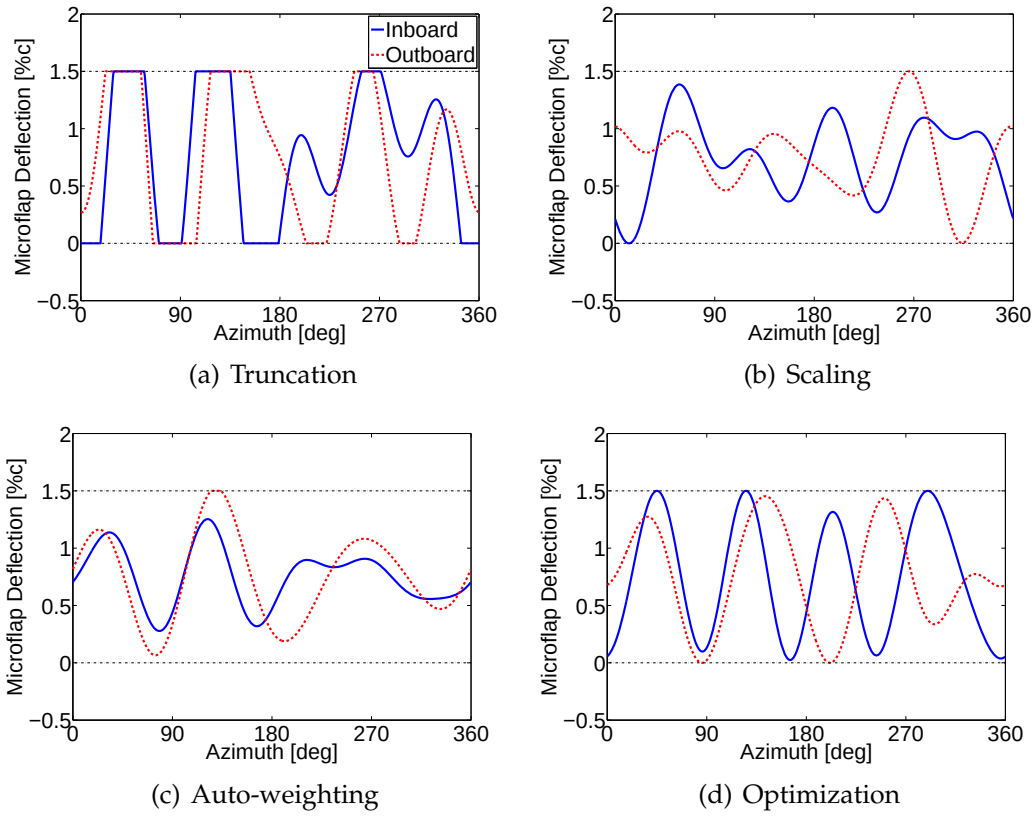

(a) Truncation

(b) Scaling

(c) Auto-weighting

(d) Optimization

Figure 8.10: Dual microflap deflection histories corresponding to the various saturation approaches during active noise reduction at a heavy BVI descending flight condition with $\mu = 0.15$.

8.2.2 High-speed Results

Results of the vibration reduction studies conducted using the various saturation approaches at a high speed level flight condition with $\mu = 0.3$ and weight coefficient $C_{\mathrm{W}} = 0.005$ are presented in this section. The 4/rev vibratory hub loads obtained using the various saturation approaches are compared to the baseline levels in Fig. 8.11. The TR and SC approaches yield 82% and 71% reduction in the vibration objective, respectively. By comparison, the AW and OPT approaches yield excellent performance reducing the vibration objective by 93% and 97%, respectively. The deflection time histories corresponding to the various saturation approaches over one rotor revolution are shown in Fig. 8.12. A relatively good performance obtained from the TR approach can be attributed to the fact that only a small portion of the flap deflection shown in Fig. 8.12(a) is being truncated. The flap deflection histories corresponding to the SC, AW, and OPT approaches show a qualitative resemblance with similar azimuthal locations for the peaks and troughs.

The vibratory hub loads obtained using the various saturation approaches for the dual plain flap configuration are shown in Fig. 8.13. The TR approach causes an increase in the longitudinal and lateral shears and yields no significant reduction in the vibration objective. The SC approach reduces the vibration objective by 62% whereas the AW and the OPT approaches yield exceptional performance with 95% and 99% reductions in the vibration objective, respectively. The inboard and outboard flap deflection time histories corresponding to the various approaches are shown in Fig. 8.14. In the TR approach, significant portions of the inboard and

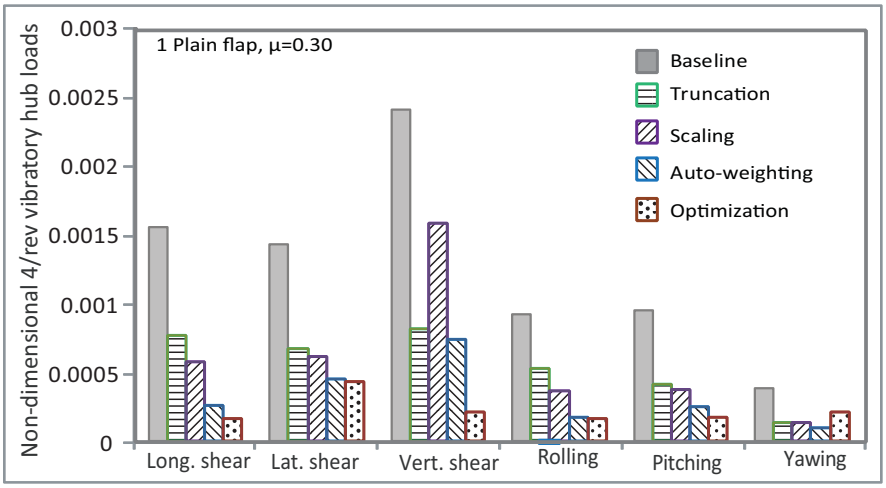

Figure 8.11: Reduction in 4/rev vibratory hub shears and moments obtained using the various saturation approaches for the single plain flap configuration at a high-speed flight condition with $\mu = 0.3$.

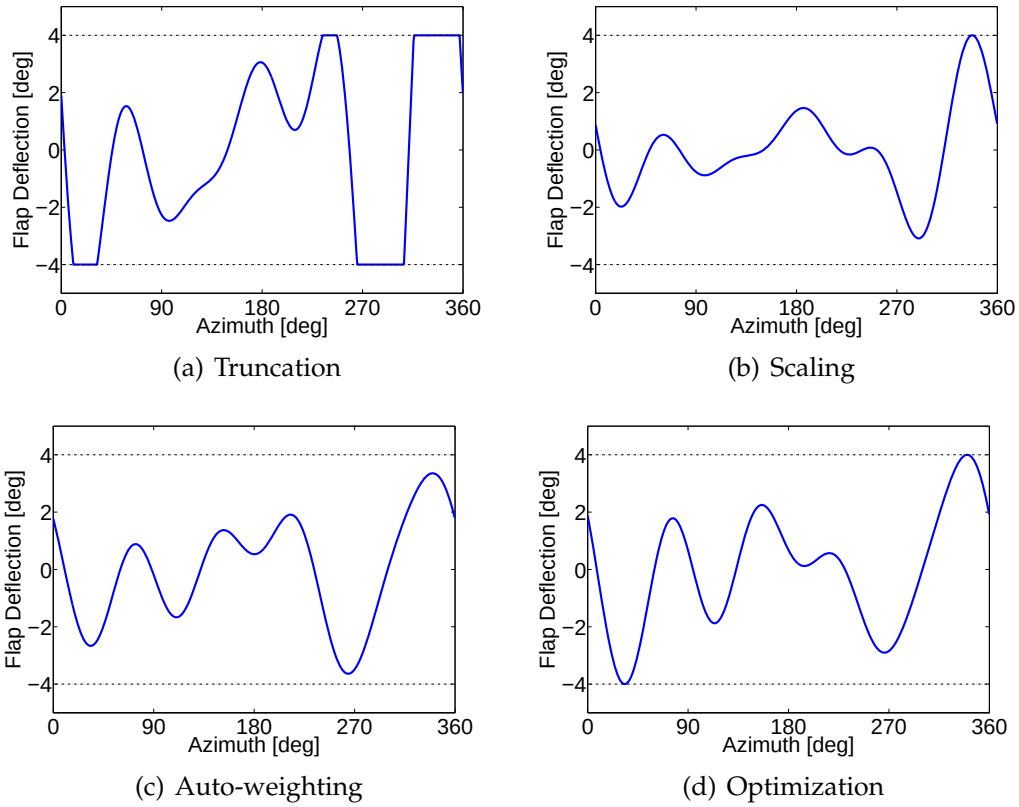

(a) Truncation

(b) Scaling

(c) Auto-weighting

(d) Optimization

Figure 8.12: Single plain flap deflection histories corresponding to the various saturation approaches at a high-speed flight condition with $\mu = 0.3$.

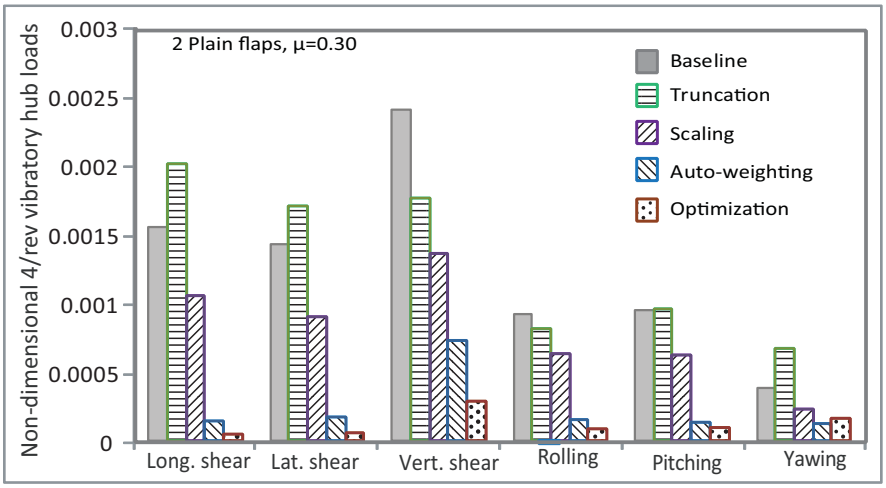

Figure 8.13: Reduction in 4/rev vibratory hub shears and moments obtained using the various saturation approaches for the dual plain flap configuration at a high-speed flight condition with $\mu = 0.3$.

outboard flap deflections are truncated, as shown in Fig. 8.14(a), resulting in its poor performance. The outboard flap is significantly under-utilized by the AW approach, shown in Fig. 8.14(c), whereas the OPT approach utilizes both the flaps to the maximum possible extent.

Similar comparisons are performed using single and dual microflap configurations as well. The 4/rev vibratory hub loads acquired from the various saturation approaches are compared in Fig. 8.15 for the single microflap configuration. The TR approach reduces the vibration objective by 38%. The SC approach causes a significant increase in the vertical hub shear resulting in a 5% increase in the vibration objective. The AW and OPT approaches yield 91% and 94% reductions in the vibration objective, respectively. The microflap deflection time histories corresponding to the various saturation approaches are shown in Fig. 8.16 for one complete rotor revolution. The microflap deflection histories corresponding to the

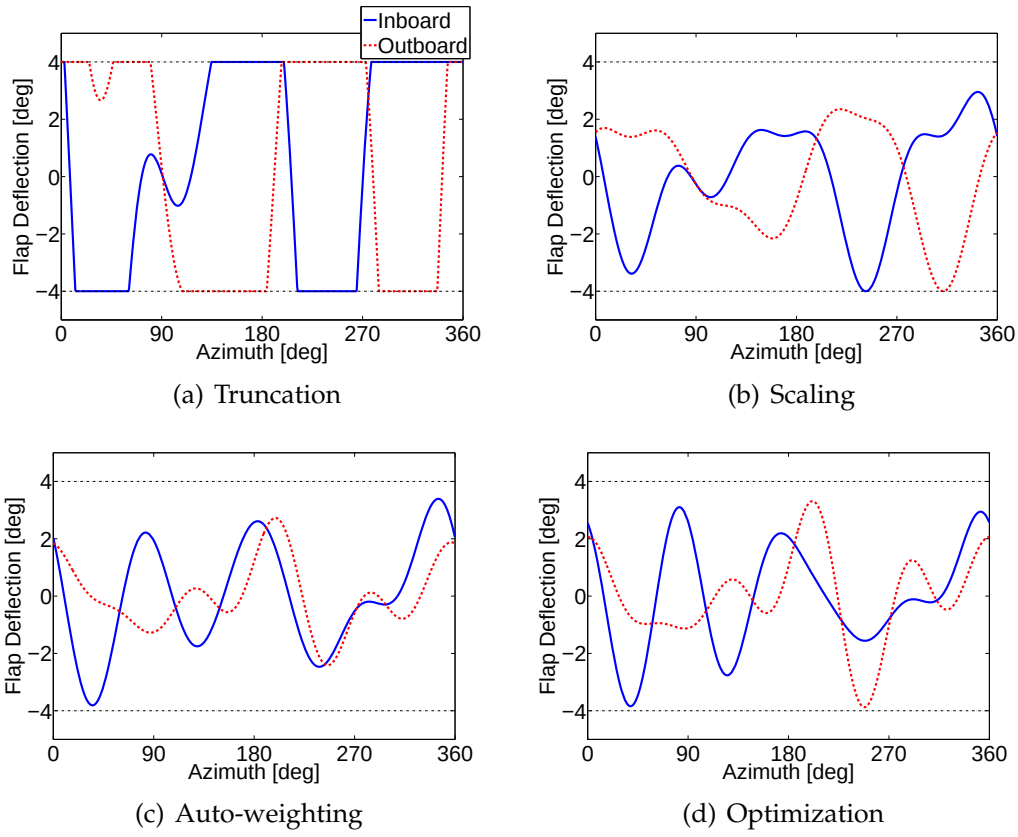

(a) Truncation

(b) Scaling

(c) Auto-weighting

(d) Optimization

Figure 8.14: Dual plain flap deflection histories corresponding to the various saturation approaches at a high-speed flight condition with $\mu = 0.3$.

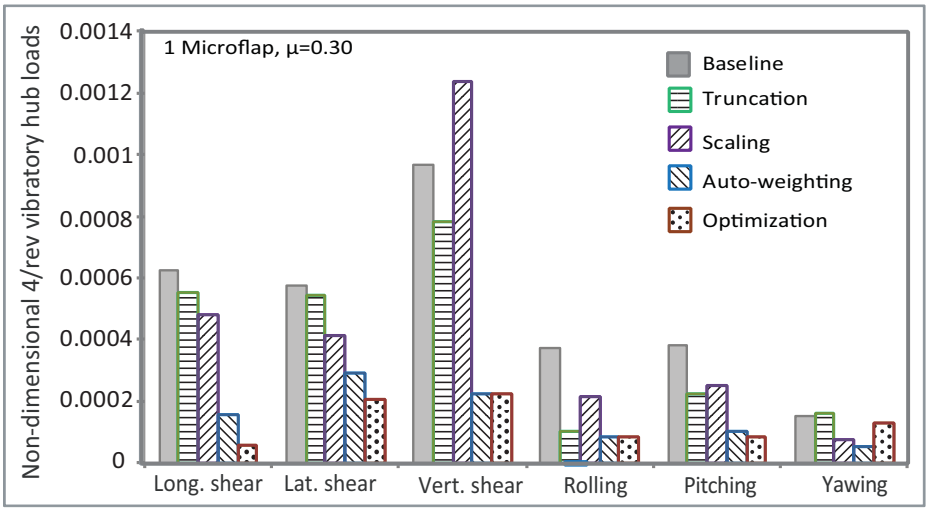

Figure 8.15: Reduction in 4/rev vibratory hub shears and moments obtained using the various saturation approaches for the single microflap configuration at a high-speed flight condition with $\mu = 0.3$.

AW and OPT approaches show similarity in the overall shape.

Vibratory hub loads obtained from the different saturation approaches for the dual microflap configuration are shown in Fig. 8.17. The TR and SC approaches yield 25% and 28% reductions in the vibration objective, respectively. However, both of them cause a small increase in the vertical hub shear. The AW and the OPT approaches perform exceptionally well with 94% and 98% reductions in the vibration objective, respectively. The microflap deflection histories corresponding to the various saturation approaches are shown in Fig. 8.18. The AW approach significantly under-utilizes the outboard microflap whereas the OPT approach utilizes both the microflaps to the maximum possible extent.

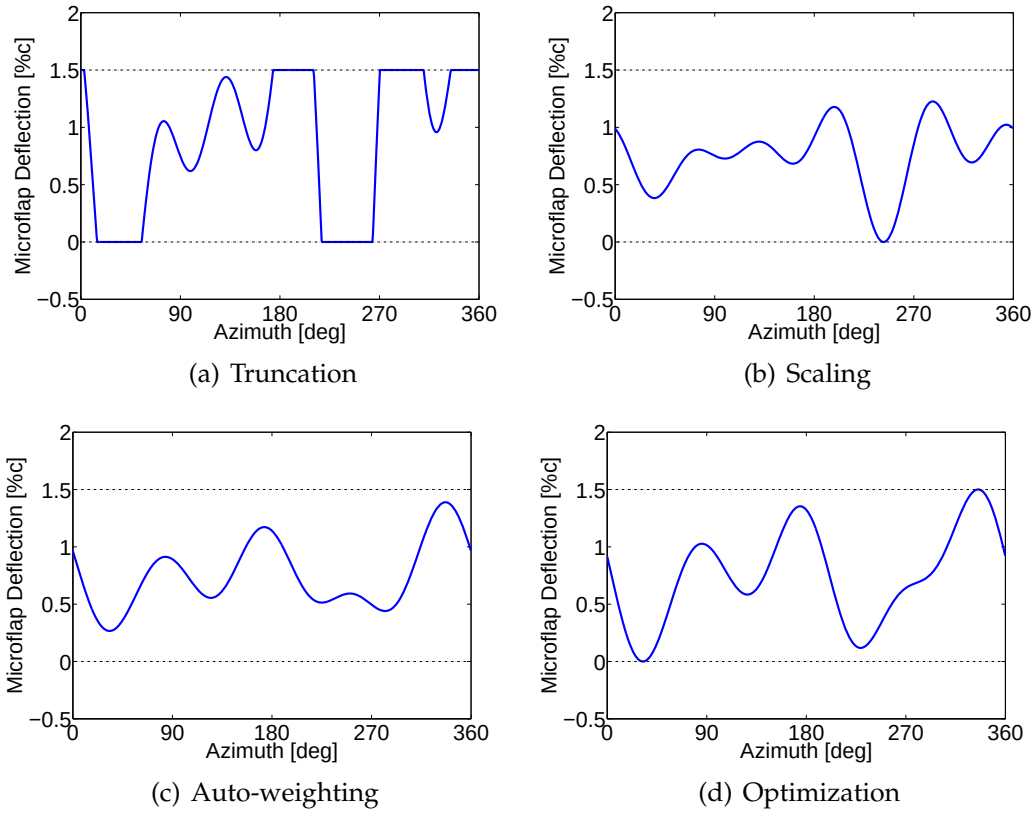

(a) Truncation (b) Scaling

(c) Auto-weighting (d) Optimization

Figure 8.16: Single microflap deflection histories corresponding to the various saturation approaches at a high-speed flight condition with $\mu = 0.3$.

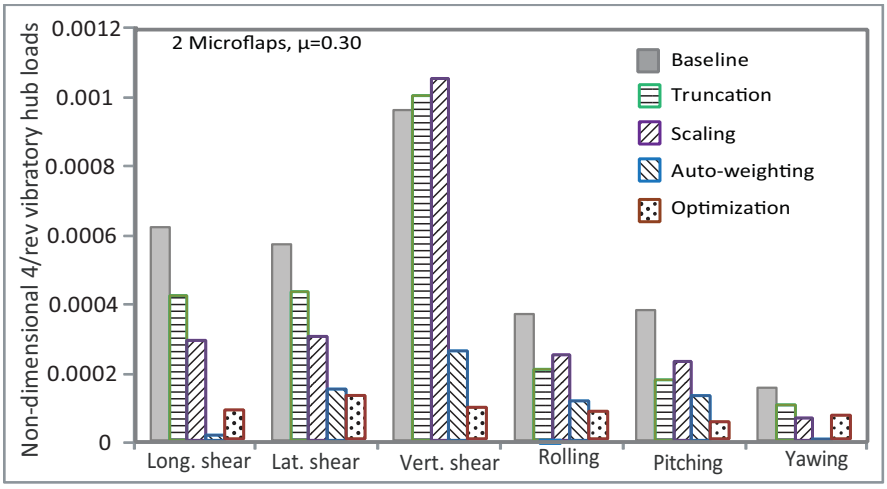

Figure 8.17: Reduction in 4/rev vibratory hub shears and moments obtained using the various saturation approaches for the dual microflap configuration at a high-speed flight condition with $\mu = 0.3$.

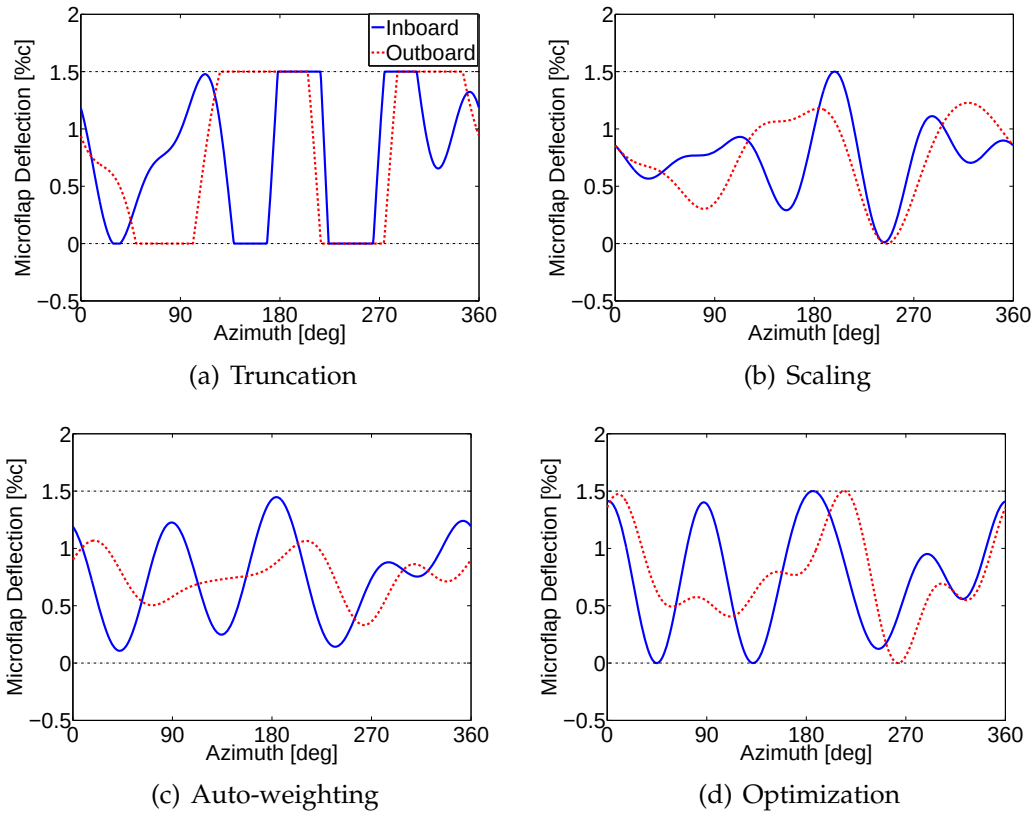

(a) Truncation

(b) Scaling

(c) Auto-weighting

(d) Optimization

Figure 8.18: Dual microflap deflection histories corresponding to the various saturation approaches at a high-speed flight condition with $\mu = 0.3$.

CHAPTER IX

CONCLUSIONS AND RECOMMENDATIONS FOR FUTURE RESEARCH

This study demonstrated the potential of microflaps for noise and vibration reduction on a helicopter rotor using closed-loop control methods. A CFD based reduced order aerodynamic model that can capture the aerodynamic effects of a microflap was developed and incorporated in to a comprehensive rotorcraft simulation code. This comprehensive code, which has the capability to perform aeroelastic and aeroacoustic calculations on various rotor configurations was used to investigate microflap's effectiveness for vibration reduction at various flight conditions and noise reduction under BVI conditions. Simultaneous vibration and noise reduction under BVI conditions was also examined. The effectiveness of the microflap in reducing vibration and noise was compared to that of a 20%c plain trailing-edge flap. Finally, a new approach for dealing with actuator saturation in the HHC algorithm was developed using nonlinear constrained optimization techniques. The vibration reduction performance of this new approach was compared

to the previous approaches.

9.1 Conclusions and New Contributions

The principal conclusions and contributions of this dissertation are summarized below:

1. Effects of a Gurney flap on the aerodynamic characteristics of a NACA0012 airfoil were studied using Reynolds Averaged Navier-Stokes (RANS) CFD computations and the results were compared with experiments. The maximum lift coefficient was approximately 20% higher with the Gurney flap. The Gurney flap also induced a negative pitching moment on the airfoil.

2. The unsteady aerodynamic characteristics of three different microflap configurations were studied using CFD computations. The simulation results indicate that the configuration with sharp trailing-edge yields the best lift-to-drag ratio and the highest pitch-down moment compared to the other configurations and hence was chosen for all the active control studies performed in this thesis.

3. A nonlinear, rational function approximation (RFA) based reduced-order aerodynamic model (ROM) was developed for the microflap using CFD based aerodynamic load response data. This model accurately reproduces the CFD results at a fraction of the computational cost for flow conditions that are characteristic of rotorcraft aerodynamic environment. However, the ROM

fails to capture strong nonlinear effects under stall conditions. This shortcoming does not detract from its effectiveness since the ROM is ideally suited for incorporation into a comprehensive rotorcraft simulation codes.

4. The aerodynamic load predictions from the CFD based and doublet-lattice (DL) based RFA models were compared to direct CFD calculations over a range of flow conditions. The new CFD based RFA model represents a huge improvement over the earlier potential flow based DL+RFA model.

5. The CFD based RFA model was incorporated into a comprehensive rotorcraft simulation code AVINOR. The control authority of microflaps for on-blade noise and vibration reduction in rotorcraft was examined using three spanwise microflap configurations: single, dual, and a segmented five-microflap configuration. The HHC control algorithm was employed for active noise and vibration reduction studies in closed-loop.

6. Active noise reduction using the microflaps was examined under a heavy BVI descending flight condition with the advance ratio $\mu = 0.15$ and descent angle $\alpha_D = 6.5^\circ$. Depending on the configuration, 3-6 dB noise reduction was obtained on the advancing side and 2-3 dB reduction was achieved on the retreating side, demonstrating the microflap's effectives in reducing BVI noise.

7. It was also found that active noise reduction using the single and dual microflap configurations produced a 45% increase in the 4/rev vertical shear

whereas the five-microflap configuration resulted in a 100% increase in the vertical shear. Similar increase in the vibratory loads during noise reduction has been identified computationally and experimentally with other active control approaches such as the conventional HHC and the ACF [102,122,128].

8. The 1.5%c microflap was compared and found to be similar in its effectiveness to a 20%c plain flap configuration for noise reduction. While both the devices yield similar reduction levels on the advancing side, the microflap yields 1 dB higher reduction on the retreating side.

9. Active vibration reduction was demonstrated using the microflap under heavy BVI descending flight condition. The single, dual, and the five-microflap configurations produced 73%, 84%, and 92% reduction in the vibration objective, respectively, demonstrating very good control authority for rotorcraft vibration reduction. However, vibration reduction using a single microflap configuration produced a 2-3 dB noise penalty on the carpet plane. This penalty was reduced for the dual and five-microflaps configurations.

10. The 1.5%c microflap and the single 20%c plain flap configuration show similar effectiveness in vibration reduction capabilities producing 73% and 76% reduction in the vibration objective, respectively.

11. Simultaneous vibration and noise reduction was examined at the heavy BVI flight condition. The dual microflap configuration yields 2 dB noise reduction on both the advancing and the retreating sides while simultaneously

reducing the 4/rev vibratory vertical hub shear magnitude by 34%. The five microflap configuration yields 3 dB noise reduction on the advancing side and 2 dB reduction on the retreating side while simultaneously reducing the 4/rev vibratory vertical hub shear magnitude by 55%. This demonstrates that simultaneous BVI noise and vibration reduction is feasible using microflaps.

12. Simultaneous vibration and noise reduction capabilities of the dual microflap were compared to that of a dual 20%c plain flap configuration. Interestingly, the microflap shows better effectiveness in reducing the noise over the entire carpet plane (both the advancing and the retreating sides) whereas the plain flap reduces only the advancing side noise. The plain flap demonstrates better effectiveness in reducing vibrations.

13. Vibration reduction was examined at a high speed cruise flight condition with $\mu = 0.3$. All three microflap configurations produced over 90% reduction in the vibration objective. Similar vibration reduction levels were obtained using the microflaps and the conventional plain flaps.

14. The microflaps were also considered for rotor performance enhancement at the high speed forward flight condition with $\mu = 0.3$, using closed loop control with combined vibration and rotor power objectives. A 1.2% performance enhancement was observed using the single microflap configuration, however, it was accompanied by a 170% increase in the vibration objective.

15. The effect of actuator saturation on the active vibration reduction performance of the HHC control algorithm was also examined. A new approach to handling actuator saturation in the HHC algorithm based on constrained nonlinear optimization techniques was developed and compared to the truncation, scaling, and auto-weighting approaches at various flight conditions. The truncation and scaling approaches were inconsistent yielding only limited vibration reduction in most cases. By comparison, the auto-weighting and optimization approaches showed very good performance. However, the optimization approach takes significantly less computational time and in the case of multiple control surfaces, it utilizes all of them to the maximum possible extent resulting in better performance.

These conclusions demonstrate the effectiveness and control authority of the microflap for vibration reduction, noise reduction, and also multi-objective control in rotorcraft. The excellent control authority of the microflap combined with its size advantage compared to the conventional plain trailing-edge flaps establish the microflap as a viable active device for on-blade rotor control.

9.2 Future Work

The present study has examined active noise reduction using microflaps under BVI conditions, which is critical for improving the community acceptance of a helicopter. However, noise reduction at high-speed cruise flight conditions still

needs to be addressed. Noise prediction at high-speed conditions will require inclusion of the quadrupole source term in the noise computations. Furthermore, it will require unsteady pressure data for the blade sections encountering transonic flow. Future studies could take these factors in to consideration and perform active noise reduction studies using microflaps at high-speed flight conditions.

The simultaneous vibration and noise reduction studies presented in this thesis have shown that active flaps and microflaps can reduce one objective while penalizing the other. Combining active control devices such as the microflap with passive structural optimization approaches that minimize vibrations and noise through modifying the mass, stiffness, and geometrical properties of the rotor blade can be an effective solution to developing quieter and smoother helicopters. Furthermore, optimization studies considering different geometries, placement schemes, and numbers of microflaps can be performed in order to develop blade designs that properly utilize microflap's control potential.

APPENDICES

Appendix A: Structural Dynamic Model and Generalized Loads

Modeling Assumptions

The basic assumptions used to develop the aeroelastic analysis model for the rotor blade are as follows:

1. The rotor blade is cantilevered at the hub, with a root offset e from the axis of rotation (see Fig. A.2).

2. The blade has a precone angle β_p (see Fig. A.2) and it has built-in pretwist distribution θ_{tw} about the elastic axis of the blade.

3. The blade has no sweep, droop or torque offset.

4. The blade cross section is assumed to be symmetric with respect to its major principal axes.

5. The blade feathering axis is coincident with the elastic axis.

6. The deflections in the blade are assumed to be moderate and the strains to be small.

7. The blade has completely coupled flap, lead-lag, torsional and axial dynamics.

8. The blade is assumed to be inextensible.

9. The rotor shaft is assumed to be rigid and body degrees of freedom are suppressed.

10. The structural effects of the microflap and the conventional trailing edge flap are neglected.

11. The distributed aerodynamic loads are obtained using CFD-based RFA aerodynamic model.

12. The induced inflow is nonuniform and is obtained by a free wake analysis included in the aeroelastic model.

13. Reverse flow effects are included by setting the lift and moment equal to zero and by changing the sign of the drag force inside the reverse flow region.

14. The speed of rotation Ω of the rotor is constant.

15. The helicopter is in trimmed, steady, level or descending flight. Either propulsive or wind tunnel trim can be implemented.

Coordinate Systems

The following six coordinate systems are used to formulate the aeroelastic model:

"0" System: This is an inertial reference frame with origin at the hub center O_H oriented such that the gravitational vector is aligned along the negative z_0 axis. The tail of the helicopter is assumed to lie in the $x_0 z_0$ plane in the direction of the positive x_0 axis.

"1" System: This is an inertial reference frame with origin at O_H. The y_1 axis is coincident with the y_0 axis, and the z_1 axis pitched forward at an angle α_R about the y_0 axis so that it is aligned with the rotor axis of rotation. The "1" system provides the non-rotating reference frame. The "0" and "1" systems are depicted in Fig. A.1.

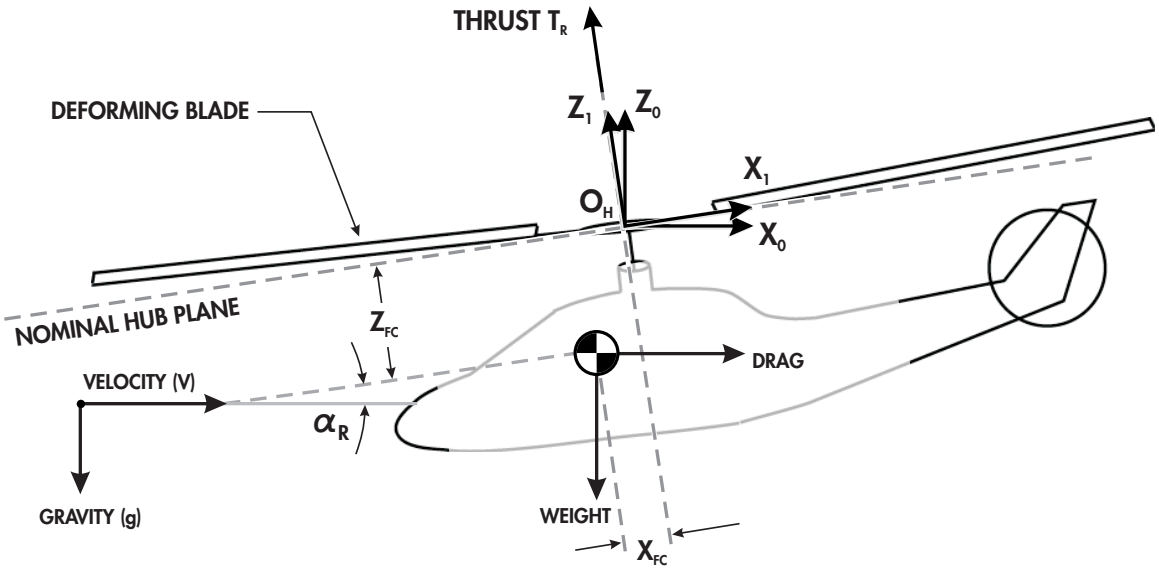

Figure A.1: Transformation from the "0" system to the "1" system

"2" System: This system has its origin at O_H. The z_2 axis is coincident with the z_1 axis but rotates with the blades about the z_1 axis. The "2" system is the rotating reference frame.

"3" System: This system rotates with the blades and has its origin at the blade root located at a distance e away from the axis of rotation along the x_2 axis, as shown in Figure A.2. The x_3 axis is "preconed" by an angle β_p around the y_2 axis such that the x_3 axis lies along the undeformed elastic axis of the

blade. The principal axes of the undeformed blade cross-section at any point along the span lie in a plane parallel to the y_3z_3 plane and are oriented at an angle $\theta_G(x)$ about the x_3 axis. Angle $\theta_G(x)$ is the sum of collective and cyclic pitch inputs at the root and geometric pretwist of the blade at the particular point along the span. The "3" system provides the undeformed reference frame.

"4" System: This is a blade attached system. Before deformation, the "3" and "4" systems are parallel. After deformation, the "4" system is translated and rotated such that the x_4 axis is tangent to the elastic axis of the blade at each blade cross-section along the span. The principal axes of the blade cross-section lie in the y_4z_4 plane, rotated at an angle $\theta_G(x)$ about the x_4 axis. The "4" system provides the deformed reference frame. The relationships between the "2", "3" and "4" systems are depicted on Fig. A.2.

"5" System: This is also a blade attached system and represents the "4" system with the torsional deformation removed, as shown in Figure A.3. Thus, the principal axes of the blade cross section are rotated at an angle $\theta_G(x) + \phi(x)$ about the x_5 axis where $\phi(x)$ is the elastic twist. This reference frame is convenient in the derivation of the aerodynamic loads. The relationships between the "3", "4" and "5" systems are depicted on Fig. A.3.

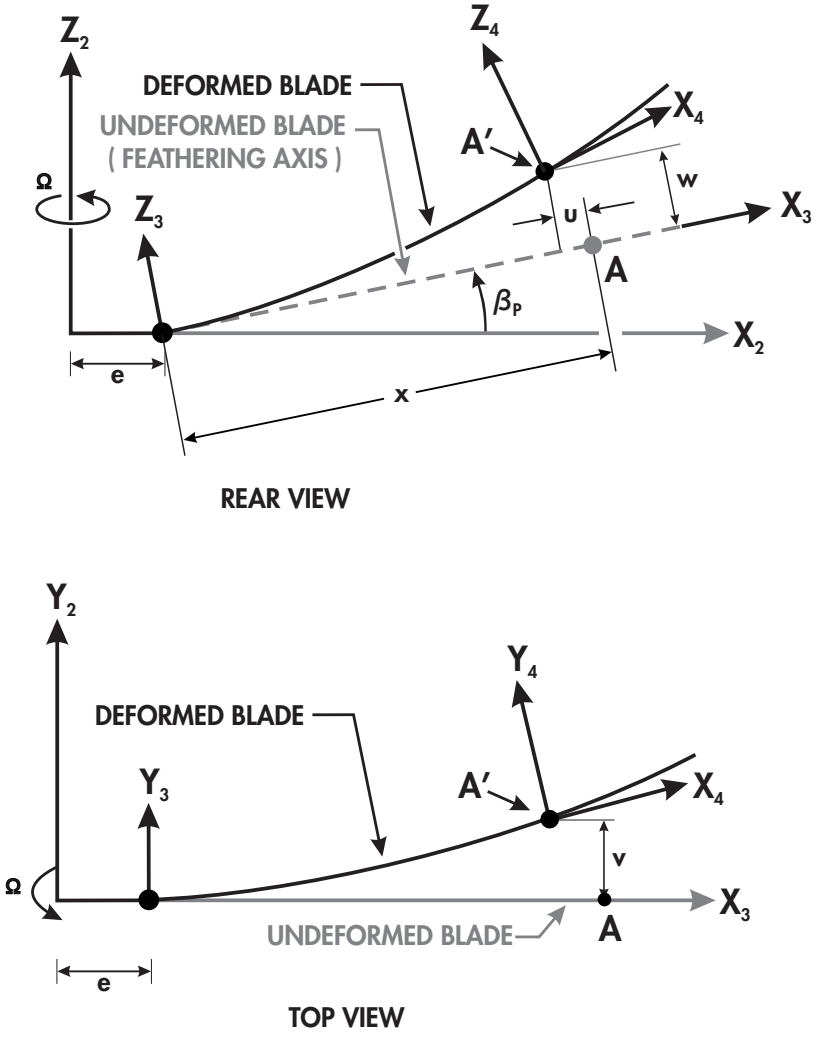

Figure A.2: The transformation from the "2" system to the "4" system

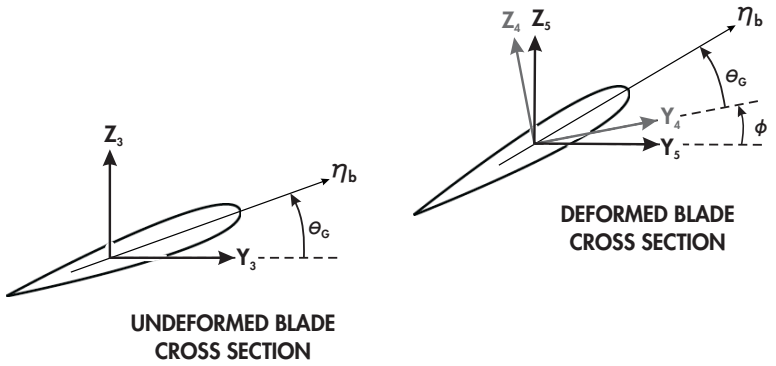

Figure A.3: The transformation from the "3" system to the "5" system

Coordinate Transformations

The set of coordinate transformation matrices that were used to move between the various systems listed above are presented below [Ref. 91, Eq. (4.1)-(4.20)]:

"0" system to "1" system

$$\begin{Bmatrix} \hat{e}_{x1} \\ \hat{e}_{y1} \\ \hat{e}_{z1} \end{Bmatrix} = \begin{bmatrix} \cos\alpha_R & 0 & \sin\alpha_R \\ 0 & 1 & 0 \\ -\sin\alpha_R & 0 & \cos\alpha_R \end{bmatrix} \begin{Bmatrix} \hat{e}_{x0} \\ \hat{e}_{y0} \\ \hat{e}_{z0} \end{Bmatrix} \tag{A.1}$$

"1" system to "2" system

$$\begin{Bmatrix} \hat{e}_{x2} \\ \hat{e}_{y2} \\ \hat{e}_{z2} \end{Bmatrix} = \begin{bmatrix} \cos\psi & \sin\psi & 0 \\ -\sin\psi & \cos\psi & 0 \\ 0 & 0 & 1 \end{bmatrix} \begin{Bmatrix} \hat{e}_{x1} \\ \hat{e}_{y1} \\ \hat{e}_{z1} \end{Bmatrix} \tag{A.2}$$

"2" system to "3" system

$$\begin{Bmatrix} \hat{e}_{x3} \\ \hat{e}_{y3} \\ \hat{e}_{z3} \end{Bmatrix} = \begin{bmatrix} 1 & 0 & \beta_p \\ 0 & 1 & 0 \\ -\beta_p & 0 & 1 \end{bmatrix} \begin{Bmatrix} \hat{e}_{x2} \\ \hat{e}_{y2} \\ \hat{e}_{z2} \end{Bmatrix} \tag{A.3}$$

"3" system to "4" system The coordinate transformation from the undeformed "3" system to the deformed "4" system is obtained using a sequence of angular rotations. The sequence used in this study is flap-lag-torsion, and consists of

1) a flap rotation by the angle $w_{,x}$ clockwise about the y_3 axis, 2) a lead-lag rotation by the angle $v_{,x}$ counterclockwise about the z_3 axis, and 3) a torsional rotation given by the twist angle ϕ counterclockwise about the x_4 axis, in that order. Hence, the coordinate transformation from the undeformed "3" system to the deformed "4" system is given by the matrix product:

$$\begin{Bmatrix} \hat{e}_{x4} \\ \hat{e}_{y4} \\ \hat{e}_{z4} \end{Bmatrix} = \begin{bmatrix} 1 & 0 & 0 \\ 0 & \cos\phi & \sin\phi \\ 0 & -\sin\phi & \cos\phi \end{bmatrix} \cdot \begin{bmatrix} 1 & v_{,x} & 0 \\ -v_{,x} & 1 & 0 \\ 0 & 0 & 1 \end{bmatrix} \cdot \begin{bmatrix} 1 & 0 & w_{,x} \\ 0 & 1 & 0 \\ -w_{,x} & 0 & 1 \end{bmatrix} \begin{Bmatrix} \hat{e}_{x3} \\ \hat{e}_{y3} \\ \hat{e}_{z3} \end{Bmatrix} \tag{A.4}$$

Note that the small angle assumptions $\cos v_{,x} \cong 1$, $\cos w_{,x} \cong 1$, $\sin v_{,x} \cong v_{,x}$, and $\sin w_{,x} \cong w_{,x}$ have been made. Performing the matrix multiplication yields:

$$\begin{Bmatrix} \hat{e}_{x4} \\ \hat{e}_{y4} \\ \hat{e}_{z4} \end{Bmatrix} = \begin{bmatrix} 1 & v_{,x} & w_{,x} \\ -v_x\cos\phi - w_{,x}\sin\phi & \cos\phi & \sin\phi - v_{,x}\, w_{,x}\cos\phi \\ v_{,x}\sin\phi - w_{,x}\cos\phi & -\sin\phi & \cos\phi + v_{,x}\, w_{,x}\sin\phi \end{bmatrix} \begin{Bmatrix} \hat{e}_{x3} \\ \hat{e}_{y3} \\ \hat{e}_{z3} \end{Bmatrix} \tag{A.5}$$

"3" system to "5" system

$$\begin{Bmatrix} \hat{e}_{x5} \\ \hat{e}_{y5} \\ \hat{e}_{z5} \end{Bmatrix} = \begin{bmatrix} 1 & v_{,x} & w_{,x} \\ -v_{,x} & 1 & -w_{,x}\, v_{,x} \\ -w_{,x} & 0 & 1 \end{bmatrix} \begin{Bmatrix} \hat{e}_{x3} \\ \hat{e}_{y3} \\ \hat{e}_{z3} \end{Bmatrix} \tag{A.6}$$

"4" system to "5" system

$$\begin{Bmatrix} \hat{e}_{x5} \\ \hat{e}_{y5} \\ \hat{e}_{z5} \end{Bmatrix} = \begin{bmatrix} 1 & 0 & 0 \\ 0 & \cos\phi & -\sin\phi \\ 0 & \sin\phi & \cos\phi \end{bmatrix} \begin{Bmatrix} \hat{e}_{x4} \\ \hat{e}_{y4} \\ \hat{e}_{z4} \end{Bmatrix} \tag{A.7}$$

Ordering Scheme

An ordering scheme is applied to eliminate the higher order nonlinear terms in the structural equations of motion, in a consistent manner. This is accomplished by assigning orders of magnitude to various commonly encountered nondimensional physical terms and then neglecting terms with an order higher than a predetermined threshold value.

It is assumed the slopes of the deformed rotor blades are of the order ϵ ($0.10 \leq \epsilon \leq 0.20$), based on the moderate deflection assumption. The ordering scheme assumes the terms of order ϵ^2 or higher can be neglected with respect to terms of order 1, i. e.

$$O(1) + O(\epsilon^2) \cong 1 \tag{A.8}$$

A careful and systematic application of this ordering scheme yields expressions of manageable size and with sufficient accuracy for rotor stability and response calculations.

To assign orders of magnitude to individual terms, they must first be expressed in nondimensional form. This is performed using the following reference quanti-

ties:

$$\begin{aligned} \text{[length]} &= R, \quad \text{rotor radius,} \\ \text{[mass]} &= M_b, \quad \text{mass of one blade,} \\ \text{[time]} &= \frac{1}{\Omega}, \quad \text{inverse of the rotor speed.} \end{aligned}$$

Orders of magnitude have been assigned to common nondimensional quantities as follows:

$$\begin{aligned} O(1): &\quad \frac{x}{R}, \frac{L_b}{R}, \frac{m_b}{(M_b/R)}, \frac{\rho_b}{(M_b/R^3)}, \mu, \psi, \cos\psi, \sin\psi, \\ &\quad a_o, R\frac{\partial}{\partial x}, \frac{1}{\Omega}\frac{\partial}{\partial t}, \frac{\partial}{\partial \psi} \\ O(\epsilon^{1/2}): &\quad \frac{L_{cs}}{R}, \theta_G, \delta \\ O(\epsilon): &\quad \frac{c_b}{R}, \frac{e}{R}, \frac{c_{cs}}{R}, \frac{m_c}{(M_b/R)}, \frac{X_h}{R}, \theta_{pt}, \lambda, \alpha_R, \beta_p, \\ &\quad \frac{v}{R}, \frac{w}{R}, v_{,x}, w_{,x}, \phi \\ O(\epsilon^{3/2}): &\quad \frac{M_c}{M_b}, \frac{X_A}{R}, \frac{X_{Ib}}{R}, \frac{X_{Ic}}{R}, \frac{X_{IIb}}{R}, \frac{X_{IIc}}{R}, C_{d0} \\ O(\epsilon^2): &\quad \frac{u}{R}, \frac{EI_{\zeta\zeta}}{M_b R^3 \Omega^2}, \frac{EI_{\eta\eta}}{M_b R^3 \Omega^2}, \frac{fC_{df}}{R^2}, \\ O(\epsilon^{5/2}): &\quad \frac{I_{MB2}}{M_b R}, \frac{I_{MB3}}{M_b R} \\ O(\epsilon^3): &\quad \frac{g}{\Omega^2 R}, \frac{GJ_b}{M_b R^3 \Omega^2} \\ O(\epsilon^{7/2}): &\quad \frac{I_{MC2}}{M_b R}, \frac{I_{MC3}}{M_b R} \end{aligned}$$

The orders of magnitude presented here are consistent with those used in Refs. 87, 92, 112.

Equations of Motion for the Elastic Blade

The hingeless blades are modeled as slender rods of linearly elastic, homogeneous material, cantilevered at an offset e from the rotor hub, using a blade model taken from Ref. 87. This blade model describes the fully coupled flap-lag-torsional dynamics of an isotropic blade. The blade model described in Ref. 87 was derived to reflect the deformation sequence flap-lag-torsion.

The equations of motion for the elastic blade consist of a set of nonlinear partial differential equations of motion, with the distributed loads left in general symbolic form. The distributed loads on the blade, not including control surface loads, can be expressed in the "3" system as:

$$\mathbf{p_b} = p_{bx3}\hat{e}_{x3} + p_{by3}\hat{e}_{y3} + p_{bz3}\hat{e}_{z3}, \tag{A.9}$$

$$\mathbf{q_{Mb}} = q_{bx3}\hat{e}_{x3} + q_{by3}\hat{e}_{y3} + q_{bz3}\hat{e}_{z3}, \tag{A.10}$$

where $\mathbf{p_b}$ and $\mathbf{q_{Mb}}$ represent the total distributed spanwise force and moment, respectively. The equations of motion for the elastic blade, derived in Ref. 91, Eqs. (4.23)-(4.25), are then given by:

Flap Equation

$$\begin{aligned}
&-[(EI_{\zeta\zeta} - EI_{\eta\eta})\sin\theta_G\cos\theta_G(v_{,xx} + 2\phi w_{,xx}) \\
&+(EI_{\zeta\zeta} - EI_{\eta\eta})\phi v_{,xx}\cos 2\theta_G + (EI_{\zeta\zeta}\sin^2\theta_G + EI_{\eta\eta}\cos^2\theta_G)w_{,xx} \\
&-TX_{IIb}(\sin\theta_G + \phi\cos\theta_G)]_{,xx} + (GJ_b\phi_{,x}\, v_{,xx})_{,x} + (w_{,x}\, T)_{,x} \\
&-(v_{,x}\, q_{bx3})_{,x} + q_{by3,x} + p_{bz3} = 0.
\end{aligned} \tag{A.11}$$

Lag Equation

$$\begin{aligned}
&-[(EI_{\zeta\zeta}\cos^2\theta_G + EI_{\eta\eta}\sin^2\theta_G)v_{,xx} + (EI_{\zeta\zeta} - EI_{\eta\eta})\phi w_{,xx}\cos 2\theta_G \\
&+(EI_{\zeta\zeta} - EI_{\eta\eta})\sin\theta_G\cos\theta_G(w_{,xx} - 2\phi v_{,xx}) \\
&-TX_{IIb}(\cos\theta_G - \phi\sin\theta_G)]_{,xx} - (GJ_b\phi_{,x}\, w_{,xx})_{,x} + (v_{,x}\, T)_{,x} \\
&+(w_{,x}\, q_{bx3})_{,x} - q_{bz3,x} + p_{by3} = 0.
\end{aligned} \tag{A.12}$$

Torsional Equation

$$\begin{aligned}
&[GJ_b(\phi_{,x} - v_{,x}\, w_{,xx})]_{,x} \\
&+(EI_{\zeta\zeta} - EI_{\eta\eta})[({v_{,xx}}^2 - {w_{,xx}}^2)\sin\theta_G\cos\theta_G - v_{,xx}\, w_{,xx}\cos 2\theta_G] \\
&+TX_{IIb}(w_{,xx}\cos\theta_G - v_{,xx}\sin\theta_G) + q_{bx3} + v_{,x}\, q_{by3} + w_{,x}\, q_{bz3} = 0,
\end{aligned} \tag{A.13}$$

where T is the axial tension.

Incorporation of the Control Surfaces in the Blade Equations of Motion

The following assumptions have been used for incorporating the effects of the microflap and the active plain flap in the dynamic equations of equilibrium:

1. The micrflap and the plain flap are constrained to slide or rotate only in the plane of the blade cross section;

2. The control surfaces are assumed to be inextensible;

3. The inertial and aerodynamic effects of the control surfaces are included in the model. The effect of the microflap/flap on the structural properties of the blade is assumed to be negligible. Thus, the control surfaces influence the behavior of the blade only through their contribution to the spanwise distributed loads on the blade.

The distributed force and moment on the blade due to the control surfaces can be represented in the "3" system by [Ref. 91, Eqs. (4.26)-(4.27)]:

$$\mathbf{p_c} = p_{cx3}\hat{e}_{x3} + p_{cy3}\hat{e}_{y3} + p_{cz3}\hat{e}_{z3}, \tag{A.14}$$

$$\mathbf{q_c} = q_{cx3}\hat{e}_{x3} + q_{cy3}\hat{e}_{y3} + q_{cz3}\hat{e}_{z3}. \tag{A.15}$$

For a single microflap/flap configuration, with the microflap/flap inboard edge located at a distance x_{cs}^1 from the blade root, the distributed loads are given by:

$$\mathbf{p_c}, \mathbf{q_c} = \begin{cases} 0 & for \quad x < x_{cs}^1 - \frac{L_{cs}}{2} \\ \mathbf{p_c^1}, \mathbf{q_c^1} & for \quad x_{cs}^1 - \frac{L_{cs}}{2} \leq x \leq x_{cs}^1 + \frac{L_{cs}}{2} \\ 0 & for \quad x > x_{cs}^1 + \frac{L_{cs}}{2} \end{cases}$$

where $\mathbf{p_{c1}^1}$ and $\mathbf{q_c^1}$ represent the distributed loads due to the single microflap/flap, and are described in the next section. For a dual microflap/flap configuration, with the inboard edge of the second microflap/flap located at a distance x_{cs}^2 from the blade root, the distributed loads are given by:

$$\mathbf{p_c}, \mathbf{q_c} = \begin{cases} 0 & for \quad x < x_{cs}^1 - \frac{L_{cs}}{2} \\ \mathbf{p_c^1}, \mathbf{q_c^1} & for \quad x_{cs}^1 - \frac{L_{cs}}{2} \leq x \leq x_{cs}^1 + \frac{L_{cs}}{2} \\ 0 & for \quad x_{cs}^1 + \frac{L_{cs}}{2} < x < x_{cs}^2 - \frac{L_{cs}}{2} \\ \mathbf{p_c^2}, \mathbf{q_c^2} & for \quad x_{cs}^2 - \frac{L_{cs}}{2} \leq x \leq x_{cs}^2 + \frac{L_{cs}}{2} \\ 0 & for \quad x > x_{cs}^2 + \frac{L_{cs}}{2} \end{cases}$$

where $\mathbf{p_c^1}$, $\mathbf{q_c^1}$ and $\mathbf{p_c^2}$, $\mathbf{q_c^2}$ represent distributed loads due to the first and second control surfaces, respectively.

The effect of the control surfaces is included in the blade equations of motion by adding the distributed loads due to the control surfaces, given in Eqs. (A.14)-(A.15), to the distributed loads for the blade alone. The equations of motion for the blade, Eqs. (A.11)-(A.12), can be rewritten to reflect this change as:

Flap Equation

$$
\begin{aligned}
&-[(EI_{\zeta\zeta} - EI_{\eta\eta})\sin\theta_G\cos\theta_G(v_{,xx} + 2\phi w_{,xx}) \\
&+(EI_{\zeta\zeta} - EI_{\eta\eta})\phi v_{,xx}\cos 2\theta_G + (EI_{\zeta\zeta}\sin^2\theta_G + EI_{\eta\eta}\cos^2\theta_G)w_{,xx} \\
&-TX_{IIb}(\sin\theta_G + \phi\cos\theta_G)]_{,xx} + (GJ_b\phi_{,x}\, v_{,xx})_{,x} + (w_{,x}\, T)_{,x} \\
&-(v_{,x}\,(q_{bx3} + q_{cx3}))_{,x} + (q_{by3} + q_{cy3})_{,x} + (p_{bz3} + p_{cz3}) \;=\; 0.
\end{aligned}
\tag{A.16}
$$

Lag Equation

$$
\begin{aligned}
&-[(EI_{\zeta\zeta}\cos^2\theta_G + EI_{\eta\eta}\sin^2\theta_G)v_{,xx} + (EI_{\zeta\zeta} - EI_{\eta\eta})\phi w_{,xx}\cos 2\theta_G \\
&+(EI_{\zeta\zeta} - EI_{\eta\eta})\sin\theta_G\cos\theta_G(w_{,xx} - 2\phi v_{,xx}) \\
&-TX_{IIb}(\cos\theta_G - \phi\sin\theta_G)]_{,xx} \\
&-(GJ_b\phi_{,x}\, w_{,xx})_{,x} + (v_{,x}\, T)_{,x} + (w_{,x}\,(q_{bx3} + q_{cx3}))_{,x} \\
&-(q_{bz3} + q_{cz3})_{,x} + (p_{by3} + p_{cy3}) \;=\; 0.
\end{aligned}
\tag{A.17}
$$

Torsion Equation

$$
\begin{aligned}
[GJ_b(\phi_{,x} - v_{,x}\, w_{,xx}\,)]_{,x} + (EI_{\zeta\zeta} - EI_{\eta\eta})[({v_{,xx}}^2 - {w_{,xx}}^2)\sin\theta_G\cos\theta_G \\
- v_{,xx}\, w_{,xx}\cos 2\theta_G] + TX_{IIb}(w_{,xx}\cos\theta_G - v_{,xx}\sin\theta_G) \\
+ (q_{bx3} + q_{cx3}) + v_{,x}\,(q_{by3} + q_{cy3}) + w_{,x}\,(q_{bz3} + q_{cz3}) \;=\; 0,
\end{aligned}
\tag{A.18}
$$

Distributed Loads

A complete description of the aeroelastic equations governing the motion of the rotor blade requires a derivation of the distributed inertial, aerodynamic, gravitational, and the structural damping loads. Distributed inertial, gravitational, and damping loads on a flapped rotor blade were derived as explicit expressions of blade displacement in Ref. 87. Expressions for distributed aerodynamic loads were derived in Ref. 91. These expressions have been used in the present analysis. The purpose of this section is to show how the complete equations of motion are formulated. This will be accomplished by establishing the blade kinematics first and subsequently the distributed loads.

Blade Kinematics

To formulate explicit expressions of the distributed loads acting on the blade, the position of an arbitrary point on the blade or control surface must be defined

in terms of the blade degrees of freedom. The approach described in this chapter is taken from Ref. 91. The kinematic description of the blade used in the derivation of the distributed loads is based on the assumptions of Euler-Bernoulli beam theory: plane sections normal to the elastic axis of the beam before deformation remain plane after deformation, and strains within cross-sections are neglected. Accordingly, an arbitrary point on the beam before deformation, represented by the vector

$$\mathbf{R_p} = e\hat{e}_{x2} + x\hat{e}_{x3} + y_o\hat{e}_{y3} + z_o\hat{e}_{z3}, \tag{A.19}$$

is described after deformation by the vector

$$\mathbf{r_p} = e\hat{e}_{x2} + (x+u)\hat{e}_{x3} + v\hat{e}_{y3} + w\hat{e}_{z3} + y_o\hat{e}_{y4} + z_o\hat{e}_{z4}. \tag{A.20}$$

where u, v, and w represent the displacement of a point on the elastic axis of the blade as illustrated in Fig. A.2. If the coordinate pair $(\bar{y}_o, \bar{z}_o)$ can be interpreted as the pair (y_o, z_o) expressed in the "5" coordinate system, i.e.

$$y_o\hat{e}_{y4} + z_o\hat{e}_{z4} = \bar{y}_o\hat{e}_{y5} + \bar{z}_o\hat{e}_{z5}, \tag{A.21}$$

then

$$\mathbf{r_p} = e\hat{e}_{x2} + (x+u)\hat{e}_{x3} + v\hat{e}_{y3} + w\hat{e}_{z3} + \bar{y}_o\hat{e}_{y5} + \bar{z}_o\hat{e}_{z5}. \tag{A.22}$$

The velocity and acceleration of a point in a reference frame that is translating and rotating relative to an inertial frame can be found using the classical relations:

$$\mathbf{v_p} = \dot{\mathbf{R}}_\mathbf{o} + \dot{\mathbf{r}} + \omega \times \mathbf{r}, \tag{A.23}$$

$$\mathbf{a_p} = \ddot{\mathbf{R}}_\mathbf{o} + \ddot{\mathbf{r}} + 2\omega \times \dot{\mathbf{r}} + \dot{\omega} \times \mathbf{r} + \omega \times (\omega \times \mathbf{r}), \tag{A.24}$$

where $\mathbf{R_o}$ is the position of the origin of the moving reference frame in the inertial frame, and ω the vector of angular velocity. The time derivatives of $\mathbf{R_o}$ are taken in the inertial frame, while those for $\mathbf{r}$ are taken in the rotating frame. For the rotor case, the inertial frame is that of the hub, described by the "1" system. The rotating frame rotates with the blades and corresponds to the "2" system. The origin of the rotating frame is assumed to coincide with the that of the non-rotating frame. Thus:

$$\ddot{\mathbf{R}}_\mathbf{o} = \dot{\mathbf{R}}_\mathbf{o} = \mathbf{R_o} = \mathbf{0}. \tag{A.25}$$

Also, $\omega = \Omega \hat{e}_{z2}$, and since Ω is constant, $\dot{\omega} = \mathbf{0}$. Hence, the velocity and acceleration of any point in the rotating reference frame ("2" system) are given by:

$$\mathbf{v_p} = \dot{\mathbf{r}}_\mathbf{p} + \Omega \hat{e}_{z2} \times \mathbf{r_p}, \tag{A.26}$$

$$\mathbf{a_p} = \ddot{\mathbf{r}}_\mathbf{p} + 2\Omega \hat{e}_{z2} \times \dot{\mathbf{r}}_\mathbf{p} + \Omega \hat{e}_{z2} \times (\Omega \hat{e}_{z2} \times \mathbf{r_p}). \tag{A.27}$$

Equations (A.26) and (A.27), taken from Ref. 91, are the fundamental kinematic relations used in the derivation of the distributed loads.

Inertial Loads

The inertial loads are obtained using D'Alembert's principle. Expressions for the inertial loads will first be formulated in the "2" system, and then transformed to the "3" system to be compatible with the blade elastic equations of motion. Given an arbitrary point in the rotating frame ("2" system), represented by the vector:

$$\mathbf{r_p} = r_{px2}\hat{e}_{x2} + r_{py2}\hat{e}_{y2} + r_{pz2}\hat{e}_{z2}, \tag{A.28}$$

the acceleration of this point can be found using Eq. (A.27). Expressed in the "2" system, this is given by:

$$\mathbf{a_p} = a_{px2}\hat{e}_{x2} + a_{py2}\hat{e}_{y2} + a_{pz2}\hat{e}_{z2}, \tag{A.29}$$

where:

$$a_{px2} = \ddot{r}_{px2} - 2\Omega\dot{r}_{py2} - \Omega^2 r_{px2}, \tag{A.30}$$

$$a_{py2} = \ddot{r}_{py2} + 2\Omega\dot{r}_{px2} - \Omega^2 r_{py2}, \tag{A.31}$$

$$a_{pz2} = \ddot{r}_{pz2}, \tag{A.32}$$

with time derivatives of $\mathbf{r_p}$ taken in the "2" system.

From Eq. (A.22), a point on the deformed blade can be expressed as:

$$\mathbf{r_b} = e\hat{e}_{x2} + (x+u)\hat{e}_{x3} + v\hat{e}_{y3} + w\hat{e}_{z3} + \bar{y}_{ob}\hat{e}_{y5} + \bar{z}_{ob}\hat{e}_{z5}. \tag{A.33}$$

The inertial forces and moments taken about the elastic axis of the blade at a given spanwise location are given by:

$$\mathbf{p_{Ib}} = -\int_{A_b} \rho_b \mathbf{a_b} dA, \tag{A.34}$$

$$\mathbf{q_{Ib}} = -\int_{A_b} \mathbf{r_{ob}} \times \rho_b \mathbf{a_b} dA, \tag{A.35}$$

where:

$$\mathbf{r_{ob}} = \bar{y}_{ob}\hat{e}_{y5} + \bar{z}_{ob}\hat{e}_{z5}. \tag{A.36}$$

The resulting spanwise distributed inertia force is expressed in the "2" system as [Ref. [91], Eqs. (5.36)-(5.39)]:

$$\mathbf{p_{Ib}} = p_{Ibx2}\hat{e}_{x2} + p_{Iby2}\hat{e}_{y2} + p_{Ibz2}\hat{e}_{z2}, \tag{A.37}$$

where the components of $\mathbf{p_{Ib}}$ are given by:

$$
\begin{aligned}
p_{Ibx2} &= m_b\Omega^2(x+e) + 2m_b\Omega\dot{v} + m_b\beta_p(\ddot{w} - w\Omega^2) \\
&\quad + m_b(u\Omega^2 - \ddot{u}) - 2m_b X_{Ib}\Omega\sin(\theta_G+\phi)(\dot{\theta}_G+\dot{\phi}), \qquad \text{(A.38)} \\
p_{Iby2} &= 2m_b\Omega\dot{w}\beta_p + m_b(v\Omega^2 - \ddot{v}) - 2m_b\Omega\dot{u} \\
&\quad + m_b X_{Ib}\cos(\theta_G+\phi)((\dot{\theta}_G+\dot{\phi})^2 + \Omega(\Omega + 2\dot{v}_{,x}) + 2\Omega(\dot{\theta}_G+\dot{\phi})(w_{,x}+\beta_p)) \\
&\quad + m_b X_{Ib}\sin(\theta_G+\phi)((\ddot{\theta}_G+\ddot{\phi}) + 2\Omega\dot{w}_{,x} - 2\Omega(\dot{\theta}_G+\dot{\phi})v_{,x}), \qquad \text{(A.39)} \\
p_{Ibz2} &= -m_b\ddot{u}\beta_p - m_b\ddot{w} \\
&\quad + m_b X_{Ib}\cos(\theta_G+\phi)(-(\ddot{\theta}_G+\ddot{\phi}) + \ddot{v}_{,x}(w_{,x}+\beta_p) + 2\dot{w}_{,x}\dot{v}_{,x} + \ddot{w}_{,x}v_{,x}) \\
&\quad + m_b X_{Ib}\sin(\theta_G+\phi)((\dot{\theta}_G+\dot{\phi})^2 - (\ddot{\theta}_G+\ddot{\phi})(w_{,x}+\beta_p)v_{,x}). \qquad \text{(A.40)}
\end{aligned}
$$

Similarly, distributed spanwise moment is expressed in the "2" system as [Ref. [91], Eqs. (5.40)-(5.43)]:

$$\mathbf{q_{Ib}} = q_{Ibx2}\hat{e}_{x2} + q_{Iby2}\hat{e}_{y2} + q_{Ibz2}\hat{e}_{z2}, \qquad \text{(A.41)}$$

where:

$$
\begin{aligned}
q_{Ibx2} &= m_b X_{Ib}\cos(\theta_G+\phi)((v\Omega^2-\ddot{v})(w_{,x}+\beta_p)v_{,x}-\ddot{w}-\ddot{u}\beta_p) \\
&\quad m_b X_{Ib}\sin(\theta_G+\phi)((\ddot{v}-v\Omega^2)+2\Omega\dot{u}-2\Omega\dot{w}\beta_p) \\
&\quad -(I_{MB2}+I_{MB3})(\ddot{\theta}_G+\ddot{\phi}) \\
&\quad +(I_{MB2}-I_{MB3})\cos(\theta_G+\phi)\sin(\theta_G+\phi)\Omega((\Omega+2\dot{v}_{,x})+2(\dot{\theta}_G+\dot{\phi})(w_{,x}+\beta_p) \\
&\quad +2(I_{MB2}\cos^2(\theta_G+\phi)+I_{MB3}\sin^2(\theta_G+\phi))\Omega((\dot{\theta}_G+\dot{\phi})v_{,x}-\dot{w}_{,x}) \\
&\quad +(I_{MB2}\sin^2(\theta_G+\phi)+I_{MB3}\cos^2(\theta_G+\phi)) \\
&\quad (2\dot{v}_{,x}\dot{w}_{,x}+v_{,x}\ddot{w}_{,x}+(w_{,x}+\beta_p)(\Omega^2 v_{,x}+\ddot{v}_{,x})), \qquad \text{(A.42)} \\
q_{Iby2} &= -m_b X_{Ib}\cos(\theta_G+\phi)(\Omega^2 x(w_{,x}+\beta_p)+\ddot{w})v_{,x} \\
&\quad +m_b X_{Ib}\sin(\theta_G+\phi)(\Omega^2(x+e)-(\Omega^2 w\beta_p+\ddot{w}w_{,x})+2\Omega\dot{v}+(u\Omega^2-\ddot{u})) \\
&\quad -(I_{MB2}+I_{MB3})(\ddot{\theta}_G+\ddot{\phi})v_{,x} \\
&\quad +(I_{MB2}-I_{MB3})\cos(\theta_G+\phi)\sin(\theta_G+\phi)((v_{,x}\Omega^2-\ddot{v}_{,x})-2(\dot{\theta}_G+\dot{\phi})\dot{w},x) \\
&\quad +(I_{MB2}\cos^2(\theta_G+\phi)+I_{MB3}\sin^2(\theta_G+\phi)) \\
&\quad (w_{,x}-\Omega^2(w_{,x}+\beta_p)-2(\dot{\theta}_G+\dot{\phi})(\Omega+\dot{v}_{,x})), \qquad \text{(A.43)} \\
q_{Ibz2} &= m_b X_{Ib}\cos(\theta_G+\phi)(-\Omega^2(x+e)-2\Omega\dot{v}+(\ddot{u}-u\Omega^2) \\
&\quad +(w\Omega^2-\ddot{w})\beta_p+(\ddot{v}-v\Omega^2)v_{,x}) \\
&\quad +m_b X_{Ib}\sin(\theta_G+\phi)(\ddot{v}-v\Omega^2)(w_{,x}+\beta_p) \\
&\quad -(I_{MB2}+I_{MB3})(\ddot{\theta}_G+\ddot{\phi})(w_{,x}+\beta_p) \\
&\quad +(I_{MB2}-I_{MB3})\cos(\theta_G+\phi)\sin(\theta_G+\phi)(\ddot{w}_{,x}-2(\dot{\theta}_G+\dot{\phi})(\Omega+\dot{v}_{,x})) \\
&\quad -(I_{MB2}\sin^2(\theta_G+\phi)+I_{MB3}\cos^2(\theta_G+\phi))(\ddot{v}_{,x}+2(\dot{\theta}_G+\dot{\phi})\dot{w}_{,x}). \qquad \text{(A.44)}
\end{aligned}
$$

Using the coordinate transformations described in the previous sections of this chapter, the distributed spanwise inertial force can be expressed in the "3" system as:

$$\mathbf{p_{Ib}} = p_{Ibx3}\hat{e}_{x3} + p_{Iby3}\hat{e}_{y3} + p_{Ibz3}\hat{e}_{z3}, \tag{A.45}$$

where:

$$p_{Ibx3} = p_{Ibx2} + \beta_p p_{Ibz2}, \tag{A.46}$$

$$p_{Ibx3} = p_{Iby2}, \tag{A.47}$$

$$p_{Ibx3} = -\beta_p p_{Ibx2} + p_{Ibz2}. \tag{A.48}$$

Similarly, the distributed spanwise moment can be expressed in the "3" system as:

$$\mathbf{q_{Ib}} = q_{Ibx3}\hat{e}_{x3} + q_{Iby3}\hat{e}_{y3} + q_{Ibz3}\hat{e}_{z3}, \tag{A.49}$$

where:

$$q_{Ibx3} = q_{Ibx2} + \beta_p q_{Ibz2}, \tag{A.50}$$

$$q_{Ibx3} = q_{Iby2}, \tag{A.51}$$

$$q_{Ibx3} = -\beta_p q_{Ibx2} + q_{Ibz2}. \tag{A.52}$$

The derivation of the inertia loads due to a control surface is identical to that for the blade and can be found in Ref. 91.

Gravitational Loads

The distributed gravitational loads can be derived by integrating the gravitational force and moment per unit volume over the blade cross-section. Gravitational acceleration g is directed along the negative z_0 axis:

$$\mathbf{g} = -g\hat{e}_{z0}. \tag{A.53}$$

Expressed in the "2" system, this becomes:

$$\mathbf{g} = g_{x2}\hat{e}_{x2} + g_{y2}\hat{e}_{y2} + g_{z2}\hat{e}_{z2}, \tag{A.54}$$

where:

$$g_{x2} = -g\sin\alpha_R\cos\psi, \tag{A.55}$$

$$g_{y2} = g\sin\alpha_R\sin\psi, \tag{A.56}$$

$$g_{z2} = -g\cos\alpha_R. \tag{A.57}$$

These expressions are then used to derive the distributed force and moment.

The distributed gravitational force is derived by integrating the gravitational force per unit volume over the blade cross-section:

$$\mathbf{p_{Gb}} = \int_{A_b} \rho_b \mathbf{g} dA. \tag{A.58}$$

This can be expressed in the "2" system as [Ref. [91], Eqs. (5.103)-(5.106)]:

$$\mathbf{p_{Gb}} = p_{Gbx2}\hat{e}_{x2} + p_{Gby2}\hat{e}_{y2} + p_{Gbz2}\hat{e}_{z2}, \tag{A.59}$$

where:

$$p_{Gbx2} = \int_{A_b} \rho_b g_{x2} dA = -m_b g \sin\alpha_R \cos\psi, \tag{A.60}$$

$$p_{Gby2} = \int_{A_b} \rho_b g_{y2} dA = m_b g \sin\alpha_R \sin\psi, \tag{A.61}$$

$$p_{Gbz2} = \int_{A_b} \rho_b g_{z2} dA = -m_b g \cos\alpha_R. \tag{A.62}$$

Similarly, the distributed gravitational moment about the elastic axis is derived by integrating the gravitational moment per unit volume over the blade cross-section:

$$\mathbf{q_{Gb}} = \int_{A_b} (\bar{y}_{0b}\hat{e}_{y5} + \bar{z}_{0b}\hat{e}_{z5}) \times \rho_b \mathbf{g} dA, \tag{A.63}$$

Expressed in the "2" system, this becomes [Ref. [91], Eqs. (5.108)-(5.111)]:

$$\mathbf{q_{Gb}} = q_{Gbx2}\hat{e}_{x2} + q_{Gby2}\hat{e}_{y2} + q_{Gbz2}\hat{e}_{z2}, \tag{A.64}$$

where:

$$q_{Gbx2} = \int_{A_b} \rho_b(\bar{y}_{0b}(g_{z2} + (w_{,x} + \beta_p)v_{,x}\, g_{y2}) - \bar{z}_{0b} g_{y2})dA, \quad \text{(A.65)}$$

$$q_{Gby2} = \int_{A_b} \rho_b(\bar{y}_{0b}(g_{z2} - (w_{,x} + \beta_p)v_{,x} + \bar{z}_{0b}((w_{,x} + \beta_p)g_{z2} + g_{x2}))dA, \quad \text{(A.66)}$$

$$q_{Gbz2} = \int_{A_b} \rho_b(-\bar{y}_{0b}(v_{,x}\, g_{y2} + g_{x2}) - \bar{z}_{0b}(w_{,x} + \beta_p)g_{y2})dA. \quad \text{(A.67)}$$

Substituting (A.55)-(A.57) into (A.65)-(A.67) leads to:

$$\begin{aligned} q_{Gbx2} = {} & -m_b g X_{Ib} \cos(\theta_G + \phi)(\cos\alpha_R - (w_{,x} + \beta_p)v_{,x} \sin\alpha_R \sin\psi) \\ & -m_b g X_{Ib} \sin(\theta_G + \phi) \sin\alpha_R \sin\phi, \end{aligned} \quad \text{(A.68)}$$

$$\begin{aligned} q_{Gby2} = {} & -m_b g X_{Ib} \cos(\theta_G + \phi)(\cos\alpha_R - (w_{,x} + \beta_p) \sin\alpha_R \cos\psi)v_{,x} \\ & -m_b g X_{Ib} \sin(\theta_G + \phi)((w_{,x} + \beta_p)\cos\alpha_R + \sin\alpha_R \cos\phi), \end{aligned} \quad \text{(A.69)}$$

$$\begin{aligned} q_{Gbz2} = {} & -m_b g X_{Ib} \cos(\theta_G + \phi) \sin\alpha_R(v_{,x} \sin\phi - \cos\phi) \\ & -m_b g X_{Ib} \sin(\theta_G + \phi) \sin\alpha_R \sin\phi). \end{aligned} \quad \text{(A.70)}$$

These expressions are then transformed to the "3" system to be compatible with the blade equations of motion. The derivation of the distributed gravitational loads due to a control surface is identical to that described for the blade and can be found in Ref. 91.

Damping Loads

Distributed structural damping loads are assumed to be of viscous type, and act only on the blade. Define the distributed damping force as:

$$\mathbf{p_D} = -g_{S_L}\dot{v}\hat{e}_{y3} - g_{S_F}\dot{w}\hat{e}_{z3}. \tag{A.71}$$

The distributed damping moment is given by:

$$\mathbf{q_D} = -g_{S_T}\dot{\phi}\hat{e}_{x4}, \tag{A.72}$$

which can be expressed in the "3" system as [Ref. 91, Eq. (5.196)]:

$$\mathbf{q_D} = -g_{ST}\dot{\phi}(\hat{e}_{x3} - v_{,x}\,\hat{e}_{y3} - w_{,x}\,\hat{e}_{z3}). \tag{A.73}$$

g_{S_L}, g_{S_F}, and g_{S_T} are the distributed structural damping factors in lag, flap and torsion, respectively.

Total Distributed Loads

The total distributed loads are found by summing the inertial, gravitational, aerodynamic, and damping contributions. The distributed aerodynamic loads are derived in Chapter IV. For the total distributed load per unit length on the blade:

$$\mathbf{p_b} = \mathbf{p_{Ib}} + \mathbf{p_{Gb}} + \mathbf{p_A} + \mathbf{p_D}. \tag{A.74}$$

where the subscripts I, G, A, and D correspond to the inertial, gravitational, aerodynamic, and damping loads respectively. For the distributed moment per unit length about the elastic axis:

$$\mathbf{q_{Mb}} = \mathbf{q_{Ib}} + \mathbf{q_{Gb}} + \mathbf{q_{A}} + \mathbf{q_{D}}. \tag{A.75}$$

For the distributed force per unit length on the blade due to the control surface:

$$\mathbf{p_c} = \mathbf{p_{Ic}} + \mathbf{p_{Gc}}. \tag{A.76}$$

For the distributed moment per unit length about the elastic axis due to the control surface:

$$\mathbf{q_c} = \mathbf{q_{Ic}} + \mathbf{q_{Gc}}. \tag{A.77}$$

Aerodynamic loads due to control surfaces are not included in Eq. (A.76) or (A.77). Instead, these loads are contained in the expressions for the aerodynamic blade loads appearing in (A.74) and (A.75).

Appendix B: Free-Wake Model and Dynamic Stall Model

Free-Wake Model

The wake analysis consists of two elements: (1) a wake geometry calculation procedure including a free wake analysis developed by Scully [116], which determines the position of the vortices; (2) an induced velocity calculation procedure as implemented in CAMRAD/JA, which calculates the nonuniform induced velocity distribution at the blades.

Wake Geometry

The rotor wake is composed of two main elements: the tip vortex, which is a strong, concentrated vorticity filament generated at the tip of the blade; and the near wake, which is an inboard sheet of trailed vorticity. The near wake is much weaker and more diffused than the tip vortex. The wake vorticity is created in the flow field as the blade rotates, and then convected with the local velocity of the fluid. The local velocity of the fluid consists of the free stream velocity, and the wake self induced velocity. Thus, the wake geometry calculation proceeds as follows: (1) the position of the blade generating the wake element is calculated, this is the point at which the wake vorticity is created; (2) the undistorted wake geometry is computed as wake elements are convected downstream from the rotor by the free stream velocity; (3) distortion of wake due to the wake self-induced velocity is computed and added to the undistorted geometry. The position of a

generic wake element is identified by its current azimuth position ψ and its age ϕ_w. Age is the nondimensional time that has elapsed since the wake element's creation. Thus, the position of a generic wake element is written as:

$$\mathbf{r}_w(\psi, \phi_w) = \mathbf{r_b}(\psi - \phi_w) + \phi_w \mathbf{V_A} + \mathbf{D}(\psi, \phi_w) \tag{B.1}$$

where $\mathbf{r_b}(\psi - \phi_w)$ is the position of the blade when it generates the wake element, $\mathbf{V_A}$ is the free stream velocity, and $\mathbf{D}(\psi, \phi_w)$ is the wake distortion.

To evaluate the wake self-induced distortion $\mathbf{D}(\psi, \phi_w)$, a free wake procedure developed by Scully [116] is employed. This procedure is used only to calculate the distorted geometry of the tip vortices, which are the dominant feature of the rotor wake. The inboard vorticity is determined by a prescribed wake model [62] to save the computational cost.

In the free wake geometry calculation, the distortion $\mathbf{D}$ is obtained by integrating in time the induced velocity at each wake element due to all the other wake elements. As the wake age increases by $\Delta\psi$, the distortion at ψ is obtained by adding the contribution of the induced velocity to the distortion at previous azimuthal step:

$$\mathbf{D}(\psi, \phi_w) = \mathbf{D}(\psi, \phi_w - \Delta\psi) + \Delta\psi \mathbf{q}(\psi) \tag{B.2}$$

The distortion in the wake at the time of its creation is zero. Hence,

$$\mathbf{D}(\psi, 0) = 0. \tag{B.3}$$

Induced Velocity Calculation

The induced velocity calculation procedure, developed by Johnson [62], is based on a vortex-lattice approximation for the wake. The tip vortex elements are modeled by line segments with a small viscous core radius, while the near wake can be represented by vortex sheet elements or by line segments with a large core radius to eliminate large induced velocities. The near wake vorticity is generally retained for only a number K_{NW} of azimuth steps behind the blade. The wake structure is illustrated in Fig. B.1.

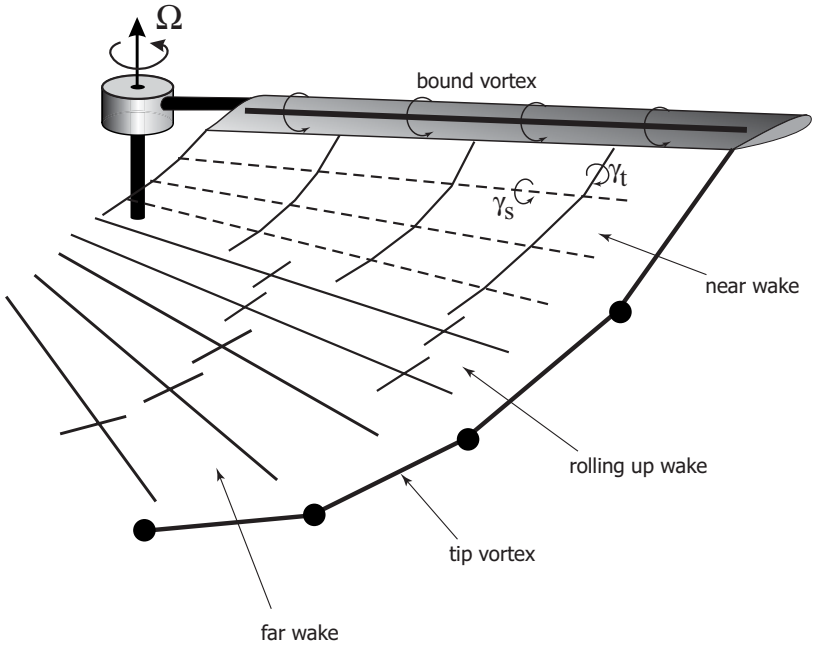

Figure B.1: Vortex-lattice approximation for rotor wake model

Conservation of vorticity on a three-dimensional blade requires the bound circulation to be trailed into the wake from the blade tip and root. The lift and circulation are concentrated at the tip of the blade, since larger dynamic pressures are present in the tip region. Therefore, a strong, concentrated tip vortex is gen-

erated. The vorticity in the tip vortex is distributed over a small but finite region, called the vortex core. The accuracy of a wake model is sensitive to the value of the strength of the tip vortex prescribed. Two different approaches are used, depending on the spanwise distribution of the bound circulation. For helicopters in low speed forward flight, the bound circulation is positive along the entire span of the blade (Fig. B.2). The distribution of the bound circulation has only one peak and is refered to as the single peak model. In the single peak model, the maximum value of the bound circulation over the blade span, $\Gamma_{\max}$, is selected for the tip vortex strength. For helicopters in high speed forward flight or under some means of active control, a spanwise circulation distribution with two peaks of opposite sign can be encountered. A large positive peak is generally located inboard and a smaller negative peak on the outboard section of blade (Fig. B.3). The dual peak model represents such a situation. The inboard and outboard peaks Γ_I and Γ_O, respectively, are identified, and the tip vortex strength assumes the value of the outboard peak.

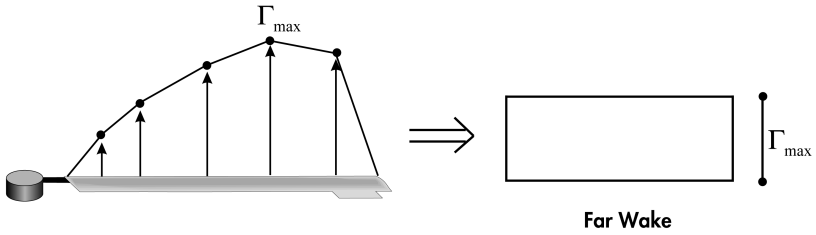

Figure B.2: Single peak circulation distribution model and the resulting far wake approximation

Given the blade displacements and circulation distribution, the wake geometry is calculated. Once the wake geometry has been determined, the influence coeffi-

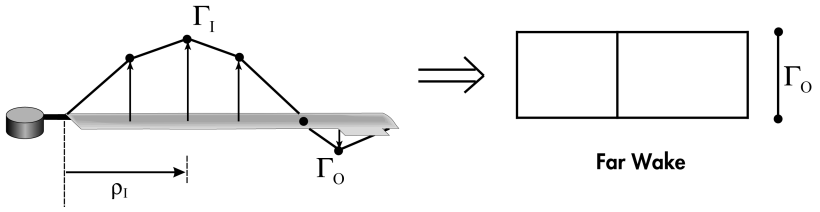

Figure B.3: CAMRAD/JA dual peak model and the resulting far wake approximation

cients are calculated and stored in the influence coefficient matrix. The induced velocity distribution is obtained by conveniently multiplying the influence coefficient matrix with the circulation distribution:

$$\mathbf{q} = \sum_{j=1}^{J} \Gamma_{Oj} \mathbf{C}_{Oj} + \sum_{j=1}^{J} \Gamma_{Ij} \mathbf{C}_{Ij} + \sum_{j=1}^{K_{NW}} \sum_{i=1}^{M} \Gamma_{ij} \mathbf{C}_{NWij}, \tag{B.4}$$

where $\Gamma_{I_j}, \Gamma_{O_j}$ are the inboard and outboard peaks, respectively, at the azimuth j; J, M are the numbers of azimuth and spanwise stations, respectively; K_{NW} is the number of azimuth stations on which the near wake extends; $\mathbf{C}_{O_j}, \mathbf{C}_{I_j}$ and $\mathbf{C}_{NW_{ij}}$ are terms of the influence coefficient matrix. For the single peak model, $\Gamma_{O_j} = \Gamma_{\max j}$ and $\Gamma_{I_j} = 0$.

Wake Modeling Improvements

As mentioned earlier, the fidelity of the wake model dictates the accuracy of BVI noise prediction. Therefore, a number of improvements were made to the CAMRAD/JA wake model by Patt, Liu, and Friedmann [78, 98, 101] in order to obtain better correlation with the HART experimental data. Two modifications are discussed below.

Wake Resolution

For accurate prediction of BVI noise, a 5° or finer azimuthal wake resolution is required, as compared to the much coarser 15° resolution that is often adequate for vibration reduction studies. The original CAMRAD/JA wake code uses a resolution of 15° for the free wake analysis. This restriction was removed in the current wake code to allow for wake resolution of up to 2°. However, due to some numerical difficulties [116] the free wake model failed to converge for the resolutions finer than 3° and therefore a resolution of 5° was used. This resolution was shown to be adequate for BVI noise prediction through validations against the HART experimental data [78, 98]. An azimuthal wake resolution of 5° is used for all the simulations in the current study.

Dual Vortex Rollup

The free wake model taken from CAMRAD/JA was based on the assumption that the inboard vortices cannot roll up, thus facilitating the use of either a vortex-sheet or an equivalent vortex-line model to model the inboard vortices. This was not compatible with the HART test data where significant increases in BVI noise levels for the "minimum vibration" case have been attributed to a dual vortex structure [122].

A dual vortex model was therefore incorporated by including a possible second inboard vortex line. This feature of the wake model becomes active only when the tip loading becomes negative, as shown in Fig. B.4. The release point of this second

vortex line is taken to be at the radial location r_I, where blade bound circulation becomes negative, and the strength of this vortex is assumed to be $\Gamma_I - \Gamma_O$, where Γ_O, the outboard circulation peak, is negative. Furthermore, the free wake distortion computation routine was also modified to include the deformation of this second inboard vortex line, including its interaction with the outer tip vortices. This was realized by evaluating the self-induced velocities by both tip vortices and secondary vortices. Moreover, a threshold criteria, suggested in Ref. 107, can be employed to determine whether to have inboard vortex line rolled up. Rollup of the inboard vortex is allowed when the radial gradient of the bound circulation $\partial\Gamma/\partial r$ at the inboard vortex release point r_I is greater than a specified threshold value. This condition represents the physical requirement that the shear in the wake be sufficiently strong so as to form a fully rolled-up, concentrated vortex.

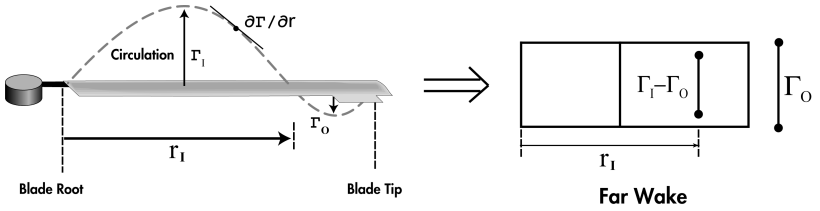

Figure B.4: Improved dual peak model, leading to dual concentrated vortex lines

Dynamic Stall Model for the Separated Flow Regime

Dynamic stall effects due to flow separation are modeled using a semi-empirical dynamic stall model based on a modified version of the ONERA dynamic stall model [33,34]. The modified aerodynamic state vector for each blade section consists of the CFD based RFA attached flow states and the ONERA separated flow

states. Dynamic stall is an important contributor to vibration levels and control loads for the relatively high advance ratio ($\mu = 0.3$) considered in this study. In the ONERA model developed by Petot [105], the three second-order differential equations governing the separated flow states are:

$$\ddot{\Pi}_j + a_j \frac{U}{b}\dot{\Pi}_j + r_j \left(\frac{U}{b}\right)^2 \Pi_j = -[r_j \left(\frac{U}{b}\right)^2 V \Delta C_j + E_j \frac{U}{b}\dot{W}_0], \tag{B.5}$$

where $j = l, m, d$ represent lift, moment, and drag respectively. The coefficients a_j, r_j, E_j are obtained empirically. The complete two-dimensional sectional air-loads are given by:

$$L = L_A + L_S, \;\; M = M_A + M_S, \;\; D = D_A + D_S, \tag{B.6}$$

where L_A, M_A, and D_A are the attached flow lift, moment, and drag, respectively, calculated using the CFD based RFA model. The lift, moment, and drag due to the separated flow are given by:

$$L_S = \frac{1}{2}\rho c_b U \Pi_l, \tag{B.7}$$

$$M_S = \frac{1}{2}\rho c_b^2 U \Pi_m, \tag{B.8}$$

$$D_S = \frac{1}{2}\rho c_b U \Pi_d. \tag{B.9}$$

The flow separation and reattachment criterion is based on the angle of attack and a correction similar to Prandtl-Glauert to account for compressibility. The critical

angle of attack for separation and reattachment is $\alpha_{cr} = 15^\circ(1 - M^2)$. Contributions to the three sectional airloads from the dynamic stall model are denoted by $\Delta C_L, \Delta C_M$, and ΔC_D. They can either be zero:

$$\Delta C_L = \Delta C_M = \Delta C_D = 0, \tag{B.10}$$

or take the following values if the flow has separated [33]:

$$\Delta C_L = (p_0 - 0.1M^4)(\alpha - \alpha_{cr}) - 0.7(1 - M)[e^{(-0.5+(1.5-M)M^2)(\alpha-\alpha_{cr})} - 1], \tag{B.11}$$

$$\Delta C_M = (-0.11 - 0.19e^{-40(M-0.6)^2})[e^{(-0.4-0.21\arctan[22(0.45-M)])(\alpha-\alpha_{cr})} - 1], \tag{B.12}$$

$$\Delta C_D = (0.008 - 0.3)\left[1 - \left(\frac{25 - \alpha}{25 - \alpha_{cr}}\right)^{\frac{25-\alpha_{cr}}{18-2\arctan(4M)}-\alpha_{cr}}\right], \tag{B.13}$$

where

$$p_0 = 0.1\frac{1 - M^8}{\sqrt{1 - M^2}}. \tag{B.14}$$

The separation criteria based on the angle of attack is given by,

1. Case 1: if $\alpha < \alpha_{cr} = 15^\circ(1 - M^2)$, $\Delta C_L = \Delta C_M = \Delta C_D = 0$.

2. Case 2: assume that at time $t = t_0$, $\alpha = \alpha_{cr}$, $\dot{\alpha} > 0$; then, for $t > t_0 + \Delta t$, $\Delta C_L, \Delta C_M$, and ΔC_D are given by Eqs. B.11-B.13.

3. Case 3: when $\alpha < \alpha_{cr}$, the flow is reattached and $\Delta C_L, \Delta C_M$, and ΔC_D are set to zero again.

The ONERA model features 18 empirical coefficients, 6 each $(r_{j0}, r_{j2}, a_{j0}, a_{j2}, E_{j2})$ associated with lift $(j = l)$, moment $(j = m)$, and drag $(j = d)$. These quantities can be found in Ref. 33.

Appendix C: Solution Procedure

Coupled Trim/Aeroelastic Response Solutions

Solution of the Blade Equations of Motion

The spatial dependence of the equations of motion is removed using Galerkin's method of weighted residuals. Three flap, two lead-lag, and two torsional free vibration modes of a rotating beam are used to represent the flexibility of the blade. Each free vibration mode was calculated using the first nine exact nonrotating modes of a uniform cantilevered beam. The displacements v and w and twist ϕ are thus represented by:

$$w \cong \sum_{i=1}^{3} q_{wi}(\psi) W_i(x), \tag{C.1}$$

$$v \cong \sum_{i=1}^{2} q_{vi}(\psi) V_i(x), \tag{C.2}$$

$$\phi \cong \sum_{i=1}^{2} q_{\phi i}(\psi) \Phi_i(x), \tag{C.3}$$

where W_i, V_i, and Φ_i are the i-th rotating flap, lead-lag, and torsional uncoupled mode shapes, respectively, with participation coefficients q_{wi}, q_{vi}, and $q_{\phi i}$. These mode shapes satisfy the boundary conditions of a hingeless blade cantilevered to

the hub, which implies:

$$w(\psi,0) = v(\psi,0) = \phi(\psi,0) = 0, \tag{C.4}$$

$$w_{,x}(\psi,0) = v_{,x}(\psi,0) = 0, \tag{C.5}$$

$$w_{,xx}(\psi,R) = v_{,xx}(\psi,R) = 0, \tag{C.6}$$

$$w_{,xxx}(\psi,R) = v_{,xxx}(\psi,R) = 0. \tag{C.7}$$

Galerkin's method is applied by substituting (C.1)-(C.3) in (A.16)-(A.18). The error residuals are then multiplied by the appropriate mode shape and integrated over the span of the blade. After having introduced the appropriate boundary conditions, seven equations of motion are obtained [Ref. 91, Eqs. (6.12)-(6.14)]:

Flap Equations $(i = 1, 2, 3)$:

$$\begin{aligned}\int_0^{L_b} \{ &-[(EI_{\zeta\zeta} - EI_{\eta\eta})\sin\theta_G \cos\theta_G (v_{,xx} + 2\phi w_{,xx}) \\ &+ (EI_{\zeta\zeta} - EI_{\eta\eta})\phi v_{,xx} \cos 2\theta_G \\ &+ (EI_{\zeta\zeta}\sin^2\theta_G + EI_{\eta\eta}\cos^2\theta_G) w_{,xx} - TX_{IIb}(\sin\theta_G + \phi\cos\theta_G)] W_{i,xx} \\ &+ (GJ_b\phi_{,x}\, v_{,xx} + w_{,x}\, T - v_{,x}\,(q_{bx3} + q_{cx3}) + (q_{by3} + q_{cy3})) W_{i,x} \\ &+ (p_{bz3} + p_{cz3}) W_i \} dx = 0. \end{aligned} \tag{C.8}$$

Lag Equations $(i = 1, 2)$:

$$\int_0^{L_b} \{-[(EI_{\zeta\zeta}\cos^2\theta_G + EI_{\eta\eta}\sin^2\theta_G)v_{,xx} + (EI_{\zeta\zeta} - EI_{\eta\eta})\phi w_{,xx}\cos 2\theta_G$$
$$+(EI_{\zeta\zeta} - EI_{\eta\eta})\sin\theta_G\cos\theta_G(w_{,xx} - 2\phi v_{,xx}) - TX_{IIb}(\cos\theta_G - \phi\sin\theta_G)]V_{i,xx}$$
$$+(-GJ_b\phi_{,x}\, w_{,xx} + v_{,x}\, T + w_{,x}\,(q_{bx3} + q_{cx3})$$
$$-(q_{bz3} + q_{cz3}))V_{i,x} + (p_{by3} + p_{cy3})V_i\}dx = 0. \tag{C.9}$$

Torsional Equations $(i = 1, 2)$:

$$\int_0^{L_b} \{[GJ_b(\phi_{,x} - v_{,x}\, w_{,xx})]\Phi_{i,x} + (EI_{\zeta\zeta} - EI_{\eta\eta})[({v_{,xx}}^2 - {w_{,xx}}^2)\sin\theta_G\cos\theta_G$$
$$-v_{,xx}\, w_{,xx}\cos 2\theta_G]\Phi_i + TX_{IIb}(w_{,xx}\cos\theta_G - v_{,xx}\sin\theta_G)\Phi_i$$
$$+((q_{bx3} + q_{cx3}) + v_{,x}\,(q_{by3} + q_{cy3}) + w_{,x}\,(q_{bz3} + q_{cz3}))\Phi_i\}dx = 0. \tag{C.10}$$

The spatial dependence of these equations is eliminated when all mode shape substitutions are made and the integration is performed. The spanwise integrations are carried out numerically in the simulation, using Gaussian quadrature. This process produces a set of seven nonlinear ordinary differential equations in terms of q_{w1}, q_{w2}, q_{w3}, q_{v1}, q_{v2}, $q_{\phi 1}$, and $q_{\phi 2}$. They can be expressed in state variable form,

where the vector $\mathbf{q_b}$ of blade degrees of freedom is:

$$\mathbf{q_b} = \begin{bmatrix} q_{w1} & q_{w2} & q_{w3} & q_{v1} & q_{v2} & q_{\phi 1} & q_{\phi 2} \end{bmatrix}^T . \tag{C.11}$$

For integration using Gaussian quadrature, the integrand is evaluated at a set number of stations along the span of the blade at locations corresponding to predefined Gaussian points. At each station, the sectional airloads are provided by the CFD based RFA model which requires solving a set of aerodynamic state equations. These aerodynamic state equations are fully coupled with the blade equations of motion given in Eqs. (C.8)-(C.10) through the blade degrees of freedom and the aerodynamic loads. The structural and aerodynamic equations include a set of trim parameters. The trim parameters are obtained by solving a set of trim equations which enforce force and moment equilibrium at the hub.

Propulsive Trim Procedure

The primary trim procedure is based on propulsive trim analysis, modeling actual free-flight conditions. A helicopter in free flight has six degrees of freedom; thus, six equilibrium equations must be satisfied. The trim procedure, taken from Ref. 31, enforces these equilibrium equations in straight and level flight conditions. A modified version of this procedure developed in Refs. 78, 98 is used for descending flight conditions.

In the case of actual helicopter flight, the pilot inputs consist of collective and

cyclic inputs (θ_0, θ_{1s},θ_{1c}) and the tail rotor pitch (θ_{0t}). For a given flight condition, the quantities C_W and μ are known, and the trim procedure solves for the equilibrium values of θ_0, θ_{1s}, θ_{1c}, ϕ_R, α_R, and θ_{0t}. These variables comprise the six-component helicopter trim vector $\mathbf{q_t}$.

Only the average values of the rotor hub forces and moments, identified by overbars, are required. Since non-uniform inflow is used in this study, the trim procedure does not require an explicit inflow relation. The complete six equilibrium equations are enforced in the present trim calculation. A simplified model for the tail rotor, developed in Ref. 31, is used. The vector $\mathbf{q_t}$ of trim variables is defined as

$$\mathbf{q_t} = \{\alpha_R, \theta_0, \theta_{1c}, \theta_{1s}, \theta_{0t}, \phi_R\}^T. \tag{C.12}$$

A schematic of a helicopter in descending flight is depicted in Fig. C.1. The equilibrium equations are formulated in the nonrotating, hub-fixed system (x_1, y_1, z_1). The helicopter weight W acts at the center of gravity of the fuselage, which is offset from the hub center by the distances X_{FC} and Z_{FC} in the $-\hat{e}_{x1}$ and $-\hat{e}_{z1}$ directions respectively. The trim procedure has a provision for accommodating the aerodynamic drag that acts at a location (the aerodynamic center) that is different from the center of gravity. However, in all the cases considered in this study, the flat plate drag always acts at the center of gravity of the fuselage, and $X_{FA} = X_{FC}$, $Y_{FA} = Y_{FC}$, and $Z_{FA} = Z_{FC}$. The lateral center of gravity offset Y_{FC} is also set to

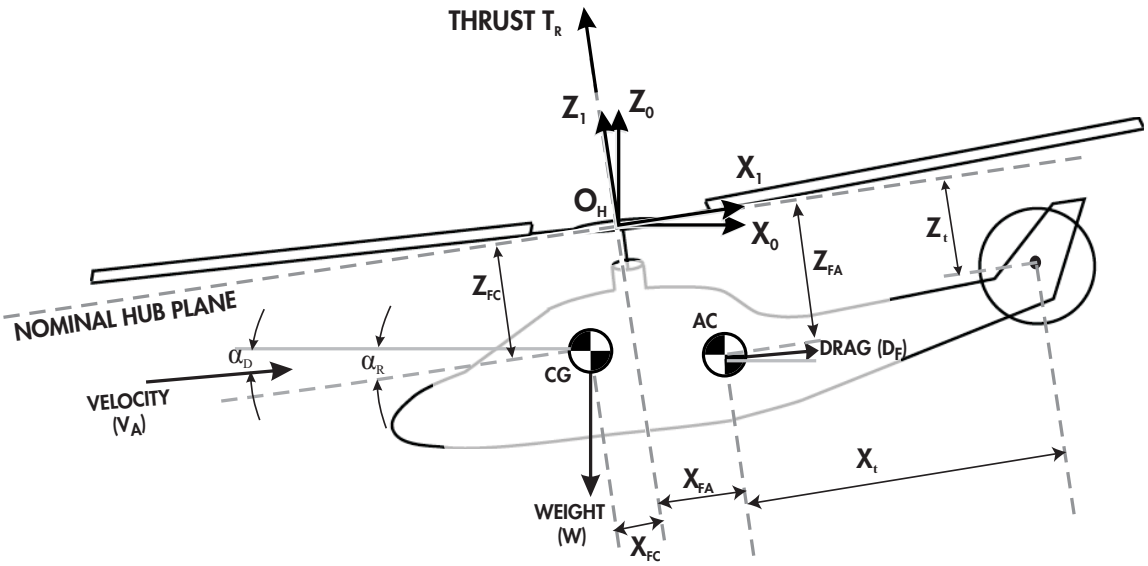

Figure C.1: A schematic of the helicopter in descending flight

zero for cases considered in this study. The flat-plate drag is given by:

$$D_f = \frac{1}{2}\rho_A \mathbf{V_A}^2 C_{df} \pi R^2. \tag{C.13}$$

A typical value for the flat-plate drag coefficient is

$$C_{df} = 0.01. \tag{C.14}$$

In descending flight, a constant angle α_D is defined as the angle between the forward flight velocity $\mathbf{V_A}$ and the horizontal plane, and is shown in Fig. C.1. The descent angle is a known quantity along with W and μ. Note that the drag force D_f will continue to act parallel to the direction of the resultant velocity $\mathbf{V_A}$. Setting the descent angle $\alpha_D = 0$, trim equations for a level flight condition similar to those found in Ref. 31 can be recovered. The trim equations are:

a. Pitching Moment

Moment equilibrium about the y_1 axis requires:

$$\begin{aligned} &\overline{M}^{pt} + W[-X_{FC}\cos\phi_R\cos\alpha_R + Z_{FC}\cos\phi_R\sin\alpha_R] \\ &-D_f[-X_{FA}\sin(\alpha_R-\alpha_D) + Z_{FA}\cos(\alpha_R-\alpha_D)] - Q_t \;=\; 0. \end{aligned} \tag{C.15}$$

b. Rolling Moment

Moment equilibrium about the x_1 axis requires:

$$\overline{M}^{rl} - Z_{FC}W\sin\phi_R + T_tZ_t = 0. \tag{C.16}$$

where T_t is the tail rotor thrust and Z_t is the vertical distance between the hub axis and the center of the tail rotor.

c. Yawing Moment

Moment equilibrium about the z_1 axis requires:

$$\overline{M}^{yw} - X_{FC}W\sin\phi_R + T_tX_t = 0. \tag{C.17}$$

where T_t is the tail rotor thrust and X_t is the horizontal distance between the hub axis and the center of the tail rotor (Fig. C.1).

d. Vertical Force

Force equilibrium in the z_1 direction requires:

$$\overline{F_T} - W\cos\alpha_R\cos\phi_R - D_f\sin(\alpha_R - \alpha_D) = 0. \tag{C.18}$$

e. Longitudinal Force

Force equilibrium in the x_1 direction requires:

$$\overline{H} - W\sin\alpha_R\cos\phi_R + D_f\cos(\alpha_R - \alpha_D) = 0. \tag{C.19}$$

f. Lateral Force

Force equilibrium in the y_1 direction requires:

$$\overline{Y} - W\sin\alpha_R\cos\phi_R + T_t = 0. \tag{C.20}$$

The advance ratio μ and inflow ratio λ were defined in Eqs. 4.15 and 4.16 as

$$\mu = \frac{V_F\cos\alpha_R}{\Omega R} \tag{C.21}$$

$$\lambda = \frac{V_F\sin\alpha_R + \nu}{\Omega R} \tag{C.22}$$

For descending flight, these equations must be modified by replacing α_R with (α_R-

α_D). Thus, the modified expressions for advance ratio μ and inflow ratio λ are:

$$\begin{aligned} \mu &= \frac{V_F \cos(\alpha_R - \alpha_D)}{\Omega R} \\ \lambda &= \frac{V_F \sin(\alpha_R - \alpha_D) + \nu}{\Omega R} \end{aligned} \tag{C.23}$$

here ν is the induced inflow velocity. For the free wake analysis, it is replaced by a nonuniform inflow distribution.

Wind-Tunnel Trim Procedure

For wind-tunnel trim, the previous trim procedure can be simplified because the force equilibrium equations are automatically satisfied and the tail rotor is absent. The prescribed quantities are α_R, θ_0, μ and the cyclic pitch components are used to trim out the pitching and rolling moments on the rotor. For the coupled wind-tunnel trim analysis implemented in the code, the following moment equations are enforced:

a. Pitching Moment

$$\begin{aligned} &\overline{M}^{pt} + W[-X_{FC}\cos\phi_R\cos\alpha_R + Z_{FC}\cos\phi_R\sin\alpha_R] \\ &\quad -D_f[-X_{FA}\sin(\alpha_R - \alpha_D) + Z_{FA}\cos(\alpha_R - \alpha_D)] \;=\; 0. \end{aligned} \tag{C.24}$$

b. Rolling Moment

$$\overline{M}^{rl} - Z_{FC} W \sin\phi_R = 0. \tag{C.25}$$

The solution procedure is similar to that for the full vehicle trim equations discussed above, except the cyclic controls (θ_{1S} and θ_{1C}) are adjusted iteratively to satisfy Eqs. (C.24) and (C.25). Thus, for wind-tunnel trim, the trim vector shortens to just two elements, matching in number the two equilibrium equations. To simulate descent flight using the wind-tunnel trim procedure, the shaft angle α_R is set to chosen value approximating the angle of the rotor in descending flight. This follows the procedure used in the experiment described in Ref. [122].

Time Integration of the Coupled Trim/Aeroelastic Equations

The complete aeroelastic model for the blade and control surface consists of three sets of equations. These are sets of nonlinear differential equations that describe the structural, aerodynamic, and the trim components of the model. The blade equations of motion (C.8)-(C.10) required for the coupled trim/aeroelastic response, can be written in the vector form:

$$\mathbf{f_b}(\mathbf{q_b}, \dot{\mathbf{q}}_\mathbf{b}, \ddot{\mathbf{q}}_\mathbf{b}, \mathbf{x_a}, \mathbf{q_t}; \psi) = \mathbf{0}. \tag{C.26}$$

where $\mathbf{q_b}$ represents the vector of blade degrees of freedom, described in Eq. (C.11), $\mathbf{x_a}$ represents the vector of aerodynamic states, and $\mathbf{q_t}$ represents the trim vector. To convert Eq. (C.26) to first order form, define a mass matrix given by:

$$\mathbf{M_b} = \frac{\partial \mathbf{f_b}}{\partial \ddot{\mathbf{q}}_\mathbf{b}} \tag{C.27}$$

This allows Eq. (C.26) to be decomposed into the form:

$$\mathbf{f_b} = \mathbf{g_b}(\mathbf{q_b}, \dot{\mathbf{q}}_\mathbf{b}, \mathbf{x_a}, \mathbf{q_t}; \psi) + \mathbf{M_b}(\mathbf{q_b}, \mathbf{q_t}; \psi)\ddot{\mathbf{q}}_\mathbf{b} = \mathbf{0}. \tag{C.28}$$

Solving for $\ddot{\mathbf{q}}_\mathbf{b}$ yields

$$\ddot{\mathbf{q}}_\mathbf{b} = -\mathbf{M}_\mathbf{b}^{-1}\mathbf{g_b}. \tag{C.29}$$

Explicit expressions for $\mathbf{M_b}$ and $\mathbf{g_b}$ can be found in Ref. 87. The second order system (C.29) can be written in the following state variable form

$$\dot{\mathbf{x}}_b = \begin{bmatrix} \mathbf{0} & \mathbf{I} \\ \mathbf{0} & \mathbf{0} \end{bmatrix} \mathbf{x_b} + \begin{bmatrix} \mathbf{0} \\ -\mathbf{M}_\mathbf{b}^{-1}\mathbf{g_b} \end{bmatrix}, \tag{C.30}$$

where $\mathbf{x_b}$ is the state vector of blade degrees of freedom:

$$\mathbf{x_b} = \begin{bmatrix} \mathbf{q_b} \\ \dot{\mathbf{q}}_\mathbf{b} \end{bmatrix}. \tag{C.31}$$

Similarly, the complete set of aerodynamic state equations is represented by the vector expression

$$\mathbf{f_a}(\mathbf{q_b}, \dot{\mathbf{q}}_\mathbf{b}, \ddot{\mathbf{q}}_\mathbf{b}, \mathbf{x_a}, \dot{\mathbf{x}}_\mathbf{a}, \mathbf{q_t}; \psi) = 0, \tag{C.32}$$

which can be written in the first order form

$$\dot{\mathbf{x}}_\mathbf{a} = \mathbf{g_a}(\mathbf{q_b}, \dot{\mathbf{q}}_\mathbf{b}, \ddot{\mathbf{q}}_\mathbf{b}, \mathbf{x_a}, \mathbf{q_t}; \psi). \tag{C.33}$$

The dependence on $\ddot{\mathbf{q}}_\mathbf{b}$ is eliminated by substituting Eq. (C.29) into Eq. (C.33), producing the reduced set of equations

$$\dot{\mathbf{x}}_\mathbf{a} = \mathbf{g}_{\mathbf{aR}}(\mathbf{x}_\mathbf{b}, \mathbf{x}_\mathbf{a}, \mathbf{q}_\mathbf{t}; \psi). \tag{C.34}$$

Define a state vector $\mathbf{y}$ as

$$\mathbf{y} = \left\{ \begin{array}{c} \mathbf{x}_\mathbf{b} \\ \\ \mathbf{x}_\mathbf{a} \end{array} \right\}, \tag{C.35}$$

then, combining Eqs. (C.30) and (C.34) yields a system of coupled first-order state variable equations of the form:

$$\dot{\mathbf{y}} = \mathbf{F}(\mathbf{y}; t). \tag{C.36}$$

This system is solved numerically using the ODE solver DE/STEP, which is a general-purpose predictor-corrector Adams-Bashforth differential system solver [117].

Solution of the Trim Equations

The dependence of the trim equations (C.15)-(C.20) on blade degrees of freedom $\mathbf{q}_\mathbf{b}$ and the aerodynamic states $\mathbf{x}_\mathbf{a}$ in the trim equations occurs through terms representing the rotor hub loads. However, only the average values of the hub loads are used in the trim equations. When only the steady state response of the system is considered, the average values of the hub loads will depend only on the

trim variables $\mathbf{q_t}$ defined in Eq. C.12. The trim equations are solved using an iterative procedure referred to as the autopilot trim procedure. The trim solution presented here is identical to that of Ref. 33. The trim equations can be written in the form:

$$\mathbf{f_t}(\mathbf{q_t}) = 0. \tag{C.37}$$

Let $\mathbf{R_{ti}}$ be the vector of trim residuals at the trim condition $\mathbf{q_{t_i}}$ at iteration i:

$$\mathbf{f_t}(\mathbf{q_{t_i}}) = \mathbf{R_{t_i}}. \tag{C.38}$$

An iterative optimal control strategy is then used to reduce the value of $\mathbf{R_{t_i}}$; based on the minimization of the performance index:

$$J = \mathbf{R_{t_i}^T R_{t_i}}. \tag{C.39}$$

This algorithm resembles a feedback controller used for vibration reduction. The trim parameters at the i^{th} iteration are then given by:

$$\mathbf{q_{t_i}} = -\mathbf{T_i^{-1}} \mathbf{R_{t_{i-1}}} + \mathbf{q_{t_{i-1}}}, \tag{C.40}$$

where $\mathbf{T_i}$ is a transfer matrix describing the sensitivities of trim residuals to changes in the trim variables:

$$\mathbf{T_i} = \frac{\partial \mathbf{R_{t_i}}}{\partial \mathbf{q_t}}. \tag{C.41}$$

where $\mathbf{T_i}$ is computed using a finite difference scheme. Under certain complex flight conditions, convergence of this procedure can be improved using a relaxation approach:

$$\mathbf{q_{t_i}} = -\alpha \mathbf{T_i^{-1}} \mathbf{R_{t_{i-1}}} + \mathbf{q_{t_{i-1}}}, \tag{C.42}$$

where α is a relaxation parameter less than unity. The use of this relaxation parameter was pioneered by Depailler [33].

Vibratory Hub Shears and Moments

The resultant force and moment at the root of the k-th blade is found by integrating the distributed inertial, gravitational, aerodynamic, and damping loads $\mathbf{p_b}, \mathbf{p_c}, \mathbf{q_b}, \mathbf{q_c}$ given in Eqs. (A.74)-(A.77), over the blade span. Following the procedure used in [Ref. 33, Eqs. (8.48)-(8.50)], the resultant shears and moments of the k-th blade, at azimuth ψ_k, may be expressed in the rotating "2" frame as:

$$\mathbf{F_{Rk}}(\psi_k) = \int_0^{L_b} (\mathbf{p_b} + \mathbf{p_c})\, dr, \tag{C.43}$$

$$\mathbf{M_{Rk}}(\psi_k) = \int_0^{L_b} (\mathbf{q_b} + \mathbf{q_c})\, dr, \tag{C.44}$$

where:

$$\psi_k = \psi + \frac{2\pi(k-1)}{N_b}. \tag{C.45}$$

Then, rotor hub shears and moments in the nonrotating "1" frame $F_H(\psi)$, $M_H(\psi)$ are computed by summing the contribution of each blade $F_{Rk}(\psi_k)$, $M_{Rk}(\psi_k)$ and by converting them from the "2" frame to the "1" frame using a coordinate transformation described in Eq. (A.2).

In an N_b-bladed helicopter, N_b/rev is the dominant harmonic of vibratory loads transferred to the hub. Other harmonics of vibratory loads are also present, but these are of lesser importance and are not considered in the active reduction problems addressed in this study. The quantities $\mathbf{F_{H4c}}$, $\mathbf{F_{H4s}}$, $\mathbf{F_{H4c}}$, and $\mathbf{F_{H4s}}$ represent the $\sin$ and $\cos$ components of the 4/rev hub shears and moments, and are found using

$$\mathbf{F_{H4c}} = \frac{1}{2}\int_0^{2\pi} \mathbf{F_H}(\psi)\cos 4\psi \; d\psi, \tag{C.46}$$

$$\mathbf{F_{H4s}} = \frac{1}{2}\int_0^{2\pi} \mathbf{F_H}(\psi)\sin 4\psi \; d\psi, \tag{C.47}$$

$$\mathbf{M_{H4c}} = \frac{1}{2}\int_0^{2\pi} \mathbf{M_H}(\psi)\cos 4\psi \; d\psi, \tag{C.48}$$

$$\mathbf{M_{H4s}} = \frac{1}{2}\int_0^{2\pi} \mathbf{M_H}(\psi)\sin 4\psi \; d\psi. \tag{C.49}$$

BIBLIOGRAPHY

BIBLIOGRAPHY

[1] I. H. Abbott and A. E. Von Doenhoff. *Theory of Wing Sections*, Dover Publications, Inc., 1959.

[2] I. H. Abbott, A. E. Von Doenhoff, and L. S. Stivers, *Summary of Airfoil Data*. NACA Report 824, 1945.

[3] R. Albertani. "Wind-Tunnel Study of Gurney Flaps Applied to Micro Aerial Vehicle Wing". *AIAA Journal*, 46(6):1560–1562, June 2008.

[4] D. A. Allwine, J. A. Strahler, D. A. Lawrence, J. E. Jenkins, and J. H. Myatt. "Nonlinear Modeling of Unsteady Aerodynamics at High Angle of Attack". In *Proceedings of the AIAA Atmospheric Flight Mechanics Conference and Exhibit*, Providence, RI, Aug 2004.

[5] K. J. Astrom and B. Wittenmark. *Adaptive Control*, Addison-Wesley, 1995.

[6] J. P. Baker, K. J. Standish, and C. P. van Dam. "Two-Dimensional Wind Tunnel and Computational Investigation of a Microtab Modified Airfoil". *Journal of Aircraft*, 44(2):563–572, March-April 2007.

[7] M. Bebesel, D. Roth, R. Dietrich, K. Pongratz, and R. Kube. "Individual Blade Root Control Demonstration Recent Activities". In *Proceedings of the 27th European Rotorcraft Forum*, pages 33.1–33.14, Moscow, Russia, September 2001.

[8] M. Bebesel, D. Roth, and K. Pongratz. "Reduction of BVI Noise on the Ground - In Flight Evaluation of Closed-Loop Controller". In *Proceedings of the 28th European Rotorcraft Forum*, pages 19.1–19.9, Bristol, England, September 2002.

[9] A. Bernhard and I. Chopra. "Hover Test of Mach-Scale Active Twist Rotor Using Piezo-Bending-Torsion Actuators". *Journal of Aircraft*, 39(4):678–688, 2002.

[10] D. S. Bernstein and A. N. Michel. "A Chronological Bibliography on Saturating Actuators". *International Journal of Robust and Nonlinear Control*, 5:375–380, 1995.

[11] S. Bieniawski and I. M. Kroo. "Flutter Suppression Using Micro-Trailing Edge Effectors". In *Proceedings of the 44th AIAA/ASME/ASCE/AHS/ACS Structures, Structural Dynamics and Materials Conference*, Norfolk, VA, Apr 2003. AIAA Paper No. 2003-1941.

[12] R. L. Bisplinghoff, H. Ashley, and R.L. Halfman. *Aeroelasticity,*, chapter 6, pages 317–325. Addison-Wesley, 1955.

[13] C. De Boor. *A Practical Guide to Splines*, Springer-Verlag, 2001.

[14] D. D. Boyd, T. F. Brooks, C. L. Burley, and J. R. Jolly. "Aeroacoustic Codes for Rotor Harmonic and BVI Noise - Camrad.Mod1/HIRES". *Journal of the American Helicopter Society*, 45(2):63–89, April 2000.

[15] K.S. Brenter, *A Computer Program Incorporating Realistic Blade Motions and Advanced Acoustic Formulation*. NASA Technical Memorandum, Vol. 87721 1986.

[16] K. S. Brentner and F. Farassat. "Helicopter Noise Prediction: The Current Status and Future Direction". *Journal of Sound and Vibration*, 170(1):79–96, 1994.

[17] K. S. Brentner and F. Farassat. "Modeling Aerodynamically Generated Sound of Helicopter Rotors". *Progress in Aerospace Sciences*, 39(2–3):83–120, February–April 2003.

[18] T. F. Brooks and E. R. Booth. "The Effect of Higher Harmonic Pitch Control on Blade-Vortex Interaction Noise and Vibration". *Journal of the American Helicopter Society*, 38(3):45–55, July 1993.

[19] T. F. Brooks, E. R. Booth, J. R. Jolly, W.T. Yeager, and M.L. Wilbur. "Reduction of Blade-Vortex Interaction Noise Through Higher Harmonic Pitch Control". *Journal of the American Helicopter Society*, 35(1):86–91, January 1990.

[20] R. Celi. "Recent Applications of Design Optimization to Rotorcraft—A Survey". *Journal of Aircraft*, 36(1):176–189, January-February 1999.

[21] S. R. Chakravarthy and S. Osher. "New Class of High Accuracy TVD Schemes for Hyperbolic Conservation Laws". In *Proceedings of the 23rd AIAA Aerospace Sciences Meeting and Exhibit*, Reno, NV, Jan 1985. AIAA Paper No. 85-0363.

[22] B. D. Charles, H. Tadghighi, and A. Hassan. "Higher Harmonic Actuation of Trailing-Edge Flaps for Rotor BVI Noise Control". In *Proceedings of the 52nd Annual Forum of the American Helicopter Society*, Washington, DC, June 1996.

[23] R. Chow and C. P. van Dam. "Unsteady Computational Investigations of Deploying Load Control Microtabs". *Journal of Aircraft*, 43(5):641–648, Sept-Oct 2006.

[24] J. G. Coder, M. D. Maughmer, and P. B. Martin. "CFD Investigation of Unsteady Rotorcraft Airfoil Aerodynamics: MiTEs and Dynamic stall". In *Proceedings of the 49th AIAA Aerospace Sciences Meeting and Exhibit*, Orlando, FL, Jan 2011. AIAA Paper No. 2011-1125.

[25] J. A. Cole, B. A. O. Vieira, J. G. Coder, A. Premi, and M. D. Maughmer. "An Experimental Investigation into the Effect of Gurney Flaps on various Airfoils". In *Proceedings of the 49th AIAA Aerospace Sciences Meeting and Exhibit*, Orlando, FL, Jan 2011. AIAA Paper No. 2011-1250.

[26] J. A. Cole, B. A. O. Vieira, J. G. Coder, A. Premi, and M. D. Maughmer. "An Experimental Investigation into the Effect of Gurney Flaps on Various Airfoils". In *Proceedings of the 49th AIAA Aerospace Sciences Meeting and Exhibit*, Orlando, FL, Jan 2011. AIAA Paper No. 2011-1250.

[27] A. M. Cooperman, R. Chow, S. J. Johnson, and C. P. van Dam. "Experimental and Computational Analysis of a Wind Turbine Airfoil". In *Proceedings of the 49th AIAA Aerospace Sciences Meeting and Exhibit*, Orlando, FL, Jan 2011. AIAA Paper No. 2011-1250.

[28] R. Cribbs and P. P. Friedmann. "Actuator Saturation and Its influence on Vibration Reduction by Actively Controlled Flaps". In *AIAA Paper No. 2001-1467. Proceedings of the 42nd AIAA/ASME/ASCE/AHS/ACS Structures, Structural Dynamics and Materials Conference*, Seattle, WA, April 2001.

[29] R. Cribbs, P. P. Friedmann, and T. Chiu. "Coupled Rotor/Flexible Fuselage Aeroelastic Model for Control of Structural Response". *AIAA Journal*, 38(10):1777–1788, 2000.

[30] S. Dawson, F. K. Straub, E. Booth, and M. Marcolini. "Wind Tunnel Test of an Active Flap Rotor: BVI Noise and Vibration Reduction". In *Proceedings of the 51st Annual Forum of the American Helicopter Society*, pages 381–392, Fort Worth, TX, May 1995.

[31] M. de Terlizzi. *Blade Vortex Interaction and Its Alleviation Using Passive and Active Control Approaches*. PhD Dissertation, UCLA, 1999.

[32] M. de Terlizzi and P. P. Friedmann. "Active Control of BVI Induced Vibrations Using a Refined Aerodynamic Model and Experimental Correlation". In *American Helicopter Society 55th Annual Forum Proceedings*, pages 599–615, Montreal, Canada, May 25-27 1999.

[33] G. Depailler. *Alleviation of Dynamic Stall Induced Vibrations on Helicopter Rotors Using Actively Controlled Flaps*. PhD Dissertation, University of Michigan, Ann Arbor, 2002.

[34] G. Depailler and P. P. Friedmann. "Reductions of Vibrations Due to Dynamic Stall in Helicopters Using an Actively Controlled Flap". In *Proceedings of the*

43rd AIAA/ASME/ASCE/AHS/ACS Structures, Structural Dynamics and Materials Conference, Denver, CO, April 2002. AIAA Paper No. 2002-1431.

[35] J. H. Edwards. "Application of Laplace Transform Methods to Airfoil Motion and Stability Calculations". In *Proceedings of the 20th Structures, Structural Dynamics and Materials Conference*, St. Louis, MO, April 1979. AIAA Paper No. 1979-772.

[36] B. Enenkl, V. Klöppel, D. Preissler, and P. Jänker. "Full Scale Rotor with Piezoelectric Actuated Blade Flaps". In *Proceedings of the Twenty-Eighth European Rotorcraft Forum*, Bristol, UK, September 2002.

[37] F. Farassat. "Linear Acoustic Formulas for Calculation of Rotating Blade Noise". *AIAA Journal*, 19(9), September 1981.

[38] F. Farassat and G. P. Succi. "The Prediction of Helicopter Rotor Discrete Frequency Noise". *Vertica*, 7(4):309–320, May 1983.

[39] J. E. Ffowcs Williams and D. L. Hawkings. "Sound Generation by Turbulence and Surfaces in Arbitrary Motion". *Philosophical Transactions of Royal Soc. London, Series A*, 264(1151):321–342, May 1969.

[40] R. Fletcher. *Practical Methods of Optimization*, John Wiley and Sons, 1987.

[41] G. F. Franklin, J. D. Powell, and A. Emami-Naeini. *Feedback Control of Dynamic Systems*, Prentice Hall, 2002.

[42] P. P. Friedmann. "Arbitrary Motion Unsteady Aerodynamics and Its Application to Rotary-Wing Aeroelasticity". *Journal of Fluids and Structures*, 1, July 1986.

[43] P. P. Friedmann. "Helicopter Vibration Reduction Using Structural Optimization with Aeroelastic/Multidisciplinary Constraints - A Survey". *Journal of Aircraft*, 28(1):8–21, 1991.

[44] P. P. Friedmann, M. de Terlizzi, and T. F. Myrtle. "New Developments in Vibration Reduction with Actively Controlled Trailing Edge Flaps". *Mathematical and Computer Modelling*, 33:1055–1083, 2001.

[45] P. P. Friedmann and D. Hodges. "Rotary Wing Aeroelasticity - Current Status and Future Trends". *AIAA Journal*, 42(10):1953–1972, October 2004.

[46] P. P. Friedmann and T. A. Millott. "Vibration Reduction in Rotorcraft Using Active Control: A Comparison of Various Approaches". *Journal of Guidance, Control, and Dynamics*, 18(4):664–673, July-August 1995.

[47] M. Fulton and R. A. Ormiston. "Small-Scale Rotor Experiments with On-Blade Elevons to Reduce Blade Vibratory Loads in Forward Flight". In *Proceedings of the 54th Annual Forum of the American Helicopter Society*, pages 433–451, Washington, DC, May 1998.

[48] R. Ganguli. "Survey of Recent Developments in Rotorcraft Design Optimization". *Journal of Aircraft*, 41(3):493–510, May-June 2004.

[49] W. Gerstenberger, R. A. Wagner, B. Kelley, and C. W. Ellis. "The Rotary Round Table: How Can Helicopter Vibrations be Minimized". *Journal of the American Helicopter Society*, 2(3), July 1957.

[50] P. Giguere, J. Lemay, and G. Dumas. "Gurney Flap Effects and Scaling for Low-speed Airfoils". In *Proceedings of the AIAA Applied Aerodynamics Conference*, San Diego, June 1995.

[51] B. Glaz, P. P. Friedmann, and L. Liu. "Helicopter Vibration Reduction Throughout the Entire Flight Envelope Using Surrogate-Based Optimization". *Journal of the American Helicopter Society*, 54(1), January 2009.

[52] B. Glaz, P. P. Friedmann, L. Liu, D. Kumar, and C. E. S. Cesnik. "The AVINOR Aeroelastic Simulation Code and Its Application to Reduced Vibration Composite Rotor Blade Design". In *Proceedings of the 50th AIAA/ASME/ASCE/AHS/ACS Structures, Structural Dynamics and Materials Conference*, Palm Springs, CA, May 2009. AIAA Paper No. 2009-2601.

[53] Hariharan, N., and Leishman, J.G. "Unsteady Aerodynamics of a Flapped Airfoil in Subsonic Flow by Indicial Concepts". *Journal of Aircraft*, 33(5):855 – 868, September-October 1996.

[54] A. A. Hassan, B. D. Charles, Tadghighi, and T. Sankhar, *Blade-Mounted Trailing Edge Flap Control for BVI Noise Reduction*. NASA CR 4426, February 1992.

[55] J. Hong and D. S. Bernstein. "Bode Integral Constants, Collocation, and Spillover in Active Noise and Vibration Control". *IEEE Transactions on Control System Technology*, 6:111–120, 1998.

[56] S. A. Jacklin. "Second Test of a Helicopter Individual Blade Control System in the NASA Ames 40 by 80 Foot Wind Tunnel". In *Proceedings of the 2nd International American Helicopter Society Aeromechanics Specialists Conference*, Bridgeport, CT, October 1995.

[57] S. A. Jacklin, A. Blaas, D. Teves, and R. Kube. "Acoustic Results from a Full-Scale Wind Tunnel Test Evaluating Individual Blade Control". In *Proceedings of the 51st Annual Forum of the American Helicopter Society*, pages 461–480, Fort Worth, TX, May 1995.

[58] S. A. Jacklin, A. Haber, G. de Simone, T. Norman, C. Kitaplioglu, and P. Shinoda. "Full-Scale Wind Tunnel Test of an Individual Blade Control System for a UH-60 Helicopter". In *Proceedings of the 51st Annual Forum of the American Helicopter Society*, Montreal, Canada, June 2002.

[59] C. S. Jang, J. C. Ross, and R. M. Cummings. "Numerical Investigation of an Airfoil With a Gurney Flap". *Journal of Aircraft Design*, 1(2):75–88, June 1998.

[60] D. Jeffrey, X. Zhang, and D. W. Hurst. "Aerodynamics of Gurney Flaps on a Single-Element High-Lift Wing". *Journal of Aircraft*, 37(2):295–301, 2000.

[61] W. Johnson, *Self-Tuning Regulators for Multicyclic Control of Helicopter Vibrations*. NASA Technical Paper 1996, 1982.

[62] W. Johnson, *CAMRAD/JA - A Comprehensive Analytical Model of Rotorcraft Aerodynamics and Dynamics, Vol I. Theory Manual*. Johnson Aeronautics, Palo Alto, CA, 1988.

[63] D. Kahaner, C. Moler, and S. Nash. *Numerical Methods and Software*, Prentice-Hall, 1989.

[64] M. Karpel, *Design for Active and Passive Flutter Suppression and Gust Alleviation*. NASA Contractor Report 3492, November 1981.

[65] J. A. C. Kentfield. "The Potential of Gurney Flaps for Improving the Aerodynamic Performance of Helicopter Rotors". In *Proceedings of the AIAA International Powered Lift Conference*, 1993. AIAA Paper No. 93-4883.

[66] M. P. Kinzel, M. D. Maughmer, and E. P. N. Duque. "Numerical Investigation on the Aerodynamics of Oscillating Airfoils with Deployable Gurney Flaps". *AIAA Journal*, 48(7):1457–1469, July 2010.

[67] M. P. Kinzel, M. D. Maughmer, and G. L. Lesieutre. "Miniature Trailing-Edge Effectors for Rotorcraft Performance Enhancement". *Journal of the American Helicopter Society*, 52(2):146–158, April 2007.

[68] P. Konstanzer, B. Enenkl, P. Aubourg, and P. Cranga. "Recent Advances in Eurocopter's Passive and Active Vibration Control". In *Proceedings of the 64th Annual Forum of the American Helicopter Society*, Montreal, Canada, May 2008.

[69] N. A. Koratkar and I. Chopra. "Wind Tunnel Testing of a Smart Rotor Model with Trailing Edge Flaps". *Journal of the American Helicopter Society*, 47(4):263–272, October 2002.

[70] M. Kretz. "Research in Multicyclic and Active Control of Rotary Wings". *Vertica*, 1(1/2):95–105, 1976.

[71] I. M. Kroo. "Aerodynamic Concepts for Future Aircraft". In *Proceedings of the 30th AIAA Fluid Dynamics Conference*, Norfolk, VA, Jun-July 1999. AIAA Paper No. 99-2003.

[72] D. Lee, J. G. Leishman, and J. D. Baeder. "A Nonlinear Indicial Method for the Calculation of Unsteady Airloads". In *Proceedings of the 59th American Helicopter Society Annual Forum*, Phoenix, AZ, May 2003.

[73] Hak-Tae Lee and I. M. Kroo. "Computational Investigation of Airfoils with Miniature Trailing Edge Control Surfaces". In *Proceedings of the 42nd AIAA Aerospace Sciences Meeting and Exhibit*, Reno, NV, Jan 2004. AIAA Paper No. 2004-1051.

[74] Hak-Tae Lee, I. M. Kroo, and S. Bieniawski. "Flutter Suppression for High Aspect Ratio Flexible Wings Using Microflaps". In *Proceedings of the 43rd AIAA/ASME/ASCE/AHS/ACS Structures, Structural Dynamics and Materials Conference*, Reno, NV, Apr 2002. AIAA Paper No. 2002-1717.

[75] Y. Li, J. Wang, and P. Zhang. "Influences of Mounting Angles and Locations on the Effects of Gurney Flaps". *Journal of Aircraft*, 40(3):494–498, May-June 2003.

[76] R. H. Liebeck. "Design of Subsonic Airfoils for High Lift". *Journal of Aircraft*, 15(9):547–561, Sept 1978.

[77] C. Lim, C. Tung, Y. Yu, C. Burley, T. F. Brooks, D. Boyd, B. G. van der Wall, O. Schneider, P. Richard, P. Beaumier, Y. Delrieux, and K. Pengel. "Hart-II: Prediction of Blade-Vortex Interaction Loading". In *Proceedings of the 29th European Rotorcraft Forum*, Friedrichschafen, Germany, September 2003.

[78] L. Liu. *BVI Induced Vibration and Noise Alleviation By Active and Passive Approaches*. PhD Dissertation, University of Michigan, Ann Arbor, 2005.

[79] L. Liu, P. P. Friedmann, I. Kim, and D. S. Bernstein. "Rotor Performance Enhancement and Vibration Reduction in Presence of Dynamic Stall Using Actively Controlled Flaps". *Journal of the American Helicopter Society*, 53(4):338–350, October 2008.

[80] L. Liu, P. P. Friedmann, and A. K. Padthe. "An Approximate Unsteady Aerodynamic Model for Flapped Airfoils Including Improved Drag Predictions". In *Proceedings of the 34th European Rotorcraft Forum*, Liverpool, UK, September 2008.

[81] Loewy, R.G. "Helicopter Vibrations: A Technological Perspective". *Journal of the American Helicopter Society*, 29(4):4 – 30, October 1984.

[82] B. Malovrh and F. Gandhi. "Localized Individual Pitch Control for Reduction of Helicopter Blade-Vortex Interaction Noise". In *Proceedings of the 28th European Rotorcraft Forum*, pages 6.1–6.10, Bristol, England, September 2002.

[83] C. G. Matalanis and J. K. Eaton. "Wake Vortex Alleviation Using Rapidly Actuated Segmented Gurney Flaps". *AIAA Journal*, 45(8):1874–1884, August 2007.

[84] M. D. Maughmer and G. Bramesfeld. "Experimental Investigation of Gurney Flaps". *Journal of Aircraft*, 45(6):2062–2067, November-December 2008.

[85] F. R. Menter. "Two-equation Eddy-Viscosity Turbulence Models for Engineering Applications". *AIAA Journal*, 32(8):1598–1605, Aug 1994.

[86] J. H. Milgram, I. Chopra, and F. K. Straub. "Rotors with Trailing Edge Flaps: Analysis and Comparison with Experimental Data". *Journal of the American Helicopter Society*, 43(4):319–332, October 1998.

[87] T. A. Millott and P. P. Friedmann, *Vibration Reduction in Helicopter Rotors Using an Actively Controlled Partial Span Trailing Edge Flap Located on the Blade*. NASA CR 4611, June 1994.

[88] B. Min, L. N. Sankar, N. Rajmohan, and J. V. R. Prasad. "Computational Invetigation of Gurney Flap Effects on Rotors in Forward Flight". *Journal of Aircraft*, 46(6):1957–1964, Nov-Dec 2009.

[89] B. Y. Min, L. Sankar, and O. A. Bauchau. "A CFD-CSD Coupled Analysis of Hart II Rotor Vibration Reduction Using Gurney Flaps". In *Proceedings of the 66th American Helicopter Society Annual Forum*, Phoenix, AZ, May 11-13 2010.

[90] R. Y. Myose, J. Lietsche, D. Scholz, H. Zingel, S. Hayashibara, and I. Heron. "Flow Visualization Study on the Effect of a Gurney Flap in a Low Reynolds Number Compressor Cascade". In *Proceedings of the 6th AIAA Aviation Technology, Integration and Operations Conference*, Wichita, KS, Sept 2006.

[91] T. F. Myrtle. *Development of an Improved Aeroelastic Model for the Investigation of Vibration Reduction in Helicopter Rotors using Trailing Edge Flaps*. PhD Dissertation, University of California, Los Angeles, 1998.

[92] T. F. Myrtle and P. P. Friedmann. "Application of a New Compressible Time Domain Aerodynamic Model to Vibration Reduction in Helicopters Using an Actively Controlled Flap". *Journal of the American Helicopter Society*, 46(1):32–43, January 2001.

[93] D. T. Yen Nakafuji, C. P. van Dam, R. L. Smith, and S. D. Collins. "Active Load Control for Airfoils using Microtabs". *Journal of Solar Energy Engineering*, 123(4):282–289, November 2001.

[94] J. Nelson and N. Koratkar. "Effect of Miniaturized Gurney Flaps on Aerodynamic Performance of Microscale Rotors". *Journal of Aircraft*, 42(2):557–560, Mar-Apr 2005.

[95] V. R. Nikolic. "Two Aspects of the Use of Full- and Partial-Span Gurney Flaps". *Journal of Aircraft*, 44(5):1745–1748, Sept-Oct 2007.

[96] Y. Niu, T. Hsu, C. T. Hsieh, C. C. Chang, and C. C. Chu. "How Does a Gurney Flap Enhance the Aerodynamic Forces". *AIAA Journal*, 48(11):2710–2714, November 2010.

[97] A. K. Padthe, L. Liu, and P. P. Friedmann. "A CFD-Based Nonlinear Reduced-Order Aerodynamic Model for Comprehensive Simulation of Rotorcraft with Active Microflaps". In *Proceedings of the 65th American Helicopter Society Annual Forum*, Grapevine, TX, May 2009.

[98] D. Patt. *Simultaneous Noise and Vibration Reduction in Rotorcraft Using Actively Controlled Flaps and Including Performance Considerations*. PhD Dissertation, University of Michigan, Ann Arbor, 2004.

[99] D. Patt, L. Liu, J. Chandrasekar, D. S. Bernstein, and P. P. Friedmann. "Higher-Harmonic-Control Algorithm for Helicopter Vibration Reduction Revisited". *Journal of Guidance, Control, and Dynamics*, 28(5):918–930, September-October 2005.

[100] D. Patt, L. Liu, and P. P. Friedmann. "Active Flaps for Noise Reduction: A Computational Study". In *American Helicopter Society 61st Annual Forum Proceedings*, Grapevine, TX, June 1-3, 2005.

[101] D. Patt, L. Liu, and P. P. Friedmann. "Rotorcraft Vibration Reduction and Noise Prediction Using a Unified Aeroelastic Response Simulation". *Journal of the American Helicopter Society*, 50(1):95–106, January 2005.

[102] D. Patt, L. Liu, and P. P. Friedmann. "Simultaneous Vibration and Noise Reduction in Rotorcraft Using Aeroelastic Simulation". *Journal of the American Helicopter Society*, 51(2):127–140, April 2006.

[103] O. Peroomian, S. Chakravarthy, and U. Goldberg. "A "Grid-Transparent" Methodology for CFD". In *AIAA Paper 97-0724*, Reno, NV, January 1997.

[104] O. Peroomian, S. Chakravarthy, S. Palaniswamy, and U. Goldberg. "Convergence Acceleration for Unified-Grid Formulation Using Preconditioned Implicit Relaxation". In *AIAA Paper 98-0116*, Reno, NV, January 1998.

[105] D. Petot. "Differential Equation Modeling of Dynamic Stall". *La Recherche Aérospatiale*, 5:59–71, 1989.

[106] W. H. Press, B. P. Flannery, S. A. Teukolsky, and W. T. Vetterling. *Numerical Recipes in FORTRAN 77*, Cambridge University Press, 1992.

[107] G. Rahier and Y. Delrieux. "Blade-Vortex Interaction Noise Prediction Using a Rotor Wake Roll-Up Model". *Journal of Aircraft*, 34(4):522–530, July-August 1997.

[108] G. Reichert. "Helicopter Vibration Control - A Survey". *Vertica*, 5(1):1–20, 1981.

[109] W. P. Rodden and E. Albano. "A Doublet-Lattice Method for Calculating Lift Distributions on Oscillating Surfaces in Subsonic Flows". *AIAA Journal*, 7(2):279–285, February 1969.

[110] K. L. Rogers, *Airplane Math Modeling Methods for Actively Control Design*. AGARD-CP-228, August 1977.

[111] B. Roget and I. Chopra. "Closed-Loop Test of a Rotor with Individually Controlled Trailing-Edge Flaps for Vibration Reduction". *Journal of the American Helicopter Society*, 55(1), 2010.

[112] A. Rosen and P. P. Friedmann, *Nonlinear Equations of Equilibrium for Elastic Helicopter or Wind Turbine Blades Undergoing Moderate Deformation*. NASA CR 159478, December 1978.

[113] D. Roth. "Advanced Vibration Reduction by IBC Technology". In *Proceedings of the 30th European Rotorcraft Forum*, Marseille, France, September 2004.

[114] K. Schittkowski. "NLQPL: A FORTRAN-Subroutine Solving Constrained Nonlinear Programming Problems". *Annals of Operations Research*, 5:485–500, 1985.

[115] O. Schneider and B. van der Wall. "Final Analysis of HART II Blade Deflection Measurement". In *Proceedings of the 29th European Rotorcraft Forum*, Friedrichschafen, Germany, September 2003.

[116] M. P. Scully. *Computation of Helicopter Rotor Wake Geometry and its Influence on Rotor Harmonic Airloads*. PhD Dissertation, Aeroelastic Research Laboratory, Massachusetts Institute of Technology, 1975.

[117] L. F. Shampine and M. K. Gordon. *Computer Solution of Ordinary Differential Equations - The Initial Value Problem*, W. H. Freeman and Co., San Francisco, CA, 1975.

[118] S. J. Shin and C. E. S. Cesnik. "Forward Flight Response of the Active Twist Rotor for Helicopter Vibration Reduction". In *Proceedings of the 42th AIAA/ASME/ASCE/AHS/ACS Structures, Structural Dynamics and Materials Conference*, number 2001-1357 in SDM2001, Seattle, Wash., April 2001.

[119] S. J. Shin, C. E. S. Cesnik, and S. R. Hall. "Control of Integral Twist-Actuated Helicopter Blades for Vibration Reduction". In *Proceedings of the American Helicopter Society 58th Annual Forum*, Montréal, Canada, June 2002.

[120] S. J. Shin, C. E. S. Cesnik, and S. R. Hall. "Closed-Loop Control Tests of the NASA/ARMY/MIT Active Twist Rotor for Vibration Reduction". In *Proceedings of the American Helicopter Society 59th Annual Forum*, Phoenix, AZ, June 2003.

[121] M. K. Singh, K. DhanaLakshmi, and S. K. Chakrabartty. "Navier-Stokes Analysis of Airfoils with Gurney Flap". *Journal of Aircraft*, 44(5):1487–1493, Sept-Oct 2007.

[122] W. Splettstoesser, R. Kube, W. Wagner, U. Seelhorst, A. Boutier, F. Micheli, E. Mercker, and K. Pengel. "Key Results From a Higher Harmonic Control Aeroacoustic Rotor Test (HART)". *Journal of the American Helicopter Society*, 42(1):58–78, January 1997.

[123] W. Splettstoesser, K. J. Schultz, R. Kube, T. F. Brooks, E. R. Booth, George Niesl, and Olivier Streby. "A Higher Harmonic Control Test in the DNW to Reduce Impulsive BVI Noise". *Journal of the American Helicopter Society*, 39(4):3–13, October 1994.

[124] W. Splettstoesser, B. van der Wall, and F. Schultz. "The Effect of Individual Blade Pitch Control of Flight Test and Simulation Results". In *Proceedings of the 24th European Rotorcraft Forum*, pages AC07.1–AC07.15, Marseilles, France, September 1998.

[125] W. R. Splettstoesser, G. Niesl, F. Cenedese, F. Nitti, and D. G. Papanikas. "Experimental Results of the European HELINOISE Aeroacoustics Rotor Test". *Journal of the American Helicopter Society*, 40(3), April 1995.

[126] A. E. Staple. "Evaluation of Active Control of Structural Response as a Means of Reducing Helicopter Vibration". In *Proceedings of the 46th Forum of the American Helicopter Society*, pages 3–17, Washington, D.C., May 1990.

[127] Bruce L. Storms and Cory S. Jang. "Lift Enhancement of an Airfoil Using a Gurney Flap and Vortex Generators". *Journal of Aircraft*, 31(3):542–547, May-June 1994.

[128] F. K. Straub, V.R. Anand, T. S. Birchette, and B. H. Lau. "Wind Tunnel Test of the SMART Active Flap Rotor". In *Proceedings of the 65th American Helicopter Society Annual Forum*, Grapevine,TX, May 2009.

[129] F. K. Straub, D. K. Kennedy, A. D. Stemple, V.R. Anand, and T. S. Birchette. "Development and whirl tower test of the SMART active flap rotor". *Proceedings of SPIE: Smart Structures and Materials 2004*, 5388:202–212, July 2004.

[130] S. M. Swanson, S. A. Jacklin, . Blaas, G. Niesl, and R. Kube. "Reduction of Helicopter BVI Noise, Vibration, and Power Consumption through Individual Blade Control". In *Proceedings of the 51st Annual Forum of the American Helicopter Society*, pages 662–680, Fort Worth, TX, May 1995.

[131] L. Tauszig. *Analysis of Helicopter Blade-Vortex Interaction Noise With Application to Adaptive-Passive and Active Alleviation Methods*. PhD Dissertation, The Pennsylvania State University, 2002.

[132] M. R. Thiel, G. A. Lesieutre, M. D. Maughmer, and G. H. Koopmann. "Actuation of an Active Gurney Flap for Rotorcraft Applications". In *47th AIAA/ASME/ASCHE/AHS/ASC Structures, Structural Dynamics & Materials Conference*, pages 1–11, Newport, RI, May 1-4 2006. AIAA Paper 2006-2181.

[133] C. Tung, R. Kube, T. Brooks, and G. Rahier. "Prediction and Measurement of Blade-Vortex Interaction". *Journal of Aircraft*, 35(2):260–266, March-April 1998.

[134] C. P. van Dam, D. T. Yen, and P. M. H. W. Vijgen. "Gurney Flap Experiments on Airfoils and Wings". *Journal of Aircraft*, 36(2):484–486, 1999.

[135] B. G. van der Wall, C. Junker, C. Burley, T. Brooks, Y. Yu, P. Raffel, and W. Wagner. "The HART II test in the LLF of the DNW - a Major Step towards Rotor Wake Understanding". In *Proceedings of the 28th European Rotorcraft Forum*, Bristol, England, September 2002.

[136] C. Venkatesan and P. P. Friedmann. "A New Approach to Finite State Modeling of Unsteady Aerodynamics". In *Proceedings of the 27th AIAA/ASME/ASCE/AHS/ACS Structures, Structural Dynamics and Materials Conference*, pages 178–191, San Antonio, TX, May 1986. AIAA Paper No. 1986-865.

[137] R. Vepa, *Finite State Modeling of Aeroelastic Systems*. NASA Contractor Report 2779, 1977.

[138] S. Vey, O. C. Paschereit, D. Greenblatt, and R. Meyer. "Flap Vortex Management by Active Gurney Flaps". In *Proceedings of the 46th AIAA Aerospace Sciences Meeting and Exhibit*, Reno, NV, Jan 2008. AIAA Paper No. 2008-286.

[139] S. P. Viswanathan and A. W. Myers. "Reduction of Helicopter Vibration Through Control of Hub Impedance". *Journal of the American Helicopter Society*, 25(4):3–12, October 1980.

[140] D. A. Wachspress and T. R. Quackenbush. "BVI Noise Prediction Using a Comprehensive Rotorcraft Analysis". In *Proceedings of the American Helicopter Society 57th Annual Forum*, Washington, DC, May 2001.

[141] D. A. Wachspress and T. R. Quackenbush. "BVI Noise Mitigation Via Steady Flap Deflection – An Analysis-Led Test Program". In *Proceedings of the American Helicopter Society 4th Decennial Specialist's Conference on Aeromechanics*, San Francisco, CA, Jan 2004.

[142] M. L. Wilbur, P. H. Mirick, Jr. W. T. Yeager, C. W. Langston, S. J. Shin, and C. E. S. Cesnik. "Vibratory Loads Reduction Testing of the NASA/Army/MIT Active Twist Rotor". In *Proceedings of the American Helicopter Society 57th Annual Forum*, Washington, D. C., May 2001.

[143] D. G. Wilson, D. E. Berg, D. W. Li, and J. R. Zayas. "Optimized Active Aerodynamic Blade Control for Load Alleviation on Large Wind Turbines". In *AWEA WINDPOWER 2008 Conference & Exhibition*, Houston, TX, June 1-4 2008.

[144] Y. H. Yu. "Rotor Blade-Vortex Interaction Noise". *Progress in Aerospace Sciences*, 36(2):97–115, February 2000.

[145] Y. H. Yu, B. Gmelin, W. Splettstoesser, J. J. Philippe, J. Prieur, and T. F. Brooks. "Reduction of Helicopter Blade-Vortex Interaction Noise by Active Rotor Control Technology". *Progress in Aerospace Sciences*, 33(10):647–687, September 1997.

[146] Y. H. Yu, C. Tung, B. van der Wall, H. J. Pausder, Casey Burley, Thomas Brooks, P. Beaumier, Y. Delrieux, E. Mercker, and K. Pengel. "The HART-II Test: Rotor Wakes and Aeroacoustics with Higher-Harmonic Pitch Control (HHC) Inputs - The Joint German/French/Dutch/US Project -". In *Proceedings of the 58th Annual Forum of the American Helicopter Society*, Montreal, Canada, June 2002.